High temperature oxidation of iron-chromium alloys

Mikkelsen, Lars

Publication date:
2003

Document Version
Publisher's PDF, also known as Version of record

RISØ

Risø-PhD-thesis

High Temperature Oxidation of Iron-Chromium Alloys

Lars Mikkelsen

Risø-PhD-2(EN)

Risø National Laboratory
Roskilde, Denmark
June 2003

Author: Lars Mikkelsen
Title: High Temperature Oxidation of Iron-Chromium Alloys
Department: Fuel Cells and Solid State Chemistry Department

This thesis is submitted in partial fulfilment of the requirements for the Ph.D. degree at University of Southern Denmark

Abstract (max. 2000 char.):

See page 3

Risø-PhD-2(EN)
June 2003

ISBN 87-550-3353-9

Contract no.:

Group's own reg. no.:

Sponsorship:

Cover :

Pages: 170
Tables:
References:

Information Service Department
Risø National Laboratory
P.O.Box 49
DK-4000 Roskilde
Denmark
Telephone +45 46774004
bibl@risoe.dk
Fax +45 46774013
www.risoe.dk

Preface

This thesis is part of the fulfilment of the requirements for the Ph.D. degree at University of Southern Denmark. The majority of the work is based on studies performed at the SOFC group at the Materials Research Department, Risø National Laboratory. Part of the studies was carried out at the Physics Department, and at the Department of Chemistry, University of Southern Denmark.

The work was carried out under the supervision of Eivind M. Skou, Department of Chemistry, University of Southern Denmark, and Søren Linderoth, Peter H. Larsen and Mogens Mogensen, Materials Research Department, Risø National Laboratory. The work was initiated in February 2000 and completed in June 2003 with the submission of the present thesis.

Lars Mikkelsen
Risø National Laboratory, June 2003

Acknowledgement

During the work, I have received much help through fruitful discussions and help during the experimental stages.

At the Physics Department, University of Southern Denmark, I would like to thank Per Morgen for providing equipment and for much help performing the Auger electron spectroscopy measurements.

I would like to thank John Nicholls, Cranfield University, for good advise on preparing fractured specimens for the use in electron microscopy.

Thanks to Jørgen Bilde-Sørensen for much help with the electron microscopy, especially the TEM work, which could not have been done without his help.

Thanks to Anette Hansson, Peter Friehling and to Charles Hatchwell for many good discussions during the present work and for many good hours.

Also thanks to the many colleagues at the SOFC group for helping with many small things, and for making the stay at Risø a pleasant experience.

Finally, thanks to my supervisors Søren Linderoth, Eivind M. Skou, Mogens Mogensen and Peter H. Larsen for many good discussions during the work.

Abstract

The high temperature oxidation of the ferritic alloy $Fe_{78}Cr_{22}$ has been investigated in the present work. The effect of small alloying additions of cerium and/or silicon was also investigated. The alloys were oxidized at 973, 1173 and 1373 K in either air or a hydrogen/argon mixture. The various reaction atmospheres contained between 0.02 and 50% water vapour.

The oxide scales formed on the various alloys at 973 K consisted of thin chromia layers.

The oxide scales grown on the alloys at 1173 K also consisted of a chromia layer. The microstructure of the chromia scales was found to depend on the reaction atmosphere. The chromia scales grown in hydrogen/argon atmospheres formed oxide whiskers and oxide ridges at the surface of the scales, while the chromia scales grown in air formed larger oxide grains near the surface. This difference in oxide microstructure was due to the vaporization of chromium species from the chromia scales grown in air. Two different growth mechanisms are proposed for the growth of oxide whiskers. The growth rate of the chromia scales was independent of the oxygen activity. This is explained by a growth mechanism of the chromia scales, where the growth is governed by the diffusion of interstitial chromium.

The addition of silicon to the iron-chromium alloy resulted in the formation of silica particles beneath the chromia scale. The presence of silicon in the alloy was found to decrease the growth rate of the chromia scale. This is explained by a blocking mechanism, where the silica particles beneath the chromia scale partly block the outwards diffusion of chromium from the alloy to the chromia scale.

The addition of cerium to the iron-chromium alloy improved the adhesion of the chromia scale to the alloy and decreased the growth rate of chromia. It was observed that the minimum concentration of cerium in the alloy should be 0.3 at.% in order to observe an effect of the cerium addition. The effect of cerium is explained by the “reactive element effect”.

The oxide scales grown on the various alloys at 1373 K exhibited the presence of thick iron rich oxides in the scales. The presence of iron rich scales is described as a result of failure of the chromia scale and subsequent breakaway oxidation of the alloy. The breakaway oxidation was initiated at the sample edges. Furthermore, the breakaway oxidation was affected by the oxygen activity in the reaction atmosphere, where a low oxygen activity protected the alloys from breakaway oxidation. A mechanism for the breakaway oxidation is put forward, which explains the observed oxidation behaviour of the alloys.

The effect of water vapour on the chromia growth rate was investigated. It was found that the presence of water vapour in the reaction atmosphere increased the growth rate of chromia. It is proposed that hydrogen dissolves in the chromia scale and thereby increases the transport of reactants through the chromia scale. Furthermore, the growth rate of chromia was observed to decrease, when the alloys were oxidized in air containing large amounts of water vapour. This is a result of vaporization of chromium containing species from the chromia scale during the oxidation. The effect

of water vapour was studied through thermogravimetric measurements in various reaction atmospheres. The measurements were partly performed on an equipment developed during this Ph.D.-study. The development was performed through a collaboration with Netzsch. The development of the novel equipment is described in this thesis.

Resumé

Høj-temperatur oxidationen af en ferritisk legering $Fe_{78}Cr_{22}$ er undersøgt i dette arbejde. Oxidationsegenskaberne af legeringen er også undersøgt efter en lille legeringstilsætning af silicium og/eller cerium. Legeringerne blev oxideret ved 973, 1173 og 1373 K i luft eller i en hydrogen/argon blanding. De forskellige reaktions gasser indeholdt mellem 0.02 og 50% vand damp.

Under oxidationen af de forskellige legeringer ved 973 K blev der dannet et oxidlag bestående af krom(III)oxid.

Under oxidation af legeringerne ved 1173 K blev der også dannet et lag bestående af krom(III)oxid. Mikrostrukturen af kromoxidlaget afhang af reaktionsgassen. Overfladen af kromoxidlaget bestod af oxidwhiskers og oxidhøjderygge når oxidet blev dannet i hydrogen/argon blandinger, mens overfladen af kromoxidlaget bestod af store oxidkorn når oxidlaget blev dannet i luft. Denne forskel skyldes afdampning af kromholdige forbindelser fra oxidlaget når det blev dannet i luft. To forskellige vækstmekanismer fremlægges til at forklare dannelsen af oxidwhiskers. Dannelseshastigheden for kromoxidlagene er uafhængigt af oxygen partialtrykket. Dette er forklaret ved hjælp af en vækstmekanisme for oxidlaget, hvor væksten er bestemt af diffusionen af interstitielle krom.

Tilsætningen af silicium til jern-krom legeringen resulterede i dannelsen af siliciumoxidpartikler under kromoxidlaget. Tilstedeværelsen af silicium i legeringen nedsatte vækshastigheden af kromoxidlaget. Dette forklares ved hjælp af en blokerings mekanisme, hvor siliciumoxidpartiklerne under kromoxidlaget delvist blokerer den udadgående diffusion af krom fra legeringen til kromoxidlaget.

Tilsætningen af cerium til jern-krom legeringen forbedrede vedhæftningen af kromoxidlaget til legeringen og nedsatte vækshastigheden af kromoxidlaget. Koncentration af cerium i legeringen skal dog være mindst 0.3 at.% for at iagttage en fordelagtig effekt af cerium. Effekten af cerium forklares ved hjælp af ”reactive element” effekten.

Under oxidation af legeringerne ved 1373 K blev der dannet et tykt oxidlag bestående af jernholdige oxider. Tilstedeværelsen af jernholdige oxider forklares ved brud af kromoxidlaget. Dette resulterer i ”breakaway” oxidation. Breakaway oxidationen startede omkring kanterne af prøverne. Breakaway oxidationen afhang af oxygen partialtrykket i reaktionsgassen, hvor et lavt oxygen partialtryk beskyttede mod breakaway oxidation. En mekanisme for breakaway oxidationen fremlægges, som forklarer de observerede oxidationsresultater.

Effekten af vandindholdet på oxidationshastigheden af kromoxidlaget er undersøgt. Tilstedeværelsen af vanddamp i reaktionsgassen forøgede oxidationshastigheden af kromoxidlaget. Det foreslås at hydrogen opløses i kromoxidlaget og derved forøger transporten af reaktanter gennem kromoxidlaget. Oxidationshastigheden af kromoxidlaget aftog når legeringerne blev oxideret i luft, som indeholdt store mængder vanddamp. Dette skyldes afdampning af kromholdige forbindelser fra kromoxidlaget under oxidationen. Effekten af vanddamp blev studeret ved hjælp af termogravimetriske målinger i forskellige reaktionsgasser. En del af målingerne blev

udført på et eksperimentelt udstyr, som blev udviklet gennem dette Ph.D.-studie. Udviklingen af udstyret blev gennemført i et samarbejde med Netzsch. Udviklingen af det nye udstyr er beskrevet i denne afhandling.

List of common symbols

μ_I	Chemical potential
η_I	Electrochemical potential
K	Boltzmann constant
a_i	Activity of species i
T	Temperature
L_{ij}	Onsager coefficient
z_i	Charge of species i
ϕ	Electrical potential
b_i	Mechanical mobility for species i
D_K	Component diffusion coefficient
W	Thermodynamic factor
E	Elementary charge
J_i	Flux for species i
$\overrightarrow{X_j}$	Driving force
u_i	Electrical mobility for species i
v_i	Mean particle velocity for species i
I_i	Current density
σ_I	Electrical conductivity
H	Haven–Ratio
G_m	Gibbs energy of migration
G_f	Gibbs energy of formation
E_A	Activation energy
t_i	Transport number of species i
k_m	Parabolic rate constant
k_p	Parabolic rate constant
k_w	Parabolic rate constant
M	Molar mass
ρ	Density
N_A	Avogadro's number
D_l	Lattice diffusion coefficient
D_{gb}	Grain boundary diffusion coefficient
W	Weight
R	Gas constant
c_i	Concentration of species i
D_i	Diffusion coefficient for species i
D_{tr}	Tracer diffusion coefficient
ΔG	Change of Gibbs free energy
ΔH	Change of Enthalpi
ΔS	Change of Entropi
p	Pressure
K_{sp}	Equilibrium constant

List of abbreviation

SOFC	Solid oxide fuel cell
TEC	Thermal expansion coeffient
TG	Thermogravimetry
SEM	Scanning electron microscopy
TEM	Transmission electron microscopy
EDX	Energy dispersive X-ray analysis
AES	Auger electron spectroscopy
XRD	X-ray diffraction
SIMS	Secondary-ion mass spectroscopy
PBR	Pilling-Bedworth ratio
RE	Reactive element
REE	Reactive element effect
Erfc(z)	Complementary error function of z
A1	$Fe_{78}Cr_{22}$
A1-Si	$Fe_{78}Cr_{22}$-$Si_{0.3}$
A1-Ce	$Fe_{78}Cr_{22}$-$Ce_{0.3}$
A1-CeSi	$Fe_{78}Cr_{22}$-$Ce_{0.15}Si_{0.15}$

Table of content

1 Introduction

1.1 Background

The solid oxide fuel cell (SOFC) is being developed as a new promising electrical power generator. It is possible with SOFC's to convert fuel (e.g. hydrogen and natural gas) to electrical power with a high efficiency [1]. Furthermore, the amount of pollution (CO_2, NO_x) is reduced during power generation in a SOFC compared to a traditional power plant [1]. The flat plate design of a SOFC stack is shown in Fig. 1.

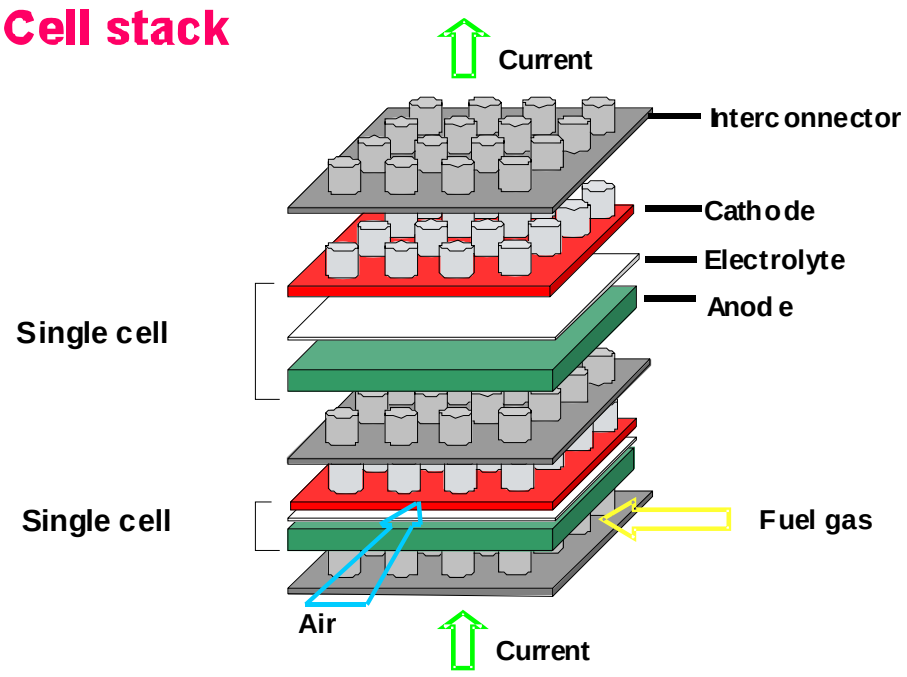

Fig. 1. Flat plate design for a SOFC stack.

The interconnectors in a SOFC stack provide the electrical contact between single cells and separate the fuel on the anode side from the air on the cathode side during operation. Doped lanthanum chromites or relatively expensive high-Cr alloy composites have previously been used as interconnector materials [2]. However, lowering of the operational temperature, from approximately 1273 K to 923-1023 K, opens the possibility of using cheaper alloys.

The interconnector plates have several requirements, such as a high electrical conductivity, gas tightness, thermal expansion matching with the cell, and chemical stability with other cell components [3]. High temperature oxidation resistant alloys, which could be suitable as interconnector materials, form Al_2O_3, Cr_2O_3 and SiO_2

scales. Chromia forming alloys are usually considered as the best metallic interconnector materials. This is due to a good balance between the slow growth rate of the oxide scale and the electrical conductivity of the oxide scale [4]. The thermal expansion coefficients (TEC) have previously been measured for iron-chromium alloys, and a ferritic alloy containing ca. 20 wt.% chromium has TEC-values that match other cell components [2]. Consequently, iron-chromium alloys have been the subject of numerous studies during the last decade for potential use as an interconnector material in a SOFC stack (see e.g. [5-8]). Chromia forming alloys are also used for a variety of other high temperature applications, e.g. gas turbines and nuclear reactors [9,10].

1.2 Objective of work

The objective of the present thesis is to investigate the oxidation behaviour of an iron-chromium alloy, which may be used as interconnector material in a SOFC stack. This includes investigations of

- The effect of oxygen and water activity in the reaction atmosphere
- The effect of oxidation time
- The effect of cerium and silicon alloying additions

1.3 Structure of the present thesis

Chapter 2 is devoted to theory, which is used in the present work. This includes the theory for growth of oxides, and thermodynamic calculations in the iron-chromium oxide system.

The development or the purchase of a thermogravimetric equipment, which can measure in high water concentrations was a starting point of the present Ph.D.-study. The thermogravimetric project, which is a significant part of the scientific development during the present work, is described in chapter 3.

The general experimental procedures used throughout the work are described in chapter 4.

The oxidation behaviour of an iron-chromium alloy is presented in chapter 5. This includes the effect of oxygen and water activity on the oxide microstructure and growth kinetics.

The effect of silicon and cerium alloying additions on the growth behaviour of an iron-chromium alloy is presented in chapter 6.

While the results presented in chapter 5 and 6 are focused on the steady state oxidation behaviour at 1173 K, the effects of temperature and oxidation time on the oxidation behaviour of iron-chromium alloys are described in chapter 7.

Thermogravimetric investigations of the oxidation behaviour are presented in chapter 8. This includes investigations, which were performed using the equipment described in chapter 3.

1.4 Publications of experimental results

L. Mikkelsen and S. Linderoth, “High Temperature Oxidation of Fe-Cr Alloy in O_2-H_2-H_2O Atmospheres; Microstructure and Kinetics”, submitted to Materials Science & Engineering A. The submitted material is included as part of chapter 5 and 7 in the present thesis.

L. Mikkelsen and S. Linderoth, “The effect of small silicon addition on the oxidation of Fe-Cr alloy”, in preparation for publication. Included as part of chapter 6 in the present thesis.

The following articles were also published during the present ph.d.-study, but not included as part of the thesis.

Mikkelsen, L. and Skou, E., Determination of the oxygen chemical diffusion coefficient in perovskites by a thermogravimetric method, Journal of Thermal Analysis and Calorimetry, 64 (3), 873-878, 2001

Mikkelsen, L.; Larsen, P.H.; Linderoth, S., High temperature oxidation of Fe22Cr-alloy, Journal of Thermal Analysis and Calorimetry, 64 (3), 879-886, 2001

Mikkelsen, L.; Andersen, I.G.K.; Skou, E., Oxygen transport in La1-xSrxFe1-yMnyO3-delta perovskites, Solid State Ionics, 152, 703-707 Part A Sp. Iss. SI, 2002

2 Theory

2.1 Transport theory

2.1.1 Introduction

Various mechanisms have been put forward to describe the ionic and electronic transport behaviour in solids. This discussion is limited to the case where the transport of ionic and electronic defects can be described by a thermal activated hopping of defects between neighboring lattice sites.

Two different approaches can be used to derive expressions for the transport of defects. The first is based on linear irreversible thermodynamics, while the second is based on a statistical treatment of defect transport. The resulting expressions using these approaches are the same when the defects behave independently [11]. In this section, the expressions will be derived from linear irreversible thermodynamics.

2.1.2 Linear irreversible thermodynamics

The flux for a particle is defined relative to a frame of reference or an average velocity. The mobility of one of the atoms in the lattice is often sufficiently low such that its sublattice can be taken as a frame of reference [12]. The flux for species i can according to linear irreversible thermodynamics be written as a linear expression

$$\overrightarrow{J_i} = \sum_j L_{ij} \overrightarrow{X_j} \qquad \text{Eq. 1}$$

where $\overrightarrow{X_j}$ is a driving force, and L_{ij} is the transport coefficient (Onsager coefficient) for the flux i with respect to the driving force j. The vector notation will be omitted in the following for a lighter notation. If the system of interest is isothermal, i.e. without thermal gradients, the driving force is the negative gradient of the electrochemical potential: $-\nabla\eta$ [11]. The electrochemical potential is given by

$$\eta_i = \mu_i + z_i e\phi \qquad \text{Eq. 2}$$

where z_i is the charge of species i, e the elementary charge, and ϕ the electrical potential. The chemical potential μ_i is given by

$$\mu_i = \mu_i^o + kT \ln a_i \qquad \text{Eq. 3}$$

where μ_i^o is a reference chemical potential, k the Boltzmann constant, T the temperature, and a_i the activity of species i. It is often assumed that defect interactions can be neglected, and hence that the Onsager cross terms ($L_{ij,}$ $i \neq j$) vanish [11]. This is assumed in the present work. The transport coefficient is assumed to be independent of the direction in the solid and will consequently be represented as a scalar. This assumption is valid for isotropic systems; the transport coefficient is in general a tensor [13]. Furthermore, it will be assumed that there is electrical neutrality and equilibrium for internal reactions in the system of interest.

The transport coefficient L_{ii} is often defined relative to the driving force. This will also be done in the present work. The diffusion coefficient and the electrical conductivity will be defined in the following.

It is common to define a mechanical mobility b_i as the ratio between the mean particle velocity v_i and the driving force for species i

$$b_i = \frac{|v_i|}{|X_i|} \qquad \text{Eq. 4}$$

The flux of a particle is equal to the product of the concentration and the mean velocity

$$J_i = c_i v_i \qquad \text{Eq. 5}$$

From Eq. 1, Eq. 4 and Eq. 5, it follows

$$L_{ii} = c_i b_i \qquad \text{Eq. 6}$$

so the transport coefficients can in general be expressed by the mechanical mobility and the concentration of species i.

2.1.3 Diffusion

For simplicity, the transport equations will be derived for transport in one dimension. For the diffusion of particles in a chemical potential gradient, the flux in one dimension becomes (via Eq. 1 and Eq. 6)

$$J_i = -c_i b_i \frac{d\mu_i}{dx} \qquad \text{Eq. 7}$$

From Eq. 3, this can be written

$$J_i = -c_i b_i kT \frac{d \ln a_i}{dx} = -b_i kT \frac{d \ln a_i}{d \ln c_i} \frac{dc_i}{dx} \qquad \text{Eq. 8}$$

The component diffusion coefficient is defined by

$$D_K = b_i kT \qquad \text{Eq. 9}$$

If ideal conditions can be assumed, the activity is equal to the concentration. In this case, Eq. 8 can be recognized as Fick's 1. law

$$J_i = -D_K \frac{dc_i}{dx} \qquad \text{Eq. 10}$$

In contrast, if the activity is not equal to the concentration, Ficks's 1. law is written

$$J_i = -D_K \frac{d \ln a_i}{d \ln c_i} \frac{dc_i}{dx} = -D_K W \frac{dc_i}{dx} \qquad \text{Eq. 11}$$

where W is the thermodynamic factor.

2.1.4 Electrical conductivity

If $\nabla\mu = 0$, the driving force for the flux of charged species is proportional to the gradient of the electrical potential, and the flux equation becomes

$$J_i = -L_{ii} z_i e \frac{d\phi}{dx} \qquad \text{Eq. 12}$$

The flux of charged species is usually expressed with the help of the current density I_i, and the transport coefficient is expressed by the electrical conductivity σ_i. The current density and the electrical conductivity are defined by

$$I_i = z_i e J_i = -L_{ii} z_i^2 e^2 \frac{d\phi}{dx} = -\sigma_i \frac{d\phi}{dx} \qquad \text{Eq. 13}$$

Eq. 13 is better known as Ohm's 1. Law. From Eq. 6 and Eq. 13 it follows

$$\sigma_i = c_i b_i z_i^2 e^2 \qquad \text{Eq. 14}$$

Instead of the mechanical mobility, it is common to use the electrical mobility u_i, which is defined as the ratio between v_i and the electrical field

$$u_i = \frac{|v_i|}{\left|\frac{d\phi}{dx}\right|} \qquad \text{Eq. 15}$$

Hence $|z_i|eb_i = u_i$, and from Eq. 14 the well known relation follows

$$\sigma_i = c_i u_i |z_i| e \qquad \text{Eq. 16}$$

From Eq. 9 and Eq. 14 it is easy to deduce the relation between the electrical conductivity and the component diffusion coefficient, which is known as Nernst-Einsteins equation

$$\sigma_i = \frac{c_i z_i^2 e^2 D_K}{kT} \qquad \text{Eq. 17}$$

The general current density equation in a simultaneous chemical and electrical potential gradient is given by (via Eq. 1, Eq. 6 and Eq. 14)

$$I_i = z_i e J_i = -c_i b_i z_i e \frac{d\eta_i}{dx} = -\frac{\sigma_i}{z_i e} \frac{d\eta_i}{dx} \qquad \text{Eq. 18}$$

2.1.5 Ionic diffusion

During measurements of transport properties, it is often the tracer diffusion coefficient, which is measured. The tracer diffusion coefficient is related to the component diffusion coefficient via the Haven-ratio (H) [12]

$$D_{tr} = HD_K \qquad \text{Eq. 19}$$

The ionic transport in solids can often be described as a thermal activated hopping of defects to neighboring lattice sites. If the diffusion mechanism involves jumps to a nearby vacant site, it can be expected that the diffusion coefficient is proportional to the concentration of vacancies. A vacancy diffusion coefficient D_v can be defined as the ratio between the component diffusion coefficient and the mole fraction x_v of the available vacant sites

$$D_K = D_V x_V \qquad \text{Eq. 20}$$

Similar expressions can be written for other diffusion mechanisms. If more than one diffusion mechanism is involved, the general expression is

$$D_K = \sum_{Def} D_{Def} x_{Def} \qquad \text{Eq. 21}$$

The temperature dependence for the component diffusion coefficient is given by a Arrhenius-type expression [14]

$$D_K = A\exp\left[\left(\Delta S_f + \Delta S_m\right)/k\right]\exp\left[-\left(\Delta H_f + \Delta H_m\right)/kT\right] \quad \text{Eq. 22}$$

where A is a constant for the solid of interest [14]. The Gibbs energy of migration of defects is given by

$$\Delta G_m = \Delta H_m - T\Delta S_m \quad \text{Eq. 23}$$

The Gibbs energy of formation of defects is given by

$$\Delta G_f = \Delta H_f - T\Delta S_f \quad \text{Eq. 24}$$

The activation energy for diffusion is given by

$$E_A = \Delta H_f + \Delta H_m \quad \text{Eq. 25}$$

and can be determined by plotting $\log(D_K)$ vs. 1/T. Details can be seen in [14].

2.2 Defect chemistry of chromia

In section 2.1, it was discussed how the diffusion of ions through oxides is governed by the transport of defects through the oxide structure. Furthermore, in section 2.3 it will be described how the growth of chromia on the alloys, which are examined in the present work, is governed by the transport of chromium and oxygen ions through the oxide. Hence, in order to understand and discuss the growth of chromia more closely, it is important to understand the defect structure of chromia.

The defect structure of chromia has been described and discussed in the literature [15-22]. An understanding of the defect structure was achieved by measuring properties in chromia such as the electrical conductivity and the diffusion of chromium and oxygen as a function of temperature and oxygen pressure. These measurements can subsequently be analysed by fitting relevant defect equations to the measured properties in order to determine the defect structure of chromia. The defect structure will be reviewed shortly in the following.

2.2.1 Corundum structure

Chromia has the corundum structure with the general formula A_2O_3, where A is a metal. The corundum structure consists of an hcp array of oxygen with two-thirds of the octahedral sites occupied by the metal. The corundum structure is shown in Fig. 2, where the closed packed layers of oxygen can be easily recognized. The metals in the lattice are not randomly distributed over the octahedral sites. Fig. 3 shows that when the corundum structure is viewed along the right crystallographic direction, the

structure consists of two layers of metals followed by an empty layer on the octahedral sites. The empty octahedral sites in the corundum structure are viewed as interstial sites in the lattice.

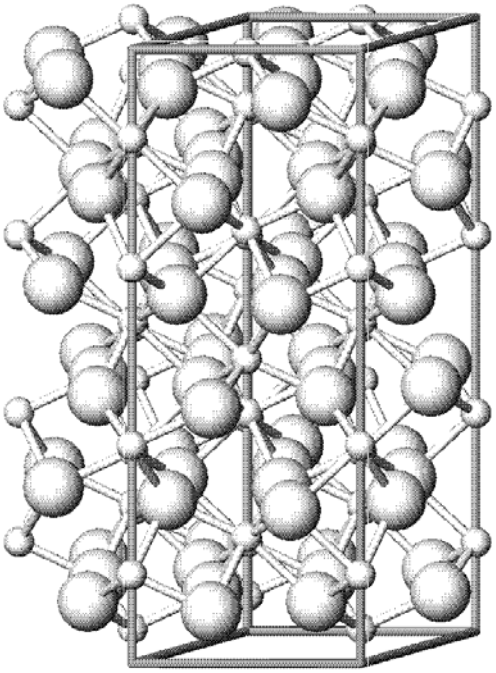

Fig. 2. The corundum structure. The hcp lattice of oxygen are the larger atoms, while the smaller atoms are the metals located at the octahedral sites [23].

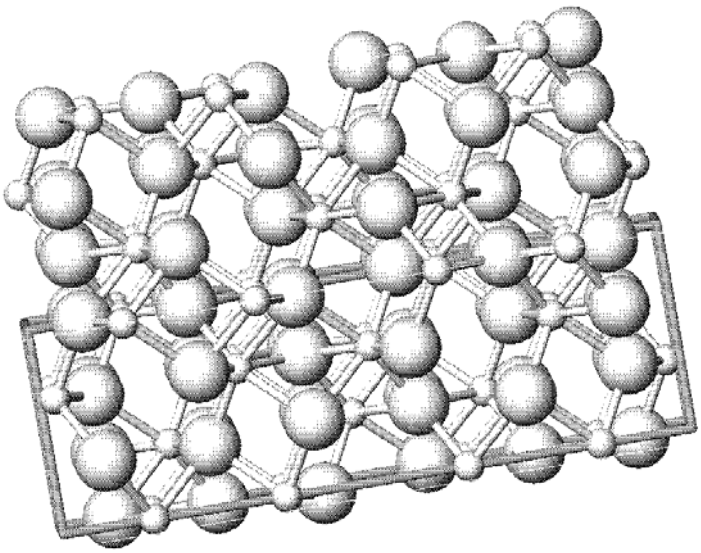

Fig. 3. The pattern of empty and occupied octahedral sites in the corundum structure is easily observed [23].

2.2.2 Diffusion in Cr_2O_3

The chromium diffusion has mostly been studied at high temperatures (> 1373 K). Fig. 4 shows a collection of chromium tracer diffusion coefficients in chromia, as a function of temperature and oxygen activity. The diffusion coefficients are thought to reflect lattice values [10].

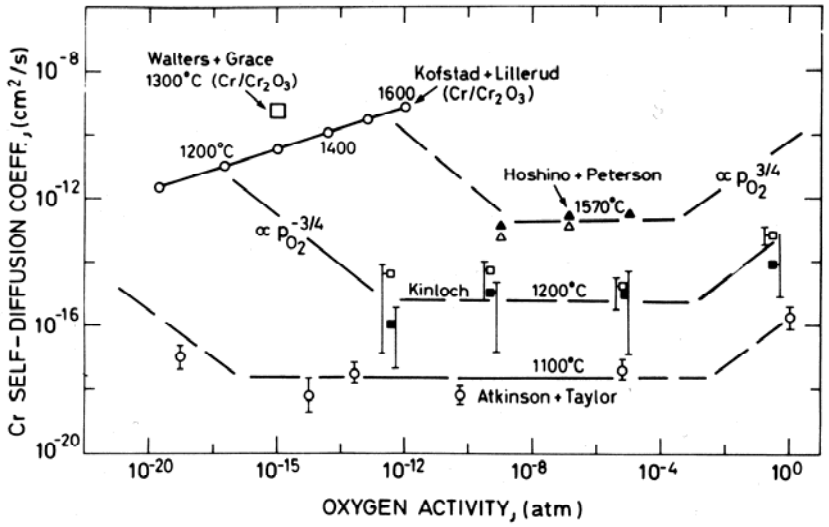

Fig. 4. Chromium tracer diffusion coefficient in chromia as a function of temperature and oxygen activity [10].

As shown in Fig. 4, the chromium diffusion coefficient appears to go through a minimum as the oxygen activity is increased. In contrast, measurements performed by Sabioni et al. [22] suggest that the chromium tracer diffusion coefficients are independent of the oxygen activity. Hence, there is great uncertainty about the oxygen activity dependency on the diffusion coefficient [16]. It is evident from Fig. 4 that the diffusion coefficients are very small (ca. 10^{-17}cm^2/s at 1373 K). The diffusion distance x can be estimated by the relation $x \approx (Dt)^{1/2}$, so the diffusion distance is ca. 2 nm, after a one hour anneal at 1373 K. Hence, it is not possible to equilibrate point defects in chromia by lattice diffusion in a reasonable time. Thus, the differences in measured values from the literature may reflect the difficulties in equilibrating the samples in different oxygen activities during the experiments. This may result in erroneous measurements. Another explanation for the differences could be different levels of impurities in the samples. It has been speculated by Sabioni et al. [22] that the concentration of mobile defects could be governed by the impurity level in the lattice, i.e. extrinsic diffusion. This may result in diffusion coefficients, which are independent of the oxygen activity [22].

In Fig. 4, curves are drawn, which indicate an oxygen activity dependence of the chromium diffusion coefficients. The slope of the curve is

$$\frac{d\log D_{Cr}}{d\log p(O_2)} = -3/4 \qquad \text{Eq. 26}$$

at low oxygen activities and

$$\frac{d\log D_{Cr}}{d\log p(O_2)} = +3/4 \qquad \text{Eq. 27}$$

at high oxygen activities. These dependencies will be discussed later.

The temperature dependency on the diffusion coefficient is described in section 2.1.5. The activation energy for chromium tracer diffusion has been determined in the 245-280 kJmol^{-1} range [19,22].

Fig. 5 shows the oxygen tracer diffusion coefficient in chromia as a function of oxygen activity [18]. The diffusion coefficients were measured at 1373 K in single crystals and reflect lattice diffusion.

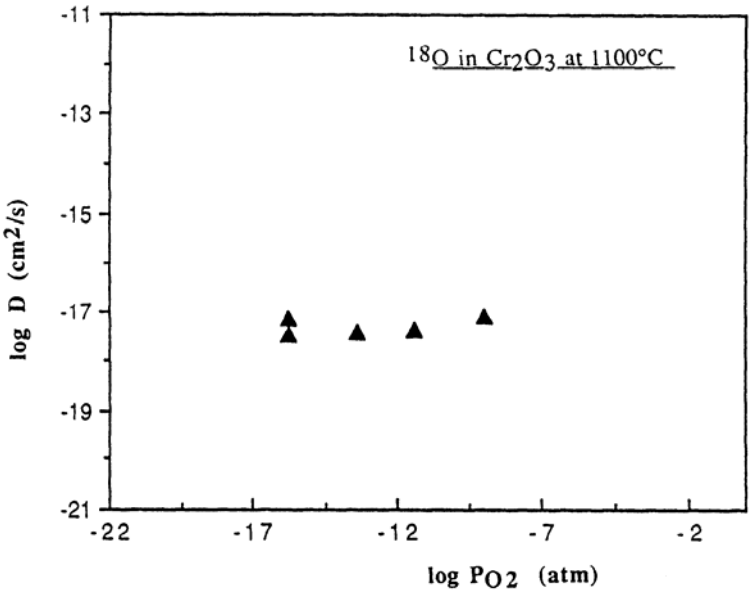

Fig. 5. Oxygen tracer diffusion coefficient in chromia as a function of oxygen activity, adapted from [18].

As shown in Fig. 5, the oxygen tracer diffusion coefficients in chromia are almost independent of the oxygen activity. This can be caused by the slow equilibration of the samples or that the defect concentration is governed by impurities i.e. extrinsic diffusion, as described earlier. The oxygen tracer diffusion coefficient is ca. 10^{-17} cm^2/s at 1373 K.

The activation energy for oxygen tracer diffusion has been determined to ca. 230 kJ/mol [18].

2.2.3 Electrical conductivity

Holt and Kofstad [15,16] have reviewed and measured the electrical conductivity of chromia. The conduction mechanism in chromia is a thermal activated hopping of electrons between chromium atoms, i.e. a small polaron mechanism [16].

The electrical conductivity for chromia can be divided in two regimes: A high temperature regime above ca. 1273 K, and a low temperature regime below ca. 1273 K [16]. The exact transition temperature depends on the sample, e.g. impurities and microstructure. Various studies have been performed on the electrical conductivity. There is general agreement in the high temperature region, but large disagreements in the low temperature region [16]. The latter may be caused by different amount of impurities in the samples, which may influence the electrical conductivity.

The electrical conductivity measured at high temperatures will be discussed first. It has been observed that the electrical conductivity is independent of the oxygen activity at high temperature [16]. The electrical conductivity is governed by the concentration of electronic defects in the oxide (cf. section 2.1.4), so the measurements indicate that the concentration of electronic defects is independent of the oxygen activity at high temperatures. The formation of electronic point defects is given by the intrinsic equilibrium

$$e^{/} + h^{\bullet} \leftrightarrow nill \qquad \text{reaction 1}$$

In chromia, the important ionic point defects are chromium and oxygen vacancies, and chromium and oxygen interstitials. The electroneutrality equation reads

$$\left[e^{/}\right] + 2\left[O_i^{//}\right] + 3\left[V_{Cr}^{///}\right] = \left[h^{\bullet}\right] + 2\left[V_O^{\bullet\bullet}\right] + 3\left[Cr_i^{\bullet\bullet\bullet}\right] \qquad \text{Eq. 28}$$

If the electronic disorder is dominating (i.e. $[e^{/}] \approx [h^{\bullet}]$), the concentration of electronic defects and hence the electrical conductivity is independent of the oxygen activity and the behaviour is said to be intrinsic. Hence, chromia exhibits intrinsic behaviour at high temperatures [16]. A Kröger-Vink diagram, where the intrinsic equilibrium dominates at intermediate oxygen activities is shown in Fig. 6.

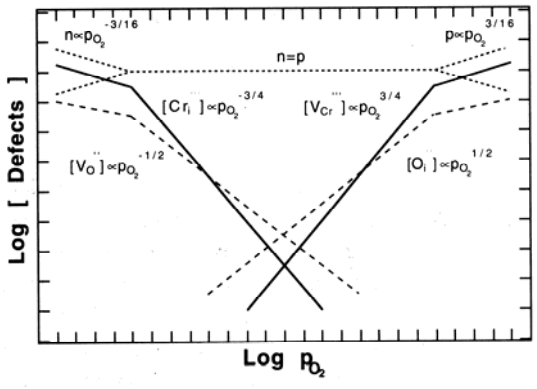

Fig. 6. Kröger-Vink diagram for a defect situation where the intrinsic equilibrium dominates [16].

The oxygen dependency on the ionic defect concentrations will be discussed later.

It has been observed that the electrical conductivity for chromia at temperatures below ca. 1273 K is dependent on the oxygen activity [15,16]. However, large differences have been observed during measurements of different samples under similar conditions [15]. This difference is possibly caused by different levels of impurities in the samples, so the electrical conductivity may be governed by impurities at low temperatures [15,16].

2.2.4 Defect structure of Cr_2O_3

Based on the measurements of the electrical conductivity and the chromium and oxygen diffusion, a defect structure for chromia can be proposed.

The corundum structure consists, as previously mentioned, of a hcp lattice of oxygen, while the metals occupy 2/3 of the octahedral sites in the structure. Cation vacancies exist in the normally occupied octahedral sites. The formation of vacancies on the normally occupied octahedral sites in Cr_2O_3 can be described by a point defect equilibrium

$$\tfrac{3}{4}O_2 \leftrightarrow \tfrac{3}{2}O_O^X + V_{Cr}^{'''} + 3h^{\bullet} \qquad \text{reaction 2}$$

The mass action law yields

$$\left[V_{Cr}^{'''}\right] = K_1\left[h^{\bullet}\right]^{-3} a(O_2)^{3/4} \qquad \text{Eq. 29}$$

The formation of chromium interstitials can be written

$$Cr_{Cr}^X + \tfrac{3}{2}O_O^X \leftrightarrow \tfrac{3}{4}O_2 + Cr_i^{\bullet\bullet\bullet} + 3e' \qquad \text{reaction 3}$$

The mass action law yields

$$\left[Cr_i^{\bullet\bullet\bullet}\right] = K_2\left[e'\right]^{-3} a(O_2)^{-3/4} \qquad \text{Eq. 30}$$

The oxygen defects in the corundum structure will now be considered. Oxygen defects can exist as vacancies in the hcp lattice or as interstitial defects. The formation of oxygen vacancies in the hcp lattice can be described by a point defect equilibrium

$$O_O^X \leftrightarrow \tfrac{1}{2}O_2 + V_O^{\bullet\bullet} + 2e' \qquad \text{reaction 4}$$

The mass action law yields

$$\left[V_O^{\bullet\bullet}\right] = K_3 \left[e'\right]^{-2} a(O_2)^{-1/2}$$ Eq. 31

The formation of oxygen interstitials can be described by

$$1/2\, O_2 \leftrightarrow O_i'' + 2h^{\bullet}$$ reaction 5

The mass action law yields

$$\left[O_i''\right] = K_4 \left[h^{\bullet}\right]^{-2} a(O_2)^{1/2}$$ Eq. 32

However, the presence of interstitial oxygen defects in the lattice are highly improbable due to the size of the oxygen anion and due to the close packed structure of oxygen ions. In contrast, the presence of oxygen interstitials may be important in grain boundaries.

The chromium diffusion at high temperatures was described in section 2.2.2, where oxygen partial dependencies were found (cf. Eq. 26 and Eq. 27). It was recognized in section 2.1.5 that the chromium diffusion is proportional to the concentration of defects (cf. Eq. 21). The chromium diffusion coefficient can be expressed as

$$D_{Cr} = \left[V_{Cr}'''\right] D_{V_{Cr}} + \left[Cr_i^{\bullet\bullet\bullet}\right] D_{Cr_i}$$ Eq. 33

From Eq. 29 and Eq. 30, it follows that the concentration of chromium vacancies increases and the concentration of chromium interstitials decreases in the lattice as the oxygen activity is increased. The oxygen dependencies given in Eq. 26 and Eq. 27 can be explained by Eq. 29 and Eq. 30 if it is assumed that the concentration of free electrons and holes are independent of the oxygen activity. This is tantamount to an electrical conductivity, which is independent of the oxygen pressure. Such an intrinsic behaviour was found for chromia at high temperatures. Hence, it is concluded that chromia is governed by an intrinsic electronic behaviour at high temperatures, which gives rise to the oxygen pressure dependencies observed in Eq. 26 and Eq. 27. Furthermore, from Eq. 29, Eq. 30 and Eq. 33, it appears that the chromium diffusion is governed by interstitial defects at low oxygen activities and by vacancies at higher oxygen activities.

The oxygen diffusion in the chromia lattice is governed by oxygen vacancies and oxygen interstitials. The oxygen activity dependencies are given by Eq. 31 and Eq. 32. The oxygen diffusion coefficient is also proportional to the defect concentrations (cf. section 2.1.5). Hence, at high temperatures, where chromia is governed by an intrinsic behaviour, the oxygen activity dependency on the oxygen diffusion coefficient by way of oxygen vacancies is given by (cf. Eq. 31)

$$\frac{d \log D_O}{d \log p(O_2)} = -1/2$$ Eq. 34

and the oxygen activity dependency on the oxygen diffusion coefficient by way of oxygen interstitials is given by

$$\frac{d\log D_O}{d\log p(O_2)} = 1/2 \qquad \text{Eq. 35}$$

Such an oxygen activity dependency was not observed in Fig. 5. Possible explanations for this discrepancy have already been proposed in section 2.2.2. However, it is unlikely that oxygen diffusion within the lattice is governed by interstitial defects, as previously mentioned. Thus, the oxygen diffusion within the lattice may be dominated by oxygen vacancies. In this case, the oxygen activity dependency on the oxygen diffusion coefficient is given by Eq. 34 in the complete oxygen activity window.

The defect structure is increasingly complex at lower temperatures [15,16]. The electroneutrality equation is given in Eq. 28. In the following, it is assumed that the level of impurities can be neglected. It has been proposed by Kofstad and Lillerud [24] that chromium defects dominate, so the electroneutrality condition is given by

$$3\left[V_{Cr}^{'''}\right] = \left[h^{\bullet}\right] \qquad \text{Eq. 36}$$

at high oxygen activities, where chromium vacancies dominate, and

$$3\left[Cr_i^{\bullet\bullet\bullet}\right] = \left[e'\right] \qquad \text{Eq. 37}$$

at low oxygen activities, where chromium interstitials dominate. If these conditions are inserted in Eq. 29 and Eq. 30, it follows that

$$\frac{d\log\left[Cr_i^{\bullet\bullet\bullet}\right]}{d\log p(O_2)} = -3/16 \qquad \text{Eq. 38}$$

at low oxygen activities and

$$\frac{d\log\left[V_{Cr}^{'''}\right]}{d\log p(O_2)} = +3/16 \qquad \text{Eq. 39}$$

at high oxygen activities. The oxygen activity dependency on the chromium diffusion coefficient by way of chromium vacancies and interstitials can readily be calculated using Eq. 38 and Eq. 39, respectively. The corresponding Kröger-Vink diagram for chromium point defects for the lower temperature case is shown in Fig. 7.

It should be noticed that Eq. 36 and Eq. 37 may be a simplified picture, since the content of extrinsic defects is neglected. However, although the electroneutrality conditions may be different, the concentration of chromium interstitials will still decrease, and the concentration of chromium vacancies will increase as a function of oxygen activity.

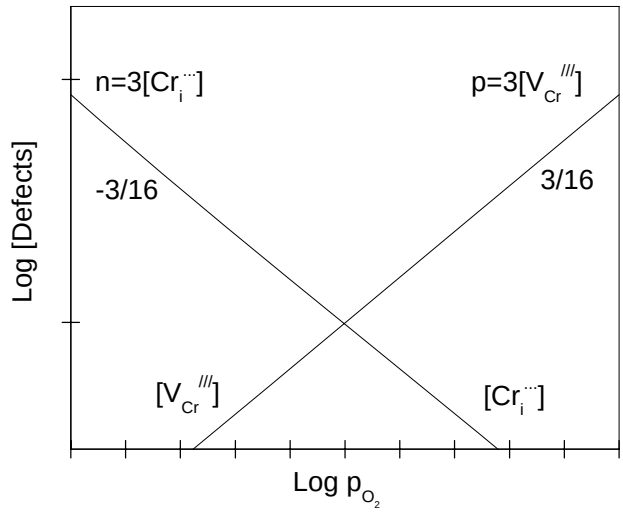

Fig. 7. Kröger-Vink diagram for chromium defects in chromia. It is assumed that the electroneutrality condition is given by $3[V_{Cr}^{///}] = [h^{\bullet}]$ and $3[Cr_i^{\bullet\bullet\bullet}] = [e']$ at high and low oxygen activities, respectively.

The oxygen dependency on the concentration of oxygen vacancies at lower temperatures can be obtained from Eq. 30, Eq. 31 and Eq. 37

$$\frac{d\log[V_O^{\bullet\bullet}]}{d\log p(O_2)} = -1/8 \qquad \text{Eq. 40}$$

and the concentration of oxygen interstitials is given by Eq. 29, Eq. 32 and Eq. 36

$$\frac{d\log[O_i'']}{d\log p(O_2)} = 1/8 \qquad \text{Eq. 41}$$

Greskovich [20] has examined the chromium nonstoichiometry of chromia. Results have only been reported at near atmospheric pressure, where a small cation deficiency has been reported, i.e. $Cr_{2-x}O_3$ ($x = 9\cdot10^{-5}$ at 1373 K in air). The concentration of chromium vacancies was examined in a small oxygen partial pressure window near atmospheric pressure. The concentration of vacancies was approximately in accordance with Eq. 39. This is in support of the proposed defect structure at lower temperatures.

2.3 The Wagner oxidation theory

2.3.1 Introduction

In this section, the Wagner oxidation theory [25-27] will be presented and discussed. This theory has played a major role on the understanding and prediction of high temperature oxidation of metals. Under certain assumptions, it provides the theoretical

foundation for the development of high temperature oxidation resistant metals and alloys.

During the formation of a dense oxide scale on an alloy, reactants and electrons are transported across the growing oxide scale. Furthermore, complex reactions take place at the alloy/scale and scale/gas interfaces. When enough oxygen is available in the reaction atmosphere, the scale growth is often limited by the transport of ions or electrons through the scale. This is the case during most high temperature oxidation of metals and alloys [10]. The theoretical basis for the Wagner theory is based on the increasing scale thickness during oxidation. The increasing thickness results in an increasing transport length for the reactants and the driving force for the diffusing species will subsequently become smaller. This decreases the rate of scale formation as the scale thickness increases.

The basic assumption in Wagner's theory is that the diffusion of reactants or the transport of electrons across the dense scale is rate determining for the overall oxidation process. This implies that the interfacial reactions are rapid, and thermodynamic equilibrium is assumed at the interfaces. Wagner's theory applies for the ideal case where the scale is dense and continuous and adheres well to the metal. The transport of ions through the scale is assumed to occur by lattice diffusion. Furthermore, ions and electrons are assumed to migrate independently of each other, and it is assumed that local equilibria exist in the oxide.

During the formation of an oxide scale, the ions are transported through the scale by lattice diffusion, grain boundary diffusion or other short circuit diffusivity paths. Furthermore, several mechanistic factors play a role as the scale thickness increases. This includes loss of scale adhesion, creation of voids, porosity etc. The implications of these additional features on the Wagner oxidation theory may be important. These effects will be discussed after the deviation of the ideal Wagner case, which will be given below. The oxidation theory will be applied for the growth of chromia on an iron-chromium alloy.

2.3.2 Parabolic rate expression

The total growth rate of the oxide scale is given as the sum of the ionic particle fluxes

$$J_{ion} = J_{Cr} + J_O \qquad \text{Eq. 42}$$

Each Cr_2O_3 molecule contains $|z_{an}|3e = z_{cat}2e = 6e$ charges, so the number n of Cr_2O_3 units formed per unit area per unit time is given by

$$\frac{dn}{dt} = J_{ion} = \frac{I_{ion}}{6e} \qquad \text{Eq. 43}$$

The ionic current density is given by [10]

$$I_{ion} = \frac{\sigma_{total}}{|z_{an}|e} t_{ion} t_{el} \frac{d\mu_O}{dx} \qquad \text{Eq. 44}$$

so it follows that

$$\frac{dn}{dt} = \frac{\sigma t_{ion} t_{el}}{12e^2} \frac{d\mu_O}{dx} \qquad \text{Eq. 45}$$

From the assumed equilibrium at the scale/gas interface it follows that

$$d\mu_O = \frac{1}{2} d\mu_{O_2} \qquad \text{Eq. 46}$$

and

$$d\mu_{O_2} = kTd \ln p_{O_2} \qquad \text{Eq. 47}$$

It follows from Eq. 45-Eq. 47 that

$$\frac{dn}{dt} = \frac{kT}{24e^2} \sigma t_{ion} t_{el} \frac{d \ln p_{O_2}}{dx} \qquad \text{Eq. 48}$$

If Eq. 48 is integrated over the thickness of the scale it becomes

$$\frac{dn}{dt} = \left\{ \frac{kT}{24e^2} \int_{p^i_{O_2}}^{p^o_{O_2}} \sigma t_{ion} t_{el} d \ln p_{O_2} \right\} \frac{1}{\Delta x} = k_M \frac{1}{\Delta x} \qquad \text{Eq. 49}$$

where $p^i_{O_2}$ is the oxygen activity at the metal/scale interface, which is assumed to be the decomposition pressure of the oxide, and $p^o_{O_2}$ is assumed to be the oxygen activity in the oxidizing atmosphere. It should be noticed that the interfacial reactions might exert a partial control over the growth rate [28,29]. In this case, $p^i_{O_2}$ might increase, and $p^o_{O_2}$ might decrease. Thus, the oxygen potential gradient given in Eq. 49 might be partly consumed by the interfacial reactions. However, the interfacial reactions are assumed to be so fast during the growth of oxide scales that they do not exert an influence on the parabolic growth rate of the oxide scales in the present work [30].

The value in the brackets is one form of the parabolic rate constant, and Eq. 49 is one form of the parabolic rate expression. The parabolic rate constant in Eq. 49 is given by the electrical conductivity and the transport numbers for ions and electrons. Instead, this can be written

$$k_M = \frac{kT}{24e^2} \int_{p^i_{O_2}}^{p^o_{O_2}} (\sigma_{Cr} + \sigma_O) t_{el} d \ln p_{O_2} \qquad \text{Eq. 50}$$

Chromia is an electronic conductor, so $t_{el} \approx 1$. Furthermore, the conductivities are related to the component coefficient through the Nernst –Einstein relation (cf. Eq. 17)

$$z_i^2 e^2 D_K c_i = kT\sigma_i \qquad \text{Eq. 51}$$

The parabolic rate constant can then be expressed as

$$k_M = \frac{c_O}{6}\int_{p_{O_2}^i}^{p_{O_2}^o}\left(\frac{3}{2}D_{Cr} + D_O\right)d\ln p_{O_2} \qquad \text{Eq. 52}$$

where c_O is the number of oxygen ions in Cr_2O_3 per volume. This important result combines the lattice diffusion coefficients and the rate of the oxide scale growth. It should be noticed that the diffusion coefficients given in Eq. 51 and Eq. 52 are component diffusion coefficients, which are related to the commonly measured tracer diffusion coefficient by the Haven-ratio; $D_i^{tr} = HD_i$ (cf. section 2.1.5). It is evident from Eq. 52 that the growth of the scale is governed by the fastest diffusing ion, unlike many other processes (e.g. sintering and creep), where the slowest moving species governs the process [10].

The parabolic rate expression in Eq. 49 is given as the number of Cr_2O_3 units formed per unit area per unit time. Such a quantity is usually not measured during the oxidation. Instead, the oxidation rate of metals is often obtained as the rate of growth of oxide thickness. In this case, the parabolic rate equation gets the form

$$\frac{dx}{dt} = k_p\frac{1}{x} \qquad \text{Eq. 53}$$

where the new rate constant k_p is related to the rate constant defined in Eq. 49 by

$$k_p\left[cm^2/s\right] = \frac{M_{Cr_2O_3}}{N_A\rho_{Cr_2O_3}}k_M \qquad \text{Eq. 54}$$

where $\rho(Cr_2O_3)$ is the density of chromia, M the molar mass, and N_A is Avogadro's number. By combining Eq. 52 and Eq. 54 it follows that

$$k_p = \frac{1}{2}\int_{p_{O_2}^i}^{p_{O_2}^o}\left(\frac{3}{2}D_{Cr} + D_O\right)d\ln p_{O_2} \qquad \text{Eq. 55}$$

2.3.3 Application for chromia

The growth rate of chromia is governed by the parabolic rate expression in Eq. 53. Hence, the growth rate can be further elucidated if the oxygen activity dependencies on the oxygen and chromium diffusion coefficients in Eq. 55 are known. It is then possible to determine the oxygen activity dependency on the parabolic rate constant. This is valuable in order to determine the growth mechanism of the chromia scale.

The discussion of the growth kinetics is initially limited to transport of reactants by way of lattice diffusion, but will later be extended to include short circuit diffusion.

The transport of chromium and oxygen through the chromia lattice is governed by point defects in the scale. The transport properties and defect structure of chromia has been discussed in section 2.1 and 2.2. According to this, the diffusion coefficient can be expressed as (cf. section 2.1.5)

$$D_{Cr} = \left[V_{Cr}^{///}\right] D_{V_{Cr}} + \left[Cr_i^{\bullet\bullet\bullet}\right] D_{Cr_i} \qquad \text{Eq. 56}$$

$$D_O = \left[V_O^{\bullet\bullet}\right] D_{V_O} + \left[O_i^{//}\right] D_{O_i} \qquad \text{Eq. 57}$$

The oxygen activity dependencies on the chromium and oxygen defects were examined in section 2.2.4. From this discussion, the oxygen activity dependency on the defect concentration below ca. 1273 K, may be written

$$\left[V_{Cr}^{///}\right] \propto pO_2^{3/16} \qquad \text{Eq. 58}$$

$$\left[Cr_i^{\bullet\bullet\bullet}\right] \propto pO_2^{-3/16} \qquad \text{Eq. 59}$$

$$\left[V_O^{\bullet\bullet}\right] \propto pO_2^{-1/8} \qquad \text{Eq. 60}$$

$$\left[O_i^{//}\right] \propto pO_2^{1/8} \qquad \text{Eq. 61}$$

Eq. 56-Eq. 61 can be combined and inserted into Eq. 55 in order to relate the measured parabolic rate constants to the examined defect structure of chromia. It is also possible to calculate the parabolic growth constant from independently measured diffusion coefficients.

During the examinations of oxide scales, simplified defect structures are often assumed such that dominant defect species are identified for the growth of the scale. This results in a simplified calculation of the rate constants of the oxide scales by Eq. 55. However, such a simplified picture may only be used if the same defect structure prevails through the entire scale. The oxide scale has an oxygen activity gradient given by the decomposition pressure at the alloy/scale interface, and the oxygen pressure in the reaction atmosphere. An oxide may have different defect species dominating at different oxygen activities. This was discussed for chromia in section 2.2.4. How can this be adopted to the parabolic rate constant? If the defect structure changes with oxygen activity (i.e. the oxide thickness), such that the scale can be divided into two parts, where different diffusion mechanisms predominate, the parabolic rate constant; k, for the entire scale growth is given by

$$k = k_1 + k_2 \qquad \text{Eq. 62}$$

where k_1 and k_2 are the parabolic rate constants for each layer [10]. The result of this is that the growth of one of the layers most likely will dominate the growth of the entire oxide scale, such that the growth of the entire scale can be approximately described by a single rate constant.

2.3.4 Grain boundary diffusion

The discussion so far has been limited to the parabolic growth kinetics governed by lattice diffusion. However, short circuit diffusion by way of grain boundaries or dislocations may be important. Examinations have revealed that grain boundary diffusion is dominating during the growth of chromia scales [31].

It is usual to adopt an effective diffusion coefficient when the transport of ions is through both lattice sites and grain boundaries. The effective diffusion coefficient is usually expressed as a linear combination of the lattice diffusion coefficient D_l and the grain boundary diffusion coefficient D_{gb}

$$D_{eff} = D_l(1-f) + D_{gb} f \qquad \text{Eq. 63}$$

where f is the fraction of diffusion sites situated in the grain boundaries. The effective diffusion coefficient in Eq. 63 can be inserted in the parabolic rate equation (Eq. 55). Hence, in order to evaluate the parabolic rate constant it is of great interest to know the oxygen activity dependency on the grain boundary diffusion coefficient, i.e. to know the diffusion mechanism in the grain boundaries. Grain boundary diffusion studies for oxygen activity dependencies have not been studied in great detail. However, it has been observed that the oxygen activity dependency on cation diffusion in the lattice and along surfaces is similar for NiO and Fe_3O_4 [32]. Similarly, Atkinson and Taylor [33] found that the grain boundary and lattice diffusion coefficient in NiO exhibited the same oxygen partial pressure dependency. These results suggest that the same type of defects governs the diffusion in the lattice and along boundaries, and that the defect structure at or near the grain boundaries can be described by the same type of defect reactions as in the lattice. It will be assumed that the grain boundary diffusion coefficients have the same oxygen activity dependency as the lattice diffusion coefficient for chromia in the present work. In this case, the effective diffusion coefficient given by Eq. 63 will have the same oxygen dependency as the lattice diffusion coefficient. The concentration and mobility of defects at boundaries and at lattice sites may, however, be very different. Thus, although the discussion so far has been limited to lattice diffusion, the discussion is also valid for the growth of chromia scales by way of grain boundary diffusion.

2.3.5 Thermogravimetric measurements

The parabolic rate constant for the growth of oxides is usually obtained by measuring the weight increase either by in-situ measurements using a thermogravimetric equipment or by oxidation in a furnace. This is also the case in the present work. If

vaporization effects from the oxide are neglected, the weight increase is a measure of the oxygen uptake during the oxidation. The parabolic rate expression may be written

$$\frac{dw}{dt} = k_w \frac{1}{w} \qquad \text{Eq. 64}$$

where w is the weight gain per unit area. The weight is related to the oxide thickness x by

$$w = \frac{3M_O}{M_{Cr_2O_3}} \rho_{Cr_2O_3} x \qquad \text{Eq. 65}$$

The parabolic rate constant in Eq. 64 is related to k_p (cf. Eq. 53) by

$$k_w = \left(\frac{3M_O \rho_{Cr_2O_3}}{M_{Cr_2O_3}} \right)^2 k_p \qquad \text{Eq. 66}$$

The parabolic rate constant defined by Eq. 64 will be determined in the present work.

2.4 Thermodynamic calculations

2.4.1 Introduction

It is important to examine the relative stability of the oxides formed during oxidation in order to predict and explain the oxidation behaviour in the present work. This may be done by calculation of the so-called Ellingham diagram, which can reveal the identity of the most stable oxides at different temperatures.

The oxidation studies described in this thesis were performed under isothermal conditions. Thus, isothermal sections of the ternary Fe-Cr-O phase diagram can be used to identify the thermodynamically stable oxides formed during oxidation.

Chromia scales were often formed during the high temperature oxidation studies performed in the present work. Chromia is characterized as a relatively volatile oxide at high temperatures in the presence of water and oxygen. Thus, the vapour pressure of chromium containing species, in equilibrium with chromia, is examined in the following.

The calculations of Fe-Cr-O phase diagrams, Ellingham diagram, and the vaporization of chromia will be described in the following. The thermodynamic calculations will be used throughout this thesis.

2.4.2 Ellingham diagram

A general oxidation reaction can be written

$$x\frac{b}{a}Me(s) + O_2(g) \leftrightarrow \frac{b}{a}Me_xO_{2a/b}(s) \qquad \text{reaction 6}$$

where Me is the metal. The change in Gibbs free energy for reaction 6 can be written as

$$\Delta G = \Delta G^o + RT\ln\frac{a(Me_xO_{2a/b})^{b/a}}{a(Me)^{xb/a}a(O_2)} \qquad \text{Eq. 67}$$

If the activity of pure metals and oxides are one, and the oxygen partial pressure is used for the oxygen activity, i.e. $a(O_2) = pO_2$, at equilibrium Eq. 67 can be written as

$$\Delta G^o = -RT\ln\frac{1}{pO_2} \qquad \text{Eq. 68}$$

ΔG^o is a function of temperature ($\Delta G^o = \Delta H^o - T\Delta S^o$), so plotting the standard Gibbs free energy for a reaction against the temperature will give straight lines provided that the standard reaction enthalpy and entropy does not change with temperature. These lines are plotted for a range of different oxides in Fig. 8. Such a diagram is called an Ellingham diagram.

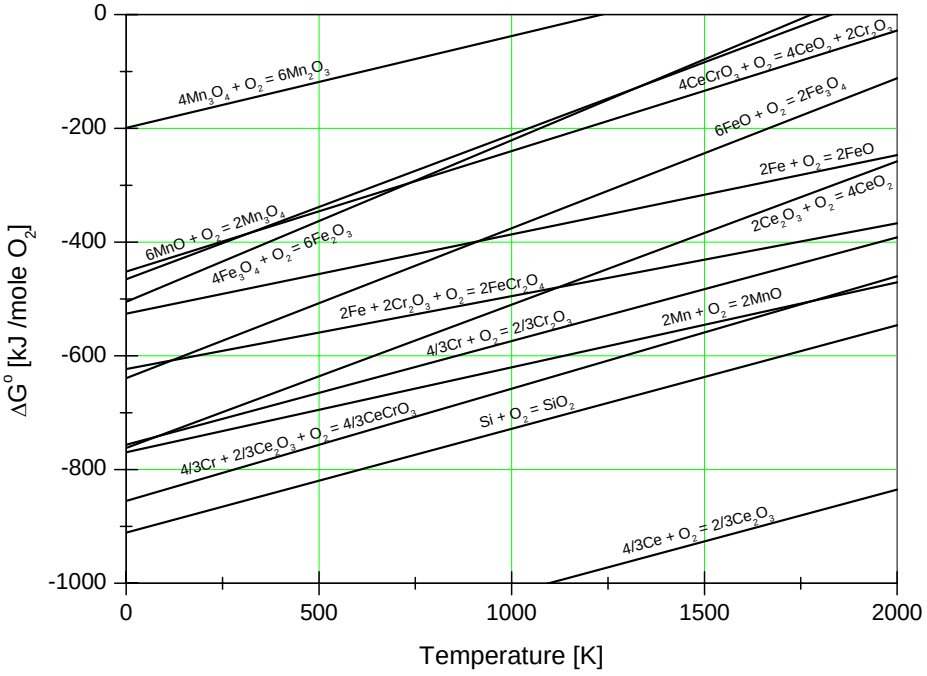

Fig. 8. Ellingham diagram for certain oxides. The thermodynamic data were taken from Ref. [34].

It should be noticed that wüstite is only stable above ca. 843 K, where the lines for the formation of wüstite and magnetite cross in Fig. 8, so the curve for wüstite formation is only valid above this temperature. The thermodynamic data were taken from Ref. [34]. At equilibrium for reaction 6, the standard Gibbs free energy change can be associated with an oxygen pressure via Eq. 68

$$pO_2 = \exp\frac{\Delta G^o}{RT} \qquad \text{Eq. 69}$$

This pressure is the decomposition pressure for the oxides, i.e. the oxygen partial pressure corresponding to the metal-oxide equilibrium. These decomposition pressures can be shown on the Ellingham diagram. From Eq. 69, it easily follows that $\Delta G^o = RT\ln(pO_2)$. Hence, straight lines can be superimposed on the Ellingham diagram, where the slope defines the oxygen activity (cf. Fig. 9). The decomposition pressure for oxides at a given temperature can be found from these lines. For example, the Cr/Cr_2O_3 decomposition pressure at 1000 K is ca. 10^{-30} bar.

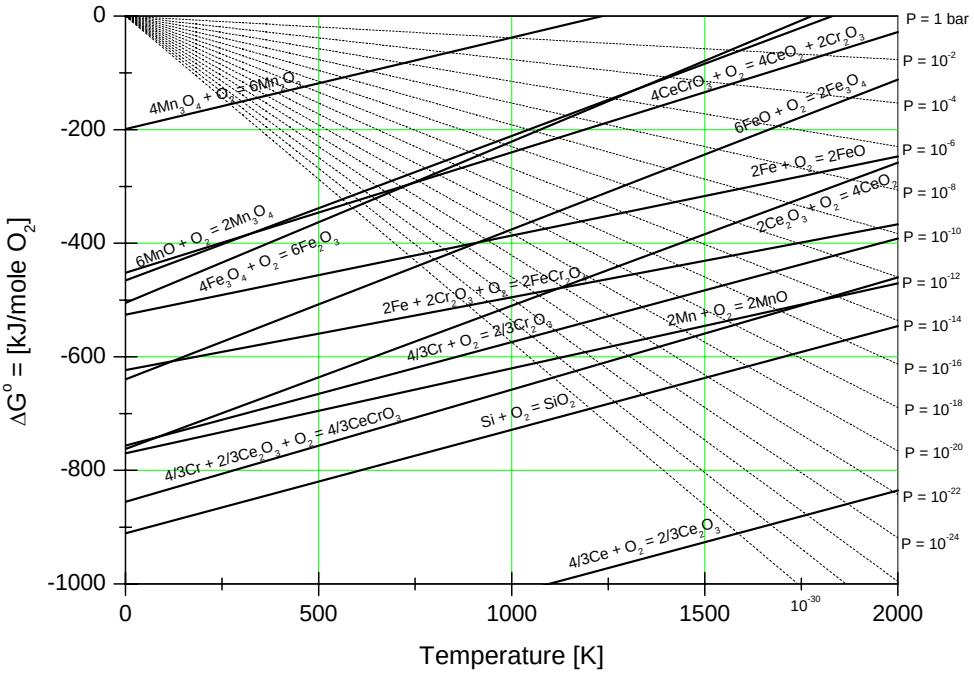

Fig. 9. Decomposition pressures superimposed on the Ellingham diagram. The thermodynamic data were taken from Ref. [34].

2.4.3 Fe-Cr – p(O_2) phase diagrams

During the high temperature oxidation of an alloy, a complex interplay between kinetic and thermodynamic considerations arises [35,36]. After the formation of dense oxide scales, an oxygen potential gradient will evolve across the oxide scale. At high temperatures, one can usually assume a condition of local equilibrium at the

alloy/scale and scale/gas interface, as discussed in section 2.3.2. Hence, the oxygen gradient across the oxide scale is given by the decomposition pressure of the oxide in equilibrium with the alloy and the oxygen activity in the reaction atmosphere. The sequence of oxides, which can exists in equilibrium as oxidation products, can be determined from a ternary Fe-Cr-O phase diagram. Thus, phase diagrams are important for a qualitative interpretation of the oxidation mechanism. The present phase diagrams are presented as isothermal alloy – $p(O_2)$ phase diagrams. The composition of the alloy is given by the mole fraction of chromium, i.e.

$$X(Cr) = \frac{n(Cr)}{n(Cr) + n(Fe)} \qquad \text{Eq. 70}$$

The phase diagrams can be used to identify the sequence of thermodynamically stable oxides from the alloy/scale interface to the reaction gas. The calculation of the phase diagrams was performed using Thermo-Calc [37], which is a program for thermodynamic calculations based on the minimization of Gibbs free energy. The present phase diagrams were calculated using the thermodynamic data given in Ref. [38].

The isothermal Fe-Cr – $p(O_2)$ phase diagrams at 973, 1173 and 1373 K are shown in Fig. 10-Fig. 12.

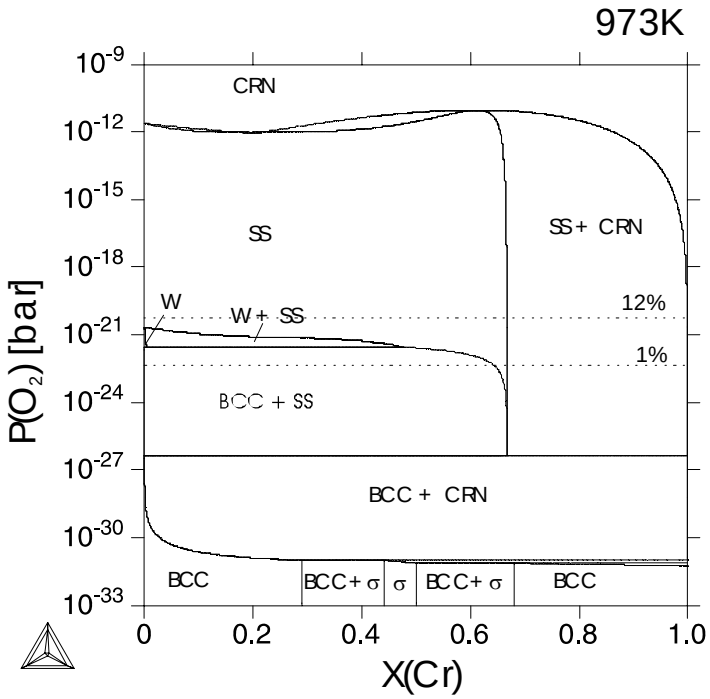

Fig. 10. Fe-Cr - $p(O_2)$ phase diagram at 973 K. The phase diagram was calculated using the Thermo-Calc [37] program with thermodynamic data from Ref. [38]. The symbols are explaining in the text.

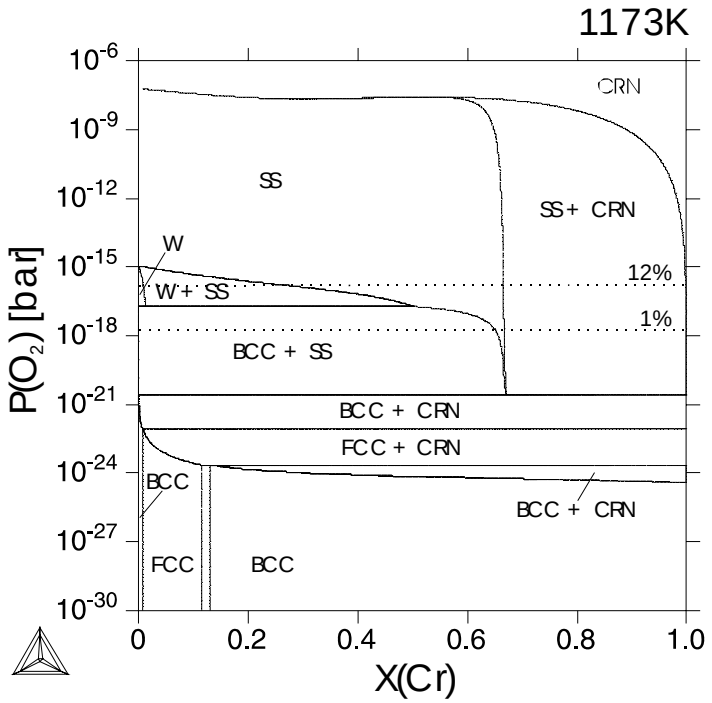

Fig. 11. Fe-Cr - $p(O_2)$ phase diagram at 1173 K. The phase diagram was calculated using the Thermo-Calc [37] program with thermodynamic data from Ref. [38]. The symbols are explaining in the text.

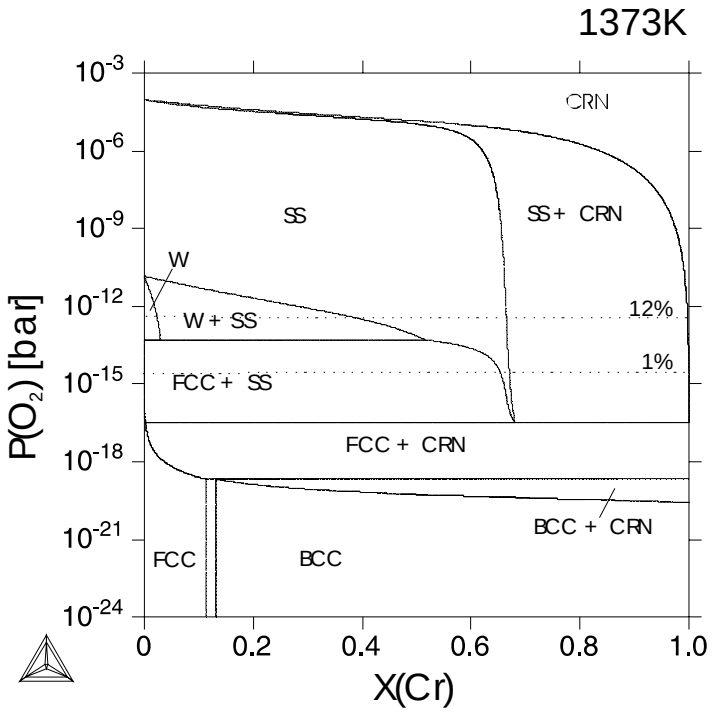

Fig. 12. Fe-Cr - $p(O_2)$ phase diagram at 1373 K. The phase diagram was calculated using the Thermo-Calc [37] program with thermodynamic data from Ref. [38]. The symbols are explaining in the text.

The corundum phase is abbreviated CRN, the spinel solid solution SS, while W denotes the wüstite phase. Metallic phases with the bcc (BCC) and fcc (FCC) structure may also be recognized in the phase diagrams. Furthermore, the sigma phase

(σ) may be recognized in Fig. 10 at 973 K. Iron-chromium alloys with changing compositions exist in equilibrium with different oxides at increasing oxygen activity. At low oxygen partial pressures, the Fe-Cr alloy exists in equilibrium with a corundum phase, which is almost identical to Cr_2O_3. At increasing oxygen partial pressure, the alloy exists in equilibrium with a spinel phase close to $FeCr_2O_4$ in composition, and finally a wüstite-based oxide containing a small amount of chromium. At higher oxygen partial pressures, the spinel phase extend from Fe_3O_4 to $FeCr_2O_4$, and Cr_2O_3 shows a complete solubility with Fe_2O_3. The solid solution corundum phase extend up to ambient pressure in the phase diagrams.

The dotted lines, which are superimposed on the phase diagrams, mark the oxygen partial pressure of the hydrogen/argon mixture containing 1% and 12% water vapour, respectively (cf. section 2.4.4). It should be noticed from Fig. 10-Fig. 12 that the wüstite phase is thermodynamically stable in the hydrogen/argon mixture containing 12% water vapour, while the phase is unstable in hydrogen/argon containing 1% water at 973–1373 K. These atmospheres were used in the present work. In the case of air, the oxygen partial pressure exceeds the top of the phase diagrams shown in Fig. 10-Fig. 12.

2.4.4 Chromium vapour species

In the present work, the formation of chromia on the specimens was either followed in-situ by thermogravimetric measurements or by oxidizing the specimens in a furnace. The oxidation rate was in both cases determined by measuring the weight gain of the specimen. The weight gain of chromia due to parabolic oxidation has been described in section 2.3. However, the specimens may also lose weight due to vaporization of chromium containing species from the formed chromia scale. Therefore, it is important to determine the partial pressures of chromium containing species in equilibrium with chromia in order to examine the effect of vaporization from the oxide.

The dominant chemical reactions involved in the formation of volatile chromium species are most likely [39,40]

$$Cr_2O_3(s) + 3/2\,O_2(g) \rightarrow 2CrO_3(g) \qquad \text{reaction 7}$$

in the absence of water vapour and

$$Cr_2O_3(s) + 3/2\,O_2(g) + 2H_2O(g) \rightarrow 2CrO_2(OH)_2(g) \qquad \text{reaction 8}$$

in the presence of water vapour and oxygen.

The temperature dependency on the partial pressures of the species given in reaction 7 and reaction 8 are shown in Fig. 13 as a function of temperature. The thermodynamic calculations have been performed in air containing 2% water vapour [39]. The gas activities were calculated using thermodynamic data from Ebbinghaus [40].

It may be recognized that the formation of the chromium oxyhydroxide, given by reaction 8, is dominant in the temperature range examined in this work (973–1373 K) in air containing 2% water vapour. The partial pressures of different chromium containing species are given as a function of water partial pressure in air at 1223 K in Fig. 14.

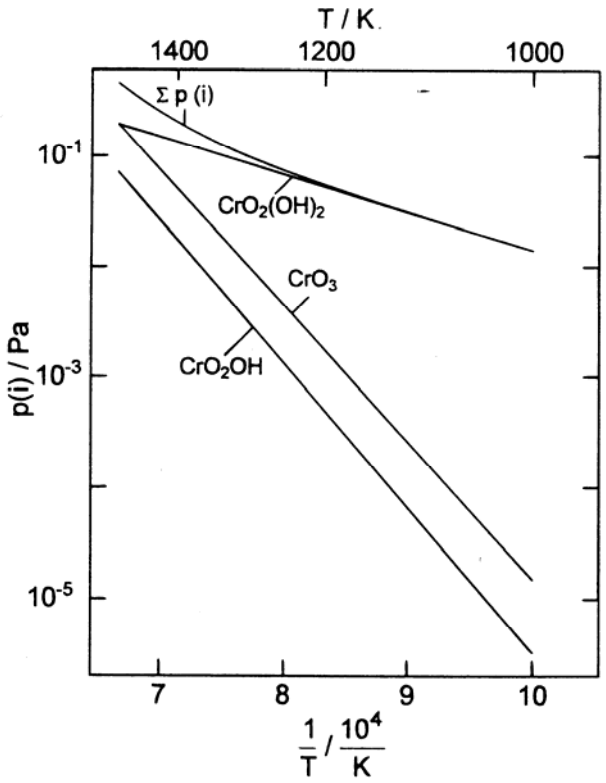

Fig. 13. Partial pressures of different chromium containing species in equilibrium with Cr_2O_3 in $p(O_2) = 0.213$ bar, $p(H_2O) = 0.02$ bar as a function of temperature. The thermodynamic data were given by [40] [39].

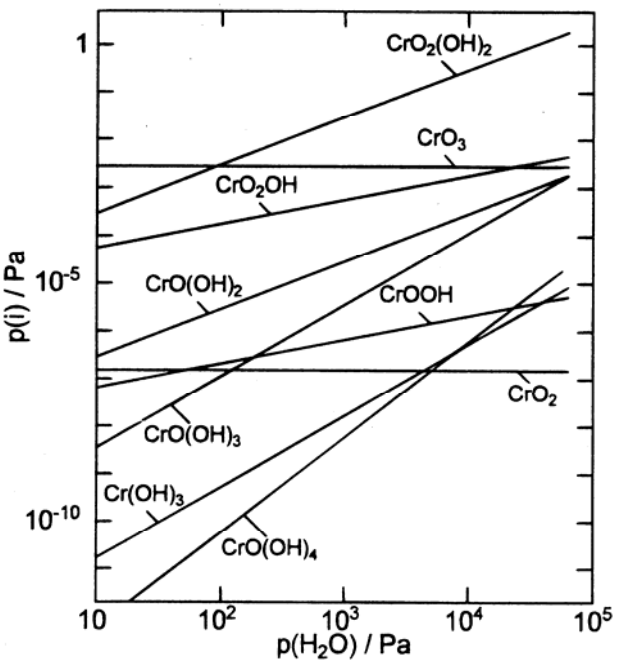

Fig. 14. Partial pressures of different chromium containing species in equilibrium with Cr_2O_3 in $p(O_2) = 0.213$ bar at 1223 K as a function of water partial pressure. The thermodynamic data were given by [40] [39].

It is evident from Fig. 14 that the chromium species given by reaction 8 is dominant in the presence of water vapour in the atmosphere. It can also be recognized that the dominant chromium species are given by reaction 7 and reaction 8.

The partial pressures of the chromium species given by reaction 7 and reaction 8 are given in Table 1-3 at the experimental conditions examined in the present work. The partial pressures were calculated at 973, 1173 and 1373 K using thermodynamic data from Ref. [40].

Table 1. The partial pressures of the chromium species given in reaction 7 and reaction 8 at 973 K at different oxygen and water partial pressures. The partial pressure are given in bar and calculated using thermodynamic data from Ref. [40].

Gas	$p(O_2)$	$p(H_2O)$	$p(CrO_3)$	$p(CrO_2(OH)_2)$
7%H_2/93%Ar	$4.3\cdot10^{-23}$	0.012	$5.2\cdot10^{-27}$	$5.3\cdot10^{-24}$
7%H_2/93%Ar	$5.5\cdot10^{-21}$	0.122	$2.0\cdot10^{-25}$	$2.0\cdot10^{-21}$
Air	0.21	0.012	$9.6\cdot10^{-11}$	$9.7\cdot10^{-8}$
Air	0.21	0.122	$9.6\cdot10^{-11}$	$9.8\cdot10^{-7}$

Table 2. The partial pressures of the chromium species given in reaction 7 and reaction 8 at 1173 K at different oxygen and water partial pressures. The partial pressure are given in bar and calculated using thermodynamic data from Ref. [40].

Gas	$p(O_2)$	$p(H_2O)$	$p(CrO_3)$	$p(CrO_2(OH)_2)$
7%H_2/93%Ar	$1.6\cdot10^{-18}$	0.012	$5.2\cdot10^{-27}$	$5.3\cdot10^{-20}$
7%H_2/93%Ar	$2.0\cdot10^{-16}$	0.122	$2.0\cdot10^{-25}$	$2.0\cdot10^{-17}$
Air	0.21	0.012	$1.4\cdot10^{-8}$	$3.6\cdot10^{-7}$
Air	0.21	0.122	$1.4\cdot10^{-8}$	$3.7\cdot10^{-6}$
Air	0.21	0.50	$1.4\cdot10^{-8}$	$1.5\cdot10^{-5}$

Table 3. The partial pressures of the chromium species given in reaction 7 and reaction 8 at 1373 K at different oxygen and water partial pressures. The partial pressure are given in bar and calculated using thermodynamic data from Ref. [40].

Gas	$p(O_2)$	$p(H_2O)$	$p(CrO_3)$	$p(CrO_2(OH)_2)$
7%H_2/93%Ar	$2.7\cdot10^{-15}$	0.012	$1.7\cdot10^{-17}$	$3.6\cdot10^{-17}$
7%H_2/93%Ar	$3.5\cdot10^{-13}$	0.122	$6.5\cdot10^{-16}$	$1.4\cdot10^{-14}$
Air	0.21	0.012	$4.5\cdot10^{-7}$	$9.4\cdot10^{-7}$
Air	0.21	0.122	$4.5\cdot10^{-7}$	$9.6\cdot10^{-6}$

It can be recognized that vaporization from chromia only is significant in the presence of air in the reaction atmosphere. Furthermore, the dominant volatile chromium species is given by reaction 8.

3 Thermogravimetric equipment

3.1 Introduction

With reduced SOFC operational temperature, iron-chromium alloys have become increasingly interesting as interconnector material SOFC stacks [4]. The advantages of using a metallic interconnector instead of a ceramic interconnector are summarized in [3]. The working temperature in SOFC's will presumably be lowered even further in the coming years, so SOFC developers worldwide are focusing on alloys as a possible interconnector material.

The oxidation behaviour of relevant alloys (cf. section 1.1) must be examined under conditions, which resemble SOFC operational conditions. If hydrogen is used as the fuel in the SOFC, the electrode reactions and the total reaction can schematically be written

$2e^- + ½O_2(g) \rightarrow O^{--}$	Cathode
$O^{--} + H_2(g) \rightarrow H_2O(g) + 2e^-$	Anode
$½O_2(g) + H_2(g) \rightarrow H_2O(g)$	Total

Thus, the operating conditions of SOFC's include very high water partial pressures at the anode side near the exhaust where most of the fuel is converted to water vapour. Hence, it is important to understand the oxidation stability of alloy candidates for interconnector materials in high water concentrations. Little is known about the corrosion stability of iron-chromium alloys in atmospheres containing large amounts of water vapour [10].

The processes occurring during high temperature oxidation are dynamic, so in-situ measurements are widely used to obtain information concerning the oxidation mechanisms. The most common technique to obtain in-situ measurements of oxidation is by thermogravimetry (TG). This technique makes it possible to follow the kinetics of high temperature corrosion in-situ [41].

The development or the purchase of a TG-equipment, which can measure in atmospheres containing large amount of water vapour, was therefore a major component of this Ph.D.-study.

3.2 Structure for the TG-project

The TG-project involved many phases before a final decision regarding the TG-equipment was made. The phases and discussions during the project were both of scientific, technical, and financial character. The different phases for the TG-project will be outlined and discussed in the following. However, it can be difficult to follow the logically development of the project during the discussion. Therefore, to guide the

reader through the different phases of the TG-project, the structure of the project is shown schematically in Fig. 15 as the project evolved in time.

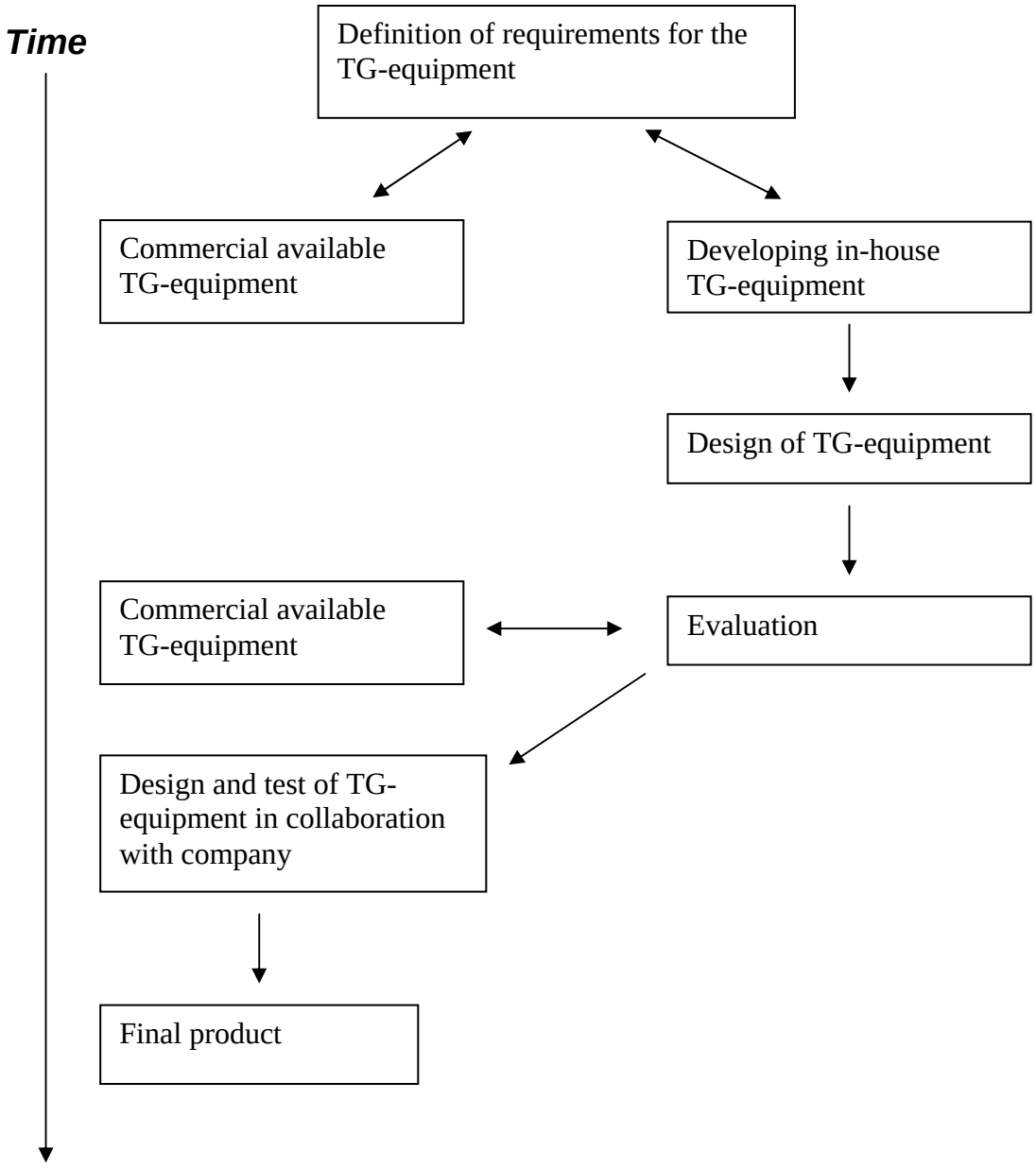

Fig. 15. Structure of the thermogravimetric project as it evolved with time.

3.3 Water vapour in conventional TG-equipment

Conventional TG-equipments often use cooling at several places in the equipment in order to avoid overheating of e.g. flanges, and to protect the balance from heat radiation in order to keep the balance isothermal. If the inlet gas passes through these cold spots, condensation of water may occur if the inlet atmosphere contains large amounts of water vapour.

Condensation of water may be detrimental for the equipment. If water condensates at hot alumina furnace tubes, it can cause local thermal gradients in the ceramic, which may result in cracks in the alumina [42]. Condensation of water may also occur in the balance chamber. This may be detrimental for the balance. Furthermore, if water vapour from the inlet gas condensates, the exact amount of water vapour, which passes the specimen, is unknown. This is obviously unsatisfactory from a scientific perspective.

Applying heating to critical cold areas, in the form of heating tapes, can in some cases surmount the condensation problem. However, such a solution is only advisable if the gas contains a small amount of water vapour. In contrast, if the dew point of the inlet gas is high, there always seems to be a tendency for condensation of water in the system.

3.4 Requirements for TG-equipment

As previously mentioned, it would be interesting to evaluate the corrosion resistance of alloys in atmospheres containing a high degree of humidity. It was therefore decided that the TG-equipment should be able to measure in atmospheres containing very high water partial pressures (> 90% water vapour). Furthermore, the system should be able to measure at temperatures up to ca. 1373 K. Beside these requirements; no additional harsh requirements were put on the TG-equipment, which cannot be meet by commercial available TG-equipments. It should be noticed that all commercial available TG-equipments for high temperature applications can match the required test temperature.

3.5 Commercial available TG-equipment

After the specification of requirements for the new TG-equipment, a search for a suitable solution was made from commercially available equipments. An enquiry was put forward to commercial companies, which were identified through prior knowledge or through the World Wide Web. However, none of the companies appeared to have an adequate TG-equipment for performing measurements in atmospheres containing a large amount of water vapour.

Instead, a possible solution was to buy a standard TG-equipment and subsequently modify it. However, most of the TG-equipments, which were examined, used cooling

at several places of the setup, as previously mentioned. It is necessary that all parts of the gas-system should be heated above ca. 373 K in order to avoid condensation of water. The stability of the commercial equipments was not known if additional heating was applied to cold areas, flanges etc. Furthermore, it could prove problematic to eliminate all cold spots in the system. Thus, the large uncertainties in modifying a commercially available setup turned our focus away from this solution. Instead, it was decided that a suitable TG-equipment should be specifically designed to measure at high temperatures in atmospheres containing a large amount of water vapour. Such a system was not available commercially, so it was decided that we should design and build the system in-house.

3.6 Design of TG-equipment

The design phase started with a visit to colleagues at the Centre for Materials Science in Oslo, who had previously built a TG-equipment, which could measure in gases containing water vapour. The design principles of their equipment were evaluated before designing a new TG-equipment.

The measurements from their equipment showed some scatter. Possible drawbacks of their system were identified as a lack of mass flow controllers for the inlet gases, possible cold spots in the system due to insufficient heating, possible non-isothermal conditions for the balance, and a possible non-laminar flow pattern of the gases. Furthermore, it was not possible to measure in gases containing in excess of 50% water vapour in their TG-equipment [43].

Mass flow controllers are necessary in order to keep a steady flow pattern throughout the experiment. This is essential for high quality measurements, so mass flow controllers were implemented in the new design. Research with atmospheres containing a large amount of water vapour has previously been performed at the SOFC research group at Risø National Laboratory. The experience through prior research is that cold spots and subsequently condensation is hard to surmount with heating tapes alone if the dew point of the inlet gas is high. A well-known solution at Risø is to build a heating box, which surrounds the equipment. Such a heating box was included in the design of the new TG-equipment in order to avoid cold spots in the system. The design of the heating box and the rest of the experimental setup is schematically shown in Fig. 16.

The temperature of the heating box is controlled by a suction and a exhaustion together with a temperature controlled heating element. The air in the heating box is kept circulating by the suction and exhaustion. The heating box is isolated in order to minimize the heat radiation.

The reaction gas is fed into the heating box at the bottom. The inlet gas can either be bubbled through a heated water bottle, or the inlet gas can bypass the water bottle. The gas is led into the furnace tube (alumina) at the top flange. The dew point of the inlet gas, which is bubbled through the water bottle, is determined from the temperature of the water. The temperature of the water is controlled by a heater. The

temperature in the heating box is adjusted to be above the dew point of the gas. This is done in order to avoid condensation of water.

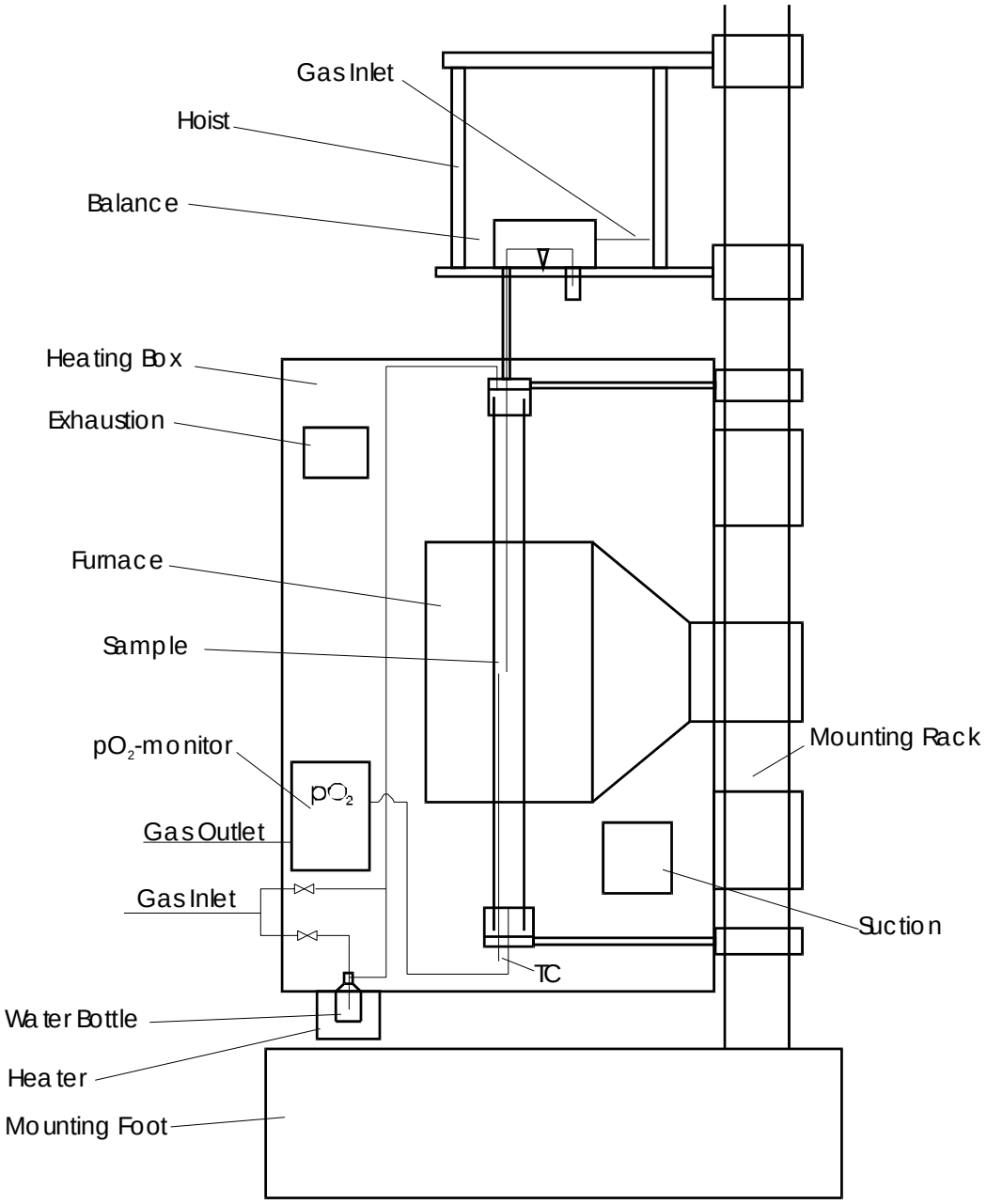

Fig. 16. Schematically design of TG-equipment, which can measure in gases containing large amount of water vapour. The system is discussed in the text.

A protective gas is introduced at the balance head. This is done in order to protect the balance from corrosive environments in the reaction gas, e.g. moisture. The protective gas is fed down along the suspension to the top flange of the alumina tube, where the protective gas is mixed with the reaction gas. This gas mixture is fed down past the suspended specimen and out through the bottom flange. This results in a flow pattern near the sample and suspension, where the flow of both the reaction gas and the

protective gas is fed downwards. A drawback of this design is that the reaction gas is mixed with the protection gas before the gas passes the specimen. This obviously decreases the dew point of the gas mixture passing the sample, since the protection gas is a dry inert gas. However, the composition of the mixed gas can be determined from the flow rates of the protective and reaction gases. The gas mixture is fed into a $p(O_2)$-monitor before it is exhausted.

Alternatively, the reaction gas can be introduced at the bottom flange and fed up through the furnace tube. In this case, the reaction gas will mix with the protective gas from the balance near the top flange, where the gas outlet also is positioned. An advantage of such a flow pattern is that the dew point of the reaction gas is not lowered by the addition of the protective gas. However, the flow pattern of the two gases will be opposite to each other. This may result in a non-laminar mixing zone, where turbulence in the gas mixture may affect the quality of the measurements. Furthermore, if the mixing zone of the gases extends down to the sample, the gas composition surrounding the specimen will be unknown. It was decided that a minor decrease of the water content in the reaction gas was acceptable, so the flow pattern in the design should be as shown in Fig. 16.

The reaction gas is, as previously mentioned, fed into the alumina tube at the top flange. The gas inlet may cause small vibrations to the suspension and hence scatter in the TG-signal. In this case, an additional short (ca. 5 cm) narrow alumina tube can be inserted inside the large alumina tube at the top flange. This short tube will surround the suspension, so the protective gas will be fed inside the tube. The reactive gas will be fed between the short tube and the furnace tube. This will make the flow direction of the reaction gas similar to the flow direction of the protective gas before the two gases are mixed. It is shown schematically in Fig. 17.

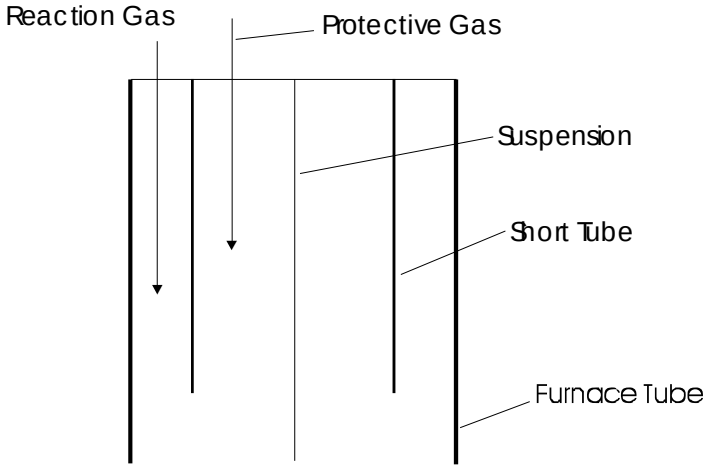

Fig. 17. Schematic drawing of a short tube inserted at the top flange inside the larger furnace tube.

The balance must not be heated above 353 K. This requires that the balance is positioned ca. 10 cm away from the heating box, which outside temperature can be up to ca. 373 K. An extra isolation of the heating box may be necessary in order to keep the heat radiation towards the balance down. Temperature variations of the balance can cause scatter in the TG-measurements. In this case, it will be necessary to surround the balance with heating elements in order to keep it isothermal.

The balance is mounted on a stable plate not only to minimize scatter from shaking, but also to decrease heat radiation between the heating box and the balance.

The content of water, which passes the specimen, should be very high. Hence, the amount of inert dry protective gas should be limited. The cross section of the tube, which connects the balance with the top flange, should be small in order to minimize the amount of protective gas around the specimen. The protective gas must be heated above the dew point of the reaction gas before it enters through the flange. Otherwise, condensation of water from the reaction gas may occur. Hence, the length of the connection tube in the heating box should be ca. 15 cm, so the heating box can heat the protective gas. Additional heating will be required around the tube, if the heating applied to the connection tube is insufficient.

The distance from the furnace to the top flange is ca. 20 cm. This results in a temperature of ca. 398 K at the top flange when the temperature of the furnace is 1373 K. The flange should not be cooled. The top flange is mounted on a metal plate, which is attached to a large rack.

A radiation shield is placed in the bottom of the alumina tube. However, the shield should not cool the bottom flange below 378-383 K. The bottom flange is also mounted on a metal plate, which is attached to the rack.

A thermocouple is positioned within the alumina tube near the end of the suspension. The TC-couple is mounted at the bottom flange. Three screws adjust the flange and alumina tube. A precise electrical linear hoist lifts the balance together with the connection tube. The connection tube rests on an O-ring fitting at the top flange.

The furnace would be a tube furnace with a heating zone of 22 cm. The furnace has a maximum temperature of 1573 K, and the surface temperature of the furnace would be maximum 373 K.

3.7 Evaluation

The evaluation of the experimental design was governed both from a technical and a financial perspective.

After building the experimental setup, the equipment would need calibration. The condensation of water in the system would most likely not be a problem. Instead, the main obstacles to overcome seemed beforehand to be related to the flow pattern of the gases and the thermal stability of the balance. The latter has a significant influence on the TG-signal. Thus, the calibration of the equipment could be time consuming. Furthermore, there was no guarantee that we would be able to build an equipment, which could measure to the standard or better than equipments provided by commercial companies. This is mainly caused by the many years of experience the companies have in solving problems regarding the gas flow etc.

In summary, the project had uncertainties in the design and subsequent building of the system. Furthermore, the process would most likely be very time consuming and hence costly to perform. It was therefore decided to re-examine the commercial companies in order to seek suitable solutions to the problems described. One solution was to collaborate with a company to develop a novel TG-equipment.

3.8 Commercial TG-systems

The market was re-scanned for suitable TG-equipments to measure in gases containing large amounts of water vapour. The survey yielded two results; Netzsch and Setaram. Both companies could provide systems, which could measure in gases containing water. However, both systems had limitations.

The Netzsch equipment could measure in almost pure water vapour. However, it could only measure up to ca. 1173 K. The quality of their measurements was very good.

The Setaram equipment could measure in gases containing up to 30% water vapour. The design of their system was basically a standard TG-setup, where the inlet gas was bubbled through a heated water bottle. The gas connection between the bottle and the inlet of the furnace tube was heated by applying standard heating tape. The design of their system was in principle similar to the design shown in Fig. 16, except for the lack of sufficient heating in their system. Since the TG-equipment was a standard TG-system, the equipment could measure up to high temperatures (> 1600 K). The quality of their measurements was also very good.

Subsequently, we examined the possibility that one of the commercial companies could design an equipment to meet our specifications given in section 3.4.

The Setaram setup could not be redesigned to measure in higher water contents than ca. 30% water vapour. Development of a possible TG-system would then require designing a new TG-setup. Setaram was not interested in designing such new equipment in collaboration with Risø National Laboratory. In contrast, Netzsch was positive regarding a possible collaborative design of a new system. Thus, a collaboration with Netzsch was initiated in order to design the new TG-equipment.

3.9 From prototype design to product

Collaboration was undertaken between Risø National Laboratory and Netzsch in order to develop the novel TG equipment that could measure in almost pure water vapour. The design of the new equipment is subject to an agreement of confidentiality. The collaboration has led to a prototype, which is presently being tested, and from which measurements are presented in this thesis. The testing may obviously led to small changes in the design of the equipment before a final product becomes available.

4 Experimental

4.1 Introduction

The general experimental procedures followed in this work are described in the following. This includes preparation, oxidation and subsequently characterization of the specimens.

4.2 Materials and specimen preparation

The alloys were prepared by arc melting in an argon atmosphere (99.998%). Prior to arc melting, a button of titanium was melted and used as a getter in order to purify the argon atmosphere by reducing residual contents of oxidants. The starting materials were arc melted on a water-cooled copper plate, as shown in Fig. 18.

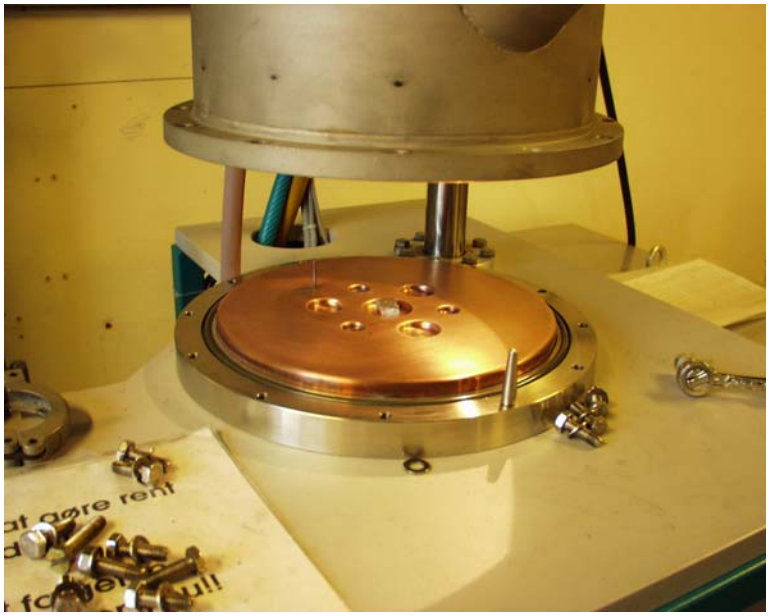

Fig. 18. Picture of the copper plate in the arc melting equipment, where the alloys were prepared.

The starting materials in the arc melting process were pure silicon, chromium (Goodfellow) with a purity of 99.95 wt.%, cerium (Goodfellow) with a purity of 99.9 wt.% and Armco iron. The composition of Armco iron is given in Table 4.

Table 4. Chemical composition of Armco iron.

Element	C	Si	Mn	P	S	Fe
wt.%	< 0.015	< 0.015	< 0.080	< 0.020	< 0.015	Balance

The cast alloy was cold rolled and subsequently annealed under a hydrogen/argon mixture (7%/93%) at 1093 K for 1 h. After the isothermal anneal, the alloys were pulled into a cold zone of the furnace tube in order to cool rapidly. The compositions of the alloys (in atomic %) are given in Table 5.

Alloy	Composition in at.%			
	Fe	Cr	Si	Ce
A1	Bal.	22	--	--
A1-Si	Bal.	21.9	0.3	--
A1-Ce	Bal.	21.9	--	0.3
A1-CeSi	Bal.	21.9	0.15	0.15

Table 5. The compositions of the alloys, which were prepared in the present work. The compositions are given in atomic percent.

The abbreviations given for the alloys in Table 5 will be used throughout this thesis. The homogeneity of the alloys was confirmed using energy dispersive X-ray analysis (EDX).

The specimens were cut with the dimension 10 x 5 x 0.5 mm^3, and a hole (Ø = 2 mm) was drilled for suspension. The samples were wet ground (water) with SiC abrasive paper (1000 grid). Finally, the specimens were ultrasonically cleaned in ethanol prior to oxidation.

4.3 The furnace

A schematic drawing of the gas system and furnace is shown in Fig. 19. The furnace tube, which was made of alumina, was positioned horizontally. A sample holder was positioned by the thermocouple (TC) within the furnace tube. The specimens were suspended on platinum hooks from the sample holder.

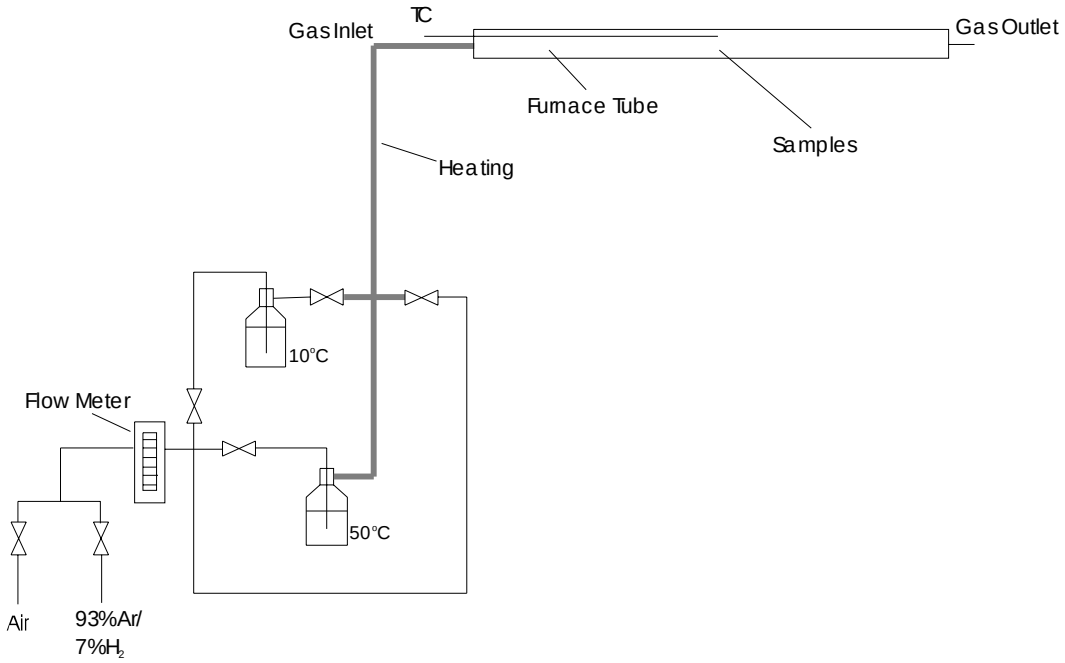

Fig. 19. A schematic drawing of the gas system and furnace.

The reaction gas was either air or a hydrogen/argon mixture. The flow of the reaction gas was controlled using a ball flow meter. The reaction gas was either bubbled through water at 10°C or 50°C, or the reaction gas was bypassed as a dry gas. The temperature of the water was either controlled by a refrigerator or by a thermostatically controlled heater. The pipe, which connects the heated water to the furnace tube, was heated in order to avoid condensation of water.

4.4 Experimental procedure during furnace tests

The specimens examined in the present work, were heated up in the horizontal tube furnace after the establishment of the reaction atmosphere in the furnace tube. The initial heating rate was 300 K/h. The isothermal dwell time was either 70 h or 504 h. The reaction atmospheres were either air or a 7%H_2/93%Ar mixture. The reaction gas was humidified by bubbling through water at 10°C or 50°C, yielding a water partial pressure of 0.012 bar and 0.122 bar, respectively. The oxygen activities for the humidified hydrogen/argon mixtures were calculated from the hydrogen/oxygen/water equilibrium. The oxygen activity was also measured at the gas outlet (cf. Fig. 19) using a pO_2-sensor in order to confirm the gas tight experimental setup. The gas flow during the oxidation was 100 ml/min. The specimens were cooled in the furnace after the isothermal segment.

4.5 Thermogravimetry

The isothermal TG measurements in this work were performed using a Netzsch STA 409 CD equipment for the measurements conducted in reaction atmospheres containing a small amount of water vapour, i.e. less than 1% water vapour. The isothermal TG measurements were also performed in reaction atmospheres containing large amounts of water vapour. These measurements were performed using the special Netzsch equipment described in chapter 3.

4.5.1 Netzsch STA 409 CD equipment

The measurements using the Netzsch STA 409 CD equipment were performed in dry gases or in atmospheres containing less than 1% water vapour. The principle design of the equipment is shown in Fig. 20. A dry protection gas is introduced at the balance chamber, while a sample gas may be introduced near the bottom of the furnace tube. The sample gas and protective gas are mixed before the mixture is fed past the specimen and out of the top of the furnace tube (cf. Fig. 20). The valve for the reaction gas is closed during experiments in dry atmospheres. The dry atmospheres (air and hydrogen/argon) were used directly from the gas manifold. No additional drying of the gas was performed. The water content in the dry reaction gases was measured using a dew point meter. In contrast, if the measurements were performed in atmospheres containing small amounts of water, the sample gas was humidified by bubbling through thermostatically controlled water.

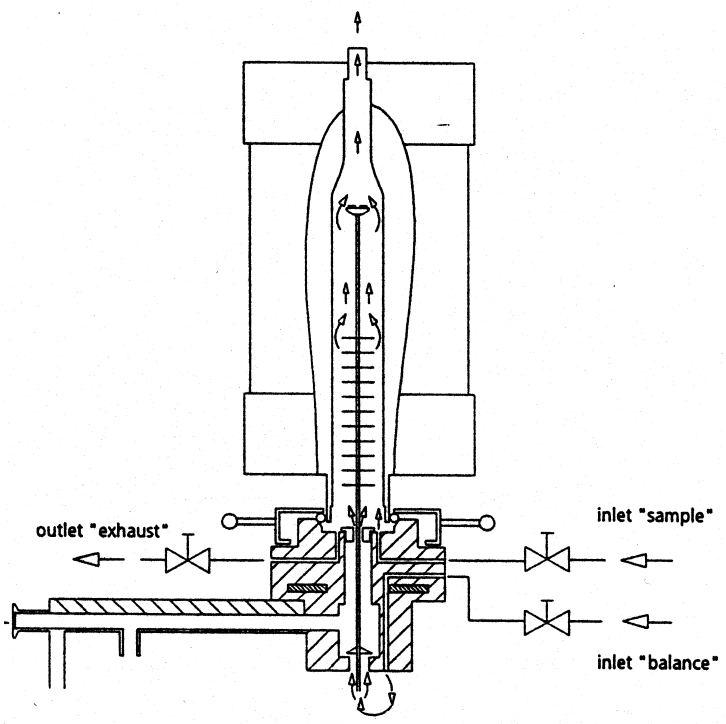

Fig. 20. Diagram showing the gas flows in a Netzsch STA 409 CD equipment, adapted from [44].

4.5.2 TG measurements

The following parameters were used during all measurements performed using the Netzsch STA 409 CD equipment and the special Netzsch equipment.

The initial heating ramp during the TG measurements was 40 K/min. The flow of the gases was controlled using mass flow controllers of type Brooks 5850. The total gas flow passing the specimens during the measurements was 60 ml/min. The measurements were corrected for buoyancy by subtracting a blank run. The isothermal dwell time was 24 h for all the conducted measurements.

4.6 X-ray diffraction

The oxide scales were characterized by X-ray diffraction (XRD) obtained at room temperature. The measurements were performed on a STOE reflection (STOE Θ/Θ) equipment using Cu-K_α radiation. The diffraction patterns were obtained in the 2Θ range of 20-100^o with a step size of 0.05^o. The oxide phases were identified with data files in the JCPDS index (PDF files).

4.7 Specimen preparation for SEM and TEM

The surface of the oxide scales was examined by scanning electron microscopy (SEM) without further coating.

Polished cross sections of the specimens were prepared for investigation using the SEM. The specimens were embedded in resin followed by preparation of the cross section. The cross sections were prepared by wet (water) grinding on SiC abrasive paper, followed by polishing with a diamond paste. The surface finish was 1 μm. The cross sections were coated with carbon in order to prevent charging.

Fractures of the specimen scales (cross section) were also prepared for examination in the SEM. The fractures were prepared by cooling the oxidized specimens in liquid nitrogen and subsequently cracking the specimens. The fractured scales were positioned vertically in order to examine how the oxide morphology changed with depth.

The oxide whiskers grown on chromia were examined using TEM. The specimens, for examination, were prepared by very gently scraping the oxide whiskers off the oxide scale with a sharp knife. The whiskers were positioned on a holey film for examination using TEM.

4.8 SEM and EDX

The surface of the oxide scales and cross sections of the specimens were analysed using a JEOL 840 SEM equipped with a Noram EDX analyser. Both secondary and backscattered electrons imaging were used in the present work. The SEM uses an Everhart-Thornley detector for detection of secondary electrons and a semiconductor (p-n junction) for detection of backscattered electrons [45]. The EDX analyses were performed both as point analysis and as line scan analysis.

4.9 TEM

Oxide whiskers grown on chromia scales were examined using a 200 kV JEOL 200 FX TEM equipped with a Noram EDX analyser.

4.10 Auger electron spectroscopy

The surface of oxide scales grown at 973 K were analysed using Auger electron spectroscopy (AES) in the present work. The analyses were performed using a PHI 560 ESCA/Auger analyser (double pass cylindrical mirror analyser). The analyses were performed with a primary electron beam voltage of 5 kV. The oxide scales were ion etched using an argon gun in order to obtain the composition through the oxide scales, i.e. the depth profiles. An acceleration voltage of 5 kV was used for the ion gun. The etch rate was calibrated on SiO_2 yielding a rate of 10.2 Å/min for a 2x2 mm^2 area [46]. The sputtering was performed on a 3x3 mm^2 area in the present work. In this case, the etch rate is 4.53 Å/min for SiO_2. The Auger electrons were detected in the 20-110 and 400-800 eV energy ranges.

5 Oxidation of Fe-Cr alloy in O_2-H_2-H_2O atmospheres

5.1 Introduction

As described in chapter 1, iron-chromium alloys are being considered for use as interconnector material in SOFC stacks, and other high temperature applications e.g. gas turbines and nuclear reactors. The oxidation behaviour of chromia forming alloys has been the subject of numerous studies. Reviews of the high temperature oxidation of alloys can be found in the literature [47-50]. The transient oxidation [51], and breakaway oxidation [9] have also been examined for chromia forming alloys. Most oxidation studies of chromia forming alloys have been performed in air or oxygen. Only a few studies have examined the oxidation behaviour under reducing conditions [24,52]. The effect of water vapour on the growth of chromia scales is receiving increasing attention [17,39,53,54]. However, most of these studies have only examined the effect of water vapour in air or oxygen on the growth of chromia scales. Few studies have examined the effect of water vapour under reducing conditions.

The purpose of this work is to examine the effect of oxygen activity and water vapour content on the oxidation behaviour of a ferritic iron-chromium alloy in a unified study. The effects of oxygen activity, and content of water vapour in the reaction atmosphere are discussed in relation to the oxide microstructure, transient oxidation, and steady state oxidation. The oxidation behaviour of $Fe_{0.78}Cr_{0.22}$ is investigated at 1173 K in air and in hydrogen/argon atmospheres, containing various amounts of water vapour.

5.2 Experimental

The iron-chromium alloy examined in this chapter has the chemical composition $Fe_{0.78}Cr_{0.22}$ (A1), where the composition is given in atomic percent.

The specimens were oxidized at 1173 K for 70 h. The reaction atmospheres were either air or a 7%H_2/93%Ar mixture containing various amounts of water vapour. The experimental conditions are summarized in Table 6.

After the oxidation, the surface of the oxide scales was examined using SEM and EDX analysis in order to elucidate the microstructure and the chemical composition of the scales. The crystalline structure of the scales was determined using XRD obtained at room temperature.

Polished cross sections of the specimens and fractures of the specimen scales (cross section) were prepared in order to investigate their growth behaviour and oxide morphology. The polished cross sections and fractured scales of the specimens were examined utilizing SEM and EDX analysis. Furthermore, the structure of the whiskers grown in this study was determined from TEM and EDX studies.

The experimental details are given in chapter 4.

Table 6. Test conditions for the A1 alloy. The specimens were oxidized in the hydrogen/argon mixture and in air, containing 1% and 12% water vapour, respectively.

Temperature / K	Gas	Dwell time / h	$p(O_2)$ / bar	$p(H_2O)$ / bar
1173	7%H_2/93%Ar	70	$1.6 \cdot 10^{-18}$	0.012
1173	7%H_2/93%Ar	70	$2.0 \cdot 10^{-16}$	0.122
1173	Air	70	0.21	0.012
1173	Air	70	0.21	0.122

5.3 Results

5.3.1 Microstructure

The SEM micrographs of the surface of scales grown for 70 h in different atmospheres are shown in Fig. 21A-D.

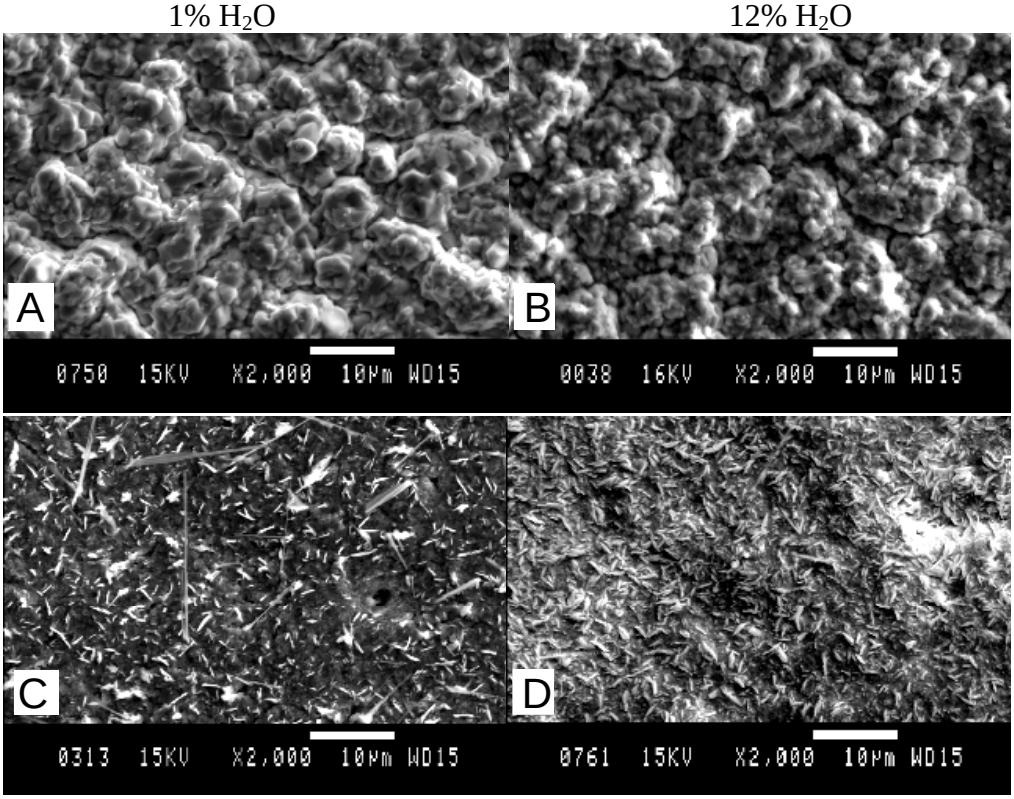

Fig. 21. SEM micrographs of the oxide scales. The scales were grown in air (A,B) and in hydrogen/argon (C,D), containing 1% (left) and 12% (right) water vapour.

The oxide formed in air (cf. Fig. 21A,B) consists of large oxide nodules, each consisting of many smaller oxide grains. The grains observed at the surface of the scales are approximately 2-3 μm in diameter. Oxidation of specimens in hydrogen/argon atmospheres (cf. Fig. 21C,D), results in an oxide morphology very different from that in air. The surface of the scales grown in hydrogen/argon consists of much finer grains. Furthermore, the oxide formed in hydrogen/argon consists of oxide whiskers and oxide ridges. The amount of water does not appear to have a significant influence on the microstructure compared to the effect of the "carrier gas" (air vs. hydrogen/argon). Interestingly however, the formation of whiskers is most profound for the specimen grown in hydrogen/argon containing 1% water vapour (cf. Fig. 21C,D).

Fractured scales of the oxides grown in air (A) and in hydrogen/argon (B), both containing 1% water, were examined using SEM (cf. Fig. 22A,B) in order to investigate whether the observed differences in oxide morphology (air vs. hydrogen/argon) (cf. Fig. 21A,C) extended all through the oxide scales.

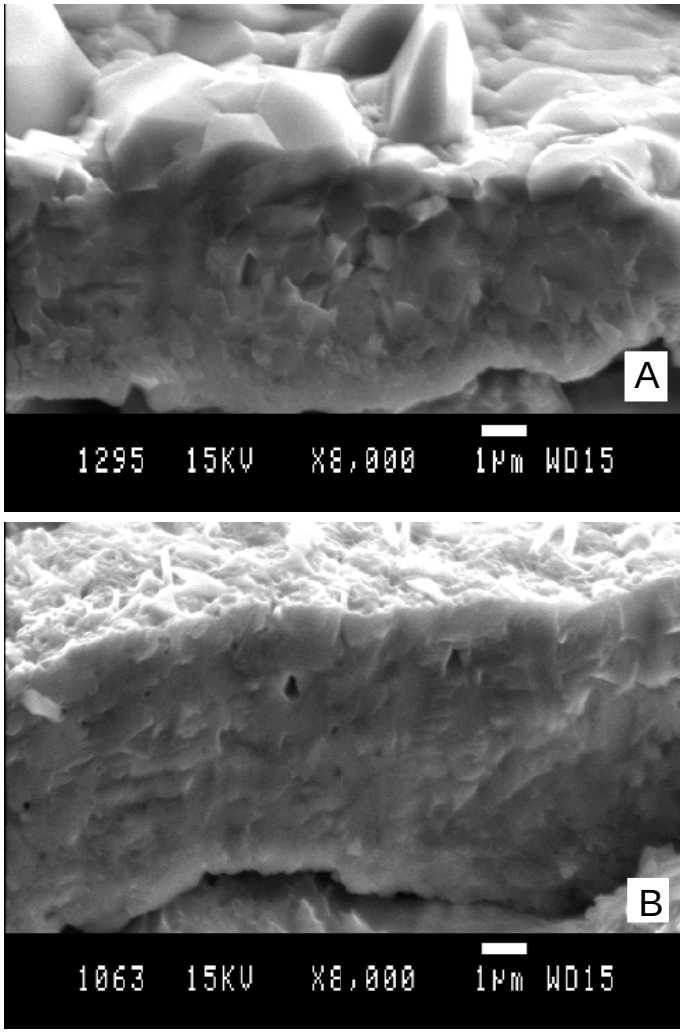

Fig. 22. SEM micrographs of fractured scales of oxides grown in air (A) and in hydrogen/argon (B), both containing 1% water vapour.

The difference in morphology for different gas atmospheres shown in Fig. 21 can also be recognized from the SEM micrographs in Fig. 22. The oxide grains at the oxide/gas interface are large when grown in air, while the surface of the scales grown in hydrogen/argon consists of whiskers, oxide ridges and small grains. However, the fractured scales show that this difference in morphology does not extend all through the oxide scales. Away from the oxide/gas interface, the oxide grains grown in air and in hydrogen/argon are similar in size. Furthermore, the size of the grains does not appear to vary across the oxide scales.

The surface of the chromia scale is bulky, both when grown in air and in hydrogen/argon. An example of this is shown in Fig. 23 for a specimen grown in hydrogen/argon containing 12% water vapour.

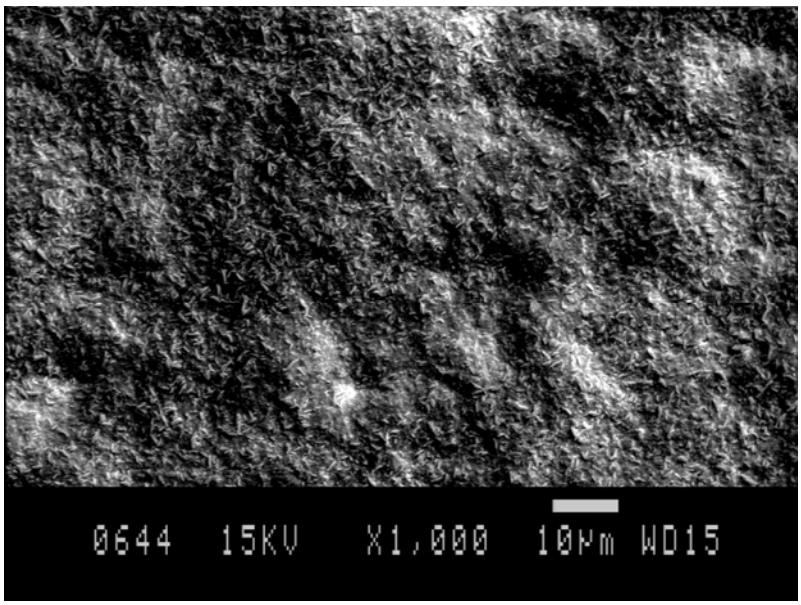

Fig. 23. Bulky oxide scale for the A1 specimen oxidized in hydrogen/ argon containing 12% water.

Polished cross sections of the specimens are shown in Fig. 24A-D. The scales grown in hydrogen/argon (cf. Fig. 24C,D) adhere well to the alloy although the scale thickness is not uniform. Small cavities can be observed at the scale/alloy interface as well as in the scale. In spite of the much higher oxygen partial pressure in air, the scales grown in air (cf. Fig. 24A,B) are slightly thinner than those grown in hydrogen/argon. Large cavities can be seen at the scale/alloy interface, and the scales are less adherent to the alloy compared to the scales grown in hydrogen/argon. The content of water vapour in the reaction atmosphere does not appear to have a significant effect on the adherence of the oxide scales to the alloy.

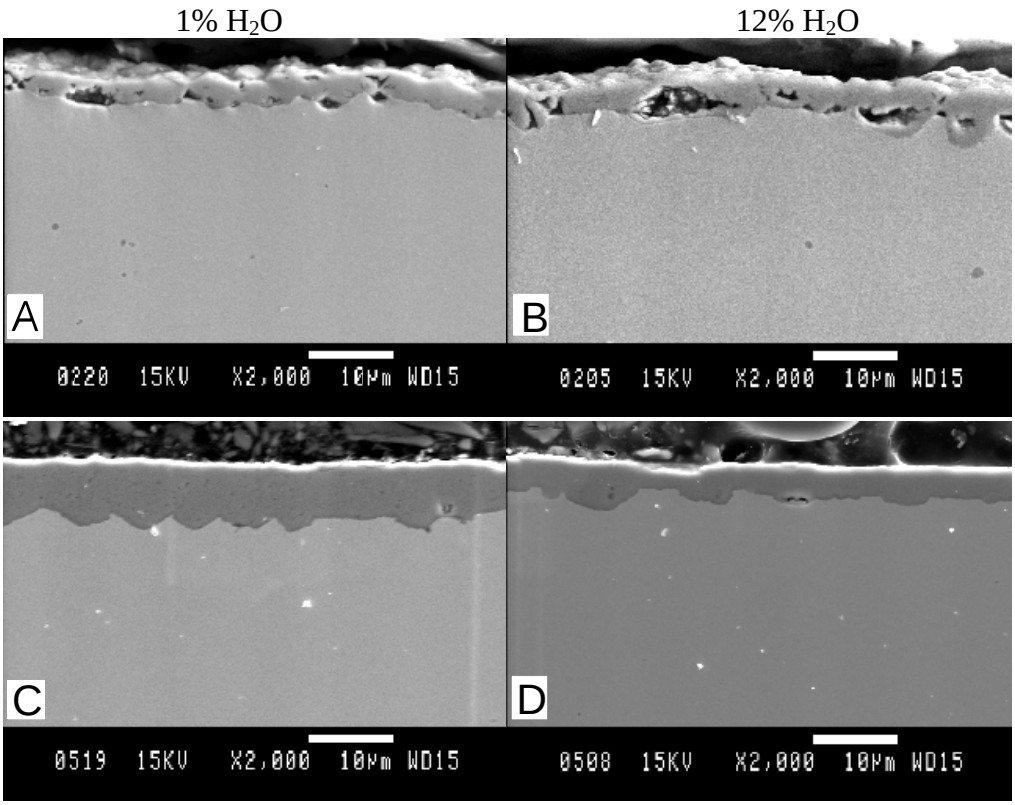

Fig. 24. SEM micrographs of cross sections of the specimen oxidized for 70 h. The samples were oxidized in air (A,B) and in hydrogen/argon (C,D), containing 1% (left) and 12% (right) water vapour.

5.3.2 XRD analysis

The diffraction patterns of the oxide scales are shown in Fig. 25. The scales grown in air contain an oxide with the corundum structure (PDF #38-1479). In contrast, the scales grown in hydrogen/argon contain an oxide with the corundum structure (PDF #38-1479), and in addition, they show reflections from a spinel phase (PDF #34-0140) with low intensity.

5.3.3 EDX analysis

The polished cross sections of the specimens were analysed using EDX line scan analysis in order to obtain the chemical compositions of the oxide scales. These results can, in combination with the XRD analysis given in section 5.3.2, reveal the nature of the phases present in the oxide scales. The EDX line scan analyses of the specimens oxidized in hydrogen/argon are shown in Fig. 26A,B.

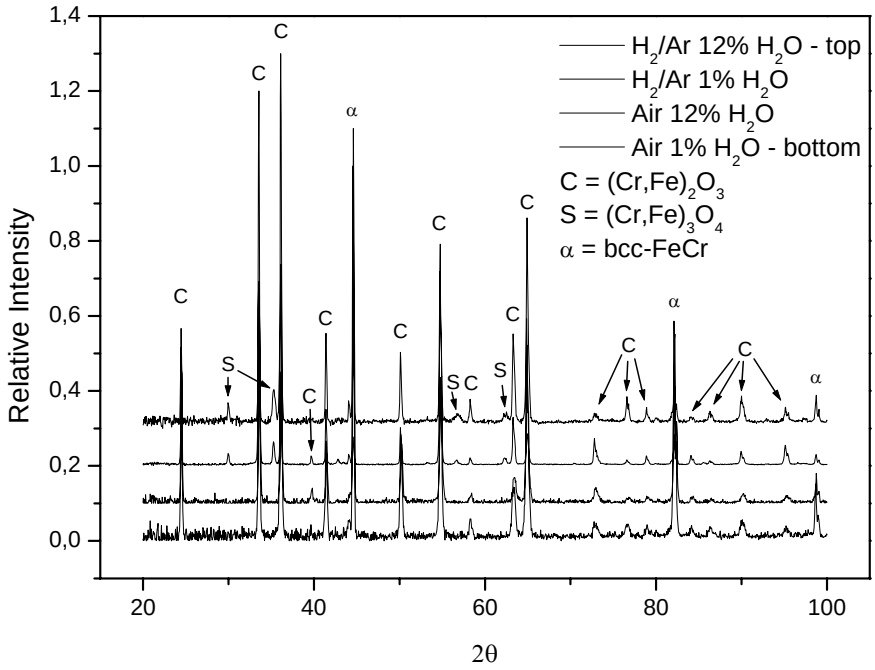

Fig. 25. Diffraction patterns of the oxide scales.

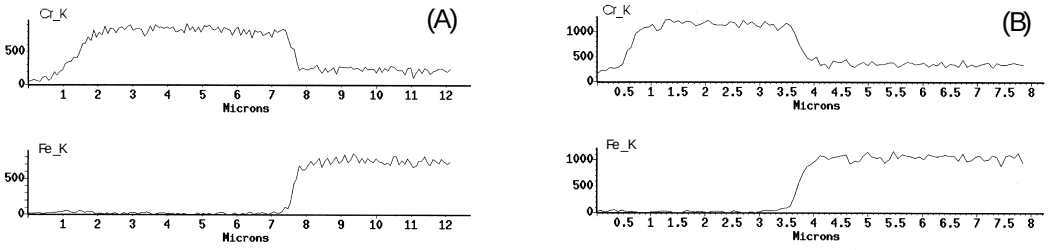

Fig. 26. EDX line scan analyses of cross sections of scales grown in hydrogen/argon containing 1% water (A) and 12% water (B). The analyses are given as the relative intensity as a function of distance.

All the EDX line scan analyses shown in this thesis were measured from the oxidizing atmosphere to the alloy, i.e. the composition of the oxides from the gas/oxide to the oxide/alloy interface is shown from left to right in the EDX analyses. The analyses show the presence of chromium in the scales. Despite the presence of a spinel phase in the diffraction patterns (cf. Fig. 25), no existence of iron was detectable in the outermost part of the scale. The EDX analyses of the specimens oxidized in air show similar results with a chromium containing scale.

5.3.4 Gravimetric measurements

The weight gains after oxidation of the specimens are shown in Fig. 27. The measurement conditions are given in Table 6. The oxidation showed a weight gain of approximately 1 mgcm^{-2} for all the samples. However, it should be noticed that the

weight gain obtained for the specimen oxidized in air containing 12% water vapour exhibited the smallest weight gain.

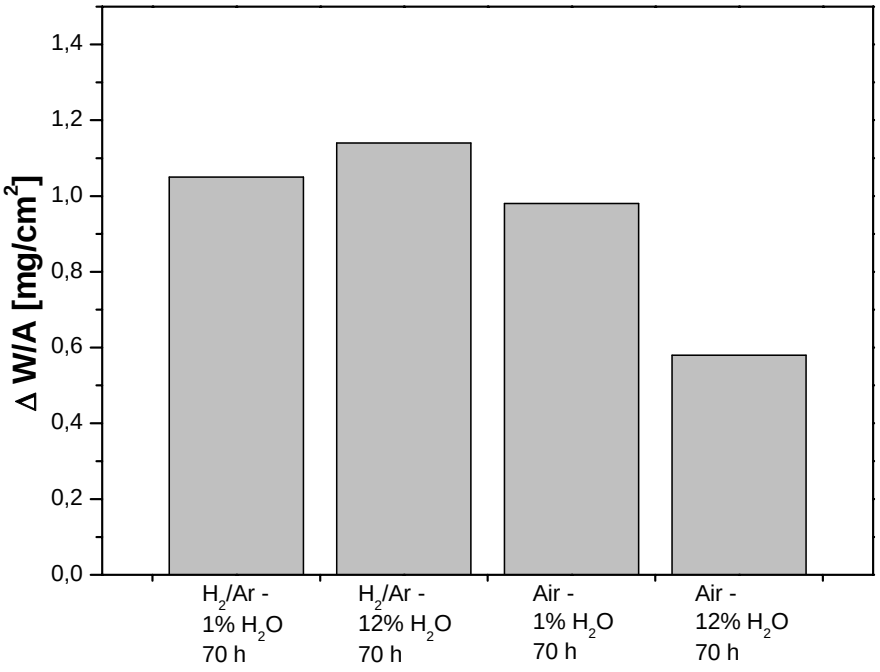

Fig. 27. Weight gain for the specimens oxidized at 1173 K for 70 h. The specimens were oxidized under different conditions, as summarized in Table 6.

5.4 Discussion

The discussion of the present results is divided into sections dealing with i) oxide microstructure and ii) the oxidation kinetics of the oxide scales. Important parameters for the interpretation of the results are the partial pressures of oxygen and water in the reaction atmospheres.

5.4.1 Microstructure

The effect of the reaction gas (air vs. hydrogen/argon) on the morphology of the outermost part of the oxide scale can easily be seen in Fig. 21 and Fig. 22. The scales grown in air consist of 2-3 µm grains at the surface, while the surface of the scales grown in hydrogen/argon consists of oxide ridges and whiskers. The content of water in the reaction gas appears to have a minor influence on this behaviour.

In the following, the growth mechanisms of oxide whiskers and ridges are discussed. The large effect of reaction gas on the oxide morphology is also described. Examples of the oxide whiskers grown in the present study are shown in Fig. 21C and Fig. 28.

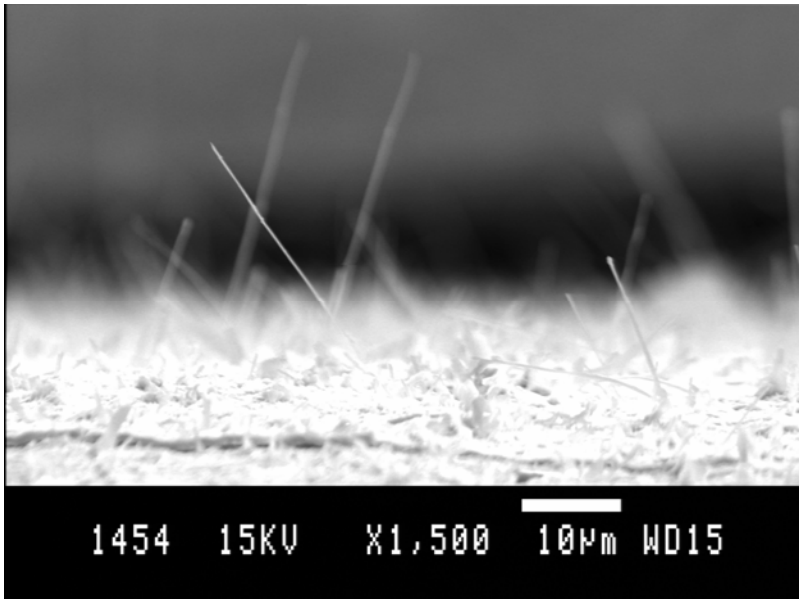

Fig. 28. SEM micrograph of the oxide whisker formation on a A1 specimen grown in hydrogen/argon containing 1% water vapour.

The whiskers were examined using TEM and EDX in order to elucidate the chemical composition and chemical phase of the whiskers. The whiskers were identified as pure chromia.

Most of the oxide whiskers are 30-50 µm long and very thin (cf. Fig. 28). Furthermore, the whiskers have a uniform thickness. This geometry strongly indicates that the whiskers are growing either (i) from the tip of the whisker or (ii) from the base of the whisker.

If the whiskers are growing from the tip, the growth is governed either by an outward diffusion of chromium along the whisker, or by a vapour phase transport of chromium species to the tip of the whisker. The latter mechanism can be rejected, since the activity of volatile chromium containing species is low in the hydrogen/argon mixture (cf. section 2.4.4). Chromium may either diffuse outwards along the whisker by way of surface diffusion on the outer surface, or by diffusion within the whisker. The geometry of the whiskers indicates that a surface diffusion mechanism on the outer surface can be rejected, since this would imply oxide formation in the lateral direction along the whisker. Such an oxide formation would result in a non-uniform geometry of the whisker. If the whiskers instead grow by diffusion within the bulk, the outward diffusivity must be much greater than the lateral diffusivity, since the geometry of the whiskers is uniform. This implies that lattice diffusion can be discarded as the mechanism for the whisker growth. Hence, an alternative high diffusivity path within the whisker should exist on the basis of the observed geometry and the proposed growth mechanism. Such a diffusion mechanism has been suggested for the growth of hematite whiskers [55,56], where the existence of a tunnel within the whisker has been revealed by TEM studies. Such a structure may also exist for the chromia whiskers observed in this work. Furthermore, the tunnel may be centered on high

diffusivity paths in the oxide beneath the whisker [57]. The diffusion of chromium along a tunnel occurs by surface diffusion. The surface diffusion coefficient is generally much larger than the corresponding lattice diffusion coefficient (of the order 10^4-10^6) [57,58]. The tunnel may act as a high diffusivity path within the whisker, so the growth of the observed chromia whiskers in this study may be governed by a rapid surface diffusion of chromium through a tunnel within the whisker. Although the transport distance to the tip of the whisker is much greater than the lateral transport distance in the whisker, the outwards growth of whiskers is facilitated by the very rapid surface diffusion of chromium in comparison with the lattice diffusion. The proposed mechanism for the formation of whiskers is shown schematically in Fig. 29.

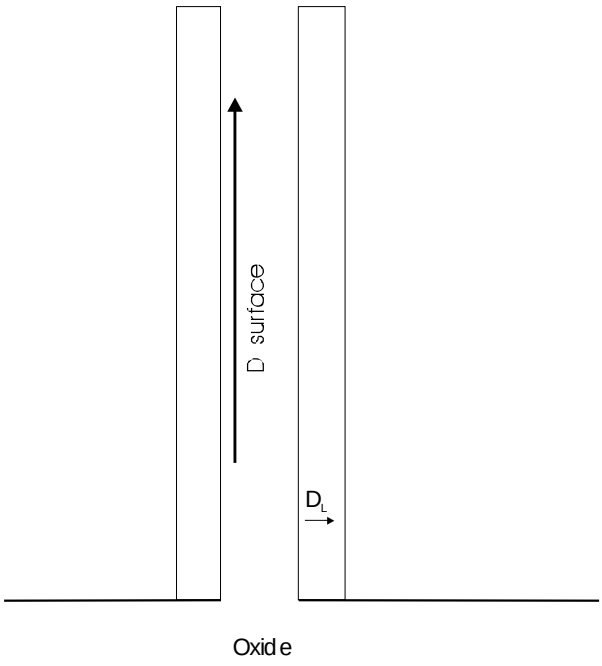

Fig. 29. Proposed mechanism for the formation of oxide whiskers by way of surface diffusion.

An alternative explanation is that the whiskers grow from the base of the oxide. In this case, the reaction takes place at the base of the whisker. This reaction could be governed by diffusion of oxidant through the tunnel mentioned above. It could also occur by dissociation of the oxidant at the base of the whisker. Raynaud and Rapp [57] showed that the dissociation of the oxidant is the rate-limiting step for the growth of whiskers. This shows that the formation of chromia takes place at the site of dissociation of the oxidant. Hence, if the whiskers grow from the base, the dissociation of the oxidant must take place near the base. This implies that if the growth is governed by diffusion of oxidant through the tunnel, the oxidant must diffuse as molecular species.

Oxide ridges were also observed on top of the chromia scales (cf. Fig. 21D). Hsu and Yurek [59] showed that the base of the oxide ridges is situated on top of grain boundaries in the oxide. The grain boundaries are proposed to extend up through the oxide ridge. In this case, the growth mechanism of oxide ridges may be explained by a similar mechanism as the growth of the oxide whiskers. Instead of surface diffusion along a tunnel, chromium may diffuse along grain boundaries to form the oxide ridges

[59]. The proposed mechanism for the growth of oxide ridges is shown schematically in Fig. 30.

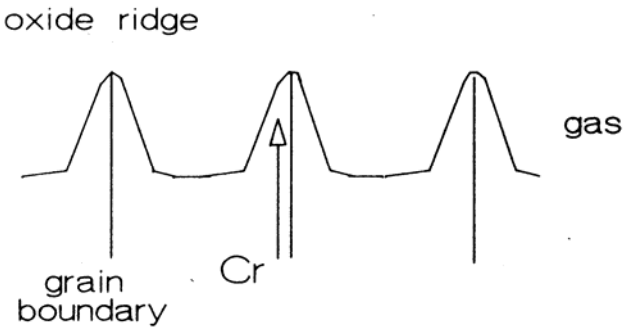

Fig. 30. Proposed mechanism for the formation of oxide ridges by way of grain boundary diffusion [52].

The fractured scale in Fig. 22B shows that the morphology containing oxide whiskers and ridges does not extend all through the scale. Rather, the oxide grains form a dense oxide scale beneath the open morphology. The limited extension of whiskers and ridges in the oxide may be explained by the chromia growth mechanism. During growth of the chromia scale, oxidation between the oxide whiskers and ridges will start when the extra transport distance outward through the oxide whisker or ridge balances the rapid surface or grain boundary diffusion of chromium. Hence, oxide ridges and whiskers will eventually start to grow in the lateral direction. The extension of the oxide ridges and whiskers, and thereby the open scale morphology, is therefore limited. The observed morphology in Fig. 22B is therefore caused by a competition of oxide growth by way of oxide whiskers and ridges, and oxide growth between oxide whiskers and ridges.

The question remains, why whiskers form in humidified hydrogen/argon atmospheres, while whiskers apparently do not form in humidified air (cf. Fig. 21). An influence of water in the formation of oxide whiskers was observed by Raynaud and Rapp [57], who studied the formation of NiO whiskers on Ni in moist oxygen. They proposed a growth mechanism for the formation of oxide whiskers, where the growth was activated by the presence of water vapour in the atmosphere. This explains the formation of oxide whiskers on the specimens oxidized in hydrogen/argon in this study. However, their growth mechanism does not explain the missing formation of whiskers on specimens grown in moist air in this study. Instead, it is proposed that the absence of whiskers for chromia scales grown in air containing water vapour in this work, is due to the simultaneous vaporization of chromium (VI) containing species from the surface of the chromia scale (cf. section 2.4.4).

It is proposed that the formation of whiskers in air is retarded by the very large surface area of the whiskers, which facilitates the simultaneous vaporization of the oxide whiskers. In order to investigate this proposal, the effect of vaporization has been examined by oxidizing a specimen in hydrogen/argon containing 1% water for 70 h followed by oxidation steps in air containing 1% water. The oxidation in air was performed in two steps of 24 h each. The morphology of the outermost oxide scale was examined after each oxidation step and is shown in Fig. 31A-C.

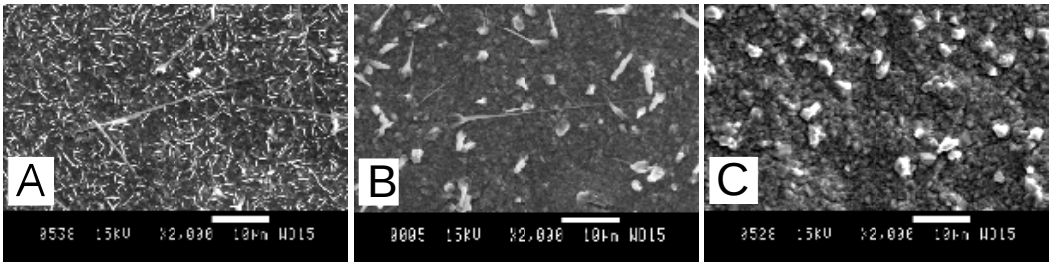

Fig. 31. SEM micrographs of an oxide scale. The specimen was oxidized in hydrogen/argon containing 1% water (A), specimen A followed by 24 h in air containing 1% water (B), specimen B followed by an additional 24 h in air containing 1% water (C).

It is clearly seen that the morphology of the outermost oxide is changing from oxide ridges and whiskers (cf. Fig. 31A) to a morphology containing larger grains (cf. Fig. 31B,C) after the oxidation in moist air. It could be argued that the oxide whiskers and ridges would be overgrown by chromia during the subsequent oxidation in moist air. However, the weight gains during the extra heat treatments are too small to justify this. Fig. 28 reveals that the whiskers extend up to 40-50 μm above the base of the scale. The proceeding oxide growth in air would not be able to cover the whiskers formed during the oxidation in humidified hydrogen/argon. This clearly demonstrates that the whiskers vaporize during the heat treatment in air.

As described, Raynaud and Rapp [57] observed the formation of oxide whiskers during the oxidation of Ni in moist oxygen. The equilibrium pressure of volatile chromium species is much larger (of the order 50-1000) than the corresponding equilibrium pressure of volatile nickel species, both in equilibrium with air containing 1% water vapour at 1173 K [37]. This difference demonstrates why oxide whiskers are missing during the growth of chromia, and observed during the growth of NiO.

The morphology of the alloy/scale interface is shown in Fig. 24. Small cavities are seen at the alloy/scale interface for the specimens grown in hydrogen/argon for 70 h, while the specimens grown in air contain considerable larger cavities. Cavities at the interface have also been observed for chromia scales grown on pure chromium [24]. The phenomenon is explained by the chromia growth mechanism, where chromium diffuses outward to react with oxygen. This diffusion mechanism creates vacancies, which coalesce and form cavities at the scale/metal interface. Another indication of the growth mechanism of chromia is the bulky surface of the scale (cf. Fig. 23). The bulky surface is a result of growth stresses within the scale. The compressive growth stresses are caused by the formation of new oxide within the oxide scale [24]. Thus, although chromium diffusion is dominating, oxygen diffusion is also contributing to the growth, and the growth mechanism is generally believed to be a counter diffusion of chromium and oxygen [24].

The scales grown in hydrogen/argon exhibit a much better adhesion to the alloy than those grown in air. The improved adhesion for scales grown under reducing conditions (vs. air) has previously been observed in the literature [3,43], but not explained. Several possible reasons for the improved adhesion may be proposed

- Hydrogen defects in chromia
- Different abilities for oxide deformation

- Scavenging of impurities

The improved adhesion in hydrogen/argon could be caused by the presence of hydrogen defects in chromia, which may change the defect chemistry and thereby the growth of the oxide [17]. The activation energy for dissociation of H_2O and O_2 on chromia is unknown, but the dissociation of H_2O is generally easier than dissociation of other oxidant molecules [57]. For example, the activation energy for the dissociation on wüstite of H_2O is much lower than the corresponding value for CO/CO_2 [60]. Hence, similar concentrations of hydrogen defects can be expected in chromia scales grown in air and in hydrogen/argon, since the atmospheres contain the same amount of water vapour. Thus, different hydrogen defect concentrations in the scale do not explain the difference in the adherence observed in this work.

Another reason for the difference in scale adhesion may be due to different abilities for the oxide to deform in air and in hydrogen/argon. The ability of the chromia scale to deform by a creep mechanism has been reported to increase with decreasing oxygen activity [61]. The plastic deformation is limited by the minority defect [17], i.e. the oxygen vacancies. The concentration of oxygen vacancies increase as the oxygen activity decreases (cf. Fig. 7). Thus, the observed dependency may be explained by the proposed defect structure of chromia in section 2.2.

Another possibility could be that hydrogen scavenges impurities such as sulfur at the alloy surface, which otherwise would be detrimental for the adherence of the chromia scale [62,63].

The effect of oxygen partial pressure on the oxide adhesion was examined by oxidizing a specimen in hydrogen/argon for 15 h, followed by oxidation in air for 55 h. The oxidation was performed at 1173 K and in atmospheres containing 1% water vapour. The cross section of the specimen is shown in Fig. 32.

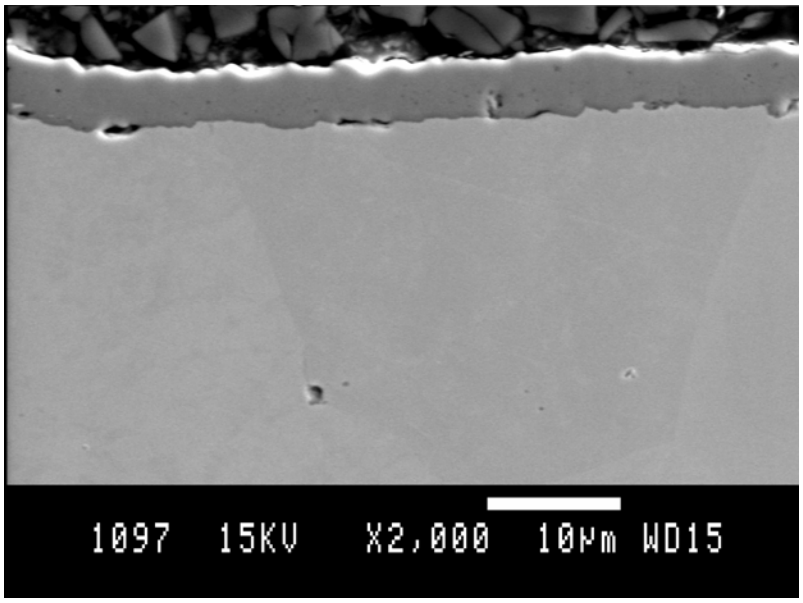

Fig. 32. SEM micrograph of cross section of a A1 specimen, which has been oxidized in hydrogen/ argon for 15 h followed by oxidation in air for 55 h, both atmospheres containing 1% water.

The total oxidation time was 70 h at 1173 K, and the cross section in Fig. 32 may be compared to the cross section shown in Fig. 24C. The scale in Fig. 32 adheres well to the alloy even though the scale was primarily grown in air. This suggests that the oxygen partial pressure itself has little effect on the scale adhesion. The adherence of the scales shown in Fig. 32 and Fig. 24C is similar, showing that the initial oxidation of the bare alloy is important for the adherence of the scale. This indicates that differences in the oxide deformation behaviour in hydrogen/argon and air are less significant. It is suggested that the most important effect is the scavenging of impurities at the alloy surface during the initial annealing in hydrogen/argon.

5.4.2 Oxidation kinetics

During the oxidation of a chromia forming iron-chromium alloy, three stages of oxidation may occur. These are termed transient, steady state and breakaway oxidation. Initially, oxidation of the bare alloy is characterized by an oxidation of both iron and chromium in the alloy [51]. This oxidation stage is termed “transient oxidation”. The transient oxidation continues until a continuous layer of chromia is formed, after which further oxidation of the alloy is governed by a steady state oxidation of a chromia scale. A slow growing chromia scale characterizes the steady state oxidation, where transport of reactants in the scale governs the growth of chromia. The steady state oxidation has been rigorously treated by Wagner [25] (cf. section 2.3). Due to the build up of compressive growth stresses in the scale, the scale may eventually crack. In this case, the protective character of the scale is lost and breakaway oxidation initiates [64].

In the following, the oxidation kinetics of the iron-chromium alloy examined in this work is discussed in relation to the transient and steady state oxidation. The breakaway oxidation is described in chapter 7. The oxidation kinetics is also discussed in relation to the partial pressures of oxygen and water in the reaction atmospheres.

5.4.2.1 Transient oxidation

The diffraction patterns for the oxides (cf. Fig. 25) reveal the formation of corundum-type oxides. The EDX line scan analyses of the cross sections (cf. Fig. 26) show that only chromium exists in the oxide scales. Hence, it is concluded that the corundum-type oxides, grown during steady state oxidation both in hydrogen/argon and in air, is chromia. The diffraction patterns in Fig. 25 obtained for the specimens oxidized in hydrogen/argon also indicate a small concentration of oxide with the spinel structure. The isothermal phase diagram for 1173 K in section 2.4.3 shows that if chromia and a spinel phase both are present in the scale, chromia is positioned closest to the alloy, while the spinel phase is present as the outermost oxide in the scale. It should also be noticed from the phase diagram that iron is present in the spinel phase.

How is the absence of the spinel phase for the specimens oxidized in air explained? The dotted lines, which are superimposed on the phase diagram, mark the oxygen

pressures (cf. Fig. 11) of the hydrogen/argon mixture containing 1% and 12% water, respectively. The spinel phase exists in equilibrium with the hydrogen/argon reaction atmospheres. Thus, the spinel phase is present at the scale/gas interface. The presence of the spinel phase is due to a small amount of iron present in the outermost part of the scale. In contrast, the phase diagram in Fig. 11 indicates that if iron is present in the outermost scale for the specimen oxidized in air, iron will be present in a solid solution corundum-type oxide. Hence, a small amount of iron may be present in the outermost oxide, and still not detected from XRD analysis of the surface. The low intensities of the reflection from the spinel phase in Fig. 25 indicate that the amount of spinel phase in the outermost oxide is very small. This is in accordance with the absence of iron in the EDX line scan analyses (cf. Fig. 26). The surfaces of the scales were subsequently analysed with EDX analysis in order to determine the relative content of chromium and iron at the surface (i.e. at the scale/gas interface). Small contents of iron were found on all specimens. The relative concentrations Cr/Fe were in the range 20 – 40.

The presence of iron containing oxides in the outermost part of the scale may be a result of the outward migration of iron through cracks in the chromia scale before a healing layer of chromia can reform [9]. However, the content of iron in the outermost part of the scales is small. Furthermore, the chromia scales are dense. It is therefore unlikely that the presence of iron containing oxides is due to cracks in the scale. Instead, the small amount of iron present is probably a result of transient oxidation of the alloy before a dense chromia layer has formed. The transient oxidation period is short for iron-chromium alloys containing 22 at.% chromium [51], so only a small amount of iron is present in the outermost part of the scale. This is in support of the results.

In summary, a small amount of iron is present in the outermost part of the oxide due to transient oxidation of the specimens. The iron is observed by the presence of a spinel phase for the specimens grown in hydrogen/argon due to the thermodynamic properties of the oxides. Furthermore, a small amount of iron was detected using EDX analysis on the surface of the specimens.

5.4.2.2 Steady state oxidation

The gravimetric results in Fig. 27 show that the weight gains for specimens oxidized for 70 h showed little dependency on the oxygen activity of the oxidizing gas. However, the specimen oxidized in air containing 12% water vapour shows a smaller weight gain. This is discussed later as an effect of the water content in the reaction atmosphere. The transient oxidation period is followed by a steady state oxidation period, where the scale growth is slow and is governed by the growth of chromia.

The steady state growth of a chromia scale is governed by a diffusion-limited growth mechanism. Such a scale growth can be described by a parabolic rate expression. It is assumed that all oxides grown for 70 h in the present work can be described by a parabolic rate expression. Hence, it is assumed that the transient oxidation period is negligible. The rate expression is often expressed by the weight gain of the specimen, i.e. by Eq. 64

$$\frac{dw}{dt} = \frac{k_w}{w} \qquad \text{Eq. 71}$$

The parabolic rate constant of chromia may be written (cf. Eq. 55 and Eq. 66)

$$k_w = \frac{1}{2}\left(\frac{3M_O\rho_{Cr_2O_3}}{M_{Cr_2O_3}}\right)^2 \int_{P_{O_2}^i}^{P_{O_2}^o}\left(\frac{3}{2}D_{Cr} + D_O\right)d\ln p_{O_2} \qquad \text{Eq. 72}$$

The diffusion coefficients in Eq. 72 are component diffusion coefficients (cf. section 2.3.2).

In the following, expressions for the oxygen and chromium diffusion coefficients will be inserted into Eq. 72. These expressions have been derived in chapter 2. It will be assumed that the expressions also are applicable if the growth of chromia is governed by short circuit diffusion, as discussed in section 2.3.4.

The growth mechanism of chromia scales is described by a counter diffusion of chromium and oxygen, where chromium diffusion is dominating [24], so oxygen defects are omitted in the discussion for simplicity, i.e. $D_{Cr} >> D_O$. If Eq. 56 is inserted into Eq. 72, it follows that

$$k_w = A\int_{P_{O_2}^i}^{P_{O_2}^o}\left(\left[V_{Cr}^{///}\right]D_{V_{Cr}} + \left[Cr_i^{\bullet\bullet\bullet}\right]D_{Cr_i}\right)d\ln p_{O_2} \qquad \text{Eq. 73}$$

where A is a constant. From Eq. 58, it follows that

$$d\ln V_{Cr}^{///} = \frac{3}{16}d\ln pO_2 \qquad \text{Eq. 74}$$

If chromia is grown predominantly by a chromium vacancy mechanism, and Eq. 74 is inserted into Eq. 73, the parabolic rate constant may be written

$$k_w = A\int_{P_{O_2}^i}^{P_{O_2}^o}\left(\frac{16}{3}D_{V_{Cr}}\right)d\left[V_{Cr}^{///}\right] \qquad \text{Eq. 75}$$

It follows that

$$k_w = A\frac{16}{3}D_{V_{Cr}}\left(\left[V_{Cr}^{///}\right]^o - \left[V_{Cr}^{///}\right]^i\right) \qquad \text{Eq. 76}$$

The concentration of chromium vacancies is much higher near the scale/gas interface than the corresponding alloy/scale interface (cf. Fig. 7), so

$$k_w = A\frac{16}{3}D_{Cr}^o(Vacancy) \qquad \text{Eq. 77}$$

The chromium diffusion coefficient in Eq. 77, is the chromium diffusion coefficient by way of vacancies near the scale/gas interface. This chromium diffusion coefficient is dependent upon the concentration of vacancies near the scale/gas interface and hence the oxygen activity in the reaction gas (cf. Fig. 7). If chromia is grown predominantly by a chromium interstitial mechanism, a similar calculation shows that the parabolic rate constant may be written

$$k_w = A\frac{16}{3}D_{Cr}^{i}(Interstitial) \qquad \text{Eq. 78}$$

The chromium diffusion coefficient in Eq. 78 is the chromium diffusion coefficient by way of interstitials near the scale/alloy interface. This diffusion coefficient is dependent upon the concentration of chromium interstitials near the scale/alloy interface and hence the oxygen activity near the alloy/scale interface. The latter is independent on the oxygen pressure in the reaction gas. Hence, the parabolic rate constant is dependent on the oxygen activity in the reaction atmosphere if chromia is grown by a vacancy mechanism. In contrast, if chromia is grown by an interstitial growth mechanism, the parabolic rate constant is independent of the oxygen activity in the reaction atmosphere.

The weak oxygen activity dependency on the growth rate of chromia (cf. Fig. 27) indicates that the growth of chromia scales is governed by interstitial chromium diffusion. This growth mechanism for chromia has also been observed for high temperature oxidation of pure chromium [24].

The weight gain of ca. 1 mgcm^{-2} obtained in this work is transferred into a parabolic rate constant of $2\cdot10^{-12}$ g^{2}cm^{-4}s^{-1} using Eq. 71. This value is in the range of values obtained from the literature [49]. The parabolic rate constant has been reported for pure chromium and for chromia forming alloys at various temperatures and oxygen activities [49]. These values may be compared to values calculated from Eq. 72, using chromium lattice diffusion coefficients from the literature. There is some scatter in the reported chromium diffusion coefficients. However, the experimentally determined parabolic rate constants are generally much higher than the calculated parabolic rate constants [31]. This indicates that the growth of chromia is governed by grain boundary diffusion rather than lattice diffusion, as previously mentioned.

The gravimetric results obtained for the specimens oxidized for 70 h in hydrogen/argon do not show an effect of the water vapour content in the reaction atmosphere (c.f. Fig. 27). However, the results show an effect of the water content for the specimens oxidized in air, where the specimen oxidized in 12% water vapour has the smallest weight gain.

The effects of moisture in the reaction gas on the oxidation behaviour of alloys have been the subject of numerous studies (see e.g. Ref. [17,53,54]), and it has long been recognized that water vapour accelerates the oxidation of metals compared to oxidation behaviour in dry atmospheres. The reasons for this are however poorly understood [10]. Such an acceleration of the oxidation is not observed in this work. This indicates that, in cases of water vapour in the reaction atmosphere, the oxidation rate is independent of the content of water in the reaction gas. Interestingly, the weight gain in this study decreased with increasing content of water vapour in air.

The vaporization of chromium species from the surface has been addressed during the discussion of oxide whiskers and in section 2.4.4. The effect of vaporization from the specimen oxidized in air containing 12% water vapour on the oxidation kinetics was addressed by an additional experiment in air containing 12% water vapour. The experimental setup was changed such that chromia powder was placed in front of the specimen in the flow direction. The results for the two types of experiments are shown in Table 7.

Table 7. Weight gain for specimen oxidized for 70 h in air containing 12% water, with chromia powder positioned in front of the specimen, and without chromia powder.

	With Cr_2O_3 powder	Without Cr_2O_3 powder
$\Delta W/A$ [$mgcm^{-2}$]	0.90	0.58

The reaction gas passing the specimen was partly saturated with volatile chromium species by placing Cr_2O_3 powder in front of the specimen. This reduced the vaporization from the specimen. The results in Table 7 clearly show the effect of the vaporization of chromia in air containing water.

These results show that chromia scales, which are grown in air containing large amounts of water vapour, are influenced by vaporization of chromium species from the surface of the specimen. The growth of the chromia scales must consequently be described by a modified parabolic rate equation, which takes into account the loss of mass due to vaporization [65]

$$\frac{dx}{dt} = \frac{k_P}{x} - k_S \qquad \text{Eq. 79}$$

As a result, the net scale thickness comes to a steady state if the normal parabolic weight gain is balanced by the vaporization of chromium species. The equilibrium pressure of $CrO_2(OH)_2(g)$, which is the dominant volatile chromium specie in moist air, is $3.7 \cdot 10^{-6}$ bar in equilibrium with air containing 12% water vapour at 1173 K (cf. Table 2). The gas flow during the experiment was 100 ml/min. This corresponds to a weight loss of approximately 1.2 mg during 70 h from vaporization if the reaction gas passing the specimens becomes fully saturated with $CrO_2(OH)_2(g)$. These results show that the magnitude of vaporization from chromia can explain the reduced mass gain for the specimen (cf. Fig. 27). Furthermore, the gas flow does not become nearly saturated with volatile chromium species from the chromia scales during the experiment. The effect of water vapour on the growth rate of chromia will be further addressed in chapter 8.

5.5 Summary

The microstructure and oxidation kinetics of the alloy $Fe_{0.78}Cr_{0.22}$ was examined at 1173 K in various reaction atmospheres. The chromia scales grown under reducing

conditions show the formation of oxide whiskers and ridges at the surface. In contrast, the chromia scales formed in air show the formation of larger (2-3 μm) grains near the surface. This difference is caused by the vaporization of chromium species from the scale grown in air. Two different growth mechanisms are given for the growth of oxide whiskers. It is the author's belief that the whiskers were formed from the top of the whiskers, but no conclusive experimental evidence is given for the growth mechanism.

The chromia scales were found to adhere much better to the alloy when grown in hydrogen/argon than in air. This is probably caused by a scavenging of impurities under reducing conditions. The water vapour content in the reaction atmosphere does not have any significant influence on the oxide microstructure.

The growth rate of the scales is independent of the oxygen activity, which is explained by an interstitial growth mechanism of the chromia scales. The growth rate decreases with increasing water content in air. This is caused by a simultaneous vaporization of chromium species from the scale during the growth.

6 The effect of silicon and cerium

6.1 Introduction

In this work, an iron-chromium alloy is studied, which may be used as interconnector material in SOFC stacks. An important requirement for the interconnector is a high electrical conductivity across the interconnector plate.

The high temperature oxidation behaviour of a Fe22Cr alloy containing a small amount of silicon has previously been examined [66]. Despite the low content of silicon in the alloy (0.30 wt.%), examinations of the oxide scale formed revealed that an almost uniform layer of silica had formed beneath a dense chromia scale.

As discussed in section 1.1, silica forming alloys are not suitable as interconnector materials for the stacking of SOFC, since silica is an insulator. However, silicon additions in alloys may only be detrimental to the electrical conductivity across an interconnector plate, if a dense silica layer is formed. In contrast, if silica is formed as distinct particles, relatively high conductivity paths may still exist for the current across the interconnector plate.

Due to the electrical insulating property of silica, it would be interesting to examine the effect of silicon alloying additions to an iron-chromium alloy, i.e. to examine if the addition of silicon to the alloy has a beneficial effect on the corrosion resistance. In contrast, if silicon does not have a beneficial effect on the corrosion resistance, it may be possible to omit silicon additions from the alloy, and thereby avoid the formation of silica.

The effect of adding silicon to an iron-chromium alloy on the corrosion resistance of the alloy is studied in this work. It is studied whether small additions of silicon to the alloy have a beneficial effect as an alloying element. The amount of silicon added to the iron-chromium alloy in this work, is too low to form a dense layer of silica under the present experimental conditions, i.e. at the present temperature and oxidation time.

Silicon is often added as an alloying element in steel. It is added to act as an oxygen getter in the liquid steel before casting [67]. Besides the beneficial effect as an alloying element during steel casting, silicon may also have beneficial effects on high temperature oxidation behaviour of alloys. During oxidation of a silicon rich alloy, a dense silica layer may form as an oxide scale. The growth rate of dense silica scales is known to be slow during high temperature oxidation [68]. Silica forming alloys are therefore often used for high temperature applications. Numerous studies have examined the effect of silicon on the oxidation behaviour of alloys [68-71]. However, most of these studies have examined alloys in which the silicon content is so high that a dense silica layer is formed during oxidation. The continued oxidation of such an alloy, after the formation of a dense silica layer, is governed by the growth of silica. Such a growth mechanism is not applicable in the present study, where silicon does not form a dense silica layer. Different growth mechanisms for the oxidation of alloys containing silicon will be discussed in detail in this chapter.

Other alloying additions than silicon may be beneficial for the corrosion resistance of the Fe-Cr alloy. The effect of cerium as an alloying element in an iron-chromium alloy is examined in this work. Cerium oxide may form during oxidation. However, cerium oxide is not an electrical insulator, and cerium is known as a beneficial alloying element for many alloys [72]. The possible differences and beneficial effects of cerium and silicon, as alloying additions to an iron-chromium alloy, are examined in this work.

Empirically, it was discovered more than 50 years ago that the addition of cerium and other rare earth metals to alloys have a beneficial effect on the oxidation behaviour of the alloys [73]. Consequently, the effect of cerium and other "reactive elements" (RE) on the oxidation behaviour of alloys has been the subject of numerous studies (see e.g. Ref. [72,74]). However, despite many proposed mechanisms for the "reactive element effect" (REE), no conclusive mechanism exists.

Considerable scatter in the oxidation behaviour of similar alloys have been observed in the literature [10]. This scatter is most likely caused by different experimental conditions during the studies, e.g. purity of the specimens, specimen preparation etc. Thus, the experimental conditions chosen during high temperature oxidation of alloys are very important. It is therefore important that the experimental conditions, for the alloys investigated in this study, are similar (alloy processing, heating etc.), in order to compare the effect of different alloying additions. Thus, although the effect of cerium has been the subject of previous studies, it is important that the oxidation behaviour of the specimens is examined under similar experimental conditions in order to obtain valid comparisons of the oxidation behaviour.

In this chapter, the effect of alloying additions on the oxidation behaviour of $Fe_{0.78}Cr_{0.22}$ at 1173 K in air and in hydrogen/argon atmospheres, containing various amounts of water vapour, is investigated. Furthermore, both cerium and silicon were added to the same iron-chromium alloy, in order to investigate the combined effect. The same content of alloying elements are added in each alloy (0.30 at.% in total), in order to compare the effect of the alloying additions on the corrosion resistance of the specimens. The oxidation behaviours of the alloys are compared to each other, but also to the oxidation behaviour of the ferritic alloy $Fe_{0.78}Cr_{0.22}$ (A1), which was studied and discussed in chapter 5.

6.2 Experimental

The chemical composition (in atomic percent), of the alloys studied in this chapter, is given in Table 8.

Table 8. The alloy compositions in atomic percent.

Alloy	Composition in at.%			
	Fe	Cr	Si	Ce
A1-Si	Bal.	21.9	0.3	--
A1-Ce	Bal.	21.9	--	0.3
A1-CeSi	Bal.	21.9	0.15	0.15

The specimens were oxidized at 1173 K for 70 h. The reaction atmospheres were either air or a 7%H_2/93%Ar mixture containing various concentrations of water. The test conditions were identical to those described in chapter 5, and are summarized in Table 9.

Table 9. Test conditions for the specimens. The specimens were either oxidized in air or in hydrogen/argon, both containing water vapour.

Temperature / K	Gas	Dwell time / h	$p(O_2)$ / bar	$p(H_2O)$ / bar
1173	7%H_2/93%Ar	70	$1.6 \cdot 10^{-18}$	0.012
1173	7%H_2/93%Ar	70	$2.0 \cdot 10^{-16}$	0.122
1173	Air	70	0.21	0.012
1173	Air	70	0.21	0.122

After the oxidation, the surface of the oxide scales was examined using SEM and EDX analysis in order to elucidate the microstructure and the chemical composition of the oxide scales. The crystalline structure of the scales was determined using XRD, which was obtained at room temperature.

Polished cross sections of the specimens and fractures of the specimen scales (cross section) were prepared in order to investigate the growth behaviour and oxide morphology of the specimens. The polished cross sections and fractured scales of the specimens were examined using SEM and EDX analysis.

The experimental details are given in chapter 4.

6.3 Results

The results are given for the specimens containing silicon and/or cerium as alloying addition. However, some of the results obtained for the iron-chromium alloy (A1) (in chapter 5) are also given here in order to facilitate a comparison of the results.

6.3.1 Oxide morphology

The effect of the reaction atmosphere on the morphology of the surface of the oxide scales was studied in chapter 5 for the A1 alloy. The effect of the reaction atmosphere on the surface of the scale for the alloys containing silicon and/or cerium is similar to the results obtained in chapter 5 for the A1 alloy. Hence, the morphology of the surface of the oxide scales grown on these alloys will not be further discussed.

Fractured scales of the oxides grown on the four different alloys (cf. Table 5) were examined using SEM in order to investigate a possible effect of the alloying addition on the morphology of the scale, i.e. grain size, porosities etc. Micrographs of the fractured scales grown in hydrogen/argon containing 1% water vapour are shown in Fig. 33 and Fig. 34. The oxides were grown on the A1-Ce (A), A1-Si (B), A1-CeSi (C) and A1 (D) alloys.

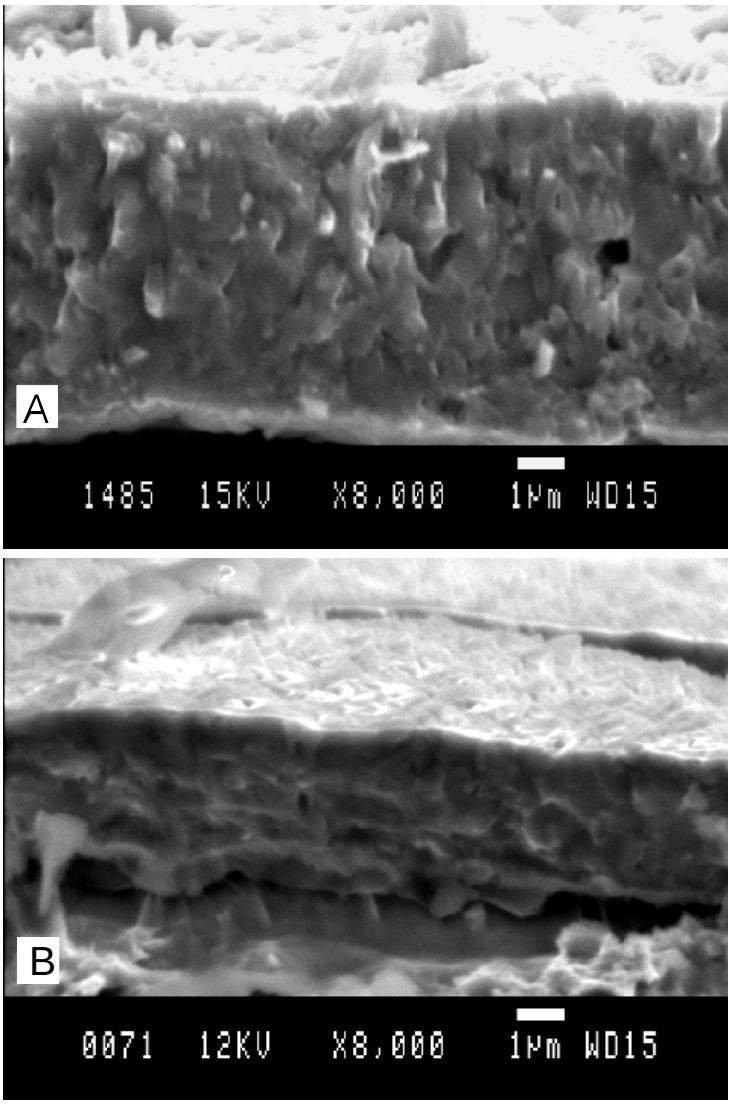

Fig. 33. SEM micrographs of fractured scales of the oxides grown on A1-Ce (A) and A1-Si (B). The oxides were grown in hydrogen/argon containing 1% water at 1173 K for 70 h.

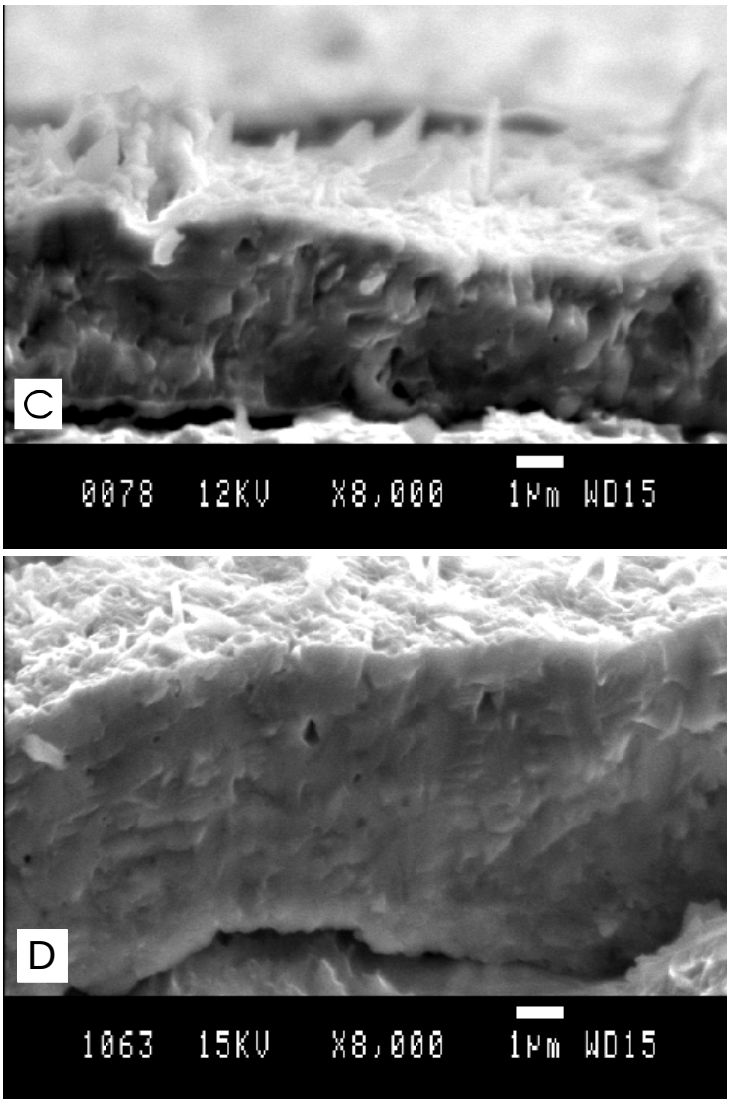

Fig. 34. SEM micrographs of fractured scales of the oxides grown on A1-CeSi (C) and A1 (D). The oxides were grown in hydrogen/argon containing 1% water at 1173 K for 70 h.

The morphology, i.e. grain size and porosity, of the scales grown on the different alloys, appear to be similar (cf. Fig. 33 and Fig. 34), although the scale thickness varies for the four alloys. The fractured scales were investigated and compared for scales grown in each of the four different atmospheres (not shown). For each atmosphere, however, the oxide morphology did not change significantly as the alloy composition changed. The effect of the reaction atmosphere on the fractured scales was discussed in chapter 5, so the results obtained for the other alloys at different atmospheres will not be discussed further.

6.3.2 Oxide/alloy morphology

Micrographs of polished cross sections of the specimens oxidized in hydrogen/argon containing 1% water vapour are shown in Fig. 35 and Fig. 36. The oxide scales were

grown on the A1-Ce (A), A1-Si (B), A1-CeSi (C) and A1 (D) alloys. The oxide scale grown on A1-Ce (cf. Fig. 35A) is uniform and adherent to the alloy and appears to be dense. The oxide scale grown on A1-Si (cf. Fig. 35B) has a different morphology. The oxide scale is not as uniform as observed in Fig. 35A. Furthermore, small distinct black islands can be observed near the alloy/scale interface. The morphology of the oxide scale grown on A1-CeSi (cf. Fig. 36C) is similar to the oxide scale grown on A1-Si (cf. Fig. 35B), although the number of black islands near the alloy/scale interface is greatly reduced. Finally, the morphology of the oxide scale grown on A1 (cf. Fig. 36D) was described in chapter 5. The cross sections of the oxide scales grown in each of the other atmospheres were also examined (not shown). However, the effect of the reaction atmosphere has already been described in chapter 5 for the A1 alloy. The results obtained for the other samples are qualitatively in agreement with the results given in Fig. 35 and Fig. 36, so the results obtained for the other alloys will not be further discussed.

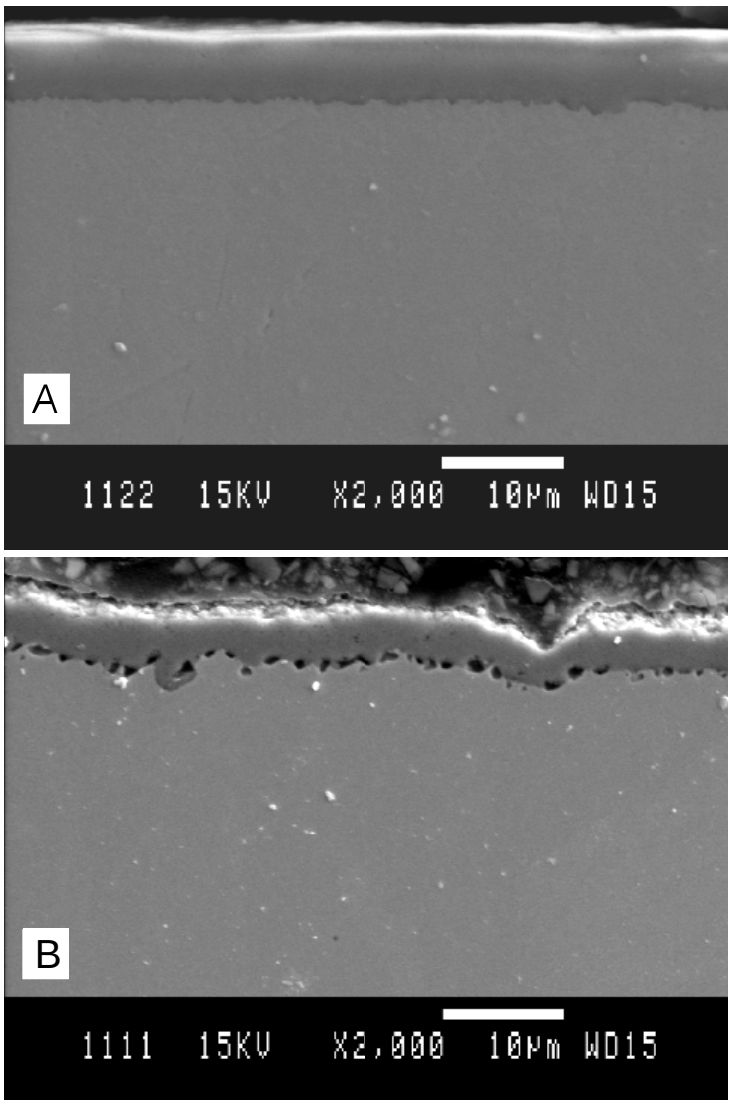

Fig. 35. SEM micrographs of cross sections of scales grown on A1-Ce (A) and A1-Si (B). The specimens were oxidized in hydrogen/argon containing 1% water vapour at 1173 K for 70 h.

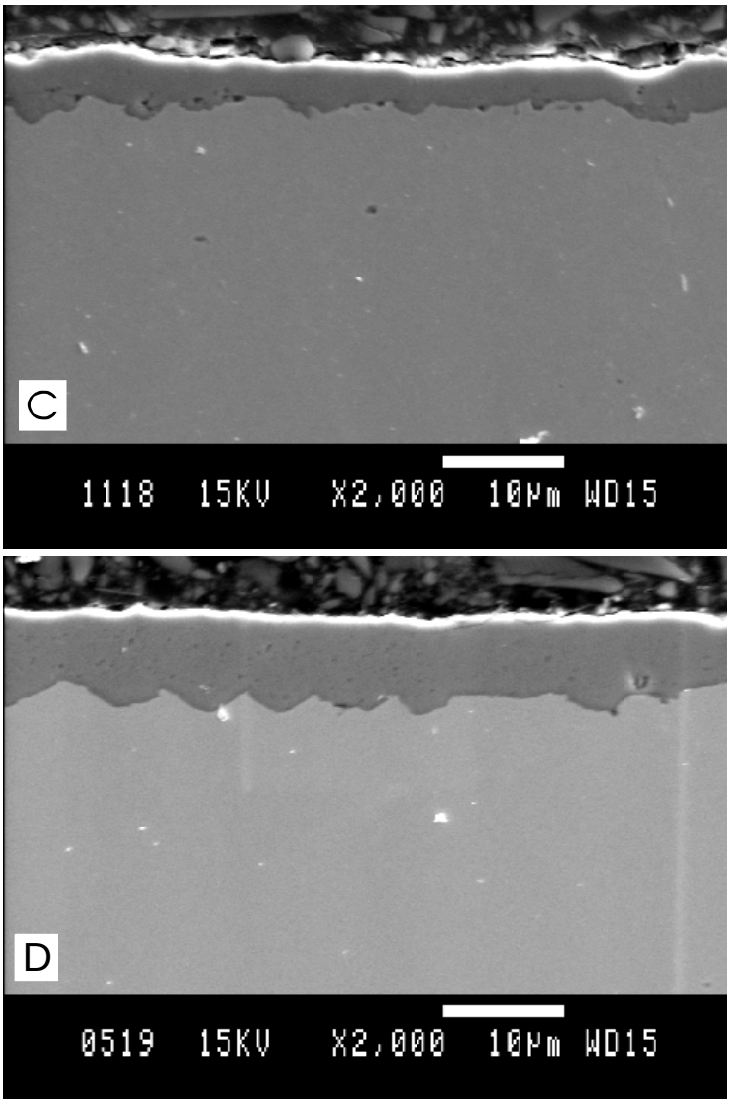

Fig. 36. SEM micrographs of cross sections of scales grown on A1-CeSi (C) and A1 (D). The specimens were oxidized in hydrogen/argon containing 1% water vapour at 1173 K for 70 h.

6.3.3 XRD analysis

The diffraction patterns obtained for the oxide scales grown on the alloys for 70 h are shown in Fig. 37-Fig. 40 for the A1-Ce (Fig. 37), A1-Si (Fig. 38), A1-CeSi (Fig. 39) and A1 (Fig. 40) alloys.

The diffraction patterns obtained for the specimens containing silicon and/or cerium are similar to the diffraction patterns obtained for the A1 alloy. It is not possible to identify any extra phases in Fig. 37-Fig. 39 originating from the alloying additions of cerium and/or silicon. It should be noticed that the relative peak intensities are different for some of the peaks. This is probably due to different texture of the oxide scales. It was not possible to identify any correlation between the different peak intensities, reaction atmosphere, and type of specimen from the diffraction patterns.

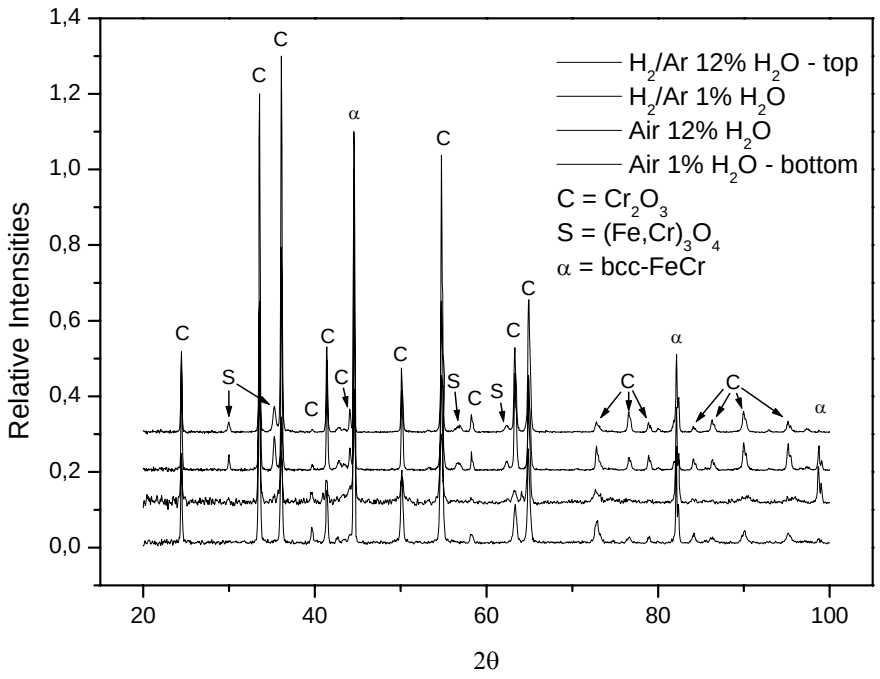

Fig. 37. Diffraction patterns of the oxide scales grown on A1-Ce specimens at 1173 K for 70 h in various reaction atmospheres.

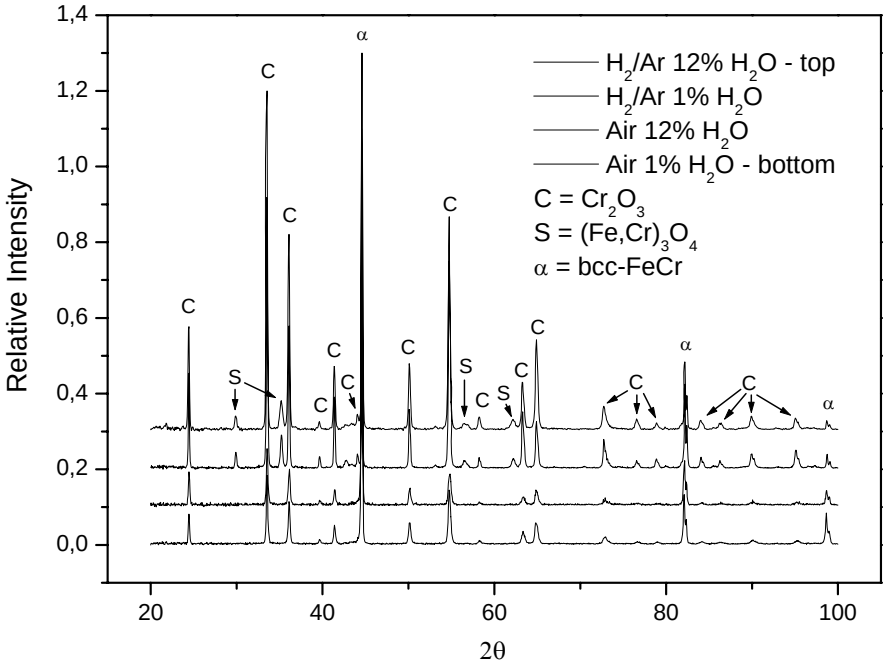

Fig. 38. Diffraction patterns of the oxide scales grown on A1-Si specimens at 1173 K for 70 h in various reaction atmospheres.

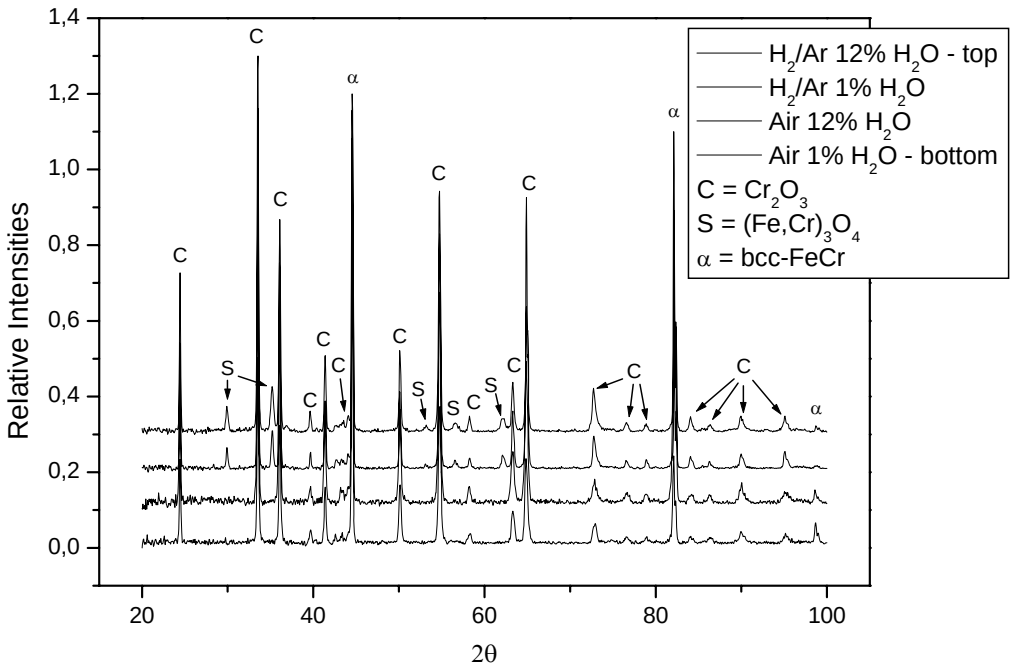

Fig. 39. Diffraction patterns of the oxide scales grown on A1-CeSi specimen at 1173 K for 70 h in various reaction atmospheres.

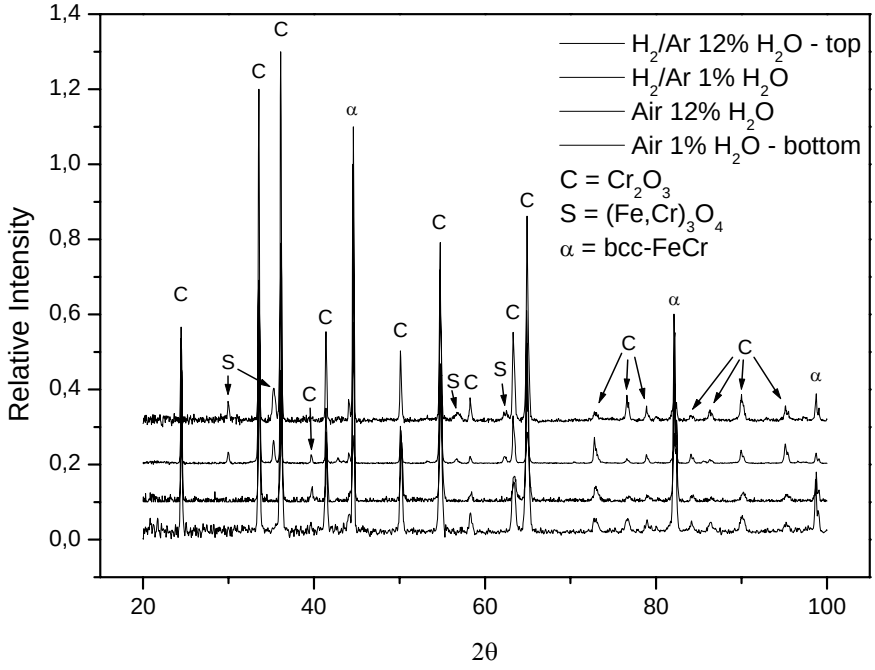

Fig. 40. Diffraction patterns of the oxide scales grown on A1 specimens at 1173 K for 70 h in various reaction atmospheres.

The diffraction patterns for the scales grown in air contain an oxide with the corundum structure (PDF #38-1479). The diffraction patterns for the scales grown in hydrogen/argon also contain an oxide with the corundum structure (PDF #38-1479), and in addition, the analyses show reflections from a spinel phase (PDF #34-0140) with low intensity.

6.3.4 EDX analysis

The polished cross sections of the specimens were analysed using EDX line scan analysis in order to obtain the chemical compositions of the oxide scales. These results can, in combination with the XRD analyses given in section 6.3.3, reveal the nature of the phases present in the oxide. The EDX line scan analyses of the oxide scales grown on the A1-Ce (A), A1-Si (B), A1-CeSi (C) and A1 (D) alloys, are given in Fig. 41A-D.

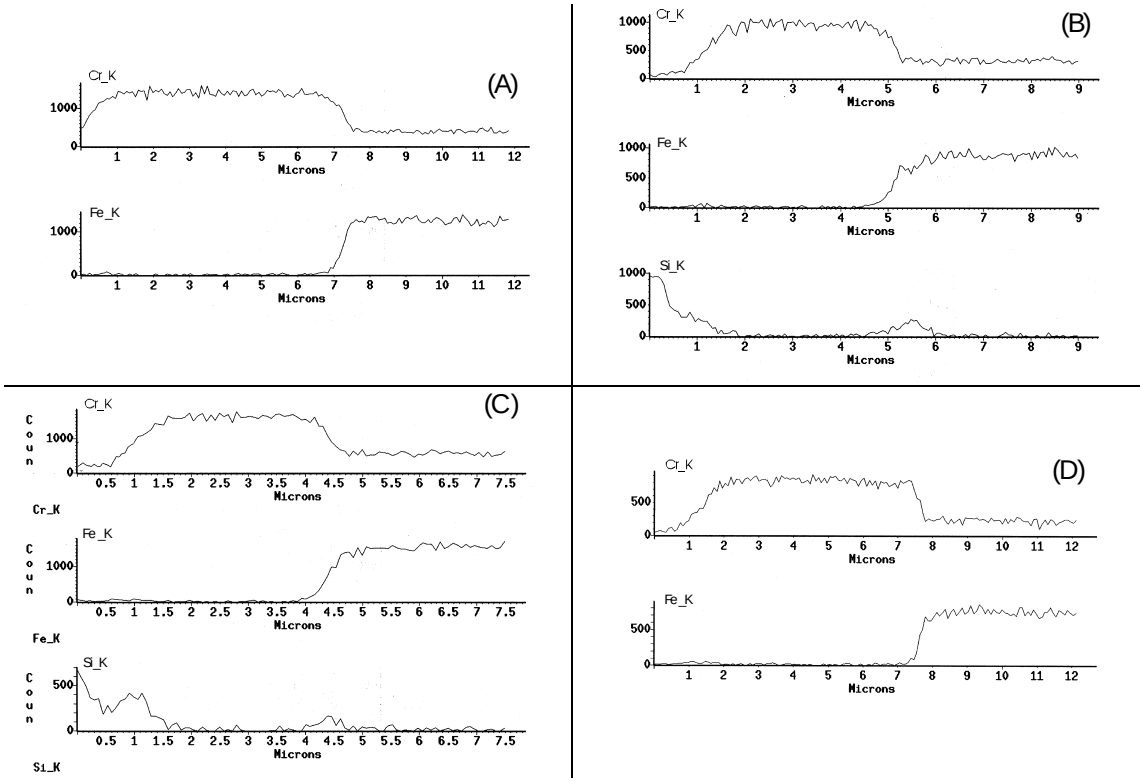

Fig. 41. EDX line scan analyses of cross sections of scales oxidized at 1173 K for 70 h in hydrogen/argon containing 1% water. The scales were grown on the A1-Ce (A), A1-Si (B), A1-CeSi (C) and A1 (D) alloys.

The EDX line scan analyses are shown for the specimens oxidized in hydrogen/argon containing 1% water vapour. The EDX analyses were also obtained for the specimens oxidized in the other reaction atmospheres. The results obtained for the specimens oxidized in the other reaction atmospheres, were similar to the results obtained in

hydrogen/argon containing 1% water. Consequently, these results are not shown. The analyses in Fig. 41A-D show the presence of pure chromium in the scale. The A1-Si and A1-CeSi specimens (cf. Fig. 41B,C) also show the presence of silicon near the interface between the chromium rich oxide and the alloy. The EDX line scan analyses were measured across the dark islands shown in the SEM micrographs in Fig. 35B and Fig. 36C. This indicates that a silicon containing oxide is present at the alloy/scale interface. Thus, the EDX analyses show that the black islands present in Fig. 35B and Fig. 36C consist of silicon rich oxide. The silicon content is also high near the oxide/gas interface, but this is caused by the presence of silicon in the mounting of the specimens. The A1-Ce and A1-CeSi specimens were analysed, for the presence of cerium, within the oxide scale and in the alloy beneath the oxide scale. However, it was not possible to identify any cerium from the cross sections. Furthermore, despite the presence of a spinel phase in the diffraction patterns for the specimens oxidized in hydrogen/argon, it was not possible to detect a significant amount of iron in the outermost part of the oxide scale

6.3.5 Gravimetric measurements

The weight gain of the specimens after oxidation is given in Table 10. The measurement conditions during the oxidation are given in Table 9.

Table 10. Weight gain for specimens oxidized at 1173 K for 70 h in various atmospheres. The composition of the specimens is given in Table 8, while the test conditions are summarized in Table 9.

$\Delta W/A$ [mgcm^{-2}]	A1-Ce	A1-Si	A1-CeSi	A1
H_2/Ar – 1%H_2O	0.90	0.58	0.54	1.05
H_2/Ar – 12%H_2O	0.83	0.39	0.23	1.14
Air – 1%H_2O	0.45	0.30	0.38	0.98
Air – 12%H_2O	0.38	0.24	0.09	0.58

The parabolic rate constant was also calculated for all the specimens using Eq. 64. This was done under the assumption that the growth of the oxide scales followed the parabolic rate expression. The transient oxidation and weight loss due to vaporization is neglected. The parabolic rate constants are given in Table 11.

The weight gains of the alloys containing alloying addition of silicon and/or cerium may be compared to the weight gains of the iron-chromium (A1) alloy. The results in Table 10 show that the weight gain of the specimens decreased after the addition of cerium and/or silicon to the A1 alloy. Furthermore, the addition of cerium to the iron-chromium alloy (A1) is the least effective in reducing the growth rate. The weight gains for the A1-Si and A1-CeSi alloys are approximately on the same level. The effect of reaction atmosphere follow the same general trend, namely that the weight gain obtained for the specimen oxidized in air containing 12% water vapour exhibited the smallest weight gain.

Table 11. Parabolic rate constants. The rate constants were determined from the weight gains given in Table 10 using Eq. 64.

k_w [$g^2cm^{-4}s^{-1}$]	A1-Ce	A1-Si	A1-CeSi	A1
H_2/Ar – 1%H_2O	$1.6 \cdot 10^{-12}$	$6.7 \cdot 10^{-13}$	$5.8 \cdot 10^{-13}$	$2.2 \cdot 10^{-12}$
H_2/Ar – 12%H_2O	$1.4 \cdot 10^{-12}$	$3.0 \cdot 10^{-13}$	$1.1 \cdot 10^{-13}$	$2.6 \cdot 10^{-12}$
Air – 1%H_2O	$4.0 \cdot 10^{-13}$	$1.8 \cdot 10^{-13}$	$2.9 \cdot 10^{-13}$	$1.9 \cdot 10^{-12}$
Air – 12%H_2O	$2.9 \cdot 10^{-13}$	$1.1 \cdot 10^{-13}$	$1.6 \cdot 10^{-14}$	$6.7 \cdot 10^{-13}$

6.4 Discussion

The effects of the various alloying additions, to the ferritic iron-chromium alloy, are discussed in the following. The effects of adding silicon and/or cerium, to the ferritic iron-chromium alloy (A1) on the microstructure and oxidation kinetics, are discussed. For each of the alloys listed in Table 8, the oxidation behaviour is compared to the oxidation behaviour of the A1 alloy. The impact of the reaction atmosphere on the oxidation behaviour is also described for each alloy. Finally, the oxidation behaviour of each of the alloys listed in Table 8 is compared in order to contrast the effect of each alloying addition.

6.4.1 Oxidation of A1-Ce

The oxide microstructure and oxidation kinetics of the A1-Ce and A1 specimens were presented in section 6.3. Contrasting the oxidation behaviour of the two alloys, several observations can be made on the effect of cerium

- The adherence of the oxide scale is improved
- The oxide scale is denser
- The alloy has a decreased weight gain

Thus, the addition of cerium to the iron-chromium alloy (A1) has a positive effect on both the oxide microstructure and the oxidation kinetics. These observations are discussed in the following. The beneficial effect of cerium and other RE additives on the oxidation behaviour of alloys has been described in the literature (see e.g. Ref. [74]). However, a combined theory for the REE is still lacking. The effects of cerium observed in this work are discussed and explained using the REE. This work will not include a complete review of the extensive literature available concerning the REE. Instead, the focus will be on the results obtained in this study, and only the most recent proposals from the literature are discussed, in order to explain the observed results. The influence of the reaction atmosphere, i.e. the oxygen activity and water vapour content in the reaction atmosphere, on the oxidation behaviour, is also discussed.

6.4.1.1 Microstructure

The diffraction patterns obtained of the oxide (cf. Fig. 37) in combination with the EDX line scan analysis of the cross section (cf. Fig. 41A), show that the oxide scale formed is chromia. Furthermore, the diffraction patterns also indicate a small amount of oxide with the spinel structure, for the scales grown in hydrogen/argon. This is a result of transient oxidation of the alloy before a dense chromia layer has formed (cf. chapter 5).

The morphology of the oxide scale and the alloy/oxide interface for the A1-Ce alloy is shown in Fig. 33A and Fig. 35A, respectively. Similar micrographs were obtained for the A1 alloy (cf. Fig. 34D and Fig. 36D). Small cavities are seen at the alloy/oxide interface and in the oxide scale for the A1 specimen (cf. Fig. 36D). In contrast, the oxide scale grown on the A1-Ce alloy adheres to the alloy and appears dense (cf. Fig. 35A). The changes of the oxidation behaviour must be related to the addition of cerium to the alloy. The changes are observed at the alloy/oxide interface and in the oxide scale, so cerium must be positioned at or near the interface, or within the oxide scale.

The oxide scales grown on the A1-Ce specimens were examined by XRD (cf. Fig. 37) in order to identify possible oxide phases originating from the presence of cerium in the oxide scale. However, the diffraction patterns are similar to the diffraction patters obtained for the ferritic Fe-Cr alloy (cf. Fig. 40). Furthermore, the EDX line scan analysis of the cross section (cf. Fig. 41A) showed the presence of chromium within the oxide scale, while it was impossible to detect cerium within or near the oxide scale. The absence of cerium from the diffraction patterns and EDX line scan analyses may be due to the cerium content being well below the detection limit of the two experimental techniques. Hence, the existence of minor amounts of cerium within or near the scale cannot be excluded as a possibility.

How does the experimental observations correlate with the thermodynamic data for the oxides? Phase diagrams are useful in order to predict the thermodynamically stable oxides formed during oxidation. The relative stabilities of the cerium containing oxides can be observed from the Ellingham diagrams shown in Fig. 8 and Fig. 9. Furthermore, the Ce_2O_3-Cr_2O_3 ceramic phase diagram is shown in Fig. 42 [75].

According to the Ellingham diagrams, Ce_2O_3 and $CeCrO_3$ are thermodynamically more stable than chromia. Thus, these oxides may form internally beneath the chromia scale [76]. The perovskite $CeCrO_3$ is stable below ca. 10^{-9} bar at 1173 K, where CeO_2 and Ce_2O_3 become stable. This may also be observed from the phase diagrams in Fig. 42, where $CeCrO_3$ exists in H_2 at 1173 K, while CeO_2 does not dissolve in chromia in equilibrium with air at 1173 K. The formation of $CeCrO_3$ below 800^{o}C in air (cf. Fig. 42B) cannot be explained from the Ellingham diagrams. Thus, according to the thermodynamic data, $CeCrO_3$ may exists within the chromia scale close to the alloy/oxide interface as a secondary phase, and cerium may exists as CeO_2 in the chromia scale closer to the reaction atmosphere. However, the concentration of oxides may be too small for detection by either EDX or XRD analysis.

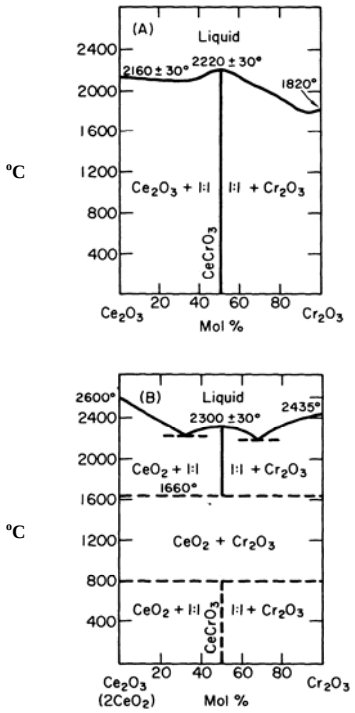

Fig. 42. The Ce_2O_3-Cr_2O_3 ceramic phase diagram in H_2 (A) and in air (B) [75]. The temperature on the vertical axis is given in ^oC.

What is the oxidation mechanism of cerium as an alloying element in an iron-chromium alloy? During the internal oxidation of the cerium containing oxide, cerium diffuses from the bulk alloy toward the alloy/chromia interface, where cerium oxidizes internally. If an oxide is formed internally during oxidation of an external oxide scale, e.g. chromia, the internally formed oxide precipitate will be positioned within the alloy or at the alloy/scale interface. The position of the oxide particle relative to an encroaching external scale is determined by the mobility of the oxide precipitate within the alloy matrix. If the oxide particles cannot move, they become imbedded into the encroaching scale. In contrast, if they can move they will move ahead of the moving interface, or they will accumulate at the moving interface. In case the particles are accumulated at the interface, the particles are said to be dragged along the moving interface [30]. Strawbridge et al. [77] have studied the position of internally formed oxides relative to an encroaching external NiO scale. They found that important parameters for the mobility of the oxide precipitates include solubility in the external scale, the ability to form a ternary oxide between the external scale and the oxide precipitate, oxidation mechanisms of the oxide precipitates and the external scale, and oxidation rates [77]. They observed that the only internally formed oxide precipitates, which became incorporated into the NiO scale, formed ternary oxides with nickel [77]. In contrast, it has been reported that oxide precipitates, which did not react with a Cu_2O external scale became imbedded into the scale as “inert markers” [76]. Thus, the interactions between internally formed oxides and external scales are complex and not fully understood.

It can be speculated that internally formed oxide precipitates only become incorporated into relatively slow growing oxides such as NiO [58] if they form ternary oxides with the scale forming element. In contrast, if the oxide precipitates do not form a ternary oxide, the oxide may be dragged along the moving alloy/oxide

interface as the scale encroaches. The oxide precipitates may become imbedded as "inert markers" in fast growing oxides such as Cu_2O [58], which might "grow past" the oxide precipitate.

If internally formed Ce_2O_3 is accumulated at the alloy/chromia interface, the cerium oxide may react with chromia in a solid-state reaction to form the perovskite $CeCrO_3$. The perovskite may also form internally as an oxide precipitate in the alloy matrix during the oxidation, as previously discussed. The perovskite may exist within the chromia scale as oxide precipitates within the chromia grains or the perovskite may segregate to the grain boundaries of the chromia scale. Closer to the chromia/gas interface, cerium may be present as CeO_2 instead. The morphology changes observed in the present work indicate that cerium is present at or near the alloy/oxide interface or within the oxide scale itself.

In previous studies, both cerium and other RE have been observed within the growing chromia scale by TEM studies, as segregates to the alloy/chromia interface and as segregates to the grain boundaries within the chromia scale [72,74,78-80]. The RE have both been identified as moving ions within the scale [74], or they have been identified as minor contents of secondary phase oxides – mainly perovskites – within the chromia scale [72,78-82]. Furthermore, the position of the RE within the scale has been proposed to be fixed relative to the alloy/chromia interface [83], and the RE has been observed to diffuse outwards to the oxide/gas interface, where they would form RE rich oxides [74]. Despite the different observations described in the literature, there is general agreement that the RE segregates to the grain boundaries of the growing chromia scale.

Due to the greater thermodynamic stability of cerium containing oxides, it appears that a cerium containing oxide will form within the chromia scales grown – possibly the $CeCrO_3$ perovskite (cf. Fig. 42). This perovskite has been observed to form within growing chromia scales [78,82]. Furthermore, cerium oxide has been identified as internally formed oxide precipitates within the alloy [30,82], even though internally formed CeO_2 was reported in Ref. [82] in contrast to the thermodynamic data presented in Fig. 8.

Thus, cerium may exist within the bulk alloy, as internally formed oxide near the interface, at the alloy/chromia interface, and as segregates to grain boundaries within the oxide scale. How does the role of cerium explain the absence of voids in the scale and the improved adhesion of the scale to the alloy (cf. Fig. 33A and Fig. 35A)? It is informative to review the mechanisms for the development of voids and porosities for the ferritic iron-chromium alloy (A1) in order to explain the absence of voids for the A1-Ce alloy. The mechanism for the formation of voids may help to explain the role of cerium during high temperature oxidation.

The mechanisms for the formation of voids at the alloy/chromia interface during the growth of chromia were discussed in section 5.4.1. The voids present in the A1 alloy can be explained by the growth mechanism of chromia. The growth of the chromia scale on the A1 alloy is governed by outward diffusion of chromium through the scale. When chromium is transported across the alloy/chromia interface from the alloy, vacancies are created in the metal lattice at the interface. These vacancies may diffuse inwards in the alloy. Typically however, the chromia scale recedes, so the

vacancies become annihilated at the interface. Thus, the tendency of vacancy formation at the interface is partly determined by the ability of the chromia scale to recede. If the alloy has an indefinite plane surface, the chromia scale can in principle follow the alloy as the alloy surface retreats. In this case, no plastic deformation of the chromia scale is needed for the chromia scale to remain adherent to the alloy. However, the alloy surface is never completely uniform. During oxidation of the alloy, the geometry of the interface and metal may change. Hence, the chromia scale needs to deform plastically near the interface in order to maintain adherence to the alloy. This may result in a build-up of stresses in the chromia scale during the growth of the scale. During the growth, voids may be created within the oxide scale near the interface due to insufficient plastic deformation by the oxide. Furthermore, the vacancies, which are formed at the interface during growth of the scale, may coalesce, in which case voids and cavities are formed at the interface.

Porosities may also develop within the scale due to compressive growth stresses in the scale, resulting in plastic deformation of the oxide scale. As previously mentioned, the compressive growth stresses are a result of the formation of new oxide within the chromia scale. The growth stresses may be relieved by plastic deformation of the oxide scale. However, the plastic deformation of the oxide grains may create porosities within the chromia scale [10].

In summary, the mechanisms causing the development of voids and porosities in the growing chromia scale are outward diffusion of chromium in the scale and the formation of new oxide within the existing chromia scale.

How does the presence of cerium in the scale and at the alloy/chromia interface explain the absence of voids in the scale, and the improved adhesion of the scale to the alloy (cf. Fig. 33A and Fig. 35A)? Several different mechanisms for the role of cerium (and other RE) have been proposed

- Change in growth mechanism
- Improved scale plasticity
- Reduced growth rate
- Interface segregation model

The voids are present in the A1 alloy due to the growth mechanism of the chromia scale, which is governed by an outward diffusion of chromium. Thus, the formation of vacancies near the interface may be reduced if the growth mechanism of chromia is changed from outward diffusion of chromium to predominantly inward diffusion of oxygen. In this case, the new oxide is formed near the alloy/chromia interface. This may prevent the formation of porosities within the scale.

The growth mechanism of alloys is often studied by sequential oxidation in O^{16}, and in O^{18} (see e.g. Ref. [83]). The distribution of isotopes within the oxide scale can subsequently be studied using secondary-ion mass spectroscopy (SIMS) analysis. This analysis technique can reveal where new oxide is formed within the scale, and thereby reveal the growth mechanism of the oxide scale.

It has been found that the presence of reactive elements, e.g. cerium, in the alloy, changes the formation of chromia from the outermost part of the scale closer to the

alloy/oxide interface [83]. This indicates that the presence of cerium in the alloy changes the transport properties within the scale from predominantly outward chromium diffusion, through grain boundaries, to a situation where the formation of new oxide is dominated by oxygen diffusion through grain boundaries of the scale.

The new oxide is formed near the alloy/chromia interface. Such a change in the growth mechanism may explain the absence of voids at the interface for the scale grown on the A1-Ce alloy (cf. Fig. 35A) in this study, since the formation of voids is governed by outward chromium diffusion. However, a change in growth mechanism, where the new oxide is formed at the alloy/chromia interface, may cause the formation of growth stresses in the oxide. This is due to the volume change associated with the formation of new oxide at the interface. If the oxide to metal volume ratio, i.e. the Pilling-Bedworth Ratio (PBR), is larger than one, the growth stresses caused by the volume change will be compressive. For Cr_2O_3/Cr, PBR > 1, so compressive growth stresses may be formed near the interface. However, the oxide scale grown on the specimens containing cerium is adherent to the alloy. This indicates that the most important parameter for the formation of voids in the chromia scale is the diffusion mode during the growth of the scale. The growth stresses generated by the formation of new oxide at the alloy/chromia interface, or within the chromia scale, are of minor importance for the formation of voids and porosities.

This discussion indicates that the change in growth mechanism is an important parameter for improved adhesion. How can the addition of cerium to the alloy change the growth mechanism for the formation of chromia? This is discussed in section 6.4.1.2.

Another cause for the improved scale adhesion for chromia scales grown on the A1-Ce alloy may be due to an improved plasticity of the oxide scale. The stresses resulting from the growth mechanism of the chromia scale may be relieved by creep of the alloy or scale [84]. An improved plasticity of the oxide scale may reduce the formation of voids and thereby cause the scale to adhere better to the alloy. It has been proposed that a smaller grain size in the oxide scale improves the plasticity of the oxide scale [80,85], and thereby improves the adhesion of the scale. To examine the possible effect of cerium on the oxide morphology, fractures of the scales were prepared and examined by SEM. Micrographs of the A1-Ce and A1 alloy are shown in Fig. 33A and Fig. 34D, respectively. As shown in the SEM micrographs, it is not possible to identify a significant morphologically change in the grain structure. The grain size of oxide scales grown on alloys containing cerium has been observed to decrease [85] in comparison with scales grown on alloys without cerium. However, despite these observed changes, studies have failed to show that the addition of RE increases the plasticity of the oxide scales [86,87].

The growth rate of the chromia scale decreased after the addition of cerium to the alloy (cf. Table 10). Hence, it could be speculated that a thinner oxide scale is an important parameter for decreasing growth stresses developed during oxidation. This may cause the scale to adhere better to the alloy during oxidation. Rahmel and Schütze [87] have recently addressed the effect of RE on the adhesion of oxide scales. They have presented an expression, which describes the adhesion of oxide scales in a quantitatively correct manner. Based on this expression, thinner oxide scales adhere better to the alloy. There is, however, considerable scatter in the literature for the

average stresses generated in oxides during isothermal oxidation [79,88]. In contrast, there is agreement that the average stresses generated in oxides during isothermal oxidation are negligible in comparison with the stresses generated during thermal cycling [64,84,88].

The improved adhesion of the chromia scales grown on the A1-Ce specimens may also be caused by a strengthening of the alloy/chromia interfacial bonds. Cerium (and other RE) has, as previously mentioned, been observed to segregate to the alloy/chromia interface and to the grain boundaries of the chromia scale during oxidation. It may be speculated if such a segregation of cerium can improve the interfacial strength and hence improve the adhesion of the chromia scale?

The most accepted effect of cerium (and other RE) in the strengthening of the alloy/chromia interface is due to a scavenging of impurities such as sulfur at or near the alloy/scale interface. Sulfur is believed to weaken the interface during oxidation (cf. section 5.4.1) [89]. This effect is known as the "sulfur effect" [62,74,90]. Although it has been verified that sulfur is detrimental for the interfacial bond, the cause for this behaviour is still unknown [30,74]. Several mechanisms for sulfur degradation have been proposed. The presence of sulfur has been suggested to lower the surface energy of the voids at the interface and thereby facilitate the growth of voids [30,74]. Furthermore, theoretical calculations indicate that the presence of sulphur weakens the alloy/oxide bond [89]. It has been argued that the large sulfur ion is unable to segregate to an intact alloy/oxide interface [30]. However, Auger studies have indicated that segregation to intact interfaces is possible [89]. Furthermore, TEM studies have showed the existence of sulfur at the interface and also within chromia grain boundaries [79,90].

As described in section 5.4.1, the oxidation of specimens in hydrogen/argon atmospheres resulted in an improved adhesion. This was attributed to a removal of impurities from the interface. The micrographs in Fig. 35A vs. Fig. 36D show improved adhesion for the specimen containing cerium. The improved adhesion for the A1-Ce alloy may also be explained by scavenging of surface impurities such as sulfur. The cerium atoms, which are present in the alloy, segregate to the interface, where they bind to the impurities and thereby improve the adhesion, i.e. cerium acts as a getter for sulfur near the alloy/chromia interface. The cerium atoms in the specimens may also bind the impurities within the alloy matrix and thereby reduce the content at the surface. RE sulfides and oxy-sulfides form very strong bonds and are very stable [84,91]. However, firm experimental evidence is lacking for these proposals [74,79].

It is possible that the removal of sulfur and other impurities from the surface of the alloy is the only interfacial strengthening effect of cerium. In this case, sulphur free interfaces are inherently strong [84]. However, not all oxide scales grown on sulphur free specimens adhere well to the alloy [89], so the presence of cerium near the interface has a beneficial effect for the adherence of the oxide scale itself [84,89]. Furthermore, theoretical calculations have indicated that reactive elements has a strengthening effect on the interfacial bonds [30,79].

The effect of cerium on improved adhesion, and on the absence of voids and porosities at the interface may be a complex mechanism, which is influenced by the

various causes mentioned above. It is the author's belief that an increased interfacial strength and the decreased outward diffusion of chromium during oxidation are the most important parameters for the improved adhesion. Improved plasticity of the chromia scale and the growth stresses generated by the formation of new oxide within the existing scale during isothermal oxidation are believed to be of minor importance. Further studies are, however, necessary in order to identify the most important parameters for the improved adhesion in the presence of cerium in the alloy. In contrast to isothermal oxidation, stresses generated, by thermal cycling, within the scale, are very important for the mechanical properties of the chromia scale [84,88,92].

6.4.1.2 Oxidation kinetics

As shown in Table 10, the addition of cerium to the alloy decreases the growth rate of the chromia scale. The growth rate of chromia scales can be described by a parabolic rate expression, where the rate constant is expressed by the diffusion coefficients of the reactants (cf. Eq. 55). Hence, the addition of cerium (and other RE) must influence the transport properties within the scale in order to reduce the growth rate of the scale. The diffusion of reactants can either be slowed down by reducing the number of moving defects within the scale, or by reducing the mobility of the defects (cf. Eq. 21). Based on this observation, several causes may be proposed for the reduced growth rate. However, the proposals must correlate with the experimental findings for alloys containing reactive elements. As previously discussed, the addition of cerium changes the growth mechanism of chromia from a predominantly outward diffusion of chromium through grain boundaries to a growth mechanism, which is governed by a predominantly inward oxygen diffusion [83]. Thus, the reduction in the growth rate may be caused by the change of growth mechanism.

The mechanisms in which the presence of cerium decreases the diffusion of reactants through the grain boundaries are unknown, but possible causes for the reduction in growth rate are proposed and discussed in the following. Emphasis will be on the most recent theories, which describe how the addition of RE can reduce the growth rate of chromia.

Several mechanisms may be proposed for the decreased growth rate of chromia after the addition of reactive elements

- Decrease in grain boundary area
- An oxide segregation model
- Change of defect chemistry in oxide
- Interface poisoning model

The mobility of the defects through the chromia scale could decrease, if the size of the transport network is decreased. This can occur by reducing the grain boundary area by increasing the average grain size in the scale. However, this study did not show any significant effect of cerium on the grain structure of the scale, as previously mentioned. Furthermore, previous studies have shown the completely opposite effect,

i.e. a decrease in grain size as an effect of cerium [85]. Hence, the reduction in growth rate is most likely not caused by a decrease in the grain boundary area for diffusion.

As previously discussed, cerium (and other RE) segregates to grain boundaries of the scale during oxidation. The change in the growth mechanism may be explained by this segregation. The growth of chromia is governed by chromium diffusion through grain boundaries. The presence of RE in the grain boundaries may block the grain boundaries. This will result in a decrease in the mobility of the defects and thereby a decreased growth rate. It has been proposed that the diffusion path for chromium is blocked, while the diffusion path for oxygen is unaffected. Both chromium and oxygen are transported through grain boundaries in the scale during the growth of chromia. Thus, it appears strange that the segregation of reactive elements to grain boundaries blocks the chromium ions, while the transport of oxygen is unaffected. This discrepancy can be explained if the RE-oxides, which are blocking the grain boundaries, are oxide ion conductors and not chromium ion conducting. In this case, chromium diffusion is blocked, while oxygen diffusion may be unaffected; depending on the properties of the RE-oxide. The RE-oxides often have the perovskite structure, as $CeCrO_3$. Indeed, oxides with the perovskite structure are oxide ion conductors instead of cation conductors [93]. Thus, a segregation of oxides to the grain boundaries may explain the decreased chromium transport and the decreased growth rate of chromia. The RE-oxides should be present in most grain boundaries in order to block the transport paths for chromium in an effective manner. In contrast, the chromium diffusion will not be blocked significantly [72]. However, a reduction in growth rate has been observed after the addition of very small amounts of RE [72]. A blocking effect of the grain boundaries is therefore questionable.

Another possibility is that the reactive elements are preferentially located on sites, which otherwise would transport chromium through grain boundaries, while the transport of oxygen would occur via other sites. Such a chemical rather than steric hindrance would block chromium transport, while oxygen transport would be unaffected [30]. However, such a proposal is highly speculative.

A segregation of sulfur at chromia grain boundaries has also been postulated to change the growth mechanism [63]. It was postulated that the growth of chromia scales is governed by oxygen grain boundary diffusion, if the oxide scale and the alloy/chromia interface are “clean”, i.e. without the presence of sulfur. In contrast, if sulfur is present at grain boundaries and at the interface, a change in the growth mechanism is observed. Thus, sulfur promotes the chromium diffusion somehow. The RE acts as a getter for sulfur, and thereby reduces the content of sulfur near the interface and scale. This decreases the outward transport of chromium and may change the growth mechanism of chromia such that the growth becomes governed by oxygen diffusion. However, this mechanism has not been verified, and the opposite effect of sulfur has been observed during the oxidation of nickel [72].

Another mechanism, which has been put forward to explain the change in growth mechanism, is a change of the defect concentrations at the grain boundaries within the growing oxide. The growth of chromia on the A1 alloy is governed by interstitial chromium defects (cf. section 5.4.2.2). The growth mechanism of chromia scales may change if the concentration of interstitial chromium in the oxide is reduced and/or if the concentration of oxygen defects is increased. The concentration of interstitial

chromium must, however, decrease in order to reduce the growth rate of chromia. Cerium may be present as CeO_2 in the oxide, as previously mentioned. If a small solubility of CeO_2 in Cr_2O_3 exists, cerium will be present as Ce^{4+} in the chromia lattice. If cerium is charge compensated by chromium interstitials, a solubility of cerium in chromia may be written

$$3CeO_2 + Cr_i^{\bullet\bullet\bullet} \xrightarrow{Cr_2O_3} 3Ce_{Cr}^{\bullet} + Cr_{Cr}^{X} + 6O_O^{X} \qquad \text{reaction 9}$$

Thus, the concentration of interstitial chromium defects decreases after the substitution of cerium in the chromia lattice. Hence, the growth rate of chromia may decrease, and the growth mechanism may change if cerium is substituted in the chromia lattice. However, the defect considerations are only applicable for cerium. A reduction in the growth rate of chromia has also been observed after the addition of other RE, e.g. yttrium. Yttrium is present as $YCrO_3$ [80] in the chromia scale, so the defect concentrations of chromium and oxygen defects in the chromia scale may not change since yttrium is present as Y^{3+}. Thus, a decrease in the content of interstitial chromium given by reaction 9 is not the only reason for the changed growth mechanism.

Tsai et al. [94] have examined the effect of yttrium doping in a chromia scale on the chromium diffusion coefficient. They found that the chromium diffusion coefficients decreased slightly in the presence of yttrium in the scale. The doping effect has also been examined for sintered chromia with and without yttrium oxide additions [95]. In this study, an increase of the chromium diffusivity was found after the addition of yttrium. These results show that large discrepancies exist for the effect of RE additions to chromia on the diffusion data. Furthermore, these results are in contrast to the blocking mechanism, which was discussed in the last paragraph, where it was proposed that the presence of RE in the chromia scale decreased the chromium transport significantly.

A recent theory, which has been proposed by Pieraggi and Rapp [96], stresses the importance of the interfacial transport across the alloy/scale interface. The mechanism has been termed the “interface poisoning model”. During the growth of chromia scales, chromium diffuses outwards from the alloy to the oxide scale. This growth mechanism results in the development of vacancies at the interface, as previously discussed. During a continued diffusion of chromium from the alloy, the vacancies, which are created in the alloy, must be annihilated. In the “interface poisoning model”, it is argued that this annihilation of vacancies at the interface is important for the overall growth rate of the scale. It is proposed that the segregation of reactive elements to the interface poisons the interface by eliminating sites for chromium vacancy annihilation. As a result, the outward chromium diffusion from the alloy through the scale is impeded. Furthermore, the oxygen diffusion through the scale is unaffected since the oxygen vacancies are annihilated at the chromia/gas interface. It is proposed that chromium diffusion becomes impeded, so oxygen diffusion through the scale becomes dominating for the growth of the chromia scale. Several experimental observations suggest, however, that the “interface poisoning model” is unacceptable. Firstly, it is commonly accepted that the growth of oxide scales is not governed by interfacial reactions, but instead governed by a diffusional transport of ions across the scale [30]. It is believed that interfacial reactions are rapid, as

mentioned in section 2.3.2. Hence, the interfacial reactions are not rate limiting in the oxidation process. Secondly, interfacial segregation of sulfur and phosphorus are known to impede interfacial reactions. However, the presence of these elements does not change the growth mechanism of chromia or reduce the growth rate of chromia scales [79]. Thirdly, experiments have been conducted on a chromia forming Ni-Cr alloy, where reactive elements were deposited on a preformed chromia scale [97]. After a subsequent oxidation, the reactive elements were only detected within the scale. However, the growth mechanism was still changed such that the growth of the chromia scale became governed by inward oxygen diffusion. This observation strongly indicates that it is the presence of reactive elements within the scale and not at the alloy/chromia interface, which is important for the change in growth behaviour.

The reduction in the growth rate of chromia is due to a change in the growth mechanism and the fact that oxygen diffusion is considerably slower than chromium diffusion through the grain boundaries. The change in growth mechanism is probably a combination of several effects. The most commonly accepted theory is that the change in growth mechanism is governed by the presence of oxide ion conducting perovskites in the grain boundaries of the growing chromia scale. However, this explanation has serious drawbacks. The most eminent is that the perovskites should cover almost all grain boundaries within the oxide. This has been questioned [72]. The change in growth direction may also be due to a lack of control of foreign defects at the grain boundaries of the growing chromia scale, as pointed out by Atkinson [98].

6.4.1.3 Effect of reaction atmosphere

The effect of the oxygen activity (hydrogen/argon vs. air) on the microstructure of the oxide scale has previously been discussed for the iron-chromium A1 alloy. It was observed that the chromia scale was less adherent in air than in hydrogen/argon. Furthermore, an effect of the oxygen activity was noticed on the morphology of the outermost region of the oxide scale in section 5.4.1. The effect was also examined for the A1-Ce alloy (not shown). The results obtained for the alloy containing cerium were similar to the results obtained for the A1 alloy. The observations previously described in section 5.4.1 will not be discussed further. However, it should be noticed that oxide whiskers were also formed on the specimens containing cerium. Different mechanisms for the growth of whiskers were discussed in section 5.4.1. It is, however, imperative for the growth of whiskers that chromium is diffusing outward from the alloy to the chromia/gas interface. In contrast, the outward growth of whiskers would not be possible. This indicates that the growth of the chromia scales, observed in this work, is governed by outward diffusion of chromium. This is in contrast to the growth mechanism, which is often observed for chromia scales formed on specimens containing cerium (and other RE), where the growth of chromia is governed by inward diffusion of oxygen, as previously discussed.

The reduction in the growth rate, after the addition of cerium to the iron-chromium alloy in this work, is not as large as that observed in the literature for similar types of alloys [74]. The oxidation temperature is an important parameter for the beneficial effect of RE. The REE for chromia forming alloys is significant only at temperatures above ca. 1173 K [74]. This observation may explain why the growth rate of the

chromia scale is only slightly reduced after the addition of cerium in this work. Thus, the REE is important in the present work, but not as significant as observed in the literature at higher temperatures. This may explain why the chromia scales are growing by outward diffusion of chromium, as seen from the formation of oxide whiskers.

Another reason for a reduced REE may be an insufficient distribution of cerium in the alloy during the arc-melting process. However, it is the author's belief that the reduced REE is caused by the low oxidation temperature used in these studies.

As shown in Table 10, the weight gain for the specimens oxidized in air containing water vapour is lower than the corresponding weight gain for the specimens oxidized in hydrogen/argon. This is an effect of vaporization of chromium species in the presence of oxygen and water vapour, as described in section 5.4.2.2. Furthermore, the parabolic rate constants, for the specimens containing cerium, are almost independent of the oxygen activity (cf. Table 11). If the growth of the chromia scales is governed by outward diffusion of chromium, the growth mechanism has been discussed in section 5.4.2.2. However, the situation may be different if the growth of chromia is governed by inward diffusion of oxygen. The oxygen diffusion coefficient may be written (cf. Eq. 57)

$$D_O = \left[V_O^{\bullet\bullet}\right] D_{V_O} + \left[O_i^{//}\right] D_{O_i} \qquad \text{Eq. 80}$$

From Eq. 60 and Eq. 61, it follows that

$$D_O = K_1 p(O_2)^{-1/8} D_{V_O} + K_2 p(O_2)^{+1/8} D_{O_i} \qquad \text{Eq. 81}$$

where K_1 and K_2 are constants. If oxygen defects are dominating during the growth of chromia, the growth is either governed by oxygen vacancies or by oxygen interstitials. The concentration of oxygen vacancies is highest at the alloy/chromia interface, where the oxygen activity is independent of the oxygen activity in the reaction atmosphere, so it can be shown by a similar argument, as described in section 5.4.2.2, that the growth of chromia is governed by oxygen vacancies.

6.4.2 Oxidation of A1-Si

Contrasting the oxidation behaviour of the A1-Si and A1 specimens given in section 6.3, several observations can be made on the effect of silicon

- The formation of a silicon rich oxide at the alloy/chromia interface
- Decrease in weight gain

Thus, it is seen that the addition of silicon to the A1 alloy has an effect on both the microstructure and the oxidation kinetics. These observations are discussed in the following.

6.4.2.1 Microstructure

The effect of the oxygen activity (hydrogen/argon vs. air) on the microstructure of the oxide scale has been discussed for the iron-chromium A1 alloy in chapter 5. An effect of the oxygen activity was observed on the morphology of the outermost oxide scale and on the adherence of the oxide scale in section 5.4.1 for the A1 alloy. The effect of the oxygen activity on the oxide morphology was also studied for the A1-Si alloy (not shown). The results obtained for the A1-Si specimens were similar to the results obtained for the A1 alloy. The observations have previously been described and will not be discussed further.

The morphology of the oxide scale and the alloy/oxide interface of the A1-Si alloy is shown in Fig. 33B and Fig. 35B, respectively. Similar micrographs were also obtained for the A1 alloy (cf. Fig. 34D and Fig. 36D). Dark islands were observed at the alloy/scale interface of the A1-Si alloy. The islands were identified as a silicon rich oxide from EDX line scan analysis of the cross sections (cf. Fig. 41B). Small porosities were observed in the chromia scale grown on both the A1 and A1-Si specimens (cf. Fig. 35B and Fig. 36D, respectively). Small dark cavities are seen at the alloy/oxide interface of the A1 alloy, while the presence of cavities at the alloy/scale interface of the A1-Si alloy is difficult to detect due to the presence of black islands of silicon containing oxide at the interface.

The diffraction patterns (cf. Fig. 38) and EDX line scan analyses (cf. Fig. 41B) of the oxide show that the scale formed is chromia. Furthermore, for the oxides grown in hydrogen/argon, the diffraction patterns also indicate a small amount of oxide with the spinel structure. This is a result of transient oxidation of the alloy before a dense chromia layer has developed (cf. chapter 5).

The oxide scales, which were grown on the specimens containing silicon, were examined by XRD (cf. Fig. 38) in order to identify possible oxide phases originating from the presence of silicon. The diffraction patterns are similar to those obtained for the ferritic Fe-Cr alloy (cf. Fig. 40), so it was not possible to identify the silicon rich oxide beneath the chromia scale. This is probably due to the thick chromia scale formed above the dark islands. The absence of reflections from the silica rich oxide may also be due to the fact that the oxide has an amorphous structure.

The EDX line scan analysis of the cross section (cf. Fig. 41B) shows the presence of silicon, chromium and iron near the interface. However, the dark silicon rich oxide precipitates beneath the chromia scale are small, so the EDX analyser may detect X-rays emerging from the surrounding alloy and chromia scale.

Phase diagrams are useful in order to predict the thermodynamically stable oxides formed during oxidation. The SiO_2-Cr_2O_3 ceramic phase diagram is shown in Fig. 43 [75].

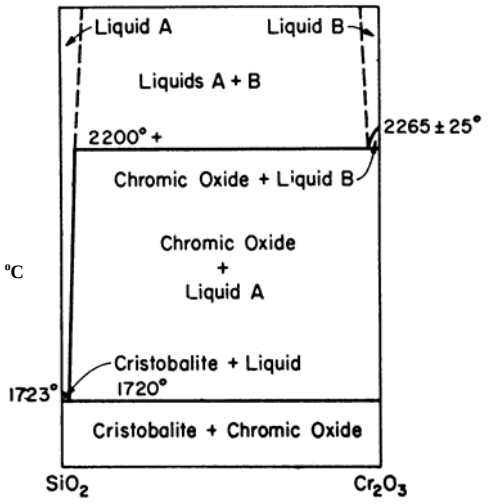

Fig. 43. The SiO_2-Cr_2O_3 ceramic phase diagram in air [75]. The temperature on the vertical axis is given in ^oC.

The phase diagram in Fig. 43 shows that silica and chromia are insoluble. Similar results have been obtained at low oxygen activities [99]. Thus, it is not thermodynamically possible for chromium to exist in the silicon rich oxide. The alloy/chromia decomposition pressure defines the oxygen activity near the silicon rich oxide. Thus, it is not possible for iron to oxidize and to exist within the silica phase [70]. From these observations, it is concluded that the silicon rich oxide consists of pure silica.

It was observed from the diffraction patterns in Fig. 38 that it was not possible to identify the silicon rich oxide beneath the chromia scale. The oxidation behaviour of alloys containing various amount of silicon has been studied in the literature. The developed silica layer has been studied using XRD and electron diffraction, where it was found that silica is amorphous below ca. 1473 K [84,100,101]. Thus, the silica precipitates formed, beneath the chromia scale in this study, most likely has an amorphous structure.

6.4.2.2 Internal formation of silica

It is evident from Fig. 35B that silica precipitates are formed beneath the chromia scale near the alloy/chromia interface of the A1-Si alloy. This oxidation behaviour is significantly different from the oxidation behaviour of the A1-Ce alloy, which was discussed in section 6.4.2.1. Thus, several questions arise

- What is the growth mechanism for the formation of silica?
- Why is silica formed beneath the chromia scale?
- Why is silica only present beneath the chromia scale and not within the chromia scale?

These questions are addressed in the following.

During the transient oxidation of the A1-Si alloy, silicon, iron and chromium may be oxidized. The content of silicon in the alloy is very low, so it is not possible to form a dense silica scale initially [68]. Instead, a dense chromia scale is readily formed at the alloy surface. The formation of a chromia scale has been described in chapter 5. After the formation of a chromia scale, the silica precipitates are formed beneath the chromia scale. Before describing the formation of the silica precipitates beneath the chromia scale, the formation of silica in the absence of an external scale will be described.

Consider an alloy matrix containing a very low amount of silicon. It is assumed that the experimental conditions are such that the alloy constituents, with the exception of silicon, are noble in the oxidizing atmosphere. Silicon may be internally oxidized or may form a dense external scale. Silica may form internally if oxygen is dissolved in the alloy matrix. The dissolution of oxygen in the alloy matrix can be written

$$O_2 \leftrightarrow 2O(diss) \qquad \text{reaction 10}$$

The content of oxygen within the alloy decreases as the distance from the alloy surface increases [76]. If equilibrium is assumed, internal oxidation will only take place if

$$N_O N_{Si} > K_{SP} \qquad \text{Eq. 82}$$

where N_O and N_{Si} are the atomic fraction of oxygen and silicon in the alloy, and K_{sp} is the solubility product for silica. The internal oxidation proceeds according to a parabolic rate expression [102], where the depth of the internal reaction zone is given by

$$\xi = 2\gamma\left(D_O t\right)^{½} \qquad \text{Eq. 83}$$

where ξ is the thickness of the internal oxidized zone at time t, D_O is the diffusion coefficient for oxygen in the alloy matrix, and γ is a dimensionless kinetic parameter [76]. The value of γ increases with N_O and decreases with N_{Si}. Detailed expressions for the value of γ may be seen in [76]. Thus, the thickness of the internal zone increases with $N_O D_O$ and decreases with $N_{Si} D_{Si}$.

In this work, the silica precipitates form internally beneath a chromia scale. The position of silica relative to the chromia scale is governed by the relative stability of chromia and silica. Silica is more stable than chromia (cf. Fig. 8), so the silica precipitates become positioned beneath the chromia scale. The oxygen activity at the alloy/chromia interface is determined by the decomposition pressure of chromia. This pressure is very low. Thus, the external chromia scale effectively decreases the content of oxygen dissolved into the alloy matrix (cf. reaction 10). As a result of this, the silica precipitates are formed near the alloy/chromia interface.

As described in this work, silica is present as distinct oxide precipitates beneath the chromia scale. The position of internally formed oxides relative to an encroaching

external scale was discussed in section 6.4.1.1. Strawbridge et al. [77] observed that the only oxide precipitates, which became incorporated in an encroaching NiO scale, formed ternary oxides with nickel in the scale. As shown in the phase diagram in Fig. 43, the silica and chromia does not form a ternary oxide. Thus, silica may not be incorporated into the growing chromia scale. It has also been proposed that internally formed oxides act as inert markers [76]. The growth of the present A1-Si alloy is probably governed by outward chromium diffusion, as discussed later. This implies that silica should be positioned at the alloy/chromia interface, as observed. However, it is difficult to envisage the silica precipitates as inert markers during the slow growth of chromia, since the presence of the silica particles beneath the chromia scale is governed by the relative thermodynamic stabilities of chromia and silica.

In summary, silica is positioned beneath the chromia scale, since silica is more stable than chromia, and since silica and chromia does not form a ternary oxide.

The silica precipitates are present as distinct particles at the interface. However, these precipitates may coalesce to form a dense silica layer beneath the chromia scale if the concentration of silicon in the alloy matrix is high enough [76]. Thus, it is interesting to determine the minimum concentration of silicon needed in the alloy for the formation of a dense silica layer beneath the chromia scale during oxidation. The parameters, which govern the transition between internal oxidation of silica and the formation of a dense layer of silica, will be discussed below.

Wagner [102] and Rapp [103] have examined the transition between internal and external oxidation in the absence of an outer scale. Furthermore, the transition has also been examined when the transition occurs beneath an external scale [100,104-106]. The latter situation applies for the present work, where silica is internally oxidized beneath the chromia scale.

Wagner [102] proposed that a critical volume fraction of internally formed oxide governs the transition between internal oxidation and formation of an external scale. As the internal precipitation occurs, the internally formed oxide increasingly blocks the inward diffusion of oxygen through the alloy matrix, since the oxygen diffusion only can occur in the alloy matrix between the oxide nuclei. Instead, the nuclei start to grow sideways and slowly coalesce to form a dense layer of oxide [76]. In the presence of a critical volume fraction of internally formed oxide precipitates, the oxygen diffusion eventually becomes sufficiently blocked such that a dense layer of oxide is formed instead. Wagner's proposal has subsequently been validated through experiments [103].

The enrichment of silicon as silica in the internal oxidation zone can be described by an enrichment factor α. The enrichment factor is given by the mole fraction of silicon as silica in the internal oxidation zone (f) divided by the mole fraction of silicon in the bulk alloy (N_{Si}^0). Wagner showed that [102]

$$\alpha = \frac{f}{N_{Si}^0} = \left[\pi^{1/2}\gamma\varphi^{1/2}\exp\left(\gamma^2\varphi\right)erfc\left(\gamma\varphi^{1/2}\right)\right]^{-1} = \frac{1}{F\left(\gamma\varphi^{1/2}\right)} \qquad \text{Eq. 84}$$

where $\varphi = D_O/D_{Si}$, γ is the parameter defined by Eq. 83, and F(z) is defined by

$$F(z) = \pi^{1/2} z \exp(z^2) erfc(z) \qquad \text{Eq. 85}$$

where erfc(z) is the complementary error function of z. The enrichment factor equals 1 if silicon is not enriched in the internally oxidized zone. In contrast, $\alpha > 1$ if an enrichment of silicon occurs in the internal oxidation zone. The volume fraction f_V of internally formed silica is defined by

$$f_V = f\left(\frac{V_{SiO_2}}{V_A}\right) = \alpha N_{Si}^0 \left(\frac{V_{SiO_2}}{V_A}\right) \qquad \text{Eq. 86}$$

where V_A is the atomic volume of the alloy, and V_{SiO2} is the molecular volume of silica. Rapp [103] found that the critical volume fraction for the transition between internal and external oxidation was $f_V = 0.3$ for the oxidation of Ag-In alloys. If this value is used in the present work, the critical bulk concentration (geometric) of silicon for the transition is given by

$$N_{Si}^0(i) = \frac{0.3}{\alpha}\left(\frac{V_A}{V_{SiO_2}}\right) = 0.3\left(\frac{V_A}{V_{SiO_2}}\right) F\left(\gamma\varphi^{1/2}\right) \qquad \text{Eq. 87}$$

In this work, silica is formed underneath a chromia scale. The content of dissolved oxygen in the alloy is very small in the presence of an external chromia scale, so the assumption $N_{Si}D_{Si} >> N_O D_O$ is valid. Using this, it has been shown that the critical silicon concentration (geometric) for the formation of a dense layer of silica beneath the chromia scale is [104]

$$N_{Si}^0(i) = \left(\frac{0.3\pi V_A D_O N_O}{4 V_{SiO_2} D_{Si}}\right)^{1/2} \qquad \text{Eq. 88}$$

The critical concentration in Eq. 88 was derived from the geometric criteria proposed by Wagner.

The relative stabilities of silica and chromia are shown in Fig. 8. The critical concentration of silicon N_{Si}^e, at which both chromia and silica exist in equilibrium with the alloy, is shown in Fig. 44. An activity of 0.22 was assumed for chromium in the alloy.

It is evident from Fig. 44 that silica is much more stable than chromia.

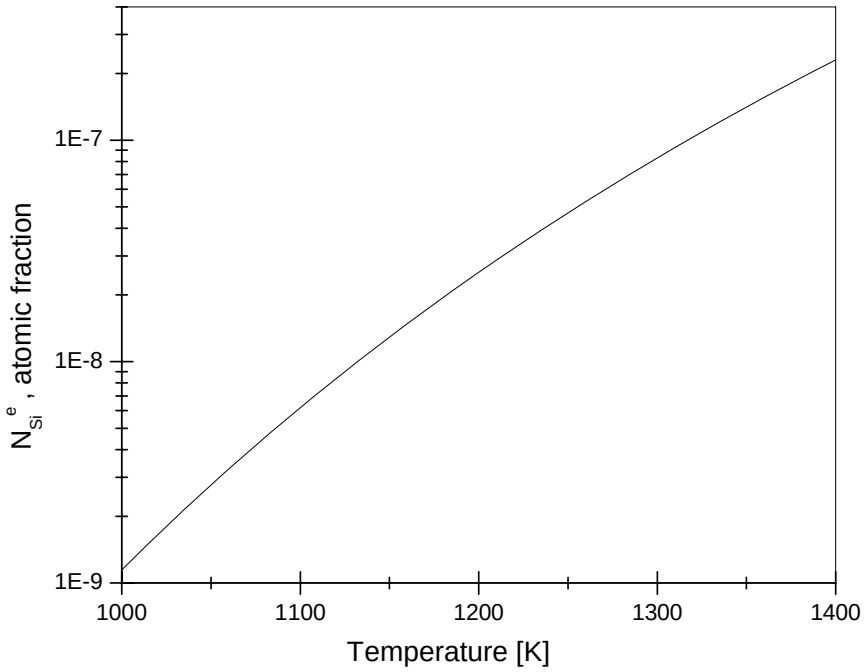

Fig. 44. The critical silicon atomic fraction in the alloy, at which both chromia and silica exist in equilibrium with the alloy, as a function of temperature. The thermodynamic data were taken from Ref. [34].

In order to maintain the growth of silica, silicon must be provided from the alloy by diffusion such that the flux through the alloy matches the flux required for the growth of the external scale. Hence, there exists a kinetic concentration of silicon in the alloy necessary for the continued growth of silica. The critical bulk concentration of silicon in the alloy is the concentration at which the concentration of silicon at the alloy/silica interface equals N_{Si}^{e} during the oxidation [107]. The silicon diffusion coefficient in the alloy is much greater than the parabolic rate constant for the formation of silica (cf. Table 12). Furthermore, N_{Si}^{e} can be assumed to be negligible (cf. Fig. 44). Using this, it can be shown that the critical silicon concentration (kinetic) for the formation of a dense layer of silica beneath the chromia scale is given by [107]

$$N_{Si}^{0}(ii) = \frac{V_A}{V_{SiO_2}} \left(\frac{\pi k_{SiO_2}}{2 D_{Si}} \right)^{½} \qquad \text{Eq. 89}$$

The content of silicon within the alloy must meet both criteria (geometric and kinetic) in order to form a dense silica layer beneath the chromia scale [104]. Thus, Eq. 88 and Eq. 89 are used to calculate an estimate of the content of silicon necessary to form a dense layer of silica beneath the chromia scale. The thermodynamic and kinetic data, which are used for the calculation, are given in Table 12.

Table 12. Thermochemical data used for the calculation of the critical silicon concentrations in Eq. 88 and Eq. 89.

Expression	Reference
$N_O = 1.5\exp(-15434K/T)$	[108]
$D_O\left[cm^2 s^{-1}\right] = 0.037\exp(-11721K/T)$	[108]
$D_{Si}\left[cm^2 s^{-1}\right] = 0.74\exp(-26434K/T)$	[109]
$V_A/V_{SiO_2} = 0.25$	[110]
$k_{SiO_2}\left[cm^2 s^{-1}\right] = 1.1\cdot 10^{-9}\exp(-14342K/T)$	[111]
$2Fe + O_2 \leftrightarrow 2FeO$ $\Delta G^o\left[kJ/mol\right] = -526 + 0.1395\cdot T$	[34]
$4/3Cr + O_2 \leftrightarrow 2/3Cr_2O_3$ $\Delta G^o\left[kJ/mol\right] = -756.5 + 0.1824\cdot T$	[34]

The value for the oxygen solubility N_O in Table 12 was measured at the equilibrium pressure between iron and wüstite. The solubility of oxygen in the alloy follows Sievert's law $N_O \propto (p(O_2))^{½}$ (cf. reaction 10). Thus, the oxygen solubility in the alloy beneath chromia may be calculated using

$$N_O\left(pO_2{}'\right) = N_O\left(pO_2{}''\right)\left(\frac{pO_2{}'}{pO_2{}''}\right)^{1/2} \qquad \text{Eq. 90}$$

where $p(O_2)'$ and $p(O_2)''$ are the decomposition pressures of chromia and wüstite, respectively. The decomposition pressures of wüstite and chromia are calculated using the thermodynamic data given in Table 12 for the formation of wüstite and chromia (cf. section 2.4). An activity of 0.22 is used for chromium, i.e. the bulk concentration. This is an approximation, since a small depletion of chromium will occur near the alloy/chromia interface during the growth of chromia [112].

The parabolic rate constant, which is given in Table 12 for the growth of silica, was determined at high oxygen pressures. Hence, it is questionable if the value can be used in the present work, where silica is formed at low pressures. It has been proposed that the growth rate decreases with decreasing partial pressure of oxygen [100]. However, the value given in Table 12 is tentatively used for the calculation, which then may give an upper limit for the kinetic critical value of silicon (cf. Eq. 89). The result of the calculation is shown in Fig. 45.

The calculation of the critical concentrations of silicon is based on thermochemical data from the literature. The thermochemical data for this particular alloy may, however, be different. Hence, Fig. 45 may only be used for a qualitative discussion of the results. Furthermore, the critical concentration of silicon is given by the kinetic criteria for the temperatures of interest for this work. This implies that the critical content of silicon is reduced if the parabolic rate constant for the growth of silica is reduced. The critical silicon concentration given by the geometric criteria is very low. This is caused by the low solubility of oxygen in the alloy at the low oxygen partial

pressure beneath the chromia scale. In this case, the silica precipitates are formed in close vicinity of the alloy/chromia interface. As a result of this, it is easier for the oxide particles to coalesce to form a dense silica layer beneath the chromia scale.

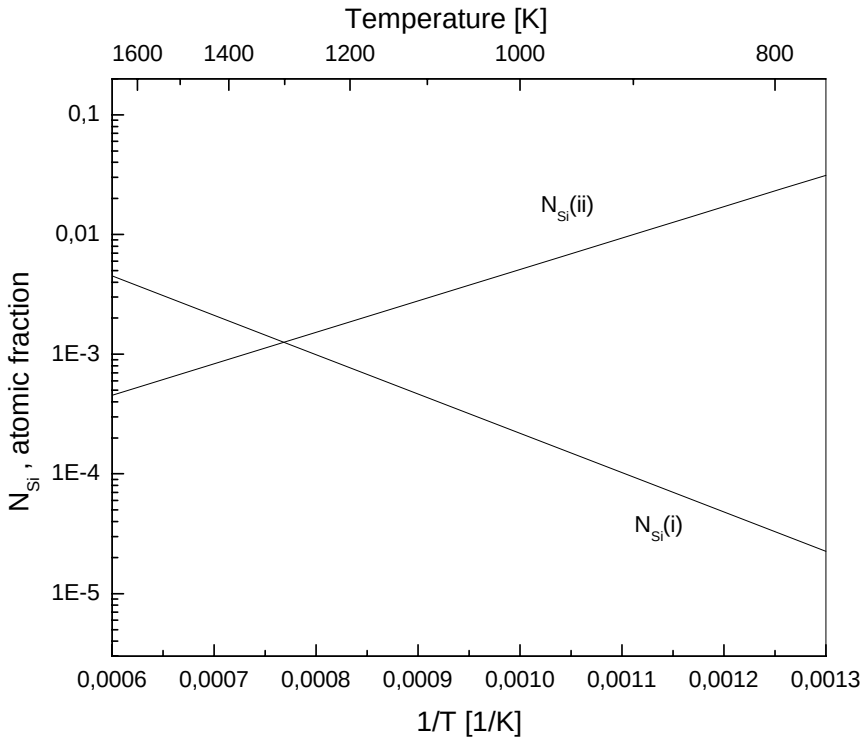

Fig. 45. Calculated critical silicon concentration to form a continuous silica scale on a ferritic iron-chromium alloy beneath a chromia scale. The critical silicon concentrations calculated using Eq. 88 and Eq. 89.

The critical content for the formation of a dense layer of silica is ca. 0.2 at.% at 1173 K, compared to the 0.3 at.% of silicon added to the alloy in this work. Thus, a dense layer of silica may be formed if the specimens were oxidized for much longer times. The present calculation is an ideal case, where a thin silica layer is formed beneath the chromia scale. Instead, the local thickness of silica may vary across the scale [113]. The silica precipitates must spread laterally beneath the chromia scale in order to form a continuous layer of silica. The lateral oxide growth is not well-understood [105], so this condition cannot be quantified. Furthermore, the chromia scale may exhibit mechanical defects during long term oxidation, which will change the results [114]. Recently, Hoelzer et al. [113] examined the oxidation behaviour of a ferritic iron-chromium steel containing only 0.1 at.% silicon. The alloy was oxidized at 1073 K for 10000 h. Despite the low silicon concentration, cross sections of the specimens revealed an almost dense layer of silica beneath the external scale, but areas of contact still existed between the steel and oxide scale. This result may indicate that the

parabolic rate constant for the formation of silica, which is used in the calculations is too high [100], since the critical silicon concentration given by Fig. 45 is ca. 0.35 at.% at 1073 K.

It was previously recognized and discussed how the addition of cerium (and other RE) to the alloy has a beneficial effect on the oxidation behaviour of the alloy. Thus, it is natural to ask if the addition of silicon to the alloy has a similar beneficial effect, i.e. can silicon be characterized as a reactive element? The effect of silicon has previously been addressed as the effect of RE [115]. It has been postulated that almost any elements with a higher affinity for oxygen than chromium could be characterized as a RE [79]. The addition of RE to alloys are characterized by certain effects on the oxidation behaviour of the alloys. This includes an improved adhesion of the scale to the alloy and a reduced growth rate of the scale. Furthermore, the growth mechanism of chromia scales changes after the addition of RE to the alloy. The addition of silicon to the alloy did not improve the adhesion of the scale in this study. Instead, porosities were observed in the chromia scales grown on the A1-Si alloy (cf. Fig. 35B). It has also been observed that the presence of silica beneath the chromia scale deteriorates the adhesion of the chromia scale, particularly during cooling [80,116]. Furthermore, the addition of silicon to alloys does to the author's knowledge not change the growth mechanism of chromia scales to a predominantly inward oxygen diffusion [117]. These results indicate that silicon does not act as a reactive element.

Although silicon does not act as a reactive element, the addition of silicon decreases the growth rate of chromia. Possible causes for the reduction in growth rate are discussed in the following.

6.4.2.3 Oxidation kinetics

It was previously discussed how the addition of RE to the alloy reduces the growth rate of chromia. This effect may be caused by the presence of reactive elements within the chromia scale, which may block the grain boundaries for chromium transport. The reduction of the growth rate of the chromia scale in the case of silicon additions to the alloy cannot be attributed to the same effect, since silicon does not exists within the chromia scale (cf. Fig. 43). The beneficial effect of adding silicon to alloys has been examined previously [100]. Numerous reasons for the effect of silicon on the oxidation behaviour of alloys have been proposed. However, the reasons for the positive effect are still not well-understood [114]. The content of silicon added to the alloys in previous studies was usually so high that a dense layer of silica formed during the oxidation [68,118]. This situation is different from that described in this study, where the silica particles do not form a dense layer (cf. Fig. 35B). The reasons for the beneficial effect of silicon in the alloys may be different in the two cases. Thus, several different models and mechanisms may be proposed for the reduction in growth rate of the A1 alloy after the addition of silicon. These include

- Change of defect chemistry in chromia
- Formation of a dense silica layer
- Formation of a porous silica layer

The models for the reduction of the growth rate are discussed below.

The effects of air and water vapour on the weight gain of the A1-Si alloy, shown in Table 10, results from the vaporization of chromium species from the chromia scale. The effect was described in section 5.4.2.2.

6.4.2.3.1 Change in defect chemistry

The phase diagram in Fig. 43 indicates that silica is insoluble in chromia. However, a small solubility of silicon in chromia has been reported elsewhere (less than 0.1 at.%) [70,119]. A doping of chromia by silicon may change the defect concentrations in chromia. Silicon is present as Si^{+4} (SiO_2), so the possible solubility of silicon in chromia may be written (cf. reaction 9)

$$3SiO_2 + Cr_i^{\bullet\bullet\bullet} \xrightarrow{Cr_2O_3} 3Si_{Cr}^{\bullet} + Cr_{Cr}^{X} + 6O_O^{X} \qquad \text{reaction 11}$$

Thus, the concentration of interstitial chromium defects decreases when chromia is doped with silicon. It was proposed in section 6.4.2.2 that the growth mechanism for chromia scales grown on the A1-Si alloy is governed by outward chromium diffusion. Furthermore, the growth rate of chromia is almost independent of the oxygen activity (cf. Table 10), so the growth of the chromia scale on the A1-Si alloy is most likely governed by chromium interstitials (cf. chapter 5). Hence, the growth rate of chromia may decrease when the chromia scale is doped with silicon, since the concentration of interstitial chromium defects decreases. No experimental evidence exists, however, for a change in the defect chemistry of chromia after the substitution of silicon in the lattice, so this proposal cannot be validated. Instead, silica may act as a diffusion barrier for chromium diffusion, since the silica particles are positioned beneath the chromia scale at the alloy/chromia interface. The possible role of silica as a diffusion barrier is discussed in the following.

Although the micrograph in Fig. 35B indicates that silica is present as distinct particles, a thin dense film of silica may exist at the interface, or a dense layer of silica may form after further oxidation (cf. Fig. 45). Therefore, different models for the reduction in growth rate will be proposed for the case where silica forms a dense layer and for the case where silica forms distinct oxide precipitates near the interface. The proposals will be discussed in relation to the observed weight changes of the A1-Si specimens (cf. Table 10).

6.4.2.3.2 Dense silica layer

If a dense layer of silica is formed beneath the chromia layer, silica may act as a diffusion barrier for the continued growth of chromia. Such a diffusion barrier may affect the continued oxidation of the alloy in different ways. Several growth mechanisms for the continued growth of chromia have been proposed [68-71,118,120]. The continued growth of the chromia scale may occur while (i) the

growth of silica has ceased, or (ii) the growth of silica continues. This will be discussed in the below. The oxidation process is shown schematically in Fig. 46.

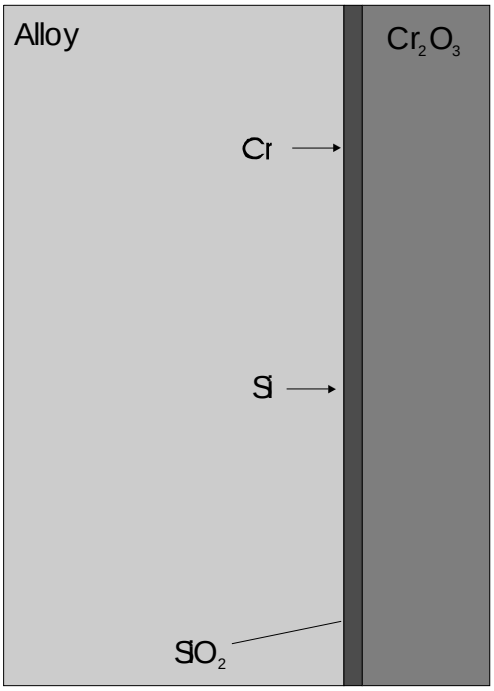

Fig. 46. A diagram of the oxidation of an alloy after the formation of a dense silica layer. The possible chromium and silicon diffusion from the alloy is indicated.

The flux of chromium through the dense silica layer may be obtained by combining Eq. 7 and Eq. 9

$$J_{Cr} = -\frac{\left[Cr_{SiO_2}\right]D_{Cr}}{kT}\frac{d\mu_{Cr}}{dx} \qquad \text{Eq. 91}$$

where the concentration of chromium is related to the solubility of chromium in silica [121], x is the thickness of the silica layer, and D_{Cr} is the chromium diffusion coefficient in silica during the oxidation [100,121]. Eq. 91 can also be written [100,121]

$$J_{Cr} = \frac{\left[Cr_{SiO_2}\right]D_{Cr}}{x}\frac{3}{4}\ln\left(\frac{pO_2^{//}}{pO_2^{/}}\right) \qquad \text{Eq. 92}$$

where $pO_2^{/}$ is the oxygen pressure at the alloy/silica interface, and $pO_2^{//}$ is the oxygen pressure at the silica/chromia interface.

During long term oxidation of a chromia forming alloy containing silicon, the growth of the silica layer beneath the chromia scale may cease [69]. The continued oxidation of the alloy is governed by the growth of chromia, where the growth of chromia may be limited by chromium diffusion through the silica layer. The diffusion of chromium through vitreous silica is very slow [100,121]. This is caused by the absence of high diffusivity paths such as grain boundaries. As described in Eq. 91 and Eq. 92, the

chromium flux through the silica layer is constant if the thickness of the silica layer and the boundary conditions for chromium at the silica interfaces remains constant. The constant chromium flux is caused by a constant driving force for chromium diffusion through the silica layer. In this case, the growth rate of the chromia scale is constant, i.e.

$$\frac{dx}{dt} = K \qquad \text{Eq. 93}$$

were K is a constant. This mechanism applies for long term oxidation, where the growth of silica has ceased. Furthermore, a constant growth rate for chromia has not been observed in the literature, so the present mechanism for the continued growth of chromia is probable not applicable for this study.

Instead of a constant silica thickness, the silica layer may grow according to a parabolic rate expression [84]. In this case, the flux of silicon from the alloy is high enough to balance the flux of silicon in the oxide (cf. Eq. 89). It follows that the oxygen activity at the alloy/silica interface is given by the decomposition pressure of silica in the alloy. Furthermore, the oxygen activity at the silica/chromia interface is given by the decomposition pressure of chromia. The continued oxidation of the alloy containing silicon, after the establishment of a growing silica layer, may be governed by the growth of a chromia layer. The growth of chromia may be limited by chromium diffusion through the growing silica layer. In this case, chromia is growing according to a parabolic rate law, if silica is growing according to a parabolic rate law [100]. If the silica layer is growing according to a parabolic rate law, the oxygen partial pressure at the alloy/silica interface is given by the decomposition pressure of silica in the alloy, as mentioned. This oxygen partial pressure is too low for the oxidation of chromium [70]. This implies that it is not possible for chromium ions to enter and diffuse though a dense layer of silica during the parabolic growth of the silica layer [70,120]. If the growth of chromia continues in this case, chromium must instead diffuse through micro cracks in the silica layer. In this case, the growth of chromia may become limited by the transport of chromium through the micro cracks. A thin silica layer, which was formed beneath a chromia during the oxidation of a ferritic iron-chromium steel [113], was investigated by TEM during the study. The TEM examinations revealed that the silica layer was pure, i.e. without micro cracks and without chromium and iron. Thus, it is unlikely that the growth of chromia continues after the formation of a dense growing layer of silica.

In contrast to the oxidation mechanisms, where the continued growth of chromia is limited by the transport of chromium through silica, the continued oxidation may be determined by the growth of silica. Such a growth mechanism have been proposed in the literature for the oxidation of iron-chromium alloys, which formed a dense layer of silica [68,70,120].

The growth mechanism of silica is not fully understood [84]. However, it is governed by a diffusion limiting mechanism, which gives rise to a parabolic rate constant. If the oxidation becomes governed by the growth of silica, silica will grow beneath a chromia layer. In this case, the alloy can be viewed as a silica forming alloy, and the chromia layer can be seen as a result of the transient oxidation period. The transient oxidation period for alloys is generally very short, but a considerable layer of dense

chromia scale may form before a dense silica scale is formed beneath chromia in this case [117]. After the formation of a dense silica layer, the chromia layer is separated from the alloy, and the continued growth of chromia ends. In this case, the oxygen potential gradient across the chromia layer will vanish, and the oxygen partial pressure at the silica/chromia interface becomes the oxygen activity in the reaction atmosphere. The parabolic rate constant of silica is considerable lower than the corresponding value for the growth of chromia [70], so the rate of weight gain during oxidation of the alloy will decrease considerably if the oxidation becomes dominated by the formation of silica during the oxidation. Such a rapid decrease in the growth rate during the oxidation of ferritic iron-chromium alloys containing silicon has previously been observed [68,70].

In summary, if the alloy forms a dense layer of silica beneath the chromia layer, the continued oxidation of the alloy is governed by the growth of silica. This will result in a rapid decrease in the parabolic rate constant. Such a reduction is not observed in this work (cf. Table 10). Furthermore, it will be shown in chapter 8 that the oxidation of the A1-Si specimens can be described by a single parabolic rate constant. Hence, as indicated by the micrograph in Fig. 35B, a dense layer of silica is not formed, and this oxidation mechanism is not applicable for the present study.

Instead, the growth rate of the chromia scales grown on the A1-Si alloy must decrease as a result of the formation of distinct silica particles at the alloy/chromia interface. This will be discussed below.

6.4.2.3.3 Porous silica layer

It is shown in Fig. 35B that silica was formed as distinct oxide particles during oxidation of the A1-Si specimen. Areas of contact still exist between the chromia scale and the alloy. However, a decrease in weight gain was still observed (cf. Table 10) as an effect of the silicon addition. Different causes for the effect of discrete silica particles on the reduction in growth rate of chromia may be proposed. Two postulates are put forward to explain how discrete silica particles can reduce the growth rate of chromia

- Diffusion barrier for chromium in the alloy
- Diffusion barrier for chromium in the oxide scale

The oxidation process is shown schematically in Fig. 47.

A possible cause for the reduced growth rate of chromia could be due to silica particles reducing the cross sectional area in the alloy for outward chromium transport. It is proposed that the silica particles act as diffusion barriers in the alloy and thereby reduce the oxidation rate. As discussed in chapter 5, the growth of chromia on the A1 alloy was limited by diffusion of reactants in the oxide. In contrast, the proposed mechanism for the effect of silica implies that the limiting step during the oxidation changes from diffusion in the oxide, to transport of chromium in the alloy. Such a change may in principle occur if a cross section of the alloy is sufficiently blocked by silica precipitates, stopping outward chromium diffusion.

However, the SEM micrograph of the cross section (cf. Fig. 35B) indicates that the area near the alloy/chromia interface only, is partly blocked by the silica particles.

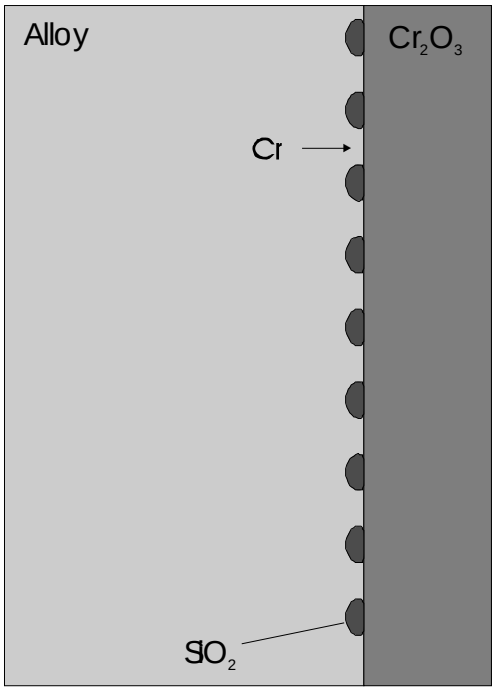

Fig. 47. A schematic of the continued oxidation of an alloy after the formation of a porous silica layer.

The limiting transport mechanism during the oxidation process may be obtained by examining the chromium depletion profile within the alloy [112]. In case the oxidation process is governed by transport in the oxide scale, the outward chromium flux from the alloy to the growing scale is adjusted such that it equals the flux of chromium in the oxide, i.e. such that the mass-balance at the alloy/chromia interface is satisfied. The flux of chromium in the alloy at the interface can be described by Fick's 1. law (cf. section 2.1)

$$J_{Cr} = -D_{Cr} \frac{dC_{Cr}}{dx} \qquad \text{Eq. 94}$$

where D_{Cr} is the diffusion coefficient of chromium in the alloy. Hence, if the oxidation is limited by transport of reactants within the chromia scale, the flux of chromium from the alloy at the interface is adjusted according to Eq. 94. This implies that the interfacial concentration of chromium in the alloy is adjusted such that the concentration gradient is given by the flux of chromium in the oxide. This gives rise to a relatively high interfacial concentration of chromium [9].

In contrast, if the growth of chromia is limited by transport of chromium in the alloy, the flux of chromium in the alloy is maximized, since the chromium, which diffuses to the interface, can be consumed by the oxidation reaction. A maximization of the chromium flux at the alloy/chromia interface implies that the interfacial concentration of chromium drops to almost zero in order to increase the outward flux of chromium through the alloy (cf. Eq. 94). Several EDX line scan analyses were performed on the

cross sections in the present work. None of the EDX analyses revealed a significant drop of the interfacial chromium concentration (cf. Fig. 41), albeit the resolution of the EDX analyser is not precise enough for measurements of the interfacial concentration. Furthermore, such a growth mechanism has to the author's knowledge not been observed in the literature for chromia forming steels.

A consequence of a near zero interfacial chromium concentration is that iron rich oxides becomes stable during oxidation. This will be discussed further in chapter 7. The EDX analyses of the cross sections did not reveal any iron in the scale.

To summarize, measurements of the interfacial content of chromium using EDX line scan analysis revealed that the interfacial content of chromium did not drop significantly, and that iron was not present in the scale. This indicates that the growth mechanism is governed by transport of reactants in the oxide. This is in agreement with the SEM micrograph of the cross section, which shows that the interface is only partly blocked by silica precipitates. Hence, the decrease in the oxidation rate for the specimens containing silicon is not caused by a diffusion blocking mechanism within the alloy.

Another cause for the reduced growth rate of chromia could be that silica acts as a chromium diffusion barrier in the chromia scale. As earlier discussed, silica is present near the alloy/chromia interface, but not within the chromia scale. The silica particles are positioned close to the alloy/chromia interface (cf. Fig. 35B), where some of the particles may be positioned *at* the interface, such that the alloy is separated from the chromia scale. Although silica does not block for chromium transport in the alloy, silica could be partially blocking transport across the alloy/chromia interface by reducing the cross sectional area of chromia. This may result in a reduced flux of chromium in the scale and hence a reduced growth rate of the chromia scale.

The growth of chromia is governed by grain boundary diffusion of chromium [31]. If parts of these high diffusivity paths are blocked at the alloy/chromia interface or within the scale, the growth rate of chromia may consequently be reduced. It is postulated that the silica particles are partially blocking the chromia grain boundaries at the alloy/chromia interface. As previously discussed, the silica particles are dragged along the alloy/chromia interface as the scale encroaches. During the oxidation process, the chromium atoms in the alloy are preferentially moving towards the grain boundaries in the chromia scale. It is plausible that the silica precipitates or silicon are dragged along with the diffusing chromium atoms such that they become positioned preferentially beneath the grain boundaries of the chromia scale. In this case, the silica particles could partly block the chromia grain boundaries for chromium transport.

Another possibility is that silica preferentially is formed near the grain boundaries as a result of the growth mechanism of chromia. The outward diffusion of chromium from the alloy creates vacancies near the interface during the oxidation. These vacancies will form preferentially beneath the grain boundaries of the chromia scale, since the chromium flux is highest here. Thus, nucleation of silica may preferentially occur at these vacancies beneath the grain boundaries of chromia [122].

In summary, silica may partially block the grain boundary transport of chromium in the scale. This proposal may explain why such a relatively small density of silica

particles at the interface has such a large impact on the growth rate of chromia. However, this proposal needs further investigation. TEM investigations at the interface are necessary in order to determine whether silica particles are positioned preferentially beneath grain boundaries of the chromia scale.

6.4.3 Oxidation of A1-CeSi

6.4.3.1 Microstructure

The morphology of the oxide scale and the cross section of the A1-CeSi alloy is shown in Fig. 34C and Fig. 36C, respectively. Small dark islands were observed at the alloy/scale interface of the A1-CeSi alloy. These islands were identified as silica using EDX line scan analysis of the cross sections (cf. Fig. 41C). Comparing with the A1-Si alloy, the content of silica beneath the chromia scale is low for the A1-CeSi alloy. This is due to the small concentration of silicon within the A1-CeSi alloy. The effect of the silicon addition on the microstructure has been discussed for the A1-Si alloy in section 6.4.2.

The SEM micrograph of the oxide morphology in Fig. 36C shows a low density of porosities within the scale of the A1-CeSi alloy. The oxide morphology may be compared to the morphologies of the A1-Si and A1-Ce alloys (cf. Fig. 35A,B). The oxide grown on the A1-Ce alloy appears to be denser and more adherent to the alloy than the oxide grown on the A1-CeSi alloy. The morphologies of the oxide scales formed on the A1-Si and A1-CeSi specimens are comparable. The results indicate that the content of cerium in the A1-CeSi alloy is too low for a beneficial REE on the oxide scale grown on the A1-CeSi specimens (cf. section 6.4.1).

The diffraction patterns in Fig. 39 and the EDX analysis in Fig. 41C for the A1-CeSi alloy show the presence of chromia in the scale. A low concentration of iron rich oxide (spinel structure), due to the transient oxidation period, is seen from the diffraction patterns of the oxides grown in the hydrogen/argon mixture (cf. Fig. 39).

The effect of the oxygen activity (hydrogen/argon vs. air) on the microstructure of the oxide scale was examined for the A1-CeSi alloy (not shown). The results obtained were similar to the results obtained for the A1 alloy in section 5.4.1. These observations have previously been described and discussed in section 5.4.1.

6.4.3.2 Oxidation kinetics

The weight gain of the A1-CeSi specimens is shown in Table 10. The weight gain of the A1-Si and A1-CeSi specimens was approximately the same. The presence of cerium in the A1-CeSi specimens had little effect on the microstructure of the chromia scale in comparison with the A1-Ce alloy. This indicates that the REE of

cerium in the A1-CeSi alloy is of minor importance for the oxidation behaviour. Thus, the content of cerium in the A1-CeSi alloy is not believed to have a large effect on the growth rate of chromia.

The reduction in the growth rate of chromia is most likely caused by the presence of silica precipitates at the interface. This result may seem surprising, since the density of silica precipitates near the interface is small for the A1-CeSi alloy. However, the result supports the proposal, where the silica precipitates are positioned preferentially beneath the grain boundaries of the chromia scale. Although the density of silica precipitates is small for the A1-CeSi specimens, the growth rate of chromia may be affected if the grain boundaries in the chromia scale are partially blocked for chromium transport at the alloy/chromia interface.

The effect of air and water vapour activity in the reaction atmosphere on the weight gain of the A1-CeSi alloy is shown in Table 10. The lower weight gain, when the specimens are oxidized in air and water vapour, is due to the vaporization of chromium species from the scale. The effect was described in section 5.4.2.2.

6.5 Summary

The microstructure and oxidation kinetics of the A1, A1-Ce, A1-Si and A1-CeSi alloys was studied. The oxidation behaviour was studied at 1173 K in various reaction atmospheres.

The addition of cerium improved the adhesion of the chromia scale and decreased the growth rate of chromia. This effect of cerium is known as the “reactive element effect”, as described in section 6.4.1. It was observed, however, that the minimum content of cerium in the alloy should be 0.3 at.% in order to observe a significant effect of the cerium addition. Thus, the addition of RE to alloys may have a beneficial effect on the oxidation behaviour of interconnector materials for the use in SOFC’s.

The addition of silicon decreased the weight gain of the iron-chromium alloy, even though a dense silica layer did not form. The silica particles formed beneath the external chromia scale as a result of internal oxidation. The growth rate decreased after the addition of a low concentration of silicon. It was proposed that the silica precipitates were positioned preferentially beneath the grain boundaries of the chromia scale, blocking part of the chromia grain boundaries for outward chromium diffusion. Although the formation of a dense silica layer would be detrimental for the electrical conductivity across the interconnector plate, the formation of distinct silica precipitates may not affect the electrical conductivity significantly. Thus, small silicon additions to ferritic iron-chromium alloys may prove to be beneficial for the use as interconnector material in SOFC stacks.

During the lifetime operation of a SOFC stack, the temperature will often be cycled between room temperature and the operational temperature. This temperature cycling increases the likelihood of cracking the chromia scale during growth [64,114]. The cracking of the chromia scale during oxidation may lead to an extensive breakaway oxidation of the alloy. The breakaway oxidation is discussed further in chapter 7.

Which effects do the cerium and silicon alloying additions have on the corrosion resistance of the ferritic iron-chromium alloy during thermal cycling oxidation?

The addition of cerium or other RE improves the adhesion of the chromia scale. This effect is particularly important during thermal cycling oxidation where the addition of RE decreases the tendency for oxide spallation [80,87].

The oxidation behaviour of silicon containing alloys has also been examined during thermal cycling [80,84,101,114,120]. It has been observed that silica has a detrimental effect on the spallation resistance for the chromia scale, particularly in cases where silica has formed a dense layer beneath the chromia layer [116]. This may be caused by (i) relative differences in the thermal expansion coefficient between silica and the alloy or between silica and chromia [84]; (ii) poor interfacial bonding between alloy/silica or silica/chromia [84,101]; (iii) volume changes associated with phase changes of silica [80,101]. Thus, although the addition of silicon decreases the growth rate of chromia, the formation of silica beneath chromia may be detrimental for the corrosion resistance of alloys during thermal cycling oxidation.

It may be interesting to examine other alloying additions than silicon, but with similar beneficial properties for the growth rate of chromia. Such an alloying addition could be aluminium. Aluminium forms an external alumina scale during oxidation if the content of aluminium in the alloy is sufficiently high [10]. Alumina forming alloys cannot, however, be used as an interconnector material in a SOFC stack, since alumina has a very low electrical conductivity [58]. Stott and Wei [117] have examined the effect of adding small amounts of aluminium to a ferritic iron-chromium alloy. They found that alumina forms internally beneath chromia. However, the alumina forms in a wide band in the alloy beneath the chromia scale in contrast to silica, which formed near the alloy/chromia interface. Thus, aluminium does not easily form a dense electrical isolating layer of alumina beneath the chromia scale, since the alumina precipitates are formed inward in the alloy matrix [117]. The formation of alumina beneath chromia may block some of the grain boundaries in chromia for outward chromium transport. Stott and Wei [117] have compared the effect of adding silicon and aluminium on the growth rate of a ferritic alloy. They found that the growth rate of chromia decreased with either alloying addition, and that the addition of silicon gave the lowest weight gain of the alloy during oxidation. This result is in support of the proposed effect of silica in the present work, since silica is formed close to the alloy/chromia interface, while alumina is formed over a wider band. Hence, silica can more effectively block the chromia grain boundaries. It can be speculated that alumina reacts with chromia at the alloy/chromia interface, since alumina and chromia form a solid solution corundum-type oxide [123]. However, a mixed oxide is usually not observed at the interface, since the dissolution and interdiffusion between the two oxides is very slow [68].

Alumina is more spallation resistant during thermal cycling than silica [84]. This may be due to a better match of the relative differences in the thermal expansion coefficients between alumina and the alloy in comparison with the alloy/silica system [84]. Thus, the addition of a small amount of aluminium to ferritic alloys may be interesting for the potential use as interconnector material in a SOFC stack, although the addition of silicon results in the lowest growth rate for chromia.

7 The effect of temperature and oxidation time

7.1 Introduction

The oxidation behaviour of the alloys oxidized at 1173 K for 70 h in various reaction atmospheres has been described and discussed in chapter 5 and 6. The oxidation behaviour of the alloys was also studied at 973 K and 1373 K in order to examine the effect of the temperature. Furthermore, the effect of the oxidation time was examined by oxidizing specimens for three weeks (504 h) at 1173 K in a hydrogen/argon mixture. These results are presented and discussed in the present chapter.

7.2 Experimental

The alloys studied in this chapter are given in Table 8, where the composition is given in atomic percent.

Alloy	Composition in at.%			
	Fe	Cr	Si	Ce
A1	Bal.	22	--	--
A1-Si	Bal.	21.9	0.3	--
A1-Ce	Bal.	21.9	--	0.3
A1-CeSi	Bal.	21.9	0.15	0.15

Table 13. The compositions of the alloys, which were examined in the present chapter.

The specimens were either oxidized at 973, 1173 or 1373 K for various times. The reaction atmospheres were either air or a 7%H_2/93%Ar mixture containing various amount of water vapour. The test conditions are summarized in Table 14.

Table 14. Test conditions for the specimens given in Table 8.

Temperature / K	Gas	Dwell time / h	$p(O_2)$ / bar	$p(H_2O)$ / bar
973 K	7%H_2/93%Ar	70	$4.3\cdot10^{-23}$	0.012
973 K	7%H_2/93%Ar	70	$5.5\cdot10^{-21}$	0.122
973 K	Air	70	0.21	0.012
973 K	Air	70	0.21	0.122
1373 K	7%H_2/93%Ar	70	$2.7\cdot10^{-15}$	0.012
1373 K	7%H_2/93%Ar	70	$3.5\cdot10^{-13}$	0.122
1373 K	Air	70	0.21	0.012
1373 K	Air	70	0.21	0.122
1173 K	7%H_2/93%Ar	504	$1.6\cdot10^{-18}$	0.012
1173 K	7%H_2/93%Ar	504	$2.0\cdot10^{-16}$	0.122

The surface of the oxide scales was examined using SEM and EDX analysis after the oxidation, in order to elucidate the microstructure and the chemical composition of the oxide scales. The crystallographic phases of the oxide scales were determined using XRD obtained at room temperature.

Polished cross sections of the specimens were prepared in order to investigate the growth behaviour and oxide morphology of the specimens. The polished cross sections of the specimens were examined using SEM and EDX analysis.

The composition of thin oxide scales formed at 973 K was determined using AES. The oxide scales were ion etched in order to obtain a depth profile of the chemical composition through the oxide scales.

The experimental details are given in chapter 4.

7.3 Results

7.3.1 Oxidation at 973 K

The scales grown at 973 K for 70 h consisted of a very thin layer of oxide. The diffraction patterns of the A1 specimens are shown in Fig. 48 as an example. The figure barely shows the existence of reflections from a corundum-type oxide for the scales grown in hydrogen/argon.

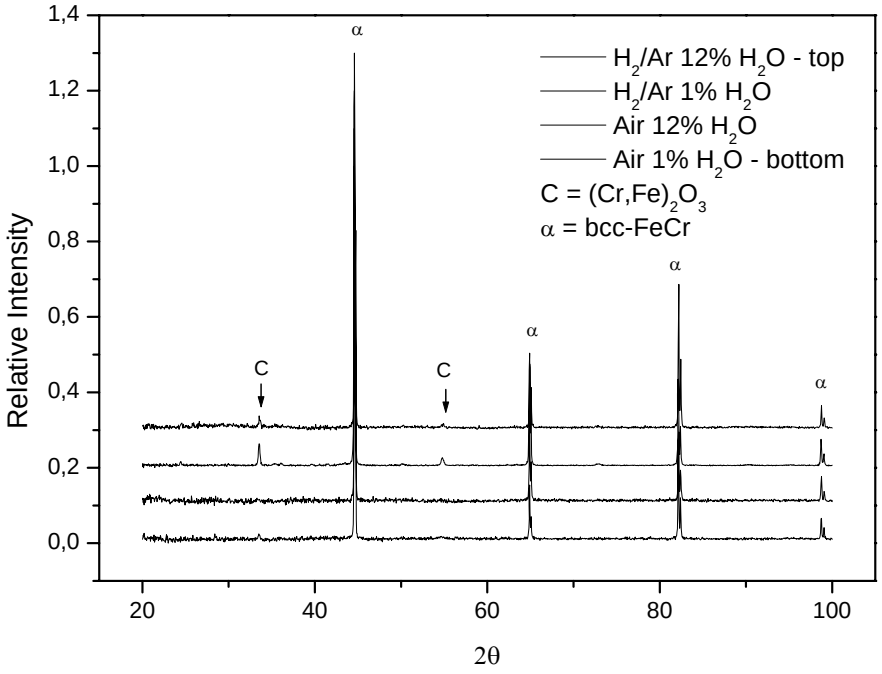

Fig. 48. Diffraction patterns of the oxide scales grown on the A1 alloy at 973 K for 70 h in different atmospheres.

The diffraction patterns obtained for the other oxide scales grown at 973 K (not shown) are similar to the results obtained for the A1 alloy (cf. Fig. 48).

The EDX analysis was ineffective for measuring the composition of the surface and cross sectional area of the oxides grown at 973 K because the oxide scales were too thin. Thus, AES depth profiling was utilized in order to determine the chemical composition of the oxide scales instead. The depth profile of the A1-Si specimen oxidized at 973 K for 70 h in hydrogen/argon containing 1% water vapour is shown in Fig. 49. Different depth profiles were measured at various spots on the specimen, but gave qualitatively similar results. The relative atomic concentrations were obtained by measuring the relative peak-to-peak heights of the intensities, and by using the relative sensitivity factors [124]. Details are given in [125]. The etch rate, for the equipment used in this study, was calibrated on SiO_2. The etching rate must, however, be calibrated on a standard similar to the oxides formed in this study, in order to convert the etch time to etch depth. Furthermore, the oxide scales were examined in order to obtain the chemical composition through the oxide scale. Thus, the relative concentrations are given as a function of sputter time in this work. The depth profile shows that the thin oxide consists of chromium oxide containing a small amount of iron. Silicon was not detected near the alloy/scale interface of the specimen. Similar depth profiles were obtained of other specimens oxidized at 973 K.

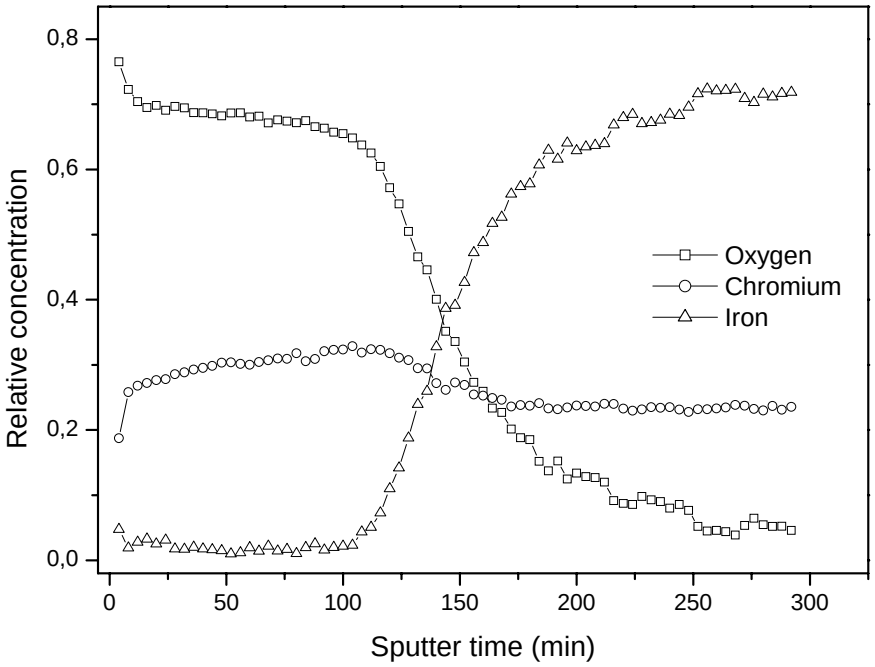

Fig. 49. AES depth profile of scale grown on the A1-Si specimen oxidized at 973 K for 70 h in hydrogen/argon containing 1% water vapour. The relative concentrations are given as a function of sputter time.

7.3.2 Oxidation at 504 h

7.3.2.1 Oxide morphology

The micrographs of polished cross sections of specimens oxidized for 504 h are shown in Fig. 50 and Fig. 51. The oxide scales were formed on A1-Ce (A), A1-Si (B), A1-CeSi (C) and A1 (D1-D2). The oxide scales were either grown in hydrogen/argon containing 1% (A,B,C,D1) or 12% water vapour (D2).

The oxide scale formed on the A1-Ce specimen is dense and adherent. The oxide scales grown on the A1-Si and A1-CeSi specimens are not as dense as observed in Fig. 50A. Both specimens show the presence of black particles near the alloy/scale interface. Previously in chapter 6, these particles were identified as silica. The content of silica precipitates near the interface is obviously lowest for the A1-CeSi specimen. The oxide scale grown on the A1 specimen in 1% water vapour (cf. Fig. 51D1) shows the presence of a relatively thick oxide scale. Porosities are present within the scale and at the alloy/scale interface.

Two different types of oxide morphologies are observed at the surface of the A1 alloy oxidized in hydrogen/argon containing 12% water vapour. A thick oxide is observed in Fig. 52 (left) in one region of the surface near an edge of the specimen, while a thin oxide is observed in Fig. 52 (right) for the rest of the specimen (similar to the surface of the specimen oxidized in 1% water).

A cross section of the thick oxide in Fig. 52 is shown in Fig. 51D2 for the A1 specimen. The morphology of the thin oxide (not shown) is similar to the specimen oxidized in 1% water vapour (cf. Fig. 51D1). The thick oxide is clearly divided into two regions, where the inner layer is more porous than the outer layer. Only a small amount of alloy can be recognized in Fig. 51D2 beneath the thick oxide. The cross sections of the other alloys oxidized for 504 h in hydrogen/argon containing 12% water vapour were also examined. However, the morphology of the specimens was similar to the results obtained for the specimens grown in 1% water vapour, so the cross section micrographs of the specimens oxidized in hydrogen/argon containing 12% water vapour are not shown.

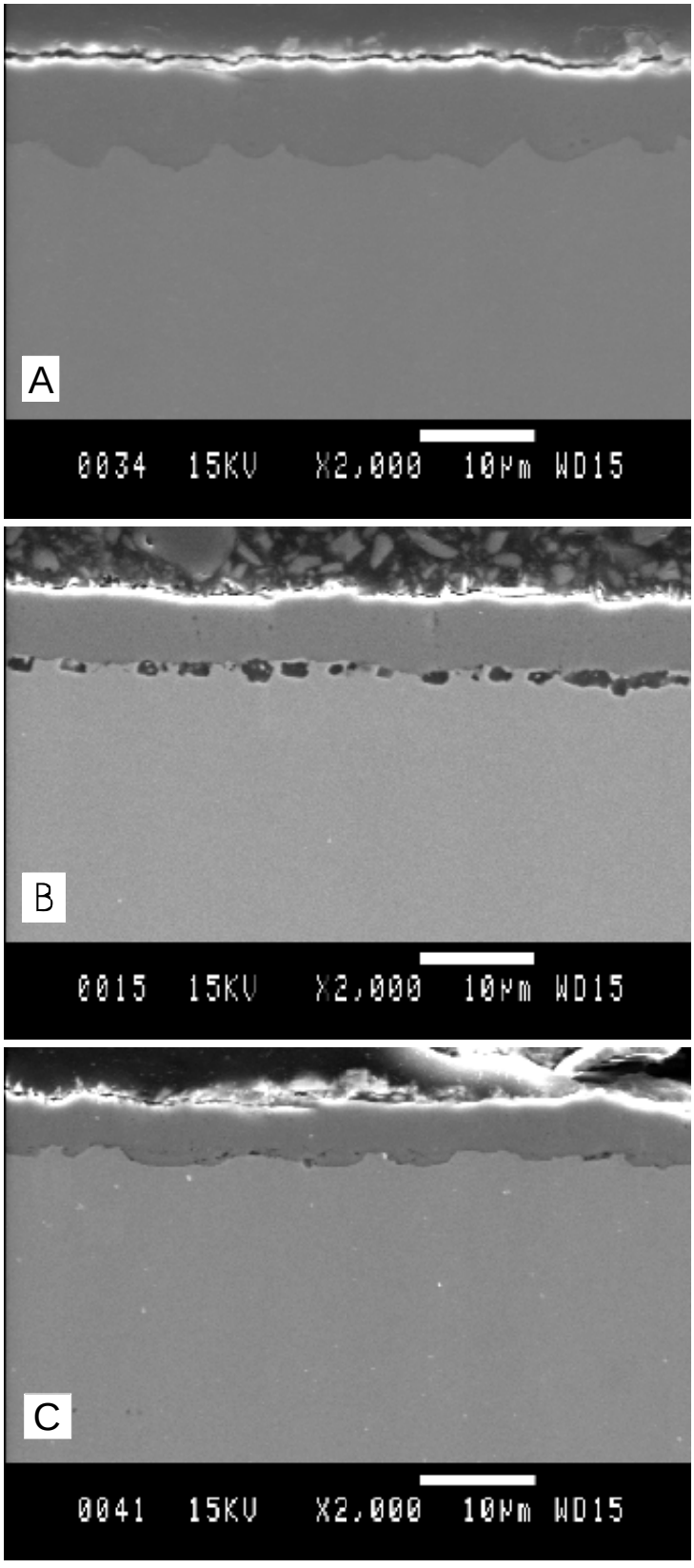

Fig. 50. SEM micrographs of cross sections of scales grown on A1-Ce (A), A1-Si (B) and A1-CeSi (C). The specimens were oxidized in hydrogen/ argon containing 12% water vapour at 1173 K for 504 h.

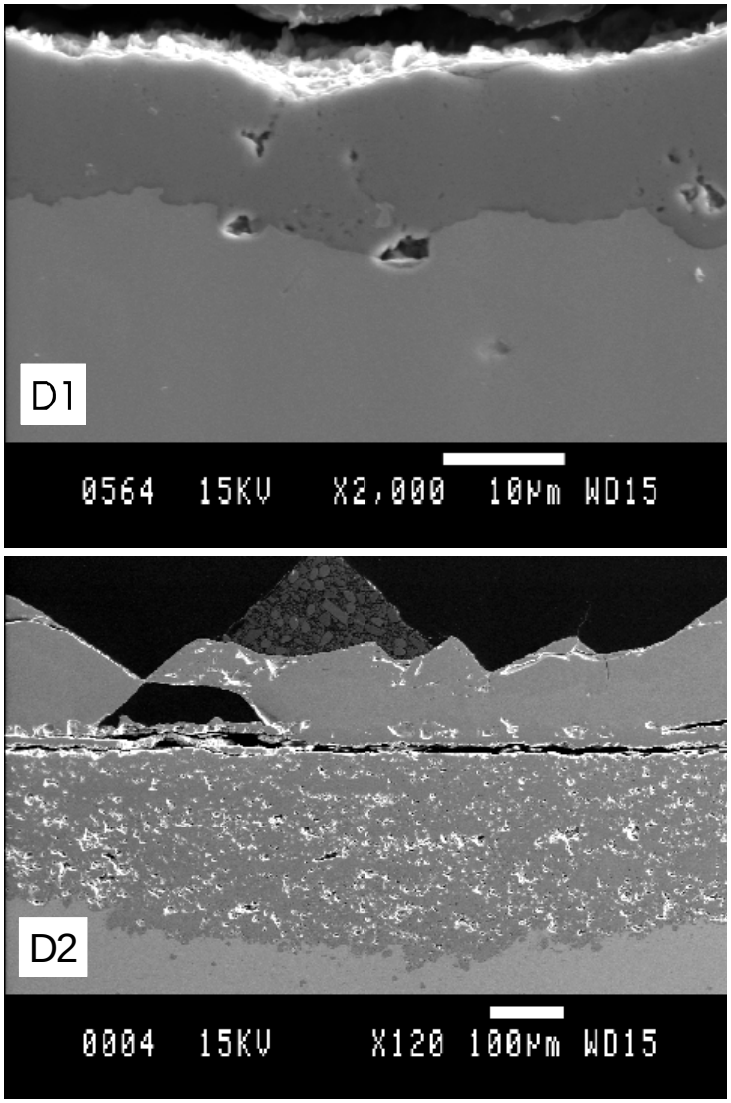

Fig. 51. SEM micrographs of cross sections of scales grown on the A1 alloy. The specimens were oxidized in hydrogen/argon containing 1% water vapour (D1) or 12% water vapour (D2) at 1173 K for 504 h.

Fig. 52. Light-optical micrograph of the surface of the oxide scale grown on A1 at 1173 K for 504 h, in hydrogen/argon containing 12% water vapour. The thick oxide is shown on the left, while the thin oxide is shown on the right.

7.3.2.2 XRD analysis

The diffraction patterns obtained of the oxide scales grown at 1173 K for 504 h are shown in Fig. 53 and Fig. 54. The oxide scales were grown in hydrogen/argon containing 1% and 12% water vapour, respectively. The diffraction patterns of the scales grown in hydrogen/argon containing 1% water vapour (cf. Fig. 53) show the existence of oxides with the corundum-type structure (PDF #38-1479) and spinel-type structure (PDF #34-0140). The diffraction patterns of the oxide scales grown on the A1-Ce, A1-Si and A1-CeSi alloys in hydrogen/argon containing 12% water vapour (cf. Fig. 54) are qualitatively similar to the patterns in Fig. 53. However, the diffraction pattern obtained for the A1 specimen in Fig. 54 is different. Diffraction patterns were obtained for both parts (cf. Fig. 52) of the oxide scale grown on the A1 specimen. The diffraction pattern of the thick oxide is shown in Fig. 54, while the diffraction pattern obtained of the thin oxide (not shown) is similar to the pattern of the A1 specimen oxidized in 1% water vapour (cf. Fig. 53). The diffraction pattern of the thick oxide shows the existence of a spinel phase (PDF #34-0140), and a halite phase (PDF #06-0615) with low intensity.

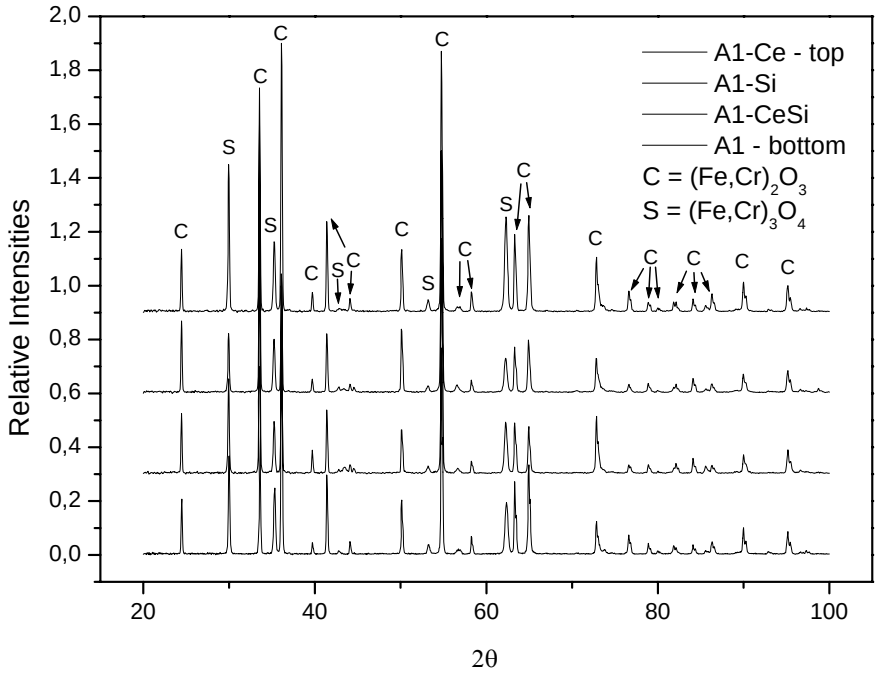

Fig. 53. Diffraction patterns of the oxide scales grown on different specimens. The oxide scales were grown at 1173 K for 504 h in hydrogen/argon containing 1% water vapour.

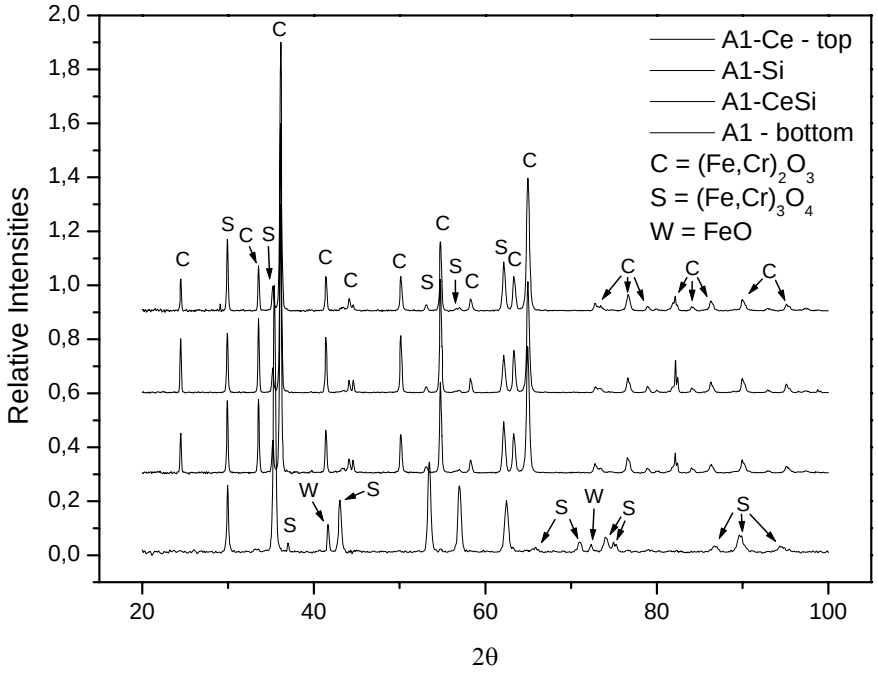

Fig. 54. Diffraction patterns of the oxide scales grown on different specimens. The oxide scales were grown at 1173 K for 504 h in hydrogen/argon containing 12% water vapour.

7.3.2.3 EDX analysis

The polished cross sections of the specimens (cf. Fig. 50 and Fig. 51) were analysed using EDX line scan analysis in order to obtain the chemical compositions of the oxide scales. The EDX line scan analyses of the oxide scales grown on the alloys A1-Ce (A), A1-Si (B), A1-CeSi (C) and A1 (D1-D2), are given in Fig. 55 (A-C) and Fig. 56 (D1-D2).

The EDX line scan analyses of the specimens oxidized for 504 h in hydrogen/argon containing 1% water vapour (A,B,C,D1) show the presence of chromium in the scale. However, a significant amount of iron is also present in the outermost part of the oxide scale. The presence of silica is clearly shown for the A1-Si alloy (cf. Fig. 55B), at the alloy/scale interface, while the concentration of silica in the A1-CeSi specimen was too small for detection. The A1-Ce and A1-CeSi specimens were analysed for the presence of cerium within the oxide scale and in the alloy beneath the oxide scale. It was not possible, however, to identify any cerium from the EDX analyses of the cross sections.

The composition of the thin oxide grown on the A1 alloy in 12% water vapour (cf. Fig. 52) is similar to the EDX analysis given in Fig. 56D1, while the line scan of the thick oxide (cf. Fig. 51D2) is given in Fig. 56D2. In Fig. 51B, the thick oxide scale consisted of two different types of oxides. This is also seen from the EDX analysis given in Fig. 56D2. The thick porous oxide closest to the alloy consists of an iron chromium oxide, while the outermost part of the oxide shows the presence of an iron oxide.

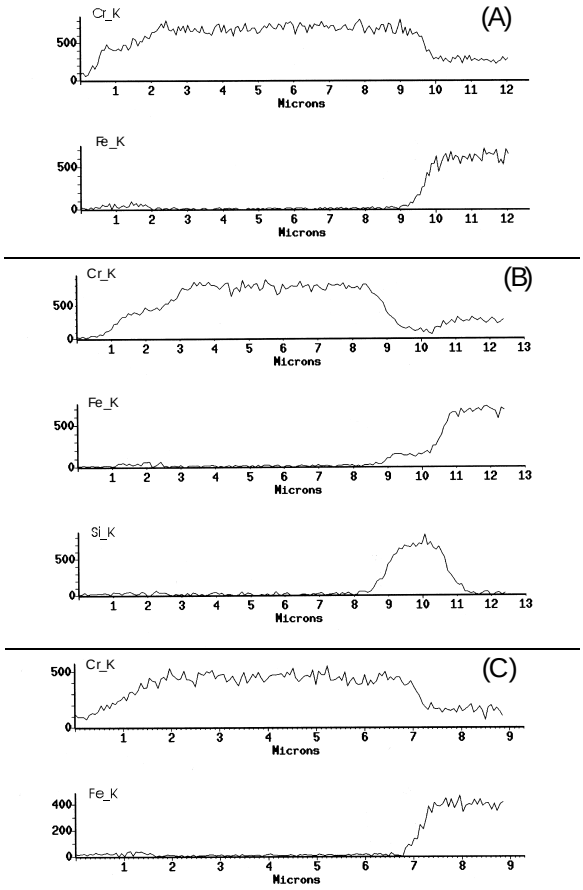

Fig. 55. EDX line scan analyses of cross sections of scales oxidized at 1173 K for 504 h in hydrogen/argon containing 1% water. The scales were grown on the alloys A1-Ce (A), A1-Si (B) and A1-CeSi (C).

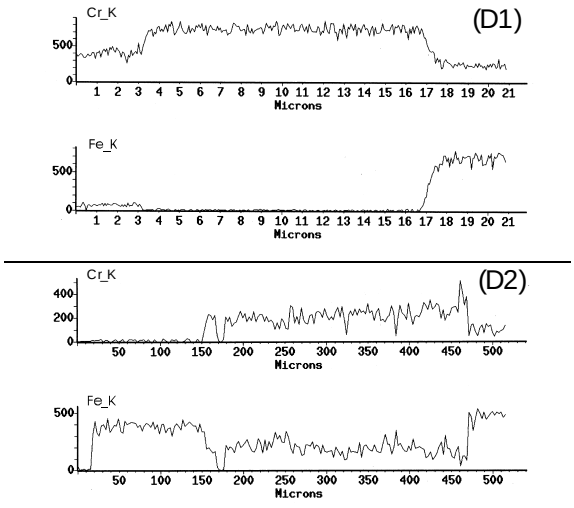

Fig. 56. EDX line scan analyses of cross sections of scales grown on the A1 alloy. The specimens were oxidized at 1173 K for 504 h in hydrogen/argon containing 1% (D1) or 12% water vapour (D2).

7.3.2.4 Gravimetric measurements

The weight gain of the specimens after oxidation for 504 h in the hydrogen/argon mixture containing various amount of water vapour is shown in Table 15. The measurement conditions are given in Table 14. The weight gains for each specimen were almost independent of the reaction atmosphere, although the specimens oxidized in hydrogen/argon containing 12% water vapour showed a small decrease in weight gain. The only discrepancy was observed for the A1 specimen oxidized in hydrogen/argon containing 12% water vapour. The large difference in weight gain is caused by the formation of the thick iron rich oxide on the specimen oxidized in 12% water vapour (cf. Fig. 52).

Table 15. Weight gain for the specimens oxidized at 1173 K for 504 h in different atmospheres. The composition of the specimens is given in Table 8, while the test conditions are summarized in Table 14.

$\Delta W/A$ [$mgcm^{-2}$]	A1-Ce	A1-Si	A1-CeSi	A1
H_2/Ar - 1%H_2O	2.02	1.33	1.31	2.75
H_2/Ar - 12%H_2O	1.60	1.10	0.84	10.5

The weight gains of the alloys containing silicon and/or cerium may be compared to the weight gain of the A1 specimen. The results in Table 15 show that the weight gain of the specimens decreased after the addition of cerium and/or silicon to the alloy. As seen in Table 15, the addition of cerium to the iron-chromium alloy (A1) is the least effective in reducing the growth rate. The weight gains of the A1-Si and A1-CeSi specimens are approximately the same.

The parabolic rate constants were calculated for the specimens using Eq. 64. This was performed under the assumption that the growth of the oxide scales followed a parabolic growth mechanism. Furthermore, it was assumed that the formation of the iron rich oxide was negligible (cf. Fig. 55 and Fig. 56D1), and that the weight loss due to vaporization can be neglected. The parabolic rate constants are given in Table 16. The parabolic rate constant was not calculated for the A1 specimen oxidized in 12% water vapour. This is due to the formation of the thick oxide (cf. Fig. 52), which indicates that the oxidation behaviour is different for this specimen compared to the other specimens, since the oxide formation is different at different regions of the specimen (cf. Fig. 51). The parabolic rate constants in Table 16 may be compared to the rate constants obtained for the same alloys oxidized under similar conditions, but only for 70 h (cf. Table 11). It is seen that the parabolic rate constants obtained after different oxidation times are approximately identical.

Table 16. Parabolic rate constants. The rate constants were calculated from the weight gains given in Table 15 using Eq. 64.

k_w [$g^2cm^{-4}s^{-1}$]	A1-Ce	A1-Si	A1-CeSi	A1
H_2/Ar - 1%H_2O	$1.02 \cdot 10^{-12}$	$4.87 \cdot 10^{-13}$	$4.73 \cdot 10^{-13}$	$2.08 \cdot 10^{-12}$
H_2/Ar - 12%H_2O	$7.05 \cdot 10^{-13}$	$3.33 \cdot 10^{-13}$	$1.94 \cdot 10^{-13}$	--

7.3.3 Oxidation at 1373 K

7.3.3.1 Oxide morphology

The SEM micrographs of polished cross sections of specimens oxidized for 70 h at 1373 K in hydrogen/argon containing 1% water vapour are shown in Fig. 57 and Fig. 58. The oxide scales were grown on the A1-Ce (A), A1-Si (B), A1-CeSi (C) and A1 (D1) alloys.

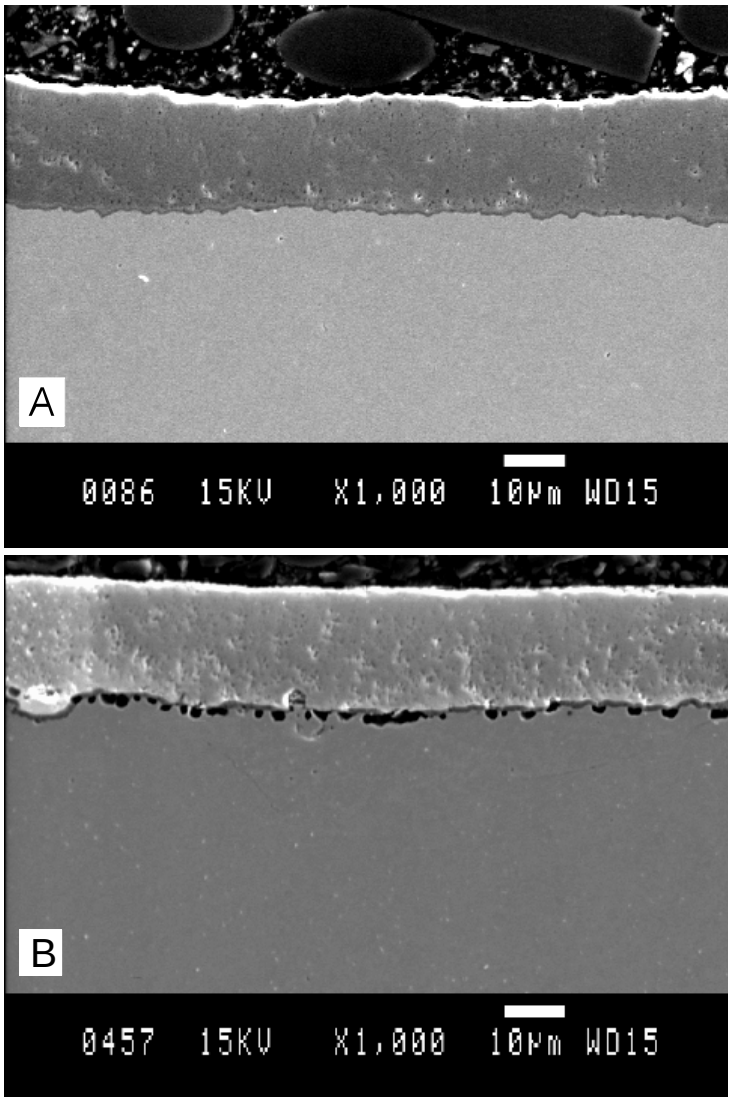

Fig. 57. SEM micrographs of cross sections of scales grown on A1-Ce (A) and A1-Si (B). The specimens were oxidized in hydrogen/argon containing 1% water vapour at 1373 K for 70 h.

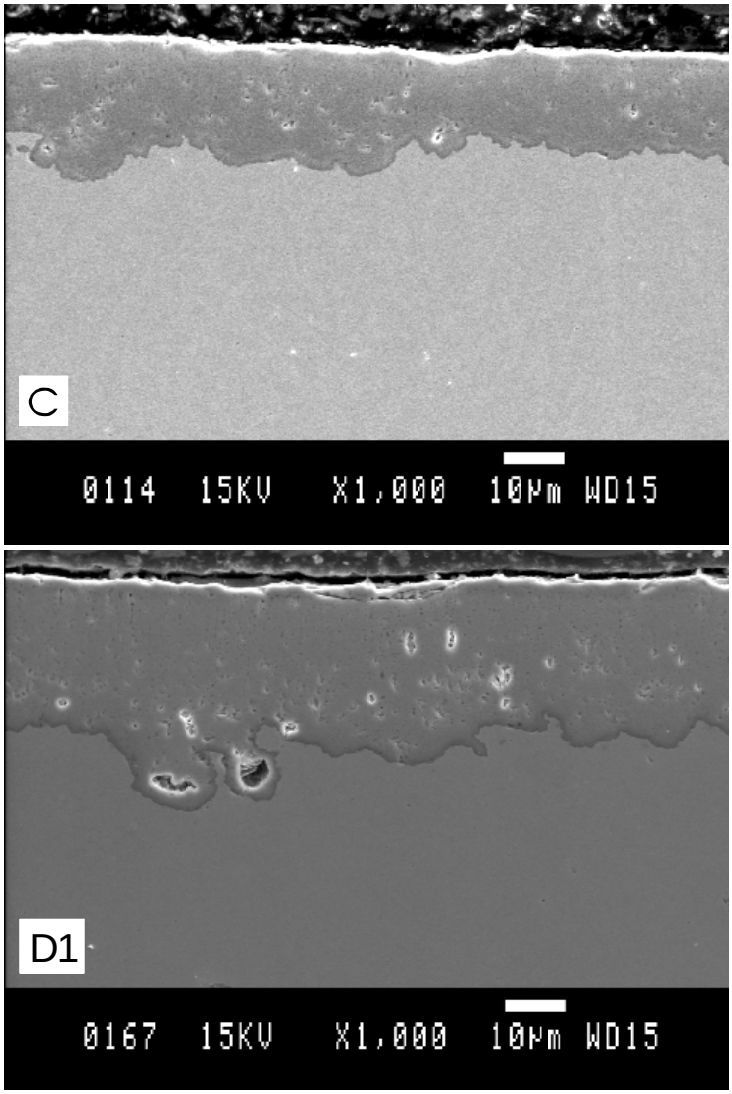

Fig. 58. SEM micrographs of cross sections of scales grown on A1-CeSi (C) and A1 (D1). The specimens were oxidized in hydrogen/argon containing 1% water vapour at 1373 K for 70 h.

The oxide scale grown on the A1 specimen (cf. Fig. 58D1) contains large voids at the interface. Furthermore, large porosities are present within the oxide scale. The scales grown on the A1-Ce and A1-CeSi specimens (cf. Fig. 57A and Fig. 58C) also contain porosities, albeit smaller than those present in the A1 specimen. It is evident that the oxide scales grown on the A1-Ce and A1-CeSi specimens are thinner than that grown on the A1 specimen. Small porosities can also be observed within the scale in Fig. 57B for the A1-Si specimen. Furthermore, a large content of silica precipitates can be observed at the alloy/oxide interface. The silica layer is nearly continuous, but areas of contact still exist between the alloy and the scale. The silica appears to be absent from the alloy/oxide interface in Fig. 58C.

The SEM micrographs of polished cross sections of scales grown on the A1 alloy are shown in Fig. 59. The specimens were either oxidized in hydrogen/argon containing 12% water vapour (D2), air containing 1% water vapour (D3) or air containing 12% water vapour (D4). In contrast to the specimen oxidized in hydrogen/argon containing 1% water vapour (cf. Fig. 58D1), the specimens shown in Fig. 59 exhibit an extensive oxidation with the formation of thick oxide layers. The thick oxides shown in Fig. 59 are clearly divided into two regions, where the inner layer is porous and the outer

layer is dense. A similar microstructure was observed in Fig. 51D2 for the A1 specimen oxidized in hydrogen/argon containing 12% water vapour for 504 h at 1173 K.

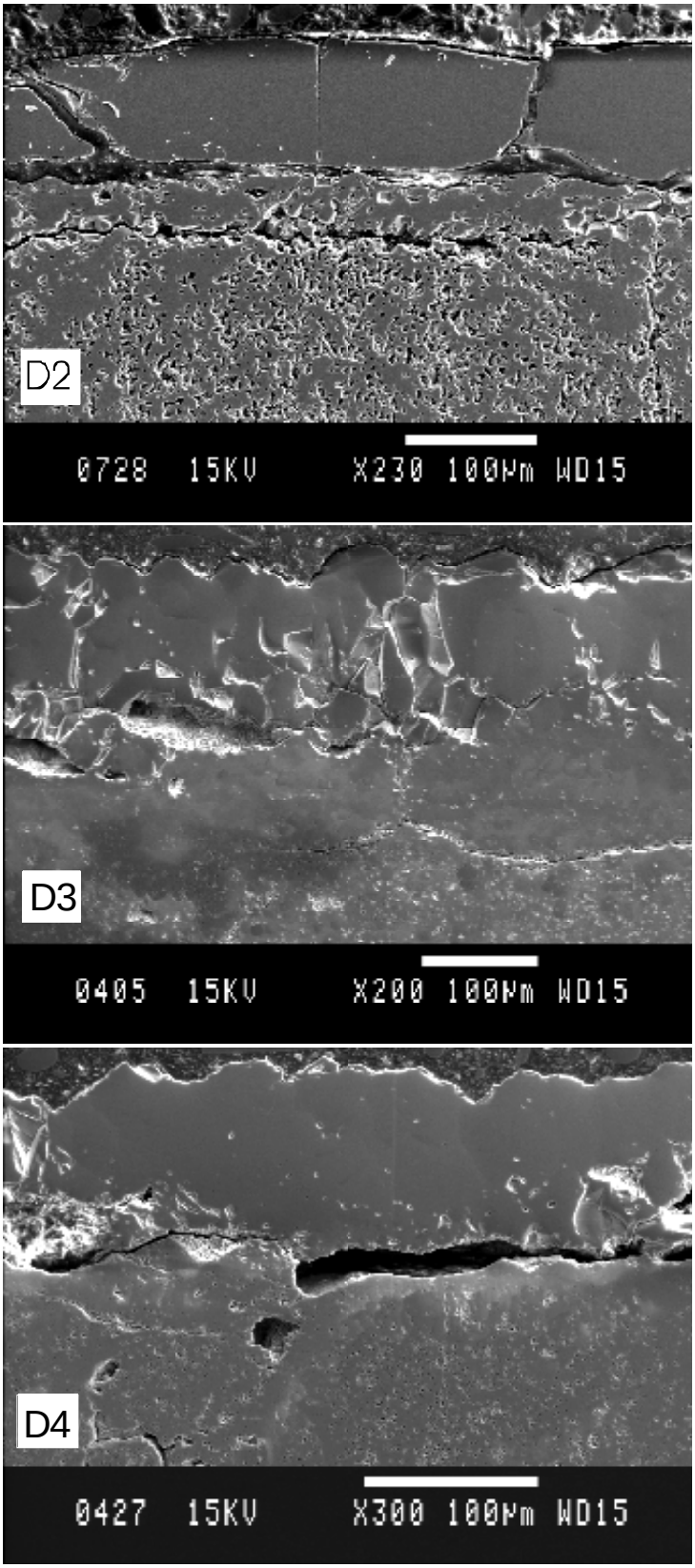

Fig. 59. SEM micrographs of cross sections of scales grown on the A1 alloy. The specimens were either oxidized in hydrogen /argon containing 12 % water vapour (D2), in air containing 1% water vapour (D3) or in air containing 12% water vapour (D4) at 1373 K for 70 h.

The polished cross sections were also prepared and examined for the other alloys (cf. Table 8) oxidized in hydrogen/argon containing 12% water vapour, and in air containing 1% or 12% water vapour (not shown). These specimens also showed extensive oxidation similar to the results given for the A1 alloy in Fig. 59. The only discrepancy was the A1-Si alloy oxidized in hydrogen/argon containing 12% water vapour, which showed a relatively thin oxide scale similar to the oxide scale grown in hydrogen/argon containing 1% water (cf. Fig. 57B).

The thick oxide completely covered the surface of certain specimens, and only partially covered specimens in other cases. In the latter case, the thick oxide was mostly present near edges and corners of the specimens. A micrograph of a cross section of the A1-Si specimen oxidized in air containing 12% water vapour is given in Fig. 60, as an example.

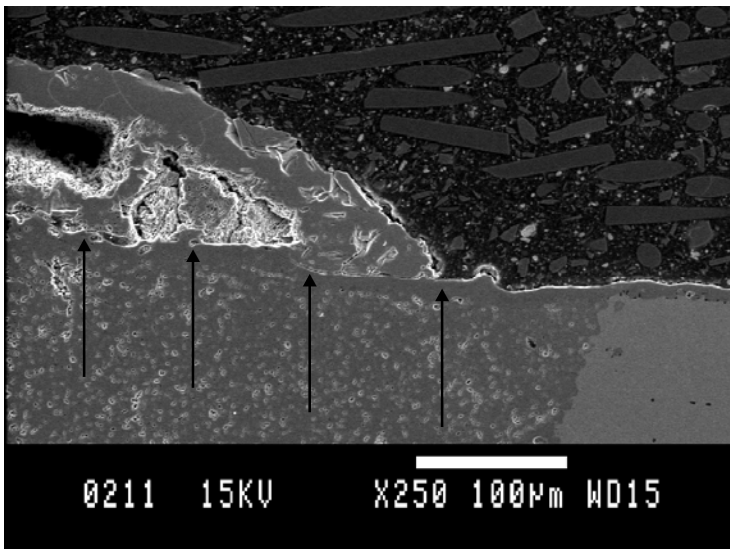

Fig. 60. SEM micrograph of cross section of the scale grown on the A1-Si alloy. The specimen was oxidized in air containing 12% water vapour at 1373 K for 70 h. The arrows indicate the original thin oxide from the right.

The specimen is partially covered with thick oxide. The thin oxide is observed on the right, while the thick oxide is seen on the left. The thin oxide scale can be followed from the right to the left into the thick oxide. The thin oxide layer separates the denser oxide at the top from the more porous oxide below. It was not possible to identify any correlation between the test conditions, type of specimen, and the fraction of specimen covered by thick oxide.

7.3.3.2 XRD analysis

The diffraction patterns obtained for the oxide scales grown at 1373 K for 70 h in hydrogen/argon containing 1% water vapour are shown in Fig. 61. The diffraction patterns of the scales show the existence of oxides with a corundum-type structure (PDF #38-1479) and a spinel-type structure (PDF #34-0140).

The diffraction patterns for the oxide scales grown on the A1 alloy are shown in Fig. 62. The oxides were grown at 1373 K for 70 h in hydrogen/argon containing 12%

water vapour, and in air containing 1% or 12% water vapour. The diffraction patterns for the scales grown in air show the existence of an oxide with the corundum-type structure for both specimens. In contrast, the diffraction pattern obtained for the specimen oxidized in hydrogen/argon containing 12% water vapour shows the existence of a spinel phase (PDF #34-0140), a halite phase (PDF #06-0615), and reflections from the ferritic alloy (PDF #06-0696) with low intensity.

The diffraction patterns were also obtained for the other specimens (A1-Ce,A1-Si,A1-CeSi) oxidized in hydrogen/argon containing 12% water vapour, and in air containing 1% or 12% water vapour (not shown). The diffraction patterns for these specimens were similar to the diffraction patterns given for the A1 alloy in Fig. 62. The diffraction patterns were obtained for the thick oxides on the specimens. The diffraction patterns for the thin oxides were similar to the diffraction patterns given in Fig. 61.

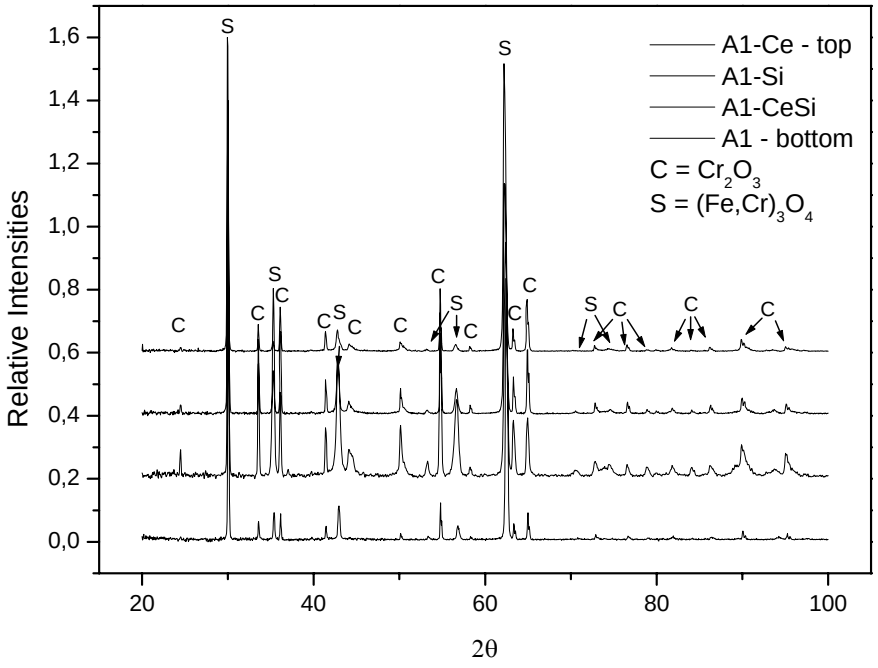

Fig. 61. Diffraction patterns for the oxide scales grown on different specimens. The oxide scales were grown at 1373 K for 70 h in hydrogen/argon containing 1% water vapour.

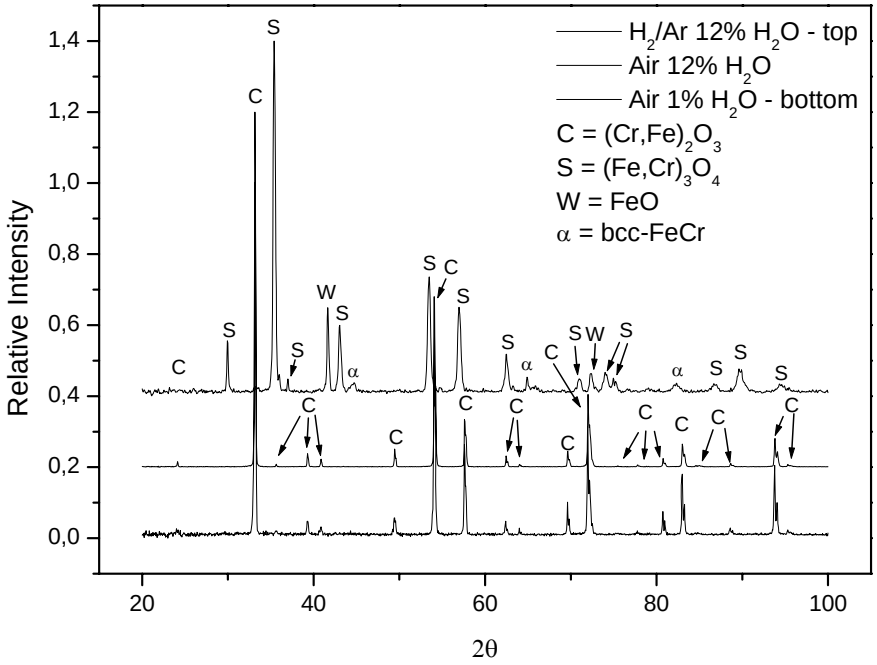

Fig. 62. Diffraction patterns of the oxide scales grown on the A1 alloy in air or in hydrogen/argon. The scales were grown at 1373 K for 70 h.

7.3.3.3 EDX analysis

The polished cross sections of the specimens (cf. Fig. 57-Fig. 59) were analysed using EDX line scan analysis in order to obtain the chemical compositions of the oxide scales. The EDX line scan analyses of the specimens oxidized in hydrogen/argon containing 1% water vapour at 1373 K for 70 h are given in Fig. 63 and Fig. 64D1.

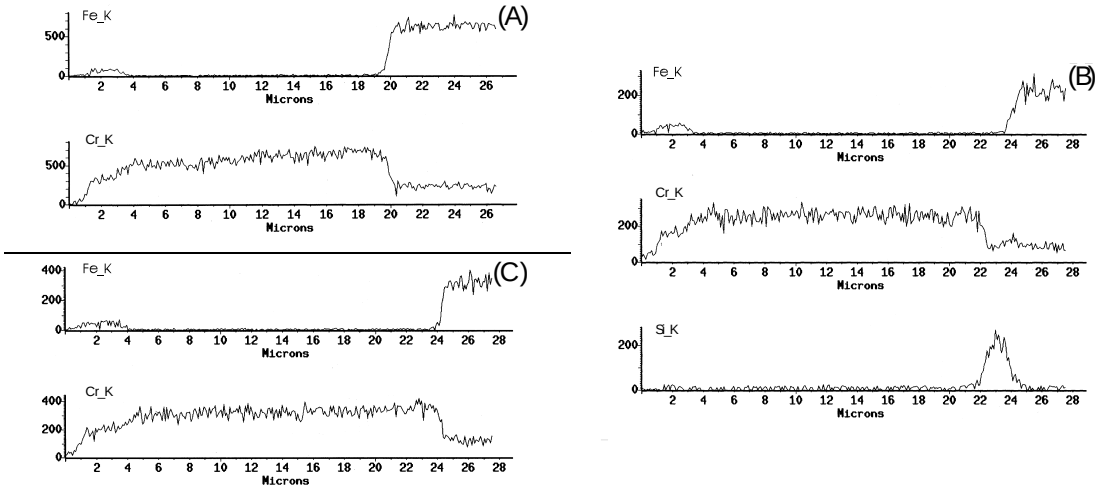

Fig. 63. EDX line scan analyses of cross sections of scales oxidized at 1373 K for 70 h in hydrogen/argon containing 1% water. The scales were grown on the A1-Ce (A), A1-Si (B) and A1-CeSi (C) specimens.

The oxide scales show the presence of chromium in the oxide scales. Furthermore, a significant amount of iron is present in the outermost region of the scales. The presence of silica at the alloy/scale interface is also seen for the A1-Si specimen (cf. Fig. 63B), while the content of silicon at the alloy/scale interface for the A1-CeSi specimen was very low. This difference was also observed from the SEM micrographs (cf. Fig. 57B and Fig. 58C).

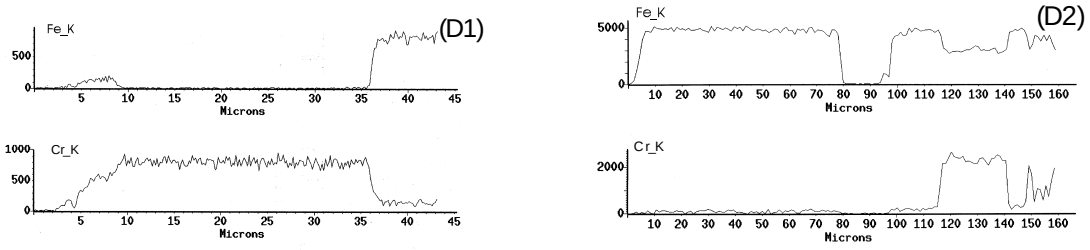

Fig. 64. EDX line scan analyses of cross sections of scales grown on the A1 alloy at 1373 K for 70 h in hydrogen/argon containing 1% water vapour (D1) and in 12% water vapour (D2).

The oxide scale grown on the A1 specimen in hydrogen/argon containing 12% water vapour (cf. Fig. 64D2), and in air containing 1% or 12% water vapour (cf. Fig. 65), consist of a thick iron rich oxide as the outermost oxide and a mixed iron-chromium oxide beneath. The different depths of the line scans shown in Fig. 63-Fig. 65 are caused by the varying oxidation behaviour shown in the micrographs in Fig. 57-Fig. 59. An absence of signals is seen in Fig. 64D2 and Fig. 65D4. This is due to the presence of large cracks between the oxide layers (cf. Fig. 58).

The other specimens oxidized in hydrogen/argon containing 12% water vapour, and in air were also examined using EDX analysis (not shown). The results obtained were similar to the results given for the A1 specimens.

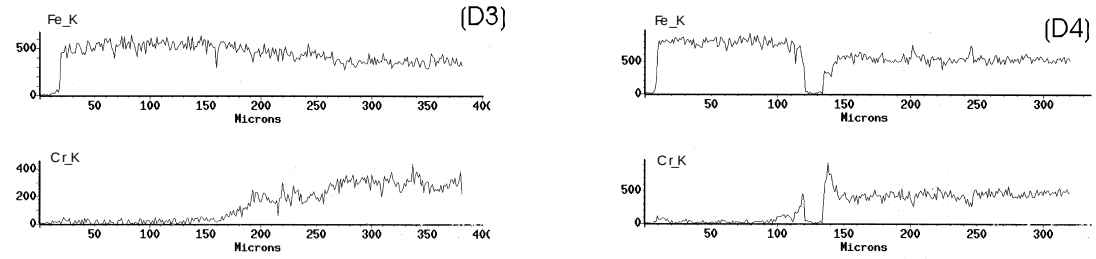

Fig. 65. EDX line scan analyses of cross sections of scales grown on the A1 alloy at 1373 K for 70 h in air containing 1% water vapour (D3) and in 12% water vapour (D4).

In Fig. 59 and Fig. 60, the thick oxide scale consisted of two different regions of oxides. These regions may be recognized from the EDX analyses in Fig. 64 and Fig. 65 (D2-D4). The thick porous oxide closest to the alloy consists of an iron chromium oxide, while the outermost denser oxide shows the existence of an iron rich oxide.

7.3.3.4 Gravimetric measurements

The weight gain of the specimens after oxidation is shown in Table 17. The measurement conditions are given in Table 14. The specimens oxidized in hydrogen/argon containing 1% water vapour clearly showed the lowest weight gain compared to the specimens oxidized in other reaction atmospheres. The large difference in weight gain is also seen from the SEM micrographs of the cross sections (cf. Fig. 58D1 and Fig. 59). Extensive oxidation was observed for all the specimens oxidized in hydrogen/argon containing 12% water vapour, and in air containing 1% or 12% water vapour. The only discrepancy was the A1-Si alloy oxidized in hydrogen/argon containing 12% water vapour, which exhibited a reduced growth rate in the formation of a protective oxide scale, as described in section 7.3.3.1. The weight gains for the specimens, which exhibit an extensive oxidation, differ. This is caused by an uneven formation of thick oxide on the sample surface. As mentioned in section 7.3.3.1, the thick oxide completely covered the surface of certain specimens, and only partially covered other specimens in other cases.

Table 17. The weight gain for specimens oxidized at 1373 K for 70 h in different atmospheres. The composition of the specimens is given in Table 8, while the test conditions are summarized in Table 14.

$\Delta W/A$ [$mgcm^{-2}$]	A1-Ce	A1-Si	A1-CeSi	A1
$H_2/Ar - 1\%H_2O$	3.29	3.16	2.52	4.45
$H_2/Ar - 12\%H_2O$	17.10	3.40	37.3	40.1
$Air - 1\%H_2O$	41.2	53.3	62.3	64.1
$Air - 12\%H_2O$	45.2	28.8	37.1	68.5

7.4 Discussion

7.4.1 Oxidation at 973 K

The oxide scales grown on the specimens at 973 K were thin. The oxide scales were identified as a corundum-type oxide using XRD (cf. Fig. 48). The identity of the corundum-type oxide was determined by AES depth profiles of the oxide scales. The depth profiles revealed that the corundum-type oxide was pure chromia (cf. Fig. 49).

The depth profile also showed the presence of a low concentration of iron. The specimens were ground with SiC abrasive paper (1000 grid) prior to the oxidation, thus the alloy/oxide interface may be bulky. This could result in an uneven thickness of the thin oxide scale. Thus, the iron may be detected from the alloy. Another possibility is that the iron is a result of transient oxidation of the specimens before a dense chromia layer has formed.

Due to the small growth rate of the oxide scales, the oxidation behaviour of the scales grown at 973 K will not be discussed further.

7.4.2 Oxidation at 1173 K for 504 h

The oxide scales grown for 504 h exhibit an increased weight gain compared to the scales grown for 70 h under similar conditions (cf. Table 15 and Table 10). Furthermore, in contrast to the specimens oxidized for 70 h, the EDX line scan analyses of the cross sections indicate the presence of iron in the outermost part of the oxide scales (cf. Fig. 55 and Fig. 56). Hence, the oxidation of the specimens oxidized for 504 h is not solely characterized by a steady state growth of chromia scales. Furthermore, part of the scale grown for 504 h in hydrogen/argon containing 12% water vapour on the A1 specimen shows an extensive corrosion, with iron rich oxides extending almost through the specimen (cf. Fig. 51D2 and Fig. 56D2). In contrast, the other specimens oxidized for 504 h showed a relatively small weight gain (cf. Table 15), and only formed a small amount of iron rich oxide (cf. Fig. 55 and Fig. 56). These observations will be discussed below.

7.4.2.1 Microstructure

The diffraction patterns obtained for the oxide scales grown on the specimens in hydrogen/argon for 504 h (cf. Fig. 53 and Fig. 54) show the presence of a corundum-type oxide and a spinel-type oxide. The only discrepancy was the diffraction pattern obtained for the thick oxide scale formed on part of the A1 specimen oxidized in hydrogen/argon containing 12% water vapour. This diffraction pattern showed the existence of a spinel-type oxide and a halite-type oxide (cf. Fig. 54).

The EDX line scan analyses (cf. Fig. 55 and Fig. 56) of the thin oxide scales showed that they consisted of chromium oxide with a small amount of iron-chromium oxide at the outermost region of the oxide scale. Thus, chromia is positioned closest to the alloy with an iron-chromium oxide as the outermost oxide. The diffraction patterns of the oxide scales indicate that the iron-chromium oxide is a spinel phase. This sequence of oxides in the oxide scale is in accordance with the phase diagram in Fig. 11, which shows that an iron-chromium spinel is in equilibrium with the reaction atmospheres (indicated in the phase diagram) and that chromia is thermodynamically more stable than the spinel phase. The amount of iron present in the EDX analyses is small, thus the concentration of the spinel phase is low. This can also be recognized from the diffraction patterns (cf. Fig. 53 and Fig. 54), where the reflections from the spinel phase have low intensities.

The EDX line scan analysis of the thick oxide scale grown in hydrogen/argon containing 12% water vapour (cf. Fig. 56D2) shows the presence of a pure iron oxide as the outermost oxide on top of an iron-chromium oxide. The only thermodynamically stable iron oxide, under the present experimental conditions, is wüstite, according to the phase diagram in Fig. 11. In contrast to the phase diagram,

the diffraction pattern shows the presence of a spinel phase together with a wüstite phase with low intensities (cf. Fig. 54). The reason for the low intensity of the wüstite phase may be understood considering the instability of the wüstite phase below ca. 843 K [126] (cf. Fig. 8). During cooling of the specimen to room temperature, most of the wüstite phase may have transformed to magnetite. This can explain the low concentration of wüstite in the diffraction pattern, which was obtained at room temperature. Thus, the outermost oxide in the thick oxide scale is magnetite containing a small amount of wüstite. The mixed iron-chromium oxide in the oxide scale is positioned closer to the alloy than the iron rich oxide (cf. Fig. 56D2), so the iron-chromium oxide is thermodynamically more stable than the iron rich oxide. This indicates that the mixed iron-chromium oxide has a spinel structure, according to the phase diagram in Fig. 11.

The effects of the cerium and silicon additions to the A1 alloy, on the microstructure were discussed in chapter 6, so it will not be discussed further in this chapter.

In contrast to the specimens oxidized for 70 h (cf. chapter 5 and 6), the specimens oxidized for 504 h show relatively large concentrations of iron in the outermost part of the scale (cf. Fig. 55 and Fig. 56), especially the A1 specimen oxidized in hydrogen/argon containing 12% water vapour. Hence, the presence of iron cannot only be attributed to the transient oxidation stage. Instead it must be caused by a formation of iron rich oxide after failure of the chromia scale. The mechanism for such a failure will be discussed in section 7.4.4.

7.4.2.2 Oxidation kinetics

The gravimetric data in Table 15 and the SEM micrographs in Fig. 50 and Fig. 51D1 indicate that the specimens do not show extensive corrosion. An exception, however, is the A1 alloy oxidized in hydrogen/argon containing 12% water vapour (cf. Fig. 51D2). Furthermore, the content of iron in the outermost region of the thin oxide scales was relatively small (cf. Fig. 55 and Fig. 56), and the scales are dense. It was observed in section 7.3.2.4 that the parabolic rate constants obtained for the specimens oxidized for 504 h (cf. Table 16), were approximately equal to the parabolic rate constants obtained for the same alloys oxidized for 70 h under similar conditions. This indicates that the oxidation of the specimens oxidized for 504 h can be described by a similar parabolic growth mechanism.

Despite the parabolic growth of the specimens, however, a small but significant amount of iron is present in the outermost region of the oxide scales. It is proposed that the iron rich oxides have formed after failure of the chromia scales. The chromia scales, however, may reheal quickly such that the amount of iron rich oxide formed remains small. In this case, the oxidation behaviour can be approximately described as a parabolic growth of chromia. Thus, the parabolic rate expression for the growth of chromia can be used, since the amount of iron rich oxide formed is small. The growth behaviour will be further discussed in section 7.4.4.

The results in Table 15 showed that the weight gain of the specimens decreased after the addition of cerium and/or silicon to the alloy. The beneficial effect of cerium and silicon additions on the steady state growth of chromia was discussed in chapter 6.

The discrepancy between the two A1 specimens, oxidized in hydrogen/argon containing varies water partial pressures, will be discussed in section 7.4.4.

7.4.3 Oxidation at 1373 K

7.4.3.1 Microstructure

The specimens oxidized at 1373 K for 70 h in hydrogen/argon containing 1% water vapour formed a dense oxide scale compared to the specimens oxidized in the other reaction atmospheres (cf. Fig. 58 and Fig. 59). The diffraction patterns (cf. Fig. 61) and the EDX analyses (cf. Fig. 64) obtained for the oxide layers grown in hydrogen/argon containing 1% water vapour showed that the oxide scales consisted of a chromia scale as the innermost oxide. The EDX analyses also showed a small content of iron in the outermost part of the oxide scales. The iron-chromium oxide was identified as a spinel-type oxide by the diffraction patterns in Fig. 61. Thus, the oxide scales grown on the specimens at 1373 K for 70 h consist of chromia as the innermost oxide and an iron-chromium spinel as the outermost oxide. This sequence of oxides is in accordance with the phase diagram in Fig. 12.

Although pores were present in the oxide scale grown on the A1-Ce specimen in hydrogen/argon containing 1% water (cf. Fig. 57A), the scale was denser and more adherent than the corresponding scale grown on the A1 specimen (cf. Fig. 58D1). This is caused by the REE of the cerium addition to the alloy. By comparing with the specimens grown at 1173 K for 70 h in similar reaction atmospheres, it appears that the effect of cerium is more pronounced at 1373 K, as previously observed by Pint [74]. A large concentration of silica is present at the alloy/chromia interface of the A1-Si specimen. In contrast, silica appears to be absent from the interface of the A1-CeSi specimen. Thus, only small particles of silica may be present when the alloying addition of silicon is low. Due to the increased growth rate of silica with increasing temperature, the amount of silica present at the alloy/chromia interface of the A1-Si alloy oxidized at 1373 K is much larger than the silica content present at the interface of the A1-Si specimens grown at 1173 K.

The specimens oxidized in hydrogen/argon containing 12% water vapour, and in air containing 1% or 12% water vapour, had different morphologies than those oxidized in hydrogen/argon containing 1% water (cf. Fig. 59). The micrographs showed extensive oxidation, with oxides extending almost all the way through the specimens. An exception was the A1-Si specimen oxidized in hydrogen/argon containing 12% water vapour, which was similar to the specimen in Fig. 57B. The thick oxides in Fig. 59 were divided into an inner highly porous region and an outer denser region.

The thick oxide covered the entire surface of the specimens in some cases, while the thick oxide were present only near edges in other cases. Thus, it appears that the

formation of thick oxides is initiated near the edges of the specimens. This will be discussed in section 7.4.4.

The EDX line scan analyses of the specimens oxidized in hydrogen/argon containing 12% water vapour showed that the oxide consisted of an iron rich oxide closest to the atmosphere, and a mixed iron-chromium oxide nearer the middle of the specimens (cf. Fig. 64). The diffraction pattern (cf. Fig. 62) shows the presence of a spinel phase and a wüstite phase. As shown in the phase diagram in Fig. 12, the only pure iron oxide stable in equilibrium with the reaction atmosphere at 1373 K is the wüstite phase. Hence, part of the wüstite phase may have transformed to magnetite during the cooling of the specimens, as previously discussed.

The EDX line scan analyses of the specimens oxidized in air containing water showed that the oxide closest to the atmosphere consists of an iron oxide (cf. Fig. 65), while the oxide nearer the middle is a mixed iron-chromium oxide. The diffraction patterns (cf. Fig. 62) show that the iron oxide is hematite. This is in accordance with the phase diagram in Fig. 12, which shows that hematite exists in equilibrium with air.

The separation in the EDX analyses, between the iron oxide and the mixed iron-chromium oxide, may also be recognized from the micrographs in Fig. 59 and Fig. 60, where the outermost dense oxides were identified as the iron oxide, while the porous oxide was identified as the mixed iron-chromium oxide. Furthermore, it was shown in Fig. 60 that the denser iron oxide was positioned above the initially formed chromia scale, while the porous iron-chromium oxide was positioned below the chromia scale. This oxidation behaviour will be discussed in section 7.4.4.

The other specimens oxidized in hydrogen/argon containing 12% water vapour and in air containing 1% or 12% water vapour, showed similar results as the A1 alloy with the formation of thick oxides.

The specimens oxidized at 1373 K showed the presence of iron in the outermost part of the scale, especially the specimens oxidized in hydrogen/argon containing 12% water vapour and in air containing water. The presence of iron cannot be attributed to the transient oxidation stage. Instead it must be caused by a formation of iron rich oxide after failure of the chromia scale. The mechanism for the failure of chromia scales and the subsequent formation of iron rich oxides is discussed in section 7.4.4. Furthermore, how can the large difference between oxidizing in hydrogen/argon containing 1% and 12% water vapour, be explained? This will also be discussed in section 7.4.4.

Although certain specimens showed complete oxidation of the alloy, the specimens were divided into sections of different oxides (cf. Fig. 59 and Fig. 65). After an extended oxidation for several hundred hours, the oxides will mix, such that the final composition of the specimens in equilibrium with the reaction atmosphere can be found from the phase diagram in Fig. 12.

7.4.3.2 Oxidation kinetics

The gravimetric data in Table 17 showed that the specimens oxidized in hydrogen/argon containing 1% water vapour had the lowest weight gain compared to the other specimens. This difference can also be observed from the different morphologies in Fig. 57 and Fig. 58. Among the specimens oxidized in hydrogen/argon containing 1% water vapour, the A1-CeSi alloy had the lowest weight gain, while the A1 alloy showed the largest weight gain. These results are similar to those obtained for scales grown at 1173 K. The effect of silicon and cerium on the growth kinetics has already been discussed in chapter 6.

An extensive oxidation was observed for the specimens oxidized in air containing water and in hydrogen/argon containing 12% water vapour. The only discrepancy is the A1-Si alloy oxidized in hydrogen/argon containing 12% water vapour, which exhibited a slow protective growth of the oxide scale. The large weight gains were caused by the formation of thick iron rich oxides on the specimens, which grow much faster than chromia [58] (cf. Fig. 59). The iron rich oxides were formed as a result of failure of the chromia scale, as discussed in section 7.4.4. Silicon additions to the alloy may be effective in increasing the protective nature of the chromia scale, since the A1-Si alloy oxidized in hydrogen/argon containing 12% water vapour exhibited a dense oxide scale. The oxidation behaviour of various specimens has been followed in-situ by TG measurements in order to investigate this. These results are given in chapter 8.

7.4.4 Breakaway oxidation

The specimens oxidized at 1173 K for 504 h showed significant concentrations of iron in the scale, which was not observed after oxidation for 70 h. Thus, the presence of iron cannot be attributed to the transient oxidation stage. Furthermore, the specimens oxidized at 1373 K for 70 h showed the formation of iron rich oxides, especially the specimens oxidized in hydrogen/argon containing 12% water vapour, and in air containing water. Instead of being a result of transient oxidation, the presence of iron must be caused by a formation of iron rich oxide after failure of the chromia scale. This regime is usually termed catastrophic, or breakaway oxidation. The oxidation behaviour was affected by the oxygen activity and by sample edge effects. These observations will be discussed in the following. However, the mechanism for the initiation of the breakaway oxidation is first described in order to understand the effect of edges and the effect of the oxygen activity.

7.4.4.1 Mechanism of breakaway oxidation

Evans et al. [9] have recently addressed the mechanisms of breakaway oxidation for chromia forming alloys. Breakaway oxidation may initiate if chromia becomes thermodynamically unstable at the alloy/scale interface, and it may initiate

mechanically by the formation of cracks in the chromia scale [9]. These different mechanisms are described below.

During the growth of a chromia scale on an iron-chromium alloy, a depletion profile of chromium will develop within the alloy. This depletion profile of chromium is a function of the parabolic rate constant for the growth of chromia, the chromium diffusion coefficient in the alloy, and the time elapsed. A boundary condition for the chromium depletion profile is that the outward flux of chromium at the alloy/chromia interface is governed by the growth rate of chromia [107,112]. The depletion profile is given in the literature for cases where it is assumed that the specimen is semi-infinite, i.e. for cases where the specimen is assumed to be so thick that the concentration of chromium at the midplane of the specimen is constant during the oxidation [107,112]. The solution for the depletion profile of chromium also gives a value for the chromium concentration in the alloy at the alloy/chromia interface; the interfacial concentration. This value is constant during the growth of the chromia scale, if the specimen can be considered semi-infinite [112]. In contrast to the semi-infinite case, the chromium depletion profiles may meet at the midplane of relatively thin-sectioned specimens during the oxidation process. In this case, the midplane and the interfacial concentration of chromium will decrease during the oxidation. Solutions for this depletion profile are given in Ref. [127]. The latter case is more important for oxidation at high temperatures and for long term oxidation [9].

The formation of iron rich oxides beneath a dense chromia scale may occur if the chromia scale becomes unstable in equilibrium with the alloy at the alloy/chromia interface. In this work, the formation of chromite is the most favoured reaction, if chromia becomes unstable (cf. Fig. 11 and Fig. 12). In this case, chromite will start to form at the alloy/chromia interface. The formation of chromite at the alloy/chromia interface will result in volume changes, which are likely to crack the original chromia scale [9]. The impacts of a mechanical failure of the chromia scale are discussed later.

The critical interfacial concentration of chromium N_{Cr}^{e}, at which both chromia and chromite exist in equilibrium with the alloy, is given in Fig. 66 as a function of temperature. The concentration was determined from the Gibbs energies of formation for the oxides, as used in section 2.4. An activity of 0.78 was assumed for iron. The activity of iron in the alloy will change as the activity of chromium in the alloy changes. However, changes of the iron activity will only have a small effect on the curve given in Fig. 66.

As seen in Fig. 66, the critical concentration of chromium is very low under the experimental conditions in this work. If the specimen can be considered semi-infinite, as previously discussed, the interfacial concentration is considerably higher than given in Fig. 66 during the formation of chromia [112]. Thus, the chromite spinel will only start to form beneath the chromia scale if the midplane and interfacial concentration of chromium decreases considerably. This is only important after extended long term oxidation at very high temperatures (> 1390 K) [9]. Consequently, this mechanism for initiation of breakaway oxidation is not applicable in this study.

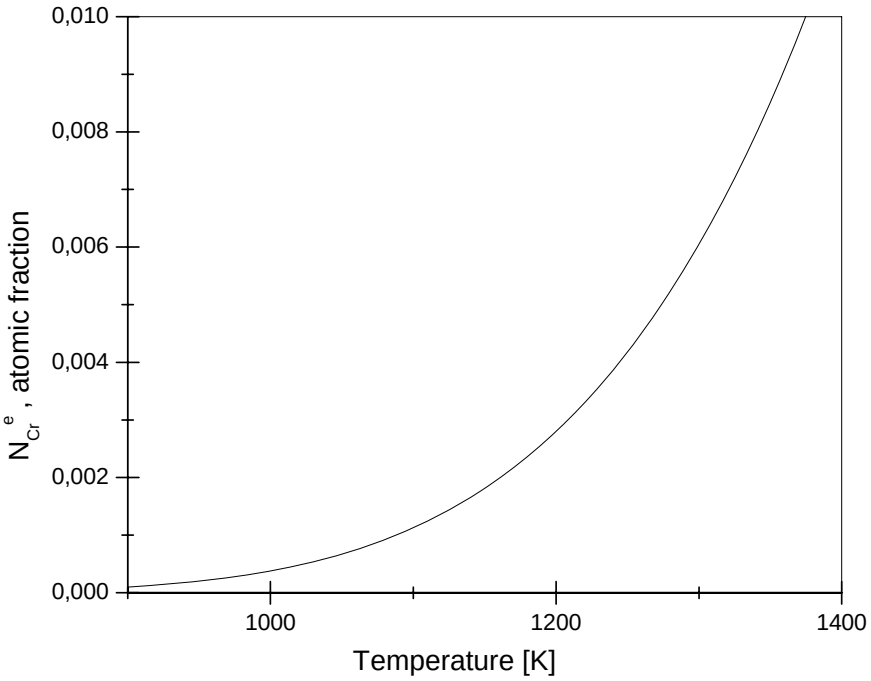

Fig. 66. The critical chromium concentration in the alloy at which both chromia and chromite exist in equilibrium with the alloy, as a function of temperature.

It should be noticed that a very thick layer of chromia forms before the alloy becomes sufficiently depleted in chromium such that chromite is formed at the alloy/chromia interface. In cases where a thick layer of chromia forms on the alloy, the breakaway oxidation is likely to be initiated mechanically by the formation of cracks in the chromia scale instead. Thus, the route for chemical failure, as discussed above, may be of minor importance. The initiation of breakaway oxidation resulting from a mechanical failure of the chromia scale will be discussed below.

The formation of cracks in chromia scales is caused by the generation of growth stresses in the oxide scale. The outward diffusion of chromium during the growth of chromia creates vacancies near the alloy/chromia interface, which may be annihilated through plastic deformation of the chromia scale. This results in a build-up of stresses in the scale. The growth stresses may also form as a result of the formation of new oxide within the existing chromia scale. This may result in compressive growth stresses, as previously discussed. The generation of growth stresses may eventually lead to the formation of cracks in the scale, if the stresses cannot be sufficiently relieved by plastic deformation [10]. The generation of growth stresses was also discussed in section 5.4.1 and 6.4.1.1.

If the cracks extend all through the chromia scale, the oxidant can migrate via the cracks to react at the alloy surface. The composition of the alloy at the interface is different from the initial bulk composition, since chromium is depleted due to the growth of the chromia scale. After the growth of a chromia scale, the interfacial concentration of chromium is given by the depletion profile, as previously mentioned.

Thus, the freshly exposed alloy surface may exhibit different oxidation behaviour than the original alloy surface.

If the interfacial content of chromium is sufficiently high, the chromia scale will form again such that the steady state growth of chromia continues. The conditions for this will be discussed later. In contrast, if the alloy surface is sufficiently depleted in chromium, the protective layer of chromia will not form again, and iron rich oxides will start to form. The growth rate of iron rich oxides is considerably higher than the growth rate of chromia, so it may result in the formation of very thick iron rich oxide layers [58,128]. The formation of iron oxide within the crack of the chromia scale may initiate a spallation of the chromia scale near the crack, since the fast formation of iron oxide within the crack may generate large compressive stresses in the chromia scale. During the initial oxidation after the spallation, both chromium and iron will oxidize. Iron will oxidize to iron oxide, which has a large growth rate, so it will form a thick oxide layer [58]. If the alloy is oxidized in air, iron exists as a sequence of oxides; wüstite, magnetite and hematite (cf. Fig. 12). However, the growth of iron oxides will be governed by the formation of wüstite, since wüstite is growing considerably faster than the other iron oxides [58]. Thus, the wüstite phase will be the major constituent of the iron oxide layer [129]. Chromia nuclei will also form on the alloy surface initially, but will be overgrown by the fast growing iron oxide. Chromia is formed internally in the alloy matrix in a zone beneath the iron oxide by reducing wüstite, since chromia is more stable than wüstite (cf. Fig. 8). During the continued oxidation, the iron oxide scale will encroach on the internally formed chromia precipitates. This will result in a solid-state reaction between chromia and wüstite to form an iron-chromium spinel. Thus the oxidation process reaches a steady state, where iron oxide is formed by outward diffusion of iron, chromia is formed internally in the alloy, and an iron-chromium spinel is formed by a solid-state reaction between chromia and wüstite. Furthermore, the continued outward diffusion of iron, from the alloy and the mixed iron-chromium oxide, to the iron oxide scale will create Kirkendall porosities in the inner layers.

Thus, a growth mechanism for the breakaway oxidation is proposed where iron oxides are formed on top of mixed iron-chromium oxides. Furthermore, porosities will be formed in the inner layers due to the outward diffusion of iron. The SEM micrographs (cf. Fig. 59) and the EDX line scan analyses (cf. Fig. 64D2 and Fig. 65) support this proposal, since they show the formation of a thick dense iron oxide on top of a porous mixed iron-chromium oxide.

An interesting detail is shown in Fig. 60, where the thin original chromia scale separates the dense iron oxide at the top from the more porous iron-chromium oxide below. This may be understood considering that chromia is formed internally, i.e. in the alloy below the original chromia scale after the failure of the chromia scale, while the iron oxide is formed by outward diffusion of iron.

The breakaway oxidation described above was initiated after the formation of cracks in the chromia scale. However, the chromia scale may heal again after the formation of cracks. In this case, the parabolic growth of chromia will continue. The possible healing of a chromia scale after the formation of cracks is of great technological interest, so the conditions for the healing of the chromia scale will be discussed below.

During the initial oxidation of an iron-chromium alloy, a chromia layer will form if the content of chromium in the alloy is sufficient. The critical concentration of chromium in the alloy may in principle be determined by a similar calculation as performed for the formation of a dense layer of silica in chapter 6, where the critical silicon concentration was given as the maximum of two criteria (cf. Eq. 88 and Eq. 89). The first criterion involves the transition from internal to external oxidation [102], while the second criterion is determined by the chromium flux through the alloy necessary to sustain the growth of the external chromia scale [27]. The first criterion has often been neglected during the determination or discussion of the critical chromium concentration [49]. However, Gesmundo and Niu [130] have recently shown that the critical chromium concentration in the alloy for the formation of an external chromia scale probably is determined by the first criterion.

In contrast to the formation of silica beneath the chromia scale, chromia becomes imbedded in the external iron oxide scale, as the external iron rich scale encroaches on the alloy. This occurs by a solid-state reaction between wüstite and chromia, as previously discussed. The chromia precipitates must spread laterally over the entire alloy surface in order to form a continuous chromia scale. The growth of a fast forming external scale makes it more difficult to form a dense chromia scale beneath the external scale, since the chromia nuclei continuously becomes incorporated in the iron rich scale, as discussed by Gesmundo et al. [105,130]. The theoretical analyses will not be further discussed here, but Gesmundo and Niu [130] determined the critical chromium concentration to 15 at.% for oxidation of an austenitic iron-chromium alloy at 1273 K, which is close to experimental determined values for an austenitic steel [131]. The critical chromium concentration has been reported to be almost independent of temperature [131]. The value is also close to experimental determined values for ferritic iron-chromium alloys [132], so a value of 15 at.% is used in the present discussion for the oxidation at 1173 and 1373 K.

After the formation of a chromia scale, a chromium depletion profile develops in the alloy. This profile determines the interfacial chromium concentration, which is constant if the specimen can be assumed to be semi-infinite. In case the chromia scale fails and the scale spalls, the freshly exposed alloy will start to oxidize. If the interfacial chromium concentration is above 15 at.%, the chromia scale will reform. However, if the chromium content is below 15 at.%, the chromia scale will not reform, and iron rich oxides will start to form, as previously described. Thus, it is interesting to determine the initial chromium concentration in the alloy necessary to reform the chromia scale if it should spall. This concentration may be determined from the depletion profile as the chromium concentration necessary to obtain an interfacial chromium concentration of 15 at.% [112,133]. During the initial growth of a new chromia scale after the spallation of a scale, the interfacial concentration of chromium in the alloy decreases sharply in order to supply chromium to the newly formed chromia scale [133]. The interface concentration will gradually increase to the value it had before the spallation, if the alloy can be considered as semi-infinite [133]. However, the chromia scale may spall again before the interfacial chromium concentration has recovered to its previous value. This problem has been examined by Whittle [133] and subsequently by Nesbitt [134]. It has been shown that the interfacial concentration of chromium only recovers 50% of the initial decrease after spallation, if the spallation occurs at regular time intervals [134]. Thus, the lifetime of an iron-

chromium alloy is obviously limited, if the chromia scale fails at regular intervals. However, many questionable assumptions were made during the analyses, as discussed by Nesbitt [134], so the analyses may only be used for a qualitative discussion.

If the chromia scale fails to reform at the interface after the spallation, the iron rich oxides will start to form. Will this necessarily result in a breakaway oxidation through the entire specimen? During the growth of the iron rich oxide, the alloy/oxide interface will recede. However, a depletion profile of chromium was formed in the alloy during the growth of the initial chromia scale, so the interfacial chromium content will gradually increase as the alloy/oxide interface recedes during the growth of the iron rich oxide. The alloy/oxide interface may eventually reach a point where the interfacial content of chromium is sufficiently high such that a chromia scale can be reformed.

The concentration profile of chromium in the alloy, inherent from the initial chromia growth, will naturally change during the formation of the iron rich scale. However, Evans et al. [131] showed that the growth of the iron rich oxide is so fast that the chromium profile can be assumed to be unaffected, while the alloy/oxide interface recedes. Thus, the depth of the attack on the alloy may in principle be determined if the chromium depletion profile is known before the failure. Breakaway oxidation through the entire specimen will occur if prior oxidation has reduced the chromium concentration throughout the specimen to below the critical level required for the formation of a chromia scale (ca. 15 at.%) [9].

7.4.4.2 Edge effects

With the exception of a A1-Si specimen, the alloys oxidized at 1373 K for 70 h in hydrogen/argon containing 12% water vapour and in air containing water, exhibited an accelerated oxidation. Some specimens exhibited breakaway oxidation over the entire sample surface, while other specimens only showed breakaway oxidation near the sample edges. An example of breakaway oxidation near an edge is shown in Fig. 67.

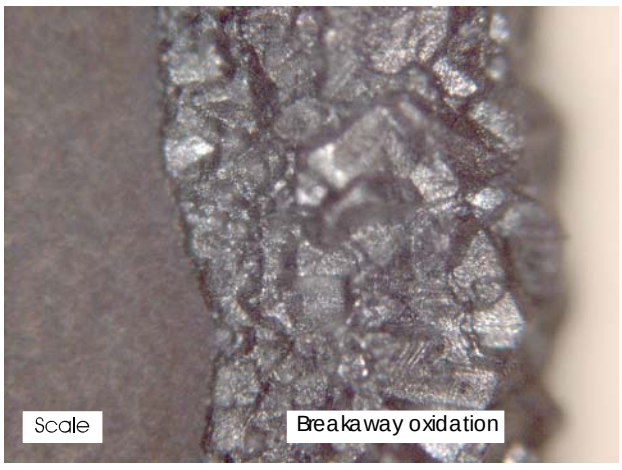

Fig. 67. Light-optical micrograph of breakaway oxidation near the edge of a specimen.

The results indicate that the breakaway oxidation initiates near edges of the specimens. As previously discussed, the breakaway oxidation is initiated mechanically by the formation of cracks in the chromia scale. Thus, it appears that the chromia scale is most prone for mechanical failure near the specimen edges. How can these edge effects be explained?

The growth of chromia scales is mainly governed by diffusion of chromium, as previously mentioned, so the newly formed oxide will form near the chromia/gas interface. During the growth of the scale, the alloy front will recede due to the consumption of chromium by the chromia scale. As a consequence of the receding alloy front, vacancies will be created at or near the alloy/scale interface. However, the oxide adherence to the alloy surface is very strong, so the oxide will also recede. When a convex alloy surface recedes, the surface area of the receding alloy surface decreases. The oxide, which adheres to the alloy substrate, is the initially formed oxide. The decreasing surface area of the alloy will create large compressive stresses in the oxide scale close to the alloy/scale interface, since the oxide will try to remain adherent to the receding alloy. The situation is shown in Fig. 68. In contrast, if the scale is growing on a concave surface, the surface area of the alloy will increase as the alloy front recedes. This will in turn create tensile stresses within the oxide scale.

This discussion shows that extra stresses are generated within the scale grown near the edges of the specimen, so cracks will tend to be formed near the edges, as shown in Fig. 67.

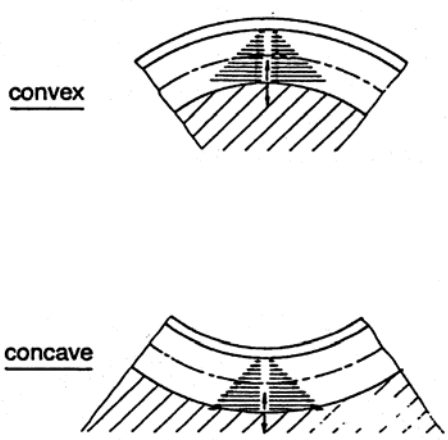

Fig. 68. A schematics of oxidation on curved surfaces. The new oxide is formed at the scale/gas interface. The oxidation on the convex surface will result in compressive stresses, while the oxidation on the concave surface will result in tensile stresses in the oxide, after [135].

7.4.4.3 Effect of the oxygen activity

The gravimetric data given in Table 15 and Table 17, and the SEM micrographs shown in Fig. 51, Fig. 58D1 and Fig. 59, reveal a large difference of the oxidation behaviour for the specimens oxidized in hydrogen/argon containing various amounts of water vapour. The specimens oxidized in hydrogen/argon containing 1% water vapour at 1173 K for 504 h, and at 1373 K for 70 h formed a relatively thin scale, while the specimens oxidized in hydrogen/argon containing 12% water vapour under

otherwise similar experimental conditions exhibited an extensive breakaway oxidation. In chapter 5 and 6, it was shown that the oxidation rate of chromia is independent of the water vapour content in the reaction atmospheres, if the oxidation behaviour can be characterized as a parabolic growth of chromia. Thus, the present discrepancy may appear strange at first sight.

The parabolic rate constants were determined for the specimens oxidized at 1173 K in hydrogen/argon containing 1% water vapour for 504 h (cf. Table 16). These values are similar to the values obtained for the specimens oxidized for 70 h under similar conditions (cf. Table 11). This indicates that the oxidation of the specimens for 504 h can be described by a similar parabolic growth mechanism. The scales grown at 1373 K in hydrogen/argon containing 1% water vapour may also grow according to a parabolic growth rate, since the scales are dense and mainly consists of chromia.

Despite the parabolic growth of the specimens, a low concentration of iron is present in the outermost part of the scales. It is proposed that cracks have formed in the chromia scale during the growth, but a healing layer of chromia has formed quickly such that the amount of iron escaped from the alloy through the cracks is relatively small. Thus, why are cracks healed again during the growth in 1% water vapour, while breakaway oxidation is initiated when the specimens were oxidized in 12% water vapour?

The discrepancy between the oxidation in hydrogen/argon atmospheres containing 1% and 12% water vapour, respectively, may be understood considering the phase diagrams in Fig. 11 and Fig. 12. After the formation of cracks in the chromia scale, iron rich oxides will start to form. The phase diagrams show the thermodynamically stable oxides in equilibrium with the relevant reaction atmosphere. As shown in the phase diagrams, the hydrogen/argon containing 1% water is in equilibrium with an iron rich oxide with the spinel structure under the test conditions. Hence, the wüstite phase is not thermodynamically stable under the given test conditions. In contrast, the wüstite phase is stable in hydrogen/argon containing 12% water vapour.

After mechanical failure of the chromia scale (i.e. formation of cracks), an iron rich oxide will start to grow on the alloy surface of the specimen oxidized in hydrogen/argon containing 12% water vapour. As previously discussed, the growth of the oxide will be dominated by the formation of wüstite. In contrast, if cracks form in the chromia scale grown in hydrogen/argon containing 1% water vapour, an iron-chromium oxide with the spinel structure will start to form on the alloy surface. The growth rate of the spinel is many orders slower than the corresponding growth rate of the wüstite phase [58,129]. The formation of wüstite within the crack may be extensive, and may cause a build-up of compressive stresses within the chromia scale. Hence, the chromia scale may crack further and spall as a result of the build-up of stresses. In contrast, the formation of the spinel is much slower and may not result in an increased spallation of the chromia scale. The chromia scale may form again beneath the iron rich oxides. However, the specimen will become increasingly depleted in chromium if a large part of the chromia scale is reformed, in contrast to a healing of a local crack in the chromia scale [134]. Thus, the formation of wüstite may lead to an increased scale spallation, which may increase the depletion of chromium within the alloy. This will eventually result in an increasing tendency for breakaway oxidation [9,134].

Another possibility is that a dense chromia layer is formed more easily (i.e. the critical chromium concentration is decreased) beneath a relatively slow growing iron-chromium spinel than beneath a fast growing wüstite scale. Indeed, Gesmundo and Viani [105] have shown this. This may be understood considering that a faster growing external scale will encroach faster on the alloy beneath. Thus an increasing part of chromium becomes imbedded into the encroaching external oxide with increasing growth rate of the external oxide. The result is that it becomes increasingly difficult to form a continuous chromia layer beneath the external scale with an increasing growth rate of the external scale. It follows that the critical concentration of chromium in the alloy increases for the formation of a dense chromia layer beneath a fast growing oxide [105].

The content of dissolved oxygen in the alloy beneath the spinel phase is less than beneath the wüstite phase, since the decomposition pressure of the iron-chromium spinel is lower than the decomposition pressure of wüstite (cf. Eq. 8). This may result in an easier formation of a dense layer of chromia beneath the spinel phase [136], since the chromia nuclei are formed in close vicinity of the alloy/oxide interface in this case, as discussed in chapter 6.

It was found that the specimens grown in hydrogen/argon containing 1% water formed a dense chromia layer after an initial failure, while the specimens grown in 12% water exhibited an increased breakaway oxidation. It is proposed that the most important reason for this discrepancy is that a dense chromia layer is formed more easily beneath a growing iron-chromium spinel than beneath a fast growing wüstite, since the difference in growth rate of the two oxides is large.

7.5 Summary

The oxidation behaviour of the A1, A1-Ce, A1-Si and A1-CeSi alloys was examined at 973, 1173 and 1373 K under various test conditions. The oxide scales grown at 973 K consisted of thin chromia scales. In contrast, the oxide scales grown at 1173 K for 504 h, and the oxide scales grown at 1373 K for 70 h showed the presence of iron in the scales. The presence of iron was a result of failure of the chromia scale. The chromia scale may reform again after failure, if the interfacial chromium content in the alloy is sufficiently high. Otherwise, breakaway oxidation of the specimen initiates.

The initiation of breakaway oxidation was discussed and a mechanism was proposed, which could explain the observed experimental results. The mechanism for breakaway oxidation takes into account the observed microstructure of the specimens and the edge effects of the specimens.

In contrast to steady state growth of chromia scales, the breakaway oxidation is highly affected by the oxygen activity in the reaction atmosphere. A low oxygen activity can protect the alloy from the catastrophic oxidation behaviour observed at larger oxygen activities. A tuning of the oxygen activity, such that wüstite is not thermodynamically

stable, may be useful for long term oxidation of Fe-Cr alloys under reducing conditions.

8 Thermogravimetric measurements

8.1 Introduction

Valuable information can often be gathered regarding the oxidation kinetics and the growth mechanism of alloys, when the specimens are isothermal oxidized in a furnace. However, the oxidation processes taking place during oxidation are dynamic, so in-situ measurements of the oxidation process are valuable during a detailed examination of the oxidation mechanism. In this study, the oxidation of the specimens was followed in-situ by thermogravimetric (TG) measurements in order to investigate the growth mechanism of the oxide scales. During the TG measurements, the total weight gain of the specimens during the oxidation is obtained. This includes the weight gain from the formation of oxide, and in addition, it includes the weight loss due to vaporization from the oxide. Hence, TG measurements of the oxidation process must be carefully analysed.

Several effects were examined during the TG measurements

- The effect of water vapour
- The effect of alloying additions
- The effect of temperature

The effect of water vapour on the weight gain was examined in order to estimate the weight loss due to the vaporization of volatile chromium species during oxidation. The effect of water vapour, however, was also examined in order to determine whether water vapour accelerates the oxidation process. The effect of alloying additions on the oxidation behaviour was described in chapter 6. The growth mechanisms are studied more detailed in this chapter by TG measurements. The effect of water vapour and alloying additions were studied through a series of TG measurements performed at 1173 K.

The breakaway oxidation of the alloys was described in chapter 7, where it was proposed that the addition of silicon to the iron-chromium alloy could have a positive effect on the resistance towards breakaway oxidation of the specimens. This proposal is examined in the present chapter through a series of TG measurements performed at 1373 K.

The effect of water vapour was examined, by varying the water vapour content in the reaction gas from dry conditions to reaction atmospheres containing large concentrations of water. The TG measurements were carried out for the A1-Ce, A1-Si, and A1 specimens. The measurements were either performed at 1173 K in hydrogen/argon, or in air, both containing varies water vapour partial pressures. Furthermore, a few measurements were carried out at 1373 K in air containing a low concentration of water vapour. The experimental details are given below.

8.2 Experimental

The isothermal TG measurements were performed, in atmospheres containing a low water vapour content (less than 1% water vapour), using a Netzsch STA 409 CD equipment. The TG measurements performed in reaction atmospheres containing a large amount of water vapour, were performed using the special Netzsch equipment, previously discussed in chapter 3. The results from the special Netzsch equipment were obtained during the modification and fine-tuning of the new equipment.

The TG measurements were performed for the A1-Ce, A1-Si, and A1 alloys. The TG measurements were conducted in hydrogen/argon and in air containing various concentrations of water vapour. Most of the experiments were performed at 1173 K, but a series of experiments were performed at 1373 K in air containing 0.7% water vapour. The experimental parameters, used for each alloy, are summarized in Table 18. The isothermal dwell time was 24 h for all the conducted measurements.

The oxide scales of the specimens were analysed using XRD obtained at room temperature after the TG measurements.

The experimental details are given in chapter 4.

Table 18. Test conditions for the alloys during the TG measurements. The specimens were isothermal oxidized for 24 h.

Gas	Temperature / K	$p(O_2)$ / bar	$p(H_2O)$ / bar
Air	1173	0.21	0.0008
Air	1173	0.21	0.007
Air	1173	0.21	0.5
7%H_2/93%Ar	1173	$4.2 \cdot 10^{-22}$	0.0002
7%H_2/93%Ar	1173	$5.2 \cdot 10^{-19}$	0.007
Air	1373	0.21	0.007

8.3 Results

8.3.1 Oxide morphology and XRD analysis

The oxide scales grown at 1173 K adhere to the alloy. The diffraction patterns (not shown) obtained for the specimens oxidized at 1173 K showed the existence of a corundum-type oxide and reflections from the ferritic alloy. In contrast, the oxides grown at 1373 K showed the presence of a thick oxide similar to the oxide scales described in section 7.3.3. This indicates the presence of a thick iron rich oxide. The only discrepancy was the A1-Si specimen, which only formed a thick oxide near the sample edges. The effect of sample edges on the oxidation behaviour was discussed in section 7.4.4.2. A micrograph of the specimen containing silicon is shown in Fig. 69, where the increased oxide formation near the edges is seen.

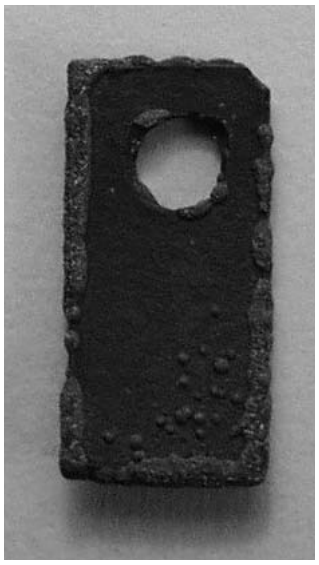

Fig. 69. Micrograph of the A1-Si specimen oxidized for 24 h at 1373 K in air containing 0.7% water vapour.

The diffraction patterns obtained for the specimens oxidized at 1373 K are shown in Fig. 70. The diffraction patterns obtained for the scales grown on the A1 and A1-Ce specimens contain an oxide with the corundum structure (PDF #33-0664). In contrast, the diffraction pattern obtained for the scale grown on the A1-Si specimen has a complex nature. The diffraction pattern shows the presence of two distinct corundum-type oxides (PDF #38-1479), and in addition, the diffraction pattern shows reflections from a spinel-type oxide (PDF #19-0629) with low intensity.

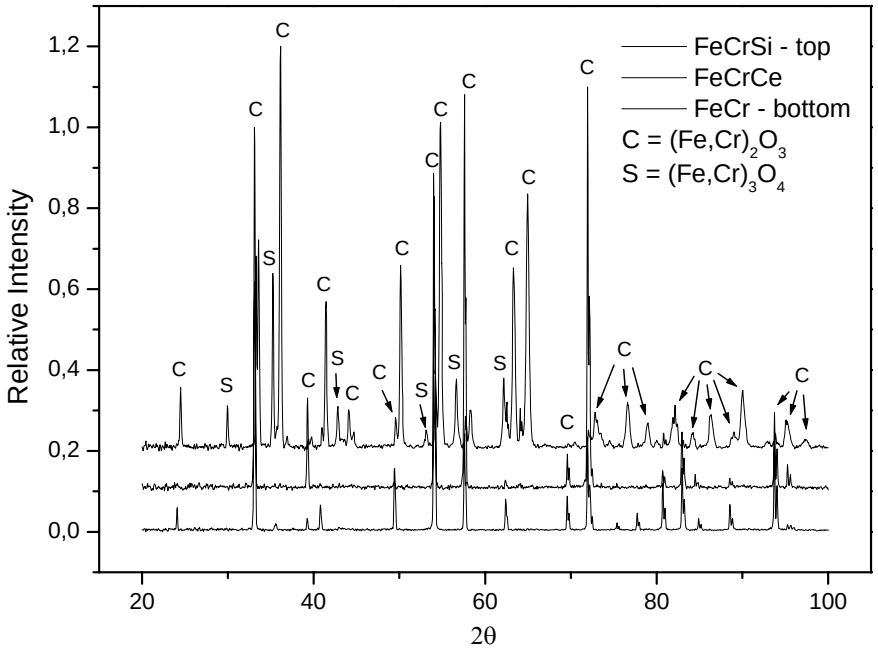

Fig. 70. Diffraction patterns obtained of the oxide scales grown on specimens oxidized for 24 h at 1373 K in air containing 0.7% water vapour.

8.3.2 TG measurements

The TG measurements performed at 1173 K in various atmospheres are shown in Fig. 71-Fig. 75. The measurements are plotted as the weight increase squared vs. time. The measurements for the specimens oxidized at 1173 K in hydrogen/argon containing 0.02% and 0.7% water vapour are shown in Fig. 71 and Fig. 72, respectively. The TG curves given in Fig. 71 and Fig. 72 show an approximately linear relationship with time. The specimens oxidized in hydrogen/argon containing 0.02% water vapour exhibited a lower weight gain than those oxidized in hydrogen/argon containing 0.7% water vapour.

The TG measurements obtained for the specimens oxidized at 1173 K in air containing various concentrations of water vapour are shown in Fig. 73-Fig. 75. In contrast to the specimens oxidized in hydrogen/argon, the weight gain of the specimens oxidized in air containing 0.7% water vapour is lower than the corresponding specimens oxidized in air containing 0.08% water vapour. The TG curves given in Fig. 73 and Fig. 74 also show an approximately linear relationship with the time elapsed. As shown in Fig. 71 and Fig. 73, the weight gain for the specimens oxidized in dry hydrogen/argon is lower than those oxidized in dry air.

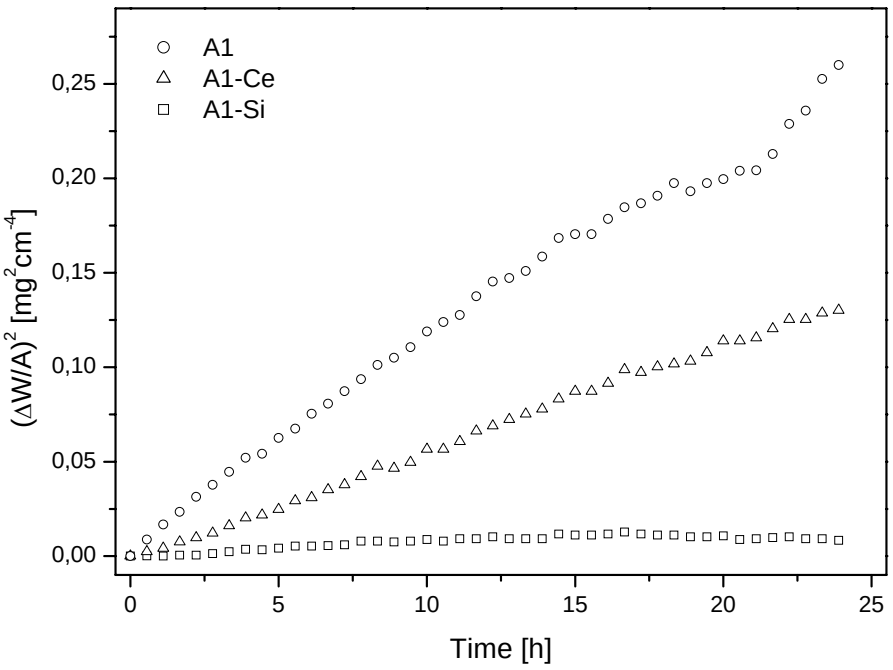

Fig. 71. TG measurements for the specimens oxidized at 1173 K for 24 h in hydrogen/argon containing 0.02% water vapour.

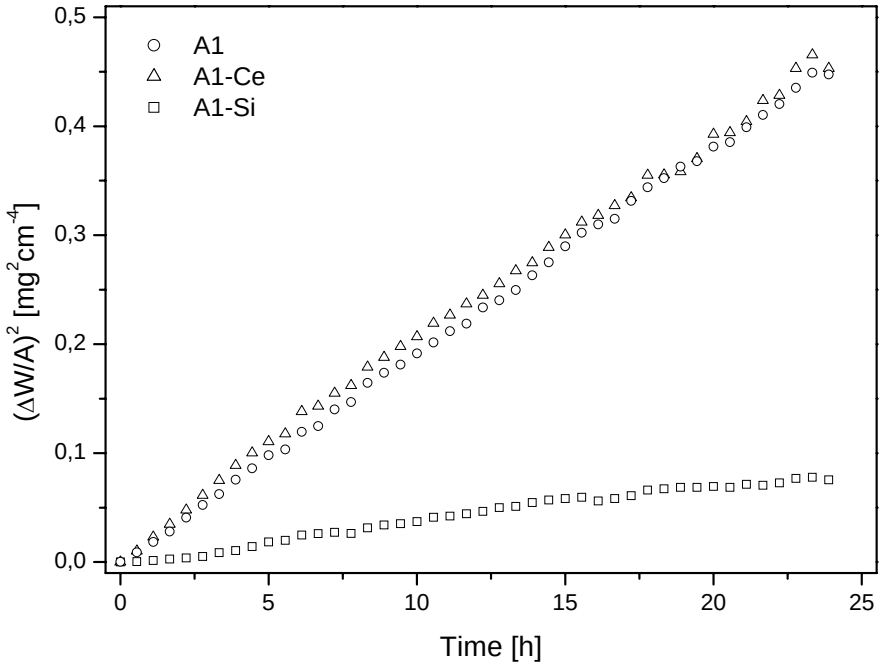

Fig. 72. TG measurements for the specimens oxidized at 1173 K for 24 h in hydrogen/argon containing 0.7% water vapour.

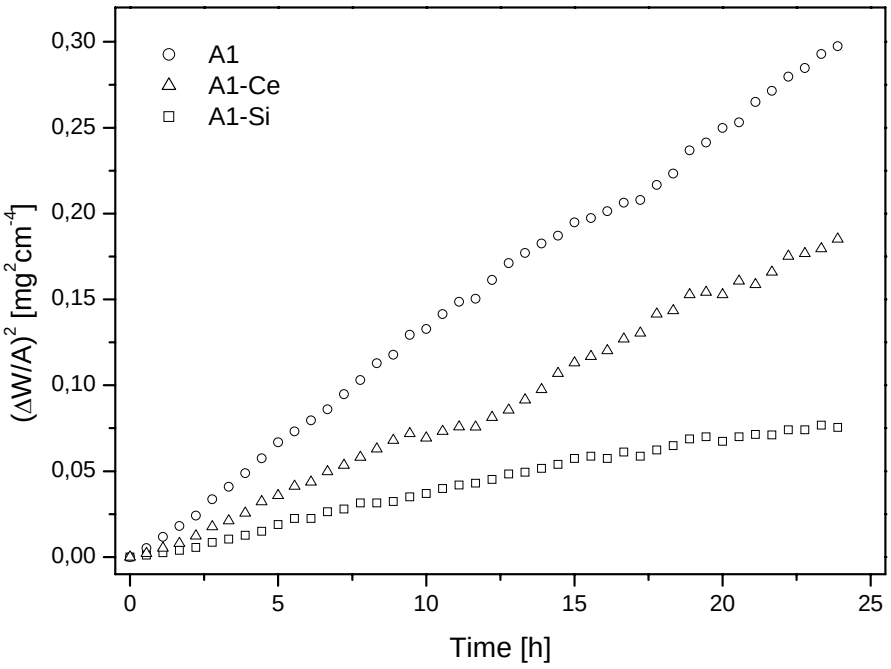

Fig. 73. TG measurements for the specimens oxidized at 1173 K for 24 h in air containing 0.08% water vapour.

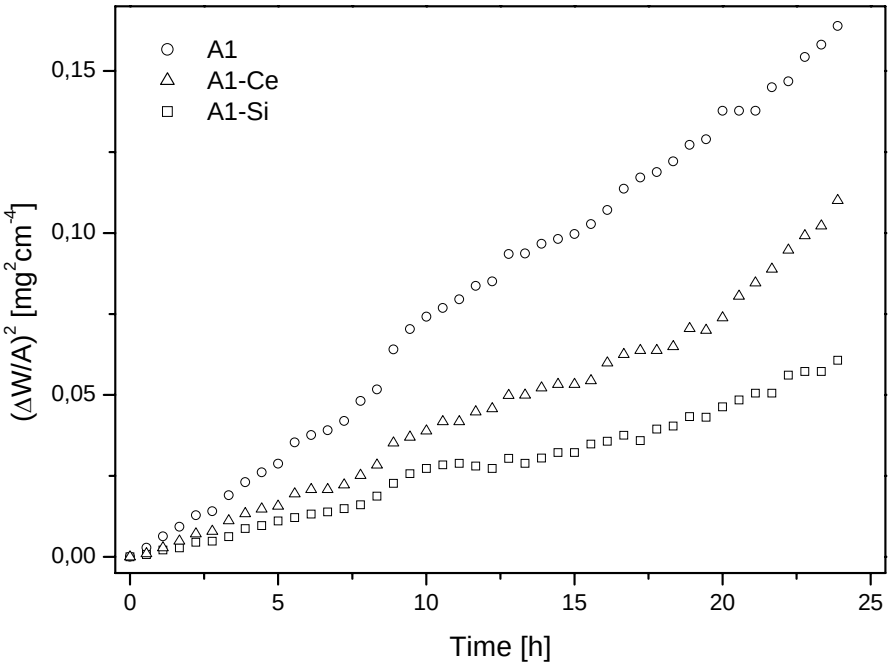

Fig. 74. TG measurements for the specimens oxidized at 1173 K for 24 h in air containing 0.7% water vapour.

The weight gain obtained for the specimens oxidized in air containing 50% water vapour is lowest (cf. Fig. 75). The TG curves do not, however, follow a linear relationship with time. Instead, the weight gains level off after an initial linear weight increase. Dotted lines are superimposed on the TG curves in Fig. 75 to indicate the initial linear relationship.

The effect of the alloying additions on the weight gain of the specimens is shown in Fig. 71-Fig. 75. The weight gain is generally in the order A1-Si < A1-Ce < A1.

The TG measurements in Fig. 71-Fig. 75 exhibit some scatter. This scatter was caused by changes in the room temperature during the measurements. The temperature in the room was logged during the measurements. Blank runs were made in order to obtain a functional dependency between the room temperature and the weight changes. However, a successful functional correlation between the scatter of the TG signals and the room temperature was not achieved.

The TG curves in Fig. 75 were obtained during the fine-tuning of the equipment. This resulted in additional scatter for the measurements performed on the special Netzsch equipment

The TG measurements of the specimens oxidized at 1373 K in air containing 0.7% water vapour are shown in Fig. 76, where the weight gain is plotted as a function of time. The specimens do not follow a parabolic rate law; instead, the A1-Ce and A1 specimens show a large, almost linear weight increase after an initial oxidation period of approximately 7 hours. The weight gain of the A1-Si specimen is much lower, albeit the growth of the oxide scale does not follow a parabolic rate expression. The fast weight increase of the specimens indicates that they are subject to a breakaway

oxidation. This is in accordance with the presence of thick iron rich oxides on the A1 and A1-Ce specimens. In contrast to the A1 and A1-Ce specimens, a thick oxide was merely formed near the sample edges of the A1-Si specimen (cf. Fig. 69). This explains the lower weight gain obtained for this specimen.

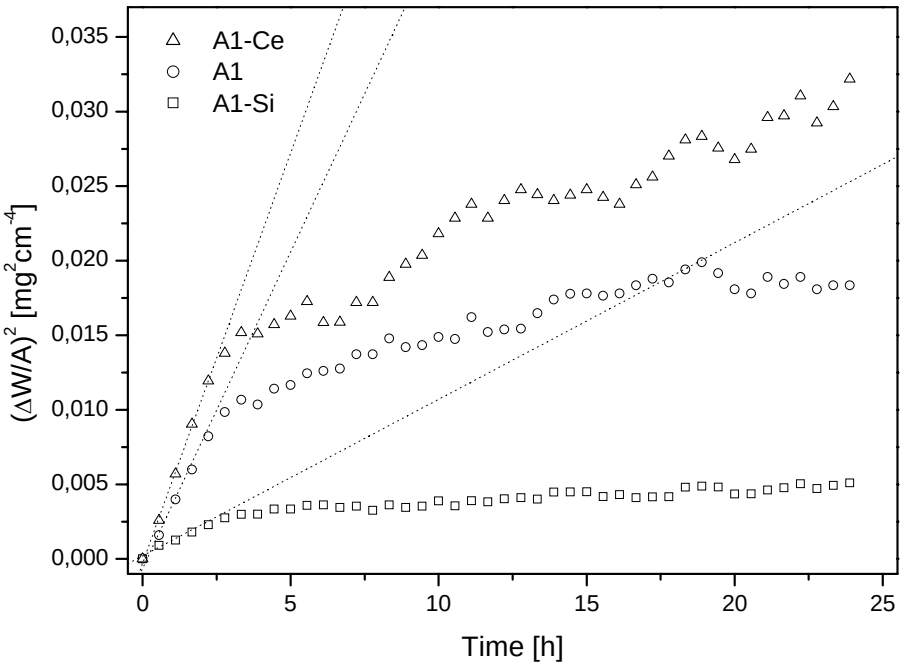

Fig. 75. TG measurements for the specimens oxidized at 1173 K for 24 h in air containing 50% water vapour.

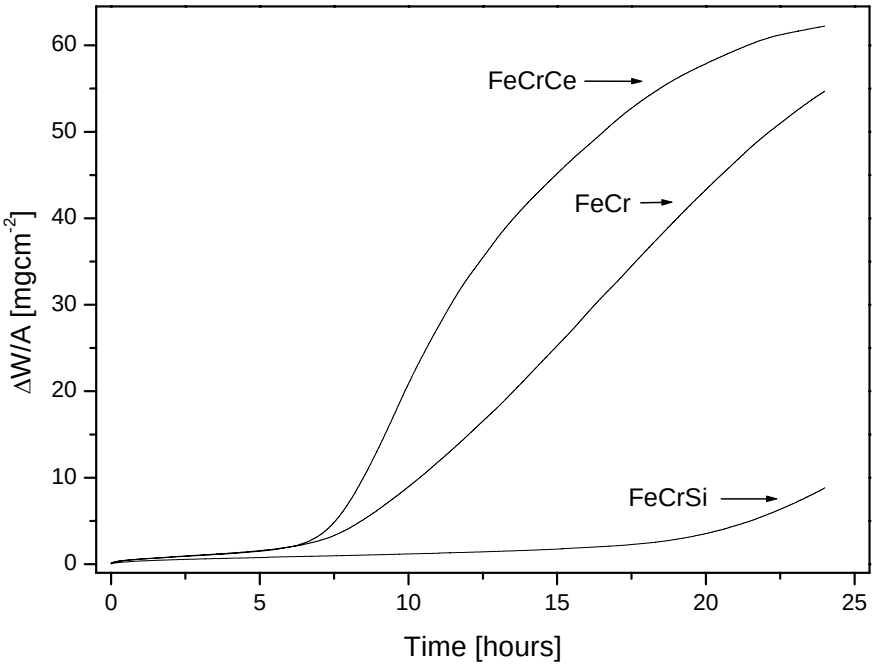

Fig. 76. TG measurements for the specimens oxidized at 1373 K for 24 h in air containing 0.7% water vapour.

8.4 Discussion

The results are discussed in terms of (i) the effect of water vapour and (ii) the effect of alloying additions. The effect of alloying additions was discussed in chapter 6, and will only be briefly discussed in the present chapter. Most of the samples studied in this chapter were oxidized at 1173 K. The oxide scales grown at 1173 K were identified as corundum-type oxides. The specimens were oxidized under similar conditions as the specimens described in chapter 5 and 6, but for a shorter period of time. This indicates that the oxide scales described in this chapter also consist of chromia. The effect of temperature on the oxidation behaviour is also investigated.

8.4.1 Oxidation at 1173 K

8.4.1.1 Effect of water vapour

Several effects of water vapour on the oxidation behaviour of iron-chromium alloys have been observed in the literature. The effects include

- Increased parabolic growth rate
- Increased tendency for breakaway oxidation
- Vaporization of chromium species

The first two effects cannot be treated as one effect. Although an increased parabolic growth rate may lead to breakaway oxidation, the increased tendency for breakaway oxidation can also be a result of the oxide scales becoming increasingly prone to mechanical failure in the presence of water vapour in the reaction atmosphere. In the present work, the breakaway oxidation was not investigated as being a direct result of the presence of water vapour. However, hypothesis for the effect of water vapour on the tendency for breakaway oxidation will be put forward. In contrast, however, water vapour was observed to affect the growth kinetics and vaporization behaviour and will therefore be discussed in more detail.

During the oxidation, the specimens gain in weight is caused by the formation of the chromia scale. However, the weight of the specimens may also decrease due to vaporization of volatile chromium species from the chromia scale during the oxidation (cf. section 2.4.4). Both effects are observed simultaneously during the TG measurements. Thus, the growth of the chromia scales must be carefully analysed. The usual parabolic rate equation, which gives a measure of the thickness of the oxide scale as a function of time, is given by (cf. Eq. 53)

$$\frac{dx}{dt} = \frac{k_P}{x} \qquad \text{Eq. 95}$$

The effect of vaporization has been analysed by Tedmon [65]. The vaporization of chromium species from the chromia scale is constant with time [65] and may be described by

$$\frac{dx}{dt} = -k_S \qquad \text{Eq. 96}$$

Hence, the total thickness of the oxide scale during oxidation may be obtained by adding Eq. 95 and Eq. 96

$$\frac{dx}{dt} = \frac{k_P}{x} - k_S \qquad \text{Eq. 97}$$

It follows that the growth of the oxide scale can be described by a modified parabolic rate equation, which is a summation of the loss due to vaporization and the increase due to the normal parabolic growth. Similar equations may be written for the weight gain of the oxide scale [65]. As described in Eq. 97, the chromia scale grows to a limiting scale thickness (or weight), which can be found by setting Eq. 97 equal to 0, i.e.

$$x = \frac{k_P}{k_S} \qquad \text{Eq. 98}$$

The interpretation of the limiting scale thickness is that the supply of chromium from the alloy to the chromia scale during the oxidation is balanced by a loss of chromium due to vaporization from the chromia scale. Once the limiting thickness of the sample is reached, the weight of the specimen decreases due to loss of chromium from the alloy beneath the oxide scale.

During TG measurements, the combined weight of the oxide and the alloy is obtained, i.e. the weight of the specimen. The weight change of the specimen is given by the oxygen uptake by chromia and the chromium loss due to vaporization. The oxygen uptake may be calculated from the thickness of the oxide using Eq. 97. Similarly, the loss of chromium due to vaporization may be determined from Eq. 96. A simple relation between the weight of the specimen and the time elapsed cannot be found. However, simplified expressions for the weight gain as a function of time, as measured by TG measurements, are given in Ref. [137]. When the vaporization from the oxide is negligible (i.e. $k_S \approx 0$), the weight gain of the specimens may be obtained using the normal parabolic rate expression (cf. section 2.3.5).

The partial pressures of volatile chromium species in equilibrium with chromia were determined and discussed in section 2.4.4. It was recognized that vaporization from chromia is only significant in the presence of air. The most abundant chromium containing species in equilibrium with chromia, in the presence of wet atmospheres, is $CrO_2(OH)_2(g)$ [39]. In the presence of air containing 0.008%, 0.7% and 50% water vapour, the equilibrium pressure of $CrO_2(OH)_2(g)$ is $2.4 \cdot 10^{-8}$ bar, $2.1 \cdot 10^{-7}$ bar and $1.5 \cdot 10^{-5}$ bar, respectively at 1173 K. This corresponds to a weight loss of 0.0017 mg, 0.014 mg and 1.04 mg, respectively, during 24 h from vaporization if the reaction gas passing the specimens becomes fully saturated with chromium containing species. A

gas flow of 60 ml/min was used in the calculation. The most abundant chromium containing species in equilibrium with chromia in dry air is $CrO_3(g)$ [39]. However, the equilibrium pressure of $CrO_3(g)$ is only $1.4 \cdot 10^{-8}$ bar in equilibrium with chromia in air at 1173 K [40]. This corresponds to a weight loss of approximately $9.4 \cdot 10^{-4}$ mg during the measurements. The partial pressures of chromium species and possible weight losses are summarized in Table 19. The contributions from both volatile chromium species are added for air containing 0.08% water vapour.

Table 19. The partial pressures of $CrO_2(OH)_2(g)$ in equilibrium with chromia at 1173 K in different atmospheres. The maximum weight loss of chromia is calculated using a gas flow of 60 ml/min past the specimens.

Gas	Air – 0.08%H_2O	Air – 0.7%H_2O	Air – 50%H_2O
Chromium pressure / bar	$3.8 \cdot 10^{-8}$	$2.1 \cdot 10^{-7}$	$1.5 \cdot 10^{-5}$
Max weight loss / mg	0.0026	0.014	1.04

The calculations given in Table 19 show that the vaporization of chromium containing species from the scale only becomes significant for air containing 50 % water.

The curves shown in Fig. 71-Fig. 74 are given as the weight increase square vs. time for the specimens oxidized at 1173 K in various reaction atmospheres. The curves show an approximately linear relationship. The parabolic rate constants may be determined from the relation (cf. Eq. 64)

$$w^2 = 2k_w t + C \qquad \text{Eq. 99}$$

where C is an integration constant. The linear relationship shows that vaporization from the chromia scale can be neglected, as calculated in Table 19.

The weight gains of the specimens oxidized in air containing 50% water vapour at 1173 K do not show a linear relationship (cf. Fig. 75). In contrast, the TG curves levels off to an almost constant value after an initial linear weight increase. The TG measurements given in Fig. 75 may be analysed using Eq. 96 and Eq. 97. However, the TG measurements show a considerable amount of scatter, so the results may only be used for a qualitative discussion. Hence, no attempts were made to analyse the curves using Eq. 96 and Eq. 97. According to Eq. 97, the growth rate of the chromia scale is highest during the initial oxidation. Furthermore, the first term in Eq. 97 dominates during the initial oxidation, where the thickness of the scale is small. The weight loss due to vaporization is constant with time, so the TG curves given in Fig. 75 can be approximated by a normal parabolic growth during the initial oxidation, where the first term in Eq. 97 dominates. Dotted lines are superimposed on the TG curves in Fig. 75 to indicate the linear relationship during the initial oxidation. Thus, parabolic rate constants may be obtained from the initial oxidation using Eq. 99.

The parabolic rate constants determined from the TG measurements in Fig. 71-Fig. 75 using Eq. 99 are given in Table 20.

Table 20. Parabolic rate constants determined from the TG measurements given in Fig. 71-Fig. 75 using Eq. 99.

k_w [$g^2cm^{-4}s^{-1}$]	A1-Ce	A1-Si	A1
H_2/Ar – 0.02% H_2O	$7.87 \cdot 10^{-13}$	$1.07 \cdot 10^{-13}$	$1.37 \cdot 10^{-12}$
H_2/Ar – 0.7% H_2O	$2.65 \cdot 10^{-12}$	$4.87 \cdot 10^{-13}$	$2.65 \cdot 10^{-12}$
Air – 0.08% H_2O	$1.10 \cdot 10^{-12}$	$4.69 \cdot 10^{-13}$	$1.73 \cdot 10^{-12}$
Air – 0.7% H_2O	$5.77 \cdot 10^{-13}$	$3.33 \cdot 10^{-13}$	$9.53 \cdot 10^{-13}$
Air – 50% H_2O	$7.64 \cdot 10^{-13}$	$1.46 \cdot 10^{-13}$	$5.89 \cdot 10^{-13}$

The magnitude of the parabolic rate constants given in Table 20 is similar to rate constants given in Table 11 for the specimens oxidized for 70 h. This lends support to the fact that the scales studied in this chapter were grown by a similar growth mechanism as those described in chapter 5 and 6, even though the oxidation time of the specimens was different.

By comparing Fig. 71 and Fig. 72, it is apparent that the presence of water vapour in the reaction atmosphere increases the oxidation rate of chromia. It was, however, observed in chapter 5 and 6 that increasing the water vapour content from 1% to 12% did not increase the growth rate of the chromia scales during oxidation at 1173 K for 70 h. This was observed for oxidation in hydrogen/argon. Thus, vaporization from the specimens could be neglected. It is concluded from the TG measurements that the presence of water accelerates the oxidation. The oxidation rate, however, appears to be independent of the amount of water present during the oxidation.

The weight gain for the specimens oxidized in dry hydrogen/argon is lower than that obtained for the samples oxidized in dry air. This indicates that sufficient water vapour is present in the dry air in order to accelerate the oxidation. Furthermore, from Fig. 73 and Fig. 74, it is evident that the presence of 0.7% water vapour decreased the weight gain of the specimens in comparison with the samples oxidized in air containing 0.08% water vapour. This may be a result of the vaporization from the chromia scale. However, the maximum weight loss given in Table 19 indicates that the vaporization from the chromia scale is of minor importance under the present test conditions. A possible explanation for the discrepancy is that the activities of the chromium species, which were calculated on the basis of thermodynamic data given by Ebbinghaus [40], are too low. However, an increased vaporization from the specimen would result in a non-parabolic oxidation behaviour, as discussed. This is not observed (cf. Fig. 74), even though the measurements showed some scatter. The reason for the discrepancy is presently unknown.

In contrast to the decrease in weight gain due to vaporization, the growth of the chromia scales increased in the presence of water vapour. An increased oxidation of steels in the presence of water vapour has previously been observed in the literature [10,17,30,53,54]. Several reasons may be proposed for the increase in the parabolic oxidation rate of chromia in the presence of water vapour

- Increased defect concentration of reactants
- Increased mobility of defects
- Increased interfacial reaction rate

- Changes in mechanical properties

It is well known that hydrogen can dissolve as protons in oxides [17]. The electrical conductivity has recently been measured for chromia in different reaction atmospheres [15,16]. It was found that hydrogen dissolves in chromia and affects the defect structure of the oxide. Hence, hydrogen may dissolve in chromia and change the defect concentration of the reactants (chromium and oxygen) and thereby change the growth rate of the chromia scale. The dissolution of hydrogen in chromia during the oxidation in the presence of water vapour may be written [17]

$$H_2O(g) \leftrightarrow 2H_i^{\bullet} + 2e^{/} + \frac{1}{2}O_2(g) \qquad \text{Eq. 100}$$

Hydrogen is present as an interstitial defect in chromia. The protons bond to oxygen ions to form hydroxide ions $OH_O^{\bullet}$ in the oxide [17]. Norby [17] has calculated possible changes in the defect structure after the dissolution of protons in the oxide. According to the electroneutrality principle, the content of negative defects will increase as the content of dissolved protons increases. Hence, the content of chromium vacancies and oxygen interstitials increases, while the content of chromium interstitials and oxygen vacancies decreases, as the content of dissolved protons increases. The growth of the chromia scales is governed by chromium interstitials, as discussed in chapter 5. This was also observed in the presence of water in the reaction atmosphere in this work. Thus, the enhanced chromia growth in the presence of water vapour cannot easily be explained from a change in the defect concentrations.

Another possible explanation may be an increased mobility of the defects after the dissolution of protons in the oxide. An important parameter for the mobility of ions is the ionic radius. As previously mentioned, the protons are bonded to the oxygen ions. The ionic radius of the hydroxide ion is considerable smaller than the ionic radius of the oxygen ion (0.95 Å vs. 1.40 Å) [138]. Thus, the hydroxide ions diffuse faster than the oxygen ions in the scale. The increased transport of oxygen through the chromia scale may increase the growth rate of chromia (cf. Eq. 55), as suggested by Galerie et al. [139]. Furthermore, an increased formation of chromia near the alloy/chromia interface after the addition of water vapour in the reaction atmosphere has been observed [53]. This indicates increased oxygen diffusion through the scale. The growth of the chromia scale is governed by diffusion through grain boundaries. Thus, the segregation of hydrogen to grain boundaries in the scale, where it may affect the transport properties, may be important, but experimental evidence is lacking [17,30].

Instead of an increased oxidation rate caused by an increased diffusivity of reactants in the oxide, the oxidation rate may increase on account of an increased interfacial reaction rate at the oxide/gas interface, in the presence of water vapour, as proposed in Ref. [140]. It was discussed in chapter 5 that the molecular dissociation of water is much easier than the corresponding molecular dissociation of oxygen (see also Ref. [141]). An increased interfacial reaction rate leads to an increase in the oxygen potential gradient over the bulk oxide scale [28,140], since the oxygen potential in the *bulk* oxide scale at the oxide/gas interface will increase. For this work, however, the growth rate is considered to be governed by the concentration of chromium interstitials at the alloy/chromia interface, as shown in section 5.4.2. Thus, the growth rate of chromia is independent of the oxygen potential at the chromia/gas interface.

Furthermore, the results obtained in the present work in chapter 5 and 6 show that the growth rate of the chromia scales do not increase as a result of an increase in the water vapour content. This indicates that the growth rate is unaffected by the interfacial reaction. Furthermore, it is believed that the interfacial reactions do not exert an influence on the parabolic growth rate of the oxide scale, as mentioned in section 2.3.2.

Another approach may be that the mechanical properties of the chromia scale changes after the dissolution of hydrogen in chromia. The stresses generated during the growth of chromia scales are relieved by plastic deformation of the oxide. The plastic deformation of the chromia scale is limited by the minority defect [17], i.e. oxygen vacancies. The dissolution of hydrogen in the oxide may decrease the content of oxygen vacancies, as previously mentioned. Thus, the presence of water vapour may change the ability of the chromia scale to deform plastically. The generation of stresses may lead to an increased formation of high diffusivity paths through the scale and thereby an increased oxidation rate. However, it is difficult to isolate the effect of water vapour from other effects on the mechanical properties [30]. Furthermore, a recent study has shown that the compressive stresses in a chromia scale decreased in the presence of water vapour [142].

The most probable cause for the increase in oxidation rate after the addition of water vapour appears to be the greater mobility of oxygen ions by way of hydroxide ions, or the change of the mechanical properties of the scale. It should be noticed, however, that the growth mechanism of the scales grown in the present thesis was governed by chromium diffusion, as observed from the presence of whiskers. Furthermore, the growth of the oxide scale is unaffected by the increase in water vapour content from 1% to 12% (cf. chapter 5 and 6). This indicates that the growth rate of the oxide is independent of the content of the hydroxide ion in the oxide. Thus, the increase in the growth rate is most likely governed by a change of mechanical properties. However, further experimental evidence is needed in order to verify the proposals.

An increased tendency for failure of the chromia scale in the presence of water vapour is well known from the literature [10,30]. A possible explanation for this can be a changed tendency for plastic deformation, as mentioned. Another possible explanation for this could be that hydrogen dissolves in the alloy matrix, when protons diffuse inward through the chromia scale. This may result in brittleness in the alloy, and subsequently loss of chromia adhesion to the metal and initiation of breakaway oxidation [17].

8.4.1.2 Effect of alloying additions

As seen from Fig. 71-Fig. 75, the oxidation rate of the A1-Si specimens is considerable lower than the A1-Ce and A1 specimens. The effect of cerium and silicon on the oxidation behaviour has already been discussed in chapter 6.

According to the proposed growth mechanism for the chromia scales grown on the A1-Ce specimens in chapter 6, the growth rate of chromia is most likely reduced by

the formation of RE oxides within the chromia scale, or by changes in defect concentrations at the grain boundaries of the chromia scale. Thus, it is plausible that the REE will increase during the oxidation as an increasing amount of RE becomes present in the chromia scale. The result of such a growth mechanism may be that the parabolic rate constant decreases during oxidation, since the chromium diffusion coefficient gradually decreases. Such an effect was not observed in the present work, where the TG measurements could be described by a single parabolic rate constant. However, the growth rate decreased only slightly as a result of the cerium additions to the alloy, thus it may not be possible to observe an effect. Furthermore, an REE may only be observed after oxidation for longer periods of time or at higher temperatures, where the REE is more pronounced [74]. In this case, the oxidation behaviour may be further complicated by grain growth in the oxide and other effects, which also changes the oxidation rate [10]. A reduction of the parabolic growth rate during the oxidation has to the author's knowledge not been reported in the literature as an effect of the RE addition.

The oxidation of the A1-Si specimens also followed a single parabolic growth rate (cf. Fig. 71-Fig. 74). During the previous discussion in chapter 6 on the effect of silicon on the chromia growth rate, it was proposed that silica formed beneath the grain boundaries of the chromia scale and thereby reduced the growth rate of the scale. It is plausible that the continuous growth of silica precipitates beneath chromia during the oxidation could reduce the grain boundary area for chromium diffusion, and thereby reduce the growth rate of the chromia scale even further. However, it was observed from the TG measurements that the growth of the chromia scales followed an approximately constant parabolic rate. Following the proposed oxidation mechanism, silica must be formed during the initial oxidation as internal oxides beneath the growing chromia scale, since the growth rate also is reduced during the initial oxidation of the specimens. This indicates that only a low concentration of silica is required at the alloy/chromia interface in order to improve the oxidation resistance. This is in support of the reduced growth rate obtained for the A1-CeSi specimens, which contained only half the amount of silicon (cf. chapter 6).

The beneficial effect of silicon to reduce the growth rate of chromia has often been described as an effect of the formation of a dense silica layer beneath the chromia scale, as discussed in chapter 6. However, the formation of a continuous silica layer would result in a significant decrease of the oxidation rate during the oxidation [68]. Furthermore, a reduction in growth rate would not occur during the initial oxidation, where a dense silica layer has not formed yet. Instead, the TG measurements are in support of the proposed oxidation mechanism described in chapter 6.

8.4.2 Oxidation at 1373 K

8.4.2.1 Oxide microstructure

The diffraction patterns obtained for the specimens oxidized at 1373 K are shown in Fig. 70. The thick oxide scales grown on the A1 and A1-Ce specimens were

corundum-type oxides. The morphology of the thick oxide on the specimens was similar to the morphology observed during the breakaway oxidation discussed in chapter 7. The outermost part of the thick iron rich oxides grown in air was identified as hematite in chapter 7. Thus, it is concluded that the corundum-type oxide grown on the A1 and A1-Ce specimens, in the present chapter, was hematite.

The diffraction pattern obtained for the A1-Si specimen revealed the presence of two distinct corundum-type oxides, and in addition, the diffraction pattern showed reflections from a spinel-type oxide. The complex diffraction pattern is probably a result of reflections obtained from both the thin oxide in the middle of the specimen and from the thick iron rich oxide near the edges (cf. Fig. 69). It was observed in chapter 7 that the thin oxides grown at 1373 K for 70 h consisted of chromia with a small amount of iron in the outermost oxide. The iron will be present in a solid solution corundum-type oxide for the specimen examined in the present chapter, since the specimen was oxidized in air. The iron concentration in the thin oxide region in the middle is considered to be low, so the reflections obtained from the thin oxide are probably similar to reflections obtained from a pure chromia scale. The thick oxide near the edges consists of hematite, as previously discussed. The hematite layer may be thin in the present case, so the reflections obtained from the spinel-type oxide may be due to the presence of magnetite beneath the hematite layer, as discussed in chapter 7.

8.4.2.2 Oxidation kinetics

The TG measurements of the specimens oxidized at 1373 K in air containing 0.7% water vapour are given in Fig. 76. The oxidation behaviour of the specimens does not follow a parabolic rate law. Instead, breakaway oxidation has occurred. This breakaway oxidation is also observed when studying the oxide morphology.

It is interesting to investigate whether the specimens in Fig. 76 follow a parabolic rate during the initial oxidation, i.e. if the initial growth is governed by a steady state growth of chromia. This is examined in Fig. 77, where the initial weight gain is plotted as a function of time. The initial weight gains were fitted with the parabolic rate law (cf. Eq. 64), which is superimposed as dotted lines on the weight gains (cf. Fig. 77). The oxide scales initially grow according to a parabolic rate law. Hence, the oxide scales have an initial protective character before the breakaway oxidation is initiated, as described in chapter 7. The oxide scale grown on the A1-Si specimen grows according to a parabolic rate law for a longer period of time than the other specimens. Thus, the A1-Si specimen is more resistant toward breakaway oxidation than the other samples. The parabolic rate constants during the initial oxidation have been calculated and are given in Table 21.

During the oxidation of the specimens at 1373 K, a short steady state oxidation was observed for all the specimens before a breakaway oxidation was initiated. The protective period was longest for the A1-Si specimen. Similarly, the steady state oxidation was slowest for the specimen containing silicon. Thus, an important parameter for the protectiveness of the scale is the thickness of the scale, especially near the edges, where the specimens are most likely to crack, as discussed in section

7.4.4.2. Interestingly, the breakaway oxidation is initiated at the same scale thickness for the specimens in Fig. 77. Thus, it is most likely the decreased growth rate of chromia, which is the most important parameter for the protectiveness of the chromia scales. In contrast, the presence of silica at the alloy/scale is probably of minor importance, during isothermal oxidation, for the protectiveness of the chromia scale.

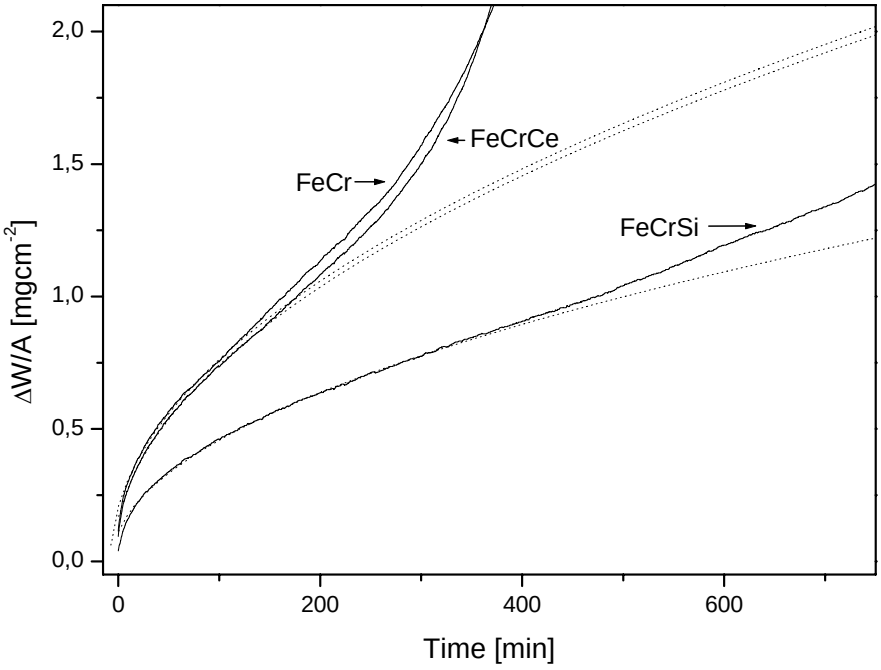

Fig. 77. The initial weight gain from Fig. 76. The superimposed dotted line are fitted to the parabolic rate law, as given in Eq. 64.

Table 21. Parabolic rate constant obtained from the initial oxidation of the specimens oxidized at 1373 K in air containing 0.7% water vapour. The parabolic rate constants were obtained from the dotted lines in Fig. 77.

	A1-Ce	A1-Si	A1
k_w [$g^2cm^{-4}s^{-1}$]	$4.36 \cdot 10^{-11}$	$1.65 \cdot 10^{-11}$	$4.48 \cdot 10^{-11}$

The rate constants obtained from the TG measurements given in Fig. 77 may be compared to parabolic rate constants obtained for the growth of chromia at 1173 K (cf. Table 20). The parabolic rate constant is related to the chromium diffusion coefficient through Eq. 78. Hence, the temperature dependency on the parabolic rate may be described by an Arrhenius-type expression (cf. Eq. 22)

$$k_p = A\exp\left(\frac{-E_A}{RT}\right) \qquad \text{Eq. 101}$$

where A is a constant and E_A is the activation energy for the diffusion of chromium through the chromia scale (cf. section 2.1). Hence, the activation energy for the

chromium diffusion may tentatively be determined using Eq. 101. The parabolic constants obtained at 1173 and 1373 K are given in Table 22 together with the calculated activation energies.

The activation energy for the chromium diffusion was reported in the 245-280 $kJmol^{-1}$ range in section 2.2.2. The activation energies given in Table 22 are in a similar range, although the uncertainties are very large, since the values were determined from only two measurements. The comparison also shows that the initially formed protective oxide in Fig. 77 most likely is chromia.

Table 22. The parabolic rate constants obtained for specimens oxidized at 1173 and 1373 K in air containing 0.7% water vapour. The activation energies were calculated using Eq. 101.

k_w [$g^2cm^{-4}s^{-1}$]	A1-Ce	A1-Si	A1
k_w (1173 K) [$g^2cm^{-4}s^{-1}$]	$5.77 \cdot 10^{-13}$	$3.33 \cdot 10^{-13}$	$9.53 \cdot 10^{-13}$
k_w (1373 K) [$g^2cm^{-4}s^{-1}$]	$4.36 \cdot 10^{-11}$	$1.65 \cdot 10^{-11}$	$4.48 \cdot 10^{-11}$
E_A [$kJmol^{-1}$]	290	191	328

8.5 Summary

The effect of water vapour on the oxidation behaviour of the A1, A1-Ce and A1-Si alloys was examined. It was found that the presence of water vapour in the reaction atmosphere increased the oxidation rate. This may be caused by a higher mobility of oxygen by way of hydroxide ions. However, the growth rate did not increase when the water vapour content was increased from 1% to 12%, as shown in chapter 5 and 6. Another possibility is an increased formation of high diffusivity paths in the chromia scale due to a change in the mechanical properties of the scale after the dissolution of hydrogen in the scale.

The oxidation rate was also observed to decrease as a result of vaporization from the chromia scale, when the specimens were oxidized in air containing 50% water vapour.

The oxidation rate of the specimens could be assigned to a single parabolic rate constant when vaporization from the specimen could be neglected. This is in support of the proposed mechanism for silica in chapter 6. However, the parabolic rate constant could change slowly, so this needs to be confirmed from additional TG measurements.

The oxidation behaviour at 1373 K showed a breakaway oxidation after an initial parabolic growth rate due to the growth of chromia. The breakaway oxidation was initiated at some critical thickness of the chromia scale.

9 Summary and Conclusion

This Ph.D. thesis presents results on the high temperature oxidation behaviour of the ferritic alloy $Fe_{78}Cr_{22}$. The effect of small alloying additions of cerium and/or silicon was also investigated.

The chromia scales grown under reducing conditions on the iron-chromium alloy exhibited the formation of oxide whiskers and ridges at the surface. In contrast, the chromia scales formed in air showed the formation of larger (2-3 μm) grains near the surface. This difference was caused by the vaporization of chromium species from the scale grown in air. Two different growth mechanisms were given for the growth of oxide whiskers. The chromia whiskers were either formed from the top of the whiskers or from the base of the whiskers. In both cases, the whiskers were formed due to a rapid diffusion of reactants through the hollow chromia whiskers.

The growth rate of the chromia scales was independent of the oxygen activity in the reaction atmosphere. This was explained by a growth mechanism of the chromia scales, where the growth was governed by interstitial chromium. This growth mechanism may be understood considering that only two-thirds of the octahedral sites in the chromia lattice are occupied by chromium.

The addition of cerium to the iron-chromium alloy improved the adhesion of the chromia scale and decreased the growth rate of chromia slightly. This effect of cerium is known from the literature as the “reactive element effect”. It was observed that the minimum content of cerium in the alloy should be 0.3 at.% in order to observe a significant effect of the cerium addition in this work. The reduction in the growth rate of chromia after the addition of cerium was small in this work. The reduction in growth rate is caused by a change in the growth mechanism of chromia, and the fact that oxygen diffusion is considerably slower than chromium diffusion through the grain boundaries. A change in the growth mechanism was not observed in this work. This was in accordance with the small reduction in growth rate.

The improved adhesion of the chromia scale in the presence of cerium in the alloy was most likely caused by a scavenging of impurities such as sulfur at the alloy/chromia interface, which otherwise would deteriorate the adhesion of the chromia scale. Another possible explanation was a decreased outward diffusion of chromium. Further studies are, however, necessary in order to identify the most important parameters for the improved adhesion in the presence of cerium in the alloy.

The addition of silicon to the iron-chromium alloy resulted in the formation of silica particles beneath the chromia scale as a result of internal oxidation. The addition of silicon resulted in a decreased growth rate of the chromia scale. The growth rate of chromia might decrease due to the formation of a dense silica layer beneath the chromia scale. In this case, the continued oxidation of the alloy would be governed by the growth of silica after the formation of a dense silica layer. The growth rate of the chromia scale was, however, observed to decrease during the initial oxidation as a result of the silicon addition. Furthermore, it was found that the growth of the chromia scale could be described by a constant parabolic rate constant. This implies that the

growth mechanism did not change during the oxidation. Thus, the decreased growth rate was not caused by the formation of a dense silica layer beneath the chromia scale. This was in support of the observed microstructure of the oxidized specimens, which indicated that silica was present as distinct particles beneath the chromia scale. Although, the silica particles did not coalesce to a dense silica layer beneath the chromia scale in this study, a calculation showed that the alloy might form a dense layer of silica after an extended oxidation period. Instead of being a result of a dense silica layer, it was proposed that the reduced growth rate of chromia was caused by a partially blocking of the chromia grain boundaries at the alloy/chromia interface. According to this proposal, only a small amount of silica was necessary beneath the grain boundaries in order to partially block the chromium diffusion. In support of the proposed growth mechanism, it was observed that the growth rate decreased after the addition of a low amount of silicon. However, the mechanism required that the silica particles were positioned preferentially beneath the grain boundaries of the scale. Thus, TEM investigations of the alloy/chromia interface are necessary in order to determine whether silica particles are positioned preferentially beneath grain boundaries of the chromia scale. The parabolic rate was observed to be constant during the TG measurements in this work. However, the parabolic rate constant might decrease slightly during the oxidation of the specimens, since an increasing amount of silica was formed at the interface during the oxidation. This might, according to the proposed mechanism, continuously decrease the parabolic rate constant during the oxidation. This can be investigated through TG measurements, where the surface area of the specimens and thereby the weight gain during the measurements is larger than those observed in this study. Furthermore, the specimens may be investigated for longer times and/or higher temperatures in order to achieve a better signal/noise ratio.

The oxide scales grown on the various alloys at 1373 K exhibited the presence of thick iron rich oxides in the scales. The presence of iron rich scales was described as a result of failure of the chromia scale and subsequent breakaway oxidation of the alloy. The breakaway oxidation was initiated at the sample edges at some critical scale thickness. In contrast to steady state growth of chromia scales, the breakaway oxidation was highly affected by the oxygen activity in the reaction atmosphere. A protection against breakaway oxidation of the alloy occurred when the oxygen activity was below the stability of wüstite. Thus, a tuning of the oxygen activity, such that wüstite is not thermodynamically stable might be useful for long term oxidation of iron-chromium alloys under reducing conditions. A mechanism for the breakaway oxidation was put forward, which explained the observed oxidation behaviour of the alloys.

The effect of water vapour on the chromia growth rate was investigated. It was found that the presence of water vapour in the reaction atmosphere increased the growth rate of chromia. It was proposed that hydrogen dissolved in the chromia scale and thereby changed the defect structure of the chromia scale. It was believed that the presence of water vapour changed the ability of the chromia scale to deform plastically by reducing the concentration of the minority defect. The generation of stresses might lead to an increased formation of high diffusivity paths through the scale and thereby an increased oxidation rate. However, the increase in oxidation rate might also be caused by an increased mobility of oxygen ions by way of hydroxide ions. Further experimental evidence is needed in order to verify the proposals. This may be gathered through measurements using the novel TG equipment in atmospheres

containing varies amounts of water vapour. The growth rate of chromia was observed to decrease, when the alloys were oxidized in air containing large amounts of water vapour. This was a result of vaporization of chromium containing species from the chromia scale during the oxidation. Thus, the presence of water vapour increased the oxidation rate through hydrogen dissolution in the chromia scale, and chromium was simultaneously lost from the scale during oxidation. The combined result, as obtained through TG measurements, must be carefully analysed.

The iron-chromium alloys investigated in the present work may be used for interconnector material in SOFC stacks.

The formation of a dense layer of silica during the oxidation would be detrimental for the electrical conductivity across the interconnector plate. Thus, the addition of silicon to iron-chromium alloys should be low such that a dense layer of silica is not formed during oxidation. Furthermore, the formation of silica at the alloy/chromia interface increases the likelihood of spallation of the chromia during thermal cycling. The SOFC stacks are often thermal cycled between room temperature and operational temperature during the life time operation. These results indicated that silicon should be avoided as alloying element for interconnector materials. The addition of aluminium as alloying element to iron-chromium interconnector materials may instead be a better choice. The content of aluminium should, however, be low such that a dense layer of alumina is not formed, which otherwise would be detrimental for the electrical conductivity across the interconnector plate. Importantly, alumina is more spallation resistant during thermal cycling than silica, and the formation of internal alumina particles might also decrease the growth rate of chromia in a similar fashion as silica.

The addition of cerium to alloys has a beneficial effect on the oxidation behaviour of interconnector materials for the use in SOFC stacks. This is mainly caused by the improved adhesion of the oxide scale to the alloy. Due to the improved adhesion, the addition of cerium increases the spallation resistance of the chromia scale through thermal cycling.

A tuning of the oxygen activity on the anode side of the fuel cell, such that wüstite is thermodynamically unstable, may be useful during long term oxidation of iron-chromium alloys for the use as interconnector material, since the breakaway oxidation is inhibited.

10 References

[1] N. Q. Minh, T. Takahashi, Science and Technology of Ceramic Fuel Cells, Elsevier, Amsterdam, 1995, pp. 1-366.
[2] S. Linderoth, P. H. Larsen, in: D. H. Doughty, L. F. Nazar, M. Arakawa, H.-P. Brack, K. Naoi (Eds.), Mater. Res. Soc. Symp. Proc., vol. 575, 2000, pp. 325-330.
[3] S. Linderoth, Surf. Coat. Technol. 80 (1996) 185
[4] P. Y. Hou, K. Huang, W. T. Bakker, in: S. C. Singhal, M. Dokiya (Eds.), Electrochemical Society Proceedings, vol. 99-19, 1999, pp. 737-748.
[5] T. Brylewski, M. Nanko, T. Maruyama, K. Przybylski, Solid State Ionics 143 (2001) 131
[6] P. Kofstad, R. BredeseN, Solid State Ionics 52 (1992) 69
[7] J. P. Abellán, V. Shemet, F. Tietz, L. Singheiser, W. J. Quadakkers, in: H. Yokokawa, S. C. Singhal (Eds.), Electrochemical Society Proceedings, vol. 2001-16, 2001, pp. 811-819.
[8] K. Honegger, A. Plas, in: H. Yokokawa, S. C. Singhal (Eds.), Electrochemical Society Proceedings, vol. 2001-16, 2001, pp. 803-810.
[9] H. E. Evans, A. T. Donaldson, T. C. Gilmour, Oxid. Met. 52 (1999) 379
[10] P. Kofstad, High Temperature Corrosion, Elsevier, London, 1988, pp. 1-558.
[11] M. H. R. Lankhorst, H. J. M. Bouwmeester, H. Verweij, J. Am. Ceram. Soc. 80 (1997) 2175
[12] S. Sunde, in: A. J. McEvoy, K. Nisancioglu (Eds.), 1997, pp. 19-32.
[13] H. Rickert, Electrochemistry of Solids, An Introduction, Springer-Verlag, Berlin, Germany, Berlin, Germany, 1982
[14] S. Elliott, The Physics and Chemistry of Solids, John Wiley & Sons, Chichester, England, Chichester, England, 1998, pp. 1-772.
[15] A. Holt, P. Kofstad, Solid State Ionics 69 (1994) 137
[16] A. Holt, P. Kofstad, Solid State Ionics 69 (1994) 127
[17] T. Norby, J. Phys. IV 3 (1993) 99
[18] A. C. S. Sabioni, A. M. Huntz, F. Millot, C. Monty, Philosophical Magazine A-Physics of Condensed Matter Structure Defects and Mechanical Properties 66 (1992) 351
[19] P. Kofstad, K. P. Lillerud, Oxid. Met. 17 (1982) 177
[20] C. Greskovich, J. Am. Ceram. Soc. 67 (1984) C111
[21] A. C. S. Sabioni, A. M. Huntz, F. Millot, C. Monty, Philosophical Magazine A-Physics of Condensed Matter Structure Defects and Mechanical Properties 66 (1992) 361
[22] A. C. S. Sabioni, B. Lesage, A. M. Huntz, J. C. Pivin, C. Monty, Philosophical Magazine A-Physics of Condensed Matter Structure Defects and Mechanical Properties 66 (1992) 333
[23] Atoms - software, 2001
[24] P. Kofstad, K. P. Lillerud, J. Electrochem. Soc. 127 (1980) 2410
[25] C. Wagner, Z. Phys. Chem. B21 (1933) 25
[26] C. Wagner, J. Electrochem. Soc. 103 (1956) 627
[27] C. Wagner, J. Electrochem. Soc. 99 (1952) 369
[28] H. J. M. Bouwmeester, H. Kruidhof, A. J. Burggraaf, Solid State Ionics 72 (1994) 185
[29] H. J. Grabke, Diffusions in Materials: Dimat2000, Pts 1 & 2 194-1 (2001) 1649

[30] D. L. Douglass, P. Kofstad, A. Rahmel, G. C. Wood, Oxid. Met. 45 (1996) 529
[31] H. V. Atkinson, Oxid. Met. 24 (1985) 177
[32] C. M. Lin, V. S. Stubican, J. Am. Ceram. Soc. 73 (1990) 587
[33] A. Atkinson, R. I. Taylor, Philosophical Magazine A-Physics of Condensed Matter Structure Defects and Mechanical Properties 43 (1981) 979
[34] O. Kubaschewski, C. B. Alcock, P. J. Spencer, Materials Thermochemistry, Pergamon Press Ltd, Oxford, 1993, pp. 1-363.
[35] A. D. Dalvi, D. E. Coates, Oxid. Met. 5 (1972) 113
[36] W. W. Smeltzer, Materials Science and Engineering 87 (1987) 35
[37] Thermo-Calc Software, 1993
[38] J. R. Taylor, A. T. Dinsdale, Z. Metallkd. 84 (1993) 335
[39] K. Hilpert, D. Das, M. Miller, D. H. Peck, R. Weiss, J. Electrochem. Soc. 143 (1996) 3642
[40] B. B. Ebbinghaus, Combust. Flame 93 (1993) 119
[41] H. J. Grabke in: H. J. Grabke, D. B. Meadowcroft (Eds.), Guidelines for Methods of Testing and Research in High Temperature Corrosion, Institute of Materials, London, 1995, pp. 52-61.
[42] Peter Halvor Larsen, Personal communication, 2003
[43] T. Tveten, ph.d.-thesis, 2000
[44] Netzsch Gerätebau GmbH, Netzsch STA 409 CD equipment, 2003
[45] P. J. Goodhew, F. J. Humphreys, Electron microscopy and analysis, Taylor § Francis Ltd., London, 1988, pp. 1-232.
[46] Per Morgen, Personal communication, 2003
[47] B. D. Bastow, G. C. Wood, D. P. Whittle, Oxid. Met. 16 (1981) 1
[48] G. C. Wood, Oxid. Met. 2 (1970) 11
[49] H. Hindam, D. P. Whittle, Oxid. Met. 18 (1982) 245
[50] G. C. Wood, F. H. Stott, Mater. Sci. Technol. 3 (1987) 519
[51] B. Chattopadhyay, G. C. Wood, J. Electrochem. Soc. 117 (1970) 1163
[52] E. A. Polman, T. Fransen, P. J. Gellings, Oxid. Met. 32 (1989) 433
[53] G. Hultquist, B. Tveten, E. Hornlund, Oxid. Met. 54 (2000) 1
[54] H. Asteman, J. E. Svensson, M. Norell, L. G. Johansson, Oxid. Met. 54 (2000) 11
[55] R. L. Tallman, E. A. Gulbransen, J. Electrochem. Soc. 114 (1967) 1227
[56] D. A. Voss, E. P. Butler, T. E. Mitchell, Metall. Trans. A 13 (1982) 929
[57] G. M. Raynaud, R. A. Rapp, Oxid. Met. 21 (1984) 89
[58] P. Kofstad, Nonstoichiometry, Diffusion and Electrical Conductivity in Binary Metal Oxides, Wiley, New York, 1972, pp. 1-382.
[59] H. S. Hsu, G. J. Yurek, Oxid. Met. 17 (1982) 55
[60] E. T. Turkdogan, W. M. Mckewan, L. Zwell, J. Phys. Chem. 69 (1965) 327
[61] K. P. Lillerud, P. Kofstad, J. Electrochem. Soc. 127 (1980) 2397
[62] P. Y. Hou, J. L. Smialek, Scr. Metall. Mater. 33 (1995) 1409
[63] D. G. Lees, Oxid. Met. 27 (1987) 75
[64] H. E. Evans, International Materials Reviews 40 (1995) 1
[65] C. S. Tedmon, J. Electrochem. Soc. 113 (1966) 766
[66] L. Mikkelsen, P. H. Larsen, S. Linderoth, Journal of Thermal Analysis and Calorimetry 64 (2001) 879
[67] C. Vogel, C. Juhl, E. Maahn, Metallurgi for ingeniører, Akademisk Forlag, 1995, pp. 1-723.
[68] F. H. Stott, G. J. Gabriel, F. I. Wei, G. C. Wood, Werkstoffe und Korrosion-Materials and Corrosion 38 (1987) 521

[69] H. E. Evans, D. A. Hilton, R. A. Holm, S. J. Webster, Oxid. Met. 19 (1983) 1
[70] G. C. Wood, Richards.JA, M. G. Hobby, J. Boustead, Corros. Sci. 9 (1969) 659
[71] R. C. Lobb, J. A. Sasse, H. E. Evans, Mater. Sci. Technol. 5 (1989) 828
[72] D. P. Moon, Mater. Sci. Technol. 5 (1989) 754
[73] L. B. Pfeil, U.K. Patent No. 459848, 1937
[74] B. A. Pint, Oxid. Met. 45 (1996) 1
[75] Phase Diagrams for Ceramists, The American Ceramic Society, Columbus, OH, 1975
[76] R. A. Rapp, Corrosion 21 (1965) 382
[77] A. Strawbridge, F. H. Stott, G. C. Wood, Corros. Sci. 35 (1993) 855
[78] N. Patibandla, T. A. Ramanarayanan, F. Cosandey, J. Electrochem. Soc. 138 (1991) 2176
[79] P. Y. Hou, J. Stringer, Materials Science and Engineering A-Structural Materials Properties Microstructure and Processing 202 (1995) 1
[80] Y. Saito, B. Onay, T. Maruyama, J. Phys. IV 3 (1993) 217
[81] S. Chevalier, J. P. Larpin, Acta Materialia 50 (2002) 3105
[82] T. A. Ramanarayanan, J. D. Mumford, C. M. Chun, R. A. Petkovic, Solid State Ionics 136 (2000) 83
[83] R. J. Hussey, M. J. Graham, Oxid. Met. 45 (1996) 349
[84] F. H. Stott, G. C. Wood, J. Stringer, Oxid. Met. 44 (1995) 113
[85] Y. He, H. Qi, X. Bai, D. Wang, Z. Li, C. Xu, W. Gao, High Temperature Materials and Processes 19 (2000) 71
[86] A. Strawbridge, P. Y. Hou, Materials at High Temperatures 12 (1994) 177
[87] A. Rahmel, M. Schutze, Oxid. Met. 38 (1992) 255
[88] A. M. Huntz, S. Daghigh, A. Piant, J. L. Lebrun, Materials Science and Engineering A-Structural Materials Properties Microstructure and Processing 248 (1998) 44
[89] P. Y. Hou, Oxid. Met. 52 (1999) 337
[90] P. Fox, D. G. Lees, G. W. Lorimer, Oxid. Met. 36 (1991) 491
[91] G. C. Wood, J. Stringer, J. Phys. IV 3 (1993) 65
[92] J. Mougin, G. Lucazeau, A. Galerie, M. Dupeux, Materials Science and Engineering A-Structural Materials Properties Microstructure and Processing 308 (2001) 118
[93] Finn Willy Poulsen, Personal Communication, 2003
[94] S. C. Tsai, A. M. Huntz, C. Dolin, Mater. Sci. Eng. A212 (1996) 6
[95] J. H. Park, W. E. King, S. J. Rothman, J. Am. Ceram. Soc. 70 (1987) 880
[96] B. Pieraggi, R. A. Rapp, J. Electrochem. Soc. 140 (1993) 2844
[97] P. Y. Hou, I. G. Brown, J. Stringer, Nuclear Instruments & Methods in Physics Research Section B- Beam Interactions with Materials and Atoms 59 (1991) 1345
[98] A. Atkinson, in: E. Lang (Ed.), The role of reactive elements in the oxidation behaviour of high temperature metals and alloys, Elsevier Science, London/New York, 1989, pp. 55-65.
[99] C. R. Wang, W. Q. Zhang, R. Z. Zhu, Materials Science and Engineering A-Structural Materials Properties Microstructure and Processing 125 (1990) 223
[100] J. Robertson, M. I. Manning, Mater. Sci. Technol. 5 (1989) 741
[101] S. N. Basu, G. J. Yurek, Oxid. Met. 35 (1991) 441
[102] C. Wagner, Zeitschrift fur Elektrochemie 63 (1959) 772
[103] R. A. Rapp, Acta Metallurgica 9 (1961) 730
[104] A. Atkinson, Corros. Sci. 22 (1982) 87

[105] F. Gesmundo, F. Viani, Oxid. Met. 25 (1986) 269
[106] F. Maak, Zeitschrift fur Metallkunde 52 (1961) 545
[107] G. Wang, B. Gleeson, D. L. Douglass, Oxid. Met. 35 (1991) 317
[108] W. Frank, H. J. Engell, A. Seeger, Transactions of the Metallurgical Society of Aime 242 (1968) 749
[109] R. J. Borg, D. Y. F. Lai, J. Appl. Phys. 41 (1970) 5193
[110] Robert C.Weast (Ed.), CRC Handbook of Chemistry and Physics, 1987, pp. 1-630.
[111] B. E. Deal, A. S. Grove, J. Appl. Phys. 36 (1965) 3770
[112] B. D. Bastow, D. P. Whittle, G. C. Wood, Oxid. Met. 12 (1978) 413
[113] D. T. Hoelzer, B. A. Pint, I. G. Wright, J. Nucl. Mater. 283 (2000) 1306
[114] B. Gleeson, M. A. Harper, Oxid. Met. 49 (1998) 373
[115] H. Nagai, T. Murai, H. Mitani, Transactions of the Japan Institute of Metals 21 (1980) 563
[116] Y. Saito, T. Maruyama, T. Amano, Materials Science and Engineering 87 (1987) 275
[117] F. H. Stott, F. I. Wei, Oxid. Met. 31 (1989) 369
[118] T. Adachi, G. H. Meier, Oxid. Met. 27 (1987) 347
[119] A. M. Huntz, M. K. Loudjani, C. Severac, C. Haut, F. Ropital, High Temperature Corrosion and Protection of Materials 4, Pts 1 and 2 251-2 (1997) 243
[120] D. L. Douglass, J. S. Armijo, Oxid. Met. 2 (1970) 207
[121] A. Atkinson, J. W. Gardner, Corros. Sci. 21 (1981) 49
[122] Anette Hansson, Personal Communication, 2003
[123] S. S. Kim, T. H. Sanders, J. Am. Ceram. Soc. 84 (2001) 1881
[124] Charles Evans & Associates, Auger Electron Emission Probabilities, 2003
[125] C. Jansson, G. T. Nielsen, J. Jakobsen, P. Morgen, Journal of Vacuum Science & Technology A-Vacuum Surfaces and Films 11 (1993) 183
[126] T. B. Massalski, Binary alloy phase diagrams, ASM International, 1990, pp. 1739-1744.
[127] H. E. Evans, A. T. Donaldson, Oxid. Met. 50 (1998) 457
[128] J. Shen, L. J. Zhou, T. F. Li, Oxid. Met. 48 (1997) 347
[129] G. Garnaud, R. A. Rapp, Oxid. Met. 11 (1977) 193
[130] F. Gesmundo, Y. Niu, Oxid. Met. 50 (1998) 1
[131] H. E. Evans, D. A. Hilton, R. A. Holm, S. J. Webster, Oxid. Met. 14 (1980) 235
[132] D. P. Whittle, G. C. Wood, D. J. Evans, D. B. Scully, Acta Metallurgica 15 (1967) 1747
[133] D. P. Whittle, Oxid. Met. 4 (1972) 171
[134] J. A. Nesbitt, J. Electrochem. Soc. 136 (1989) 1518
[135] J. Nicholls, Course in High Temperature corrosion, Göteborg, 2001
[136] J. A. Nesbitt, J. Electrochem. Soc. 136 (1989) 1511
[137] H. Taimatsu, J. Electrochem. Soc. 146 (1999) 3686
[138] H. Nickel, Y. Wouters, M. Thiele, W. J. Quadakkers, Fresenius Journal of Analytical Chemistry 361 (1998) 540
[139] A. Galerie, Y. Wouters, M. Caillet, High Temperature Corrosion and Protection of Materials 5, Pts 1 and 2 369-3 (2001) 231
[140] G. Hultquist, B. Tveten, E. Hornlund, M. Limback, R. Haugsrud, Oxid. Met. 56 (2001) 313
[141] N. Sakai, K. Yamaji, H. Negishi, T. Horita, H. Yokokawa, Y. P. Xiong, M. B. Phillipps, Electrochemistry 68 (2000) 499

[142] J. Mougin, A. Galerie, G. Lucazeau, L. Abello, High Temperature Corrosion and Protection of Materials 5, Pts 1 and 2 369-3 (2001) 841

Risø's research is aimed at solving concrete problems in the society.

Research targets are set through continuous dialogue with business, the political system and researchers.

The effects of our research are sustainable energy supply and new technology for the health sector.